CRANFIELD UNIVERSITY

NIALL SMYTH

Effect on Fatigue Performance of Residual Stress induced via Laser Shock Peening in Mechanically Damaged 2024-T351 Aluminium Sheet

SCHOOL OF APPLIED SCIENCES

PhD THESIS

Supervisor: Prof. P.E. Irving

December 2014

CRANFIELD UNIVERSITY

SCHOOL OF APPLIED SCIENCES

PhD THESIS

Academic Year 2014-2015

NIALL SMYTH

Effect on Fatigue Performance of Residual Stress induced via Laser Shock Peening in Mechanically Damaged 2024-T351 Aluminium Sheet

Supervisor: Prof. P.E. Irving

December 2014

Abstract

During manufacture and maintenance the fuselage skin of aircraft are susceptible to damage in the form of scratches. Normally not considered to be of major concern to aircraft structural integrity some airlines discovered fatigue cracks had initiated at the root of scratches. Crack propagation was in the through thickness direction and if left untreated could cause rapid decompression of the passenger cabin. Standard repair methodology requires patches be riveted around scratch damage and in extreme cases could require entire replacement of affected skin panels.

Laser shock peening (LSP) is an emerging surface treatment that has been shown to improve fatigue performance of safety critical components by inducing a surface layer of compressive residual stress. In this work LSP was applied along the scratch damage in an effort to restore pristine fatigue performance. The aim of the project was to model the effect on fatigue crack growth rate of residual stress fields induced via LSP and to validate predictions by comparison to experimental test results.

The scratches were recreated under controlled laboratory conditions using a diamond tipped tool. This process allowed creation of reproducible V shaped scribes to controlled depth, wall angle and root radius. Scribes of depth 50 and 150 µm with root radius 5 µm were created in dogbone shaped samples of 2 mm thick 2024-T351 clad aluminium. Samples were tested in fatigue at an R = 0.1 and maximum stress of 200 MPa. The scribe damage reduced fatigue life compared to the pristine material by a factor of 22. Scribed samples were processed using LSP treatment from different providers that created known residual stress fields in the material. The fatigue life of scribed samples after peening varied from a further decrease to a 13 times increase dependent on the residual stress field induced.

An elastic-plastic crack closure based finite element model was created to determine the effect on stress intensity factor and stress ratio of residual stress. Fatigue lives calculated were within a factor of 2 of experimental lives. It was predicted that crack closure was present during up to 80% of the applied load cycle due to the compressive residual stress field. However plasticity induced crack closure actually reduced after peening because the compressive residual stress field induced a smaller plastic zone at the crack tip and hence reduced the plastic wake.

A residual stress based fatigue life sensitivity study was performed to optimise the profile of the residual stress field for improved fatigue performance. The required profile was created in test samples using LSP. The fatigue life of peened samples increased by a factor of up to 15 however pristine life was not fully recovered. A restriction imposed by the industrial application was peening applied to one face

only. This created an unbalanced stress field that resulted in sample distortion to maintain equilibrium. The distortion induced out of plane bending stresses during testing and caused premature crack initiation on the unpeened face. However using interrupted fatigue tests it was found that although crack initiation also occurred at the root of the scribes the cracks were arrested after 24 μm of propagation. This was consistent with the findings of the crack growth prediction model.

Acknowledgements

I would sincerely like to thank my supervisor Prof. Phil Irving for his support, guidance and patience during of my PhD. I would like to thank Dr. Isidro Durazo-Cardenas and Ben Hopper for their advice and assistance with experimental testing. I would like to thank Dr. Domenico Furfari my industrial supervisor from Airbus and Prof. Mike Fitzpatrick and Dr. Burak Toparli from the Open University for the helpful comments and suggestions at our review meetings. I would like to thank my friends Jeremy Doucet and Dr. Daniel Gagar with whom I shared the high and lows of PhD life with. Finally I would like to thank my parents and family for their enduring support and encouragement.

Contents

List of Figures

List of Tables

1 Introduction

Several commercial airlines have discovered during routine inspections scratches on the fuselage skin of their aircraft. These scratches were located along the circumferential lap joints and longitudinal butt joints as illustrated in Figure 1.1. The cause of the scratches was attributed [1] to the use of improper and sharp tools (putty knives, razor blades etc.) during paint stripping and joint sealant removal prior to repainting of the aircraft fuselage. The joints extend the length of the fuselage and so the scratch marks have the potential to be multiple metres in length. Aircraft fuselage skin is load bearing and highly stressed in the region of joints. The scratches are of the order of 100 µm deep and although they are not of concern to the aircrafts static structural strength, the scratches are a point of stress concentration and during service are source for fatigue crack initiation.

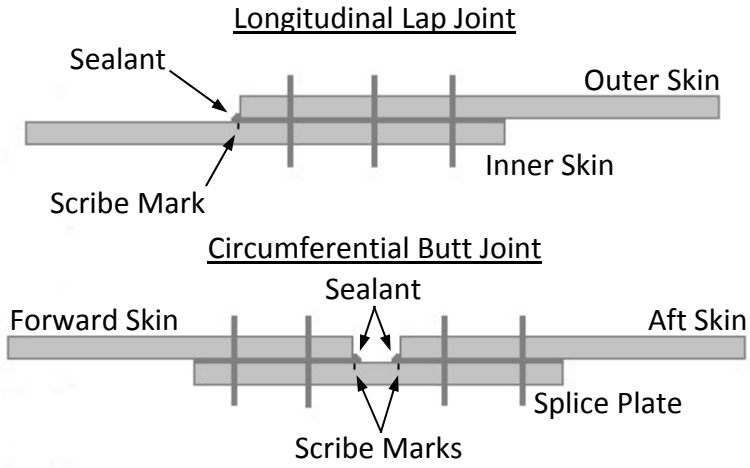

Figure 1.1: Schematic of aircraft longitudinal and circumferential joints demonstrating location of scratch damage

Modern aircraft are designed using the damage tolerance methodology. This ensures that the duration between service intervals allows repair of a fatigue crack before it can propagate to a critical length. Fatigue crack initiation in fuselage skin is usually at fastener holes or at skin panel edges and so the cracks are relativity easy to detect. As mentioned the scratches were caused prior to fuselage repainting meaning they can be hidden by the new paint or sealant and this can make detection difficult during maintenance inspections. Also fatigue cracks can initiate at multiple sites along the scratches and then coalesce to form a single crack of considerable length. Crack propagation from the scratches is in the skin through thickness direction as shown in Figure 1.2. When the crack has reached the opposing skin surface it will then propagate along the fuselage. The potential consequence of the scratch damage on

fatigue life was of such concern that several aviation authorities have issued airworthiness notices detailing specific inspection requirements for airlines [1-3].

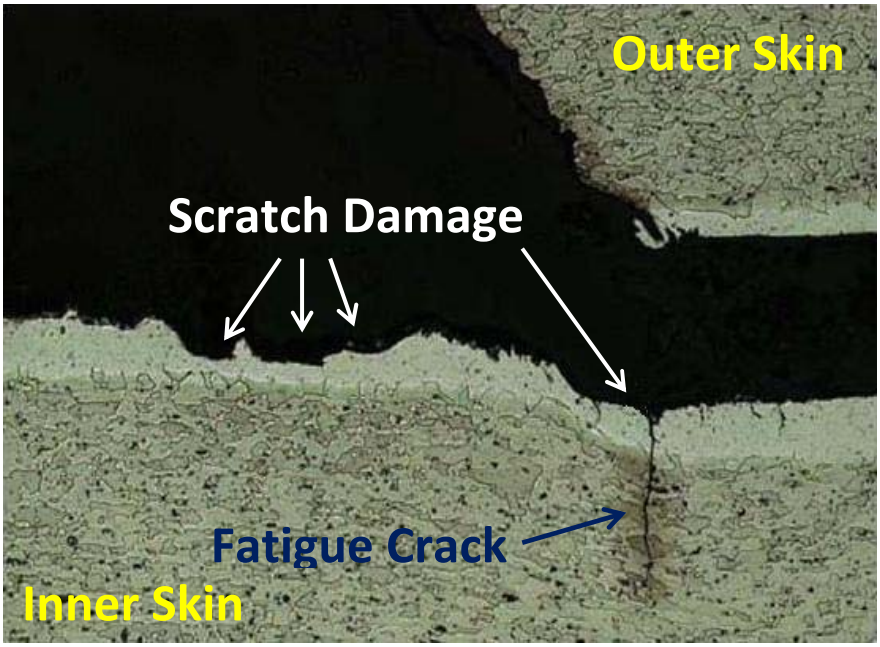

Figure 1.2: Cross section through skin joint showing fatigue crack propagation from scratch damage [4]

The standard repair method for scratches would require cutting out the affected section and repair with a riveted patch or replacement the entire skin panel. This procedure is both labour intensive and expensive. In fact one airline was forced to retire six Boeing 737-200 aircraft early due to scribe marks at fuselage joints with the airline stating the aircraft were beyond economical repair [5].

An alternative solution was proposed; surface treat the fuselage skin where the scratches are found using Laser Shock Peening (LSP). The LSP process involves firing a focused beam of laser light at the surface of the material creating a residual compressive stress field. The idea is that the compressive residual stress field will act to inhibit fatigue crack initiation or arrest propagation of the through thickness direction fatigue cracks. The advantages normally associated with LSP compared to other surface treatments is that it offers a deeper compressive residual stress field, is more controllable and it does not damage the surface finish. The associated disadvantages are it has a relatively high cost and can be a slower process.

There are two scenarios when LSP is applied to the structure. The first is during aircraft manufacture and the second as repair after detection of scratches during maintenance. There are key differences between these two scenarios. As a manufacturing process LSP can be applied to both sides of the fuselage skin and the

scratch damage, if it were to occur, would happen after peening. In contrast as a repair method it would only be practical to apply LSP on one side of the fuselage skin and peening would be applied to an already scratch that may already have caused initiation of a fatigue crack. In the current research LSP was considered as a repair process only.

Extensive work has been published in the literature to develop LSP processing techniques. The effect on fatigue life of LSP has also received significant attention for various application requirements. However no systematic studies have been published that connect the LSP induced residual stress field with the effect on baseline fatigue life. Furthermore very limited work has been published on the application of LSP treatment to thin sheet material such as fuselage skin. The aim of this project was to fill this gap in the current knowledge.

1.1 Project Objectives

The objectives of the research were:

- To measure the effect on fatigue crack initiation, propagation and total life of laser shock peened thin sheet aluminium containing mechanical defects in the form of surface scratches (scribe marks). To compare the effect on fatigue life of different residual stress fields induced by laser shock peening.
- To develop a fatigue life prediction model for scribed thin sheet material that contain residual stress fields.
- To investigate using elastic-plastic finite element analysis the effect on crack closure of residual stress.
- To use the fatigue life prediction model to investigate the effect on fatigue life of the characteristic features of residual stress fields. To use the findings of the study to determine the residual stress field to restore the fatigue life of the mechanically damaged material to that of pristine material. To validate the proposed repair via sample manufacture, laser peen treatment and fatigue testing.

1.2 Methodology

The methods used to achieve the objectives are described. The mechanical scratch damage found on aircraft at the fuselage joints is variable in depth and shape along the scratch line. The variability of damage is not ideal for controlled investigation of the effectiveness of laser shock peening as a repair method. To simulate in a laboratory setting the scratch damage, a diamond tipped tool was used. The diamond tool produced a consistent rounded tip V shaped notch along the scribed line to precisely controlled depths.

The effect on fatigue life of scribe depth, loading condition and laser shock peening treatment was studied using dogbone shaped test specimens of 2 mm thick 2024-T351 clad aluminium. The test samples were first scribed to depths of 50 or 150 µm and then tested in constant amplitude fatigue loading until sample fracture. Fatigue testing in two applied loading conditions was considered separately, tension-tension and four point bend. Fatigue tests were also performed at reduced maximum applied load levels. The effect on fatigue performance of various LSP treatments was considered. In all instances the samples were peened after the samples were scribed. The peened test samples were characterised by measuring the effect on sample distortion of LSP using a coordinate measurement machine and by measurement of the LSP induced residual stress field using the incremental hole drilling method (note: measurement of the residual stress fields was performed by research partners at The Open University).

After fatigue testing the sample fracture surfaces were studied using a scanning electron microscope. The effect of scratch geometry and laser peening treatment on the fatigue mechanisms occurring was investigated. The effect of LSP on fatigue crack growth was investigated by measurement of striation spacings on the fracture surface.

To understand the effect on fatigue crack growth of LSP a fatigue life prediction approach was developed. A 2D finite element model that used elastic material properties was created of the scratch geometry in 2 mm thick aircraft fuselage material. The model assumed crack initiation occurred on the first applied load cycle based on gathered experimental evidence. The crack was advanced from the scribe root and stress intensities factors (SIF) were calculated at multiple crack lengths. Residual stress was input to the FE model as an initial condition and the effect on SIF range and stress ratio was determined. This data was then input to fatigue crack growth equations based on experimentally measured crack growth rates and fatigue lives were calculated. A finite element model that used elastic-plastic material properties was also developed. The effect of the induced residual stress fields on plasticity induced crack closure was studied by use of contact conditions along the crack path in the model.

A method was developed to determine an optimum residual stress field profile. This approach considered the effect on fatigue life of various aspects of the residual stress profile such as depth and peak stress. Once determined the optimum profile was peened by the project's LSP partners and fatigue samples tested to determine validity of the predictions.

1.3 Thesis Structure

In chapter 2 a literature review is presented. The theoretical background of fracture mechanics and classical fatigue life prediction methodologies are presented. The sources of residual stress in components and its effect on fatigue performance and crack closure are reviewed. Methods used to predict the effect on fatigue crack growth of residual stress are detailed and specific note is made of comparisons between fatigue life predictions and experimental measurement of fatigue life. The effect on fatigue performance of scratch damage is reviewed. Finally a description of the LSP technique is provided and applications of LSP to improve fatigue performance are reviewed. Particular attention is paid to applications of LSP to thin sheet material (< 3 mm).

In chapter 2.4.7 the experimental procedures are described. The test material is characterised and the test sample geometries are presented. The method used to 'simulate' real world scratches in the laboratory using diamond tipped tools is detailed. The parameters are given of the LSP systems used for peening treatment. The fatigue test procedures and test parameters used are described. The procedures used for fractographic inspection are detailed.

The experimental results are in Chapter 4. The physical effect on the fatigue specimens of LSP treatment is described. Tension-tension and four-point bend fatigue test results are presented. Calculated fatigue crack growth rates from striation-spacing measurements and crack length at final fracture are given.

In chapter 5 modelling techniques used to study the effect on stress intensity factor of residual stress are described. A finite element model was developed and is detailed. The effect on the residual stress field of crack advance from the scribe root is studied. Also the effect on the stress intensity factor and the stress ratio are reported.

Chapter 6 expands the FE model presented in chapter 5 to include elastic-plastic material effects. Specifically the effect of prior loading history on the current crack tip stress state in the form of plasticity induced crack closure is investigated. The effect of residual stress on crack closure was studied and the results of the analysis are presented.

Presented in chapter 7 are predicted fatigue lives of cracks advanced from the root of scribes through residual stress fields induced by LSP. Comparison is made between predicted results and experimental results. The main characteristic features of residual stress fields induced by LSP are identified and the effect on fatigue performance of these features are analysed. Based on the sensitivity study

recommendations are made for the required residual stress field to restore the fatigue performance of the damaged samples to the pristine state.

The research results are discussed in chapter 8. Chapter 9 presents the conclusions from the research and recommendations for future work are made in chapter 10.

2 Literature Review

A literature review is given in this chapter. In section 2.1 a brief overview of the fundamentals of fatigue and fracture mechanics is provided. Also reviewed are fatigue crack growth (FCG) prediction models, short crack effects and finally a short section on striation spacings sometimes found on fatigue fracture surfaces.

In section 2.2 the effect on fatigue performance of scratch damage is reviewed. This focuses mainly on work performed at Cranfield University but also the limited other investigations found in the literature. In section 2.3 the effect on FCGR of crack closure is reviewed. Particular attention was paid to measurement and modelling of crack closure in the presence of residual stress fields.

Finally reviewed in section 2.4 is residual stress. The sources of residual stress in components is outlined and methods of measurement are detailed. Reported effects on fatigue performance of residual stress are reviewed and particular attention is given to residual stress fields in thin sections. Also fatigue life predictions methodologies that include residual stress in effects are decribed.

2.1 Fatigue and Fracture Mechanics

In this section a brief overview of the concepts of fatigue and fracture mechanics are given. Fracture mechanics is based on the assumption that all engineering materials contain flaws or cracks where the applied stress will concentrate and from which failure starts. For a detailed review of fracture mechanics see reference books by Anderson [6] and Hertzberg [7].

In 1920 Griffith [8] established that a crack can form or grow only if a process causes the total energy to decrease or remain constant. The Griffith energy balance for an incremental increase in the crack area, dA, is expressed as:

$$\frac{dE}{dA} = \frac{d\prod}{dA} + \frac{dW_s}{dA} = 0 \quad (2.1)$$

Where E is the total energy, $\prod$ is the potential energy supplied by the internal strain energy and external forces and W_s is the energy required to create new surfaces. The term $-d\prod/dA$ is referred to as the strain energy release rate (SERR or G). It has been demonstrated [9] that the SERR is equal to:

$$G = \frac{\pi\sigma^2 a}{E} \quad \text{plane stress} \quad (2.2)$$

$$G = (1-\nu^2)\frac{\pi\sigma^2 a}{E} \quad \text{plane strain} \quad (2.3)$$

The SERR can be correlated to the stress intensity factor (SIF or K) using equations 2.4 and 2.5. The derivation of SIF is described below.

$$K = \sqrt{GE} \quad \text{plane stress} \quad (2.4)$$

$$K = \sqrt{\frac{GE}{1-\nu^2}} \quad \text{plane strain} \quad (2.5)$$

When the applied load plane is perpendicular to the crack plane it is termed mode I loading. The crack tip stress field in mode I can be obtained using the following equation.

$$\lim_{r\to 0} \sigma_{ij}^{(I)} = \frac{K_I}{\sqrt{2\pi r}} f_{ij}^{(I)} \quad (2.6)$$

Where σ_{ij} is the stress tensor acting on the infinite element $dx \times dy$ whose distance from the crack tip is defined by the polar coordinate r and θ as illustrated in Figure 2.1.

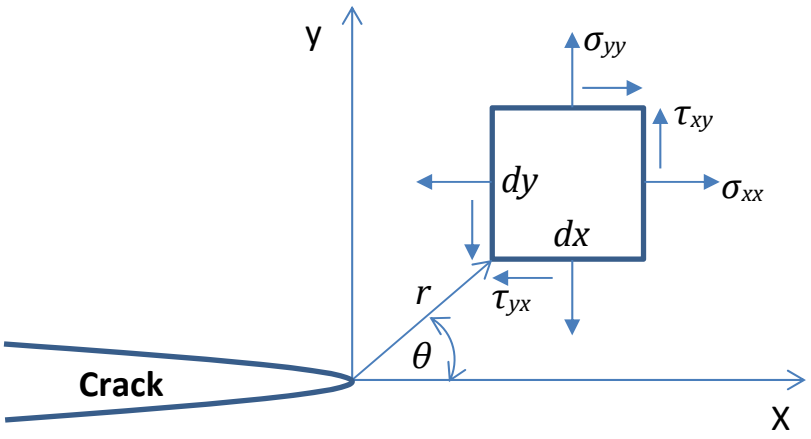

Figure 2.1: Coordinate system at crack tip

The stress field at the crack tip can be expressed as:

$$\sigma_{xx} = \frac{K_I}{\sqrt{2\pi r}} cos\left(\frac{\theta}{2}\right)\left[1 - sin\left(\frac{\theta}{2}\right) sin\left(\frac{3\theta}{2}\right)\right] \quad (2.7)$$

$$\sigma_{yy} = \frac{K_I}{\sqrt{2\pi r}} cos\left(\frac{\theta}{2}\right)\left[1 + sin\left(\frac{\theta}{2}\right) sin\left(\frac{3\theta}{2}\right)\right] \quad (2.8)$$

$$\tau_{xy} = \frac{K_I}{\sqrt{2\pi r}} cos\left(\frac{\theta}{2}\right) \sin\left(\frac{\theta}{2}\right) \cos\left(\frac{3\theta}{2}\right) \quad (2.9)$$

And the displacement relationships are:

$$u_x = \frac{K_I}{2\mu}\sqrt{\frac{r}{2\pi}}\,cos\left(\frac{\theta}{2}\right)\left[k - 1 + 2sin^2\left(\frac{\theta}{2}\right)\right] \quad (2.10)$$

$$u_y = \frac{K_I}{2\mu}\sqrt{\frac{r}{2\pi}}\,sin\left(\frac{\theta}{2}\right)\left[k + 1 - 2cos^2\left(\frac{\theta}{2}\right)\right] \quad (2.11)$$

A closed form solution of K_I, as shown in equation 2.12, can then be derived for a through crack in an infinite plate subjected to remote tensile stress.

$$K_I = \sigma\sqrt{\pi a} \quad (2.12)$$

This can then be related to a crack in a finite plate by use of the non-dimensional geometry factor β as shown in equation 2.13.

$$K_I = \beta\sigma\sqrt{\pi a} \quad (2.13)$$

The stress intensity factor (SIF or K) is one of the most important concepts in linear elastic fracture mechanics and characterises the stress distribution in the vicinity of the crack tip. It is valid only if gross yielding does not occur. However it is sometimes necessary to account for the effect of plasticity in the vicinity of the crack tip. This is achieved by adding the size of the plastic zone (r_p) to the crack length (a) to form an effective crack length (a_{eff}) as shown in equation 2.14.

$$a_{eff} = a + r_p \quad (2.14)$$

For conditions of plane stress the plastic zone size can be estimated using equation 2.15. An empirical based estimate of applicability of plane stress is $r_p > (t/2)$. Therefore equation 2.15 becomes equation 2.16.

$$r_p = \frac{1}{2\pi}\left(\frac{K}{\sigma_y}\right)^2 \quad (2.15)$$

$$t < 0.32\left(\frac{K}{\sigma_y}\right)^2 \quad (2.16)$$

For conditions of plane strain the plastic zone size is assumed to be one third that of plane stress as shown in equation 2.17. An empirical based estimate of applicability of plane strain is $r_p > (t/50)$. Therefore equation 2.17 becomes equation 2.18.

$$r_p = \frac{1}{6\pi}\left(\frac{K}{\sigma_y}\right)^2 \quad (2.17)$$

$$t<2.5\left(\frac{K}{\sigma_y}\right)^2 \quad (2.18)$$

Fatigue is the progressive and localized damage that occurs when a material is subjected to cyclic loading. The maximum applied stress to cause failure by fatigue can be far less than the ultimate tensile stress or even the yield stress of the material. Fatigue failure starts on a microscopic scale as a minute crack or defect that gradually grows under the action of cyclic stress until complete fracture occurs. For a detailed overview of fatigue consult the following reference books by Suresh [10] and Schijve [11].

A component or structure throughout its service life is usually subjected to cyclic stress with varying upper and lower stress bounds. This type of loading is generally referred to as variable amplitude loading however for simplification purposes it is normal to assume constant amplitude loading usually in the form of a sinusoidal waveform as illustrated in Figure 2.2. The terminology used throughout this thesis to describe the parameters of the waveform is shown in Figure 2.2.

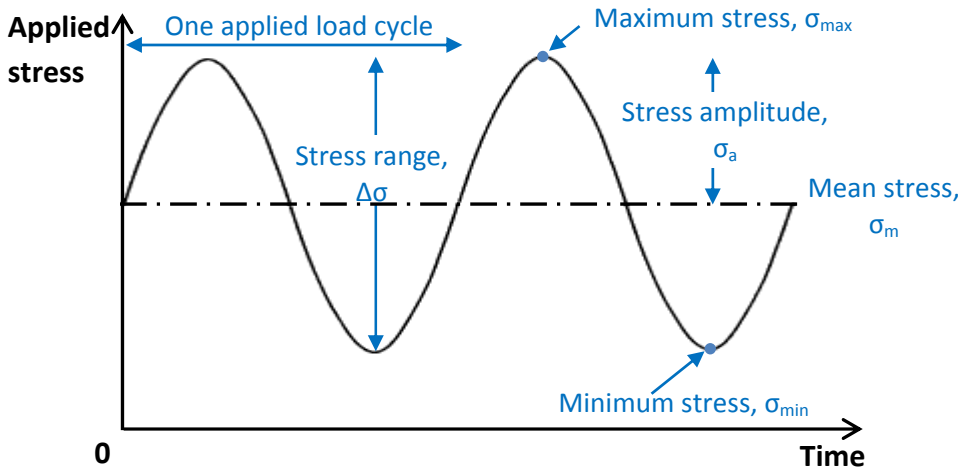

Figure 2.2: Nomenclature to describe test parameters involved in fatigue testing

The total fatigue life can be characterised by four stages: crack nucleation, stage I crack growth, stage II crack growth and ultimate ductile fracture. These stages are described briefly below however it should be noted that the transition from one stage to another is a continuous process.

1. Crack nucleation

Above a critical level of cyclic stress grains on the surface of a material develop bands during cyclic loading. These bands result due to sliding or shearing of atomic planes within crystals and are called slip bands. With continued cycling the slip bands

broaden and intensify until separation occurs and a crack is formed. Other causes of crack initiation include dislocations and defects in the material. The number of cycles to initiate a crack frequently account for the majority of the total fatigue life.

2. Stage I crack-growth

Stage I crack growth is when the crack initially develops along the slip plane of the grain in which it was formed. This stage is characterised by the crack being orientated at an angle to the surface but not normal to the applied load. Crack nucleation and stage I crack growth are governed by the stress concentration factor K_t where K_t is the ratio of local stress to global stress.

3. Stage II crack-growth

The transition from stage I to stage II occurs when the crack tip plastic zone is large enough to activate many independent slip systems. These slip systems are no longer dependent upon crystallographic orientation and therefore the crack can propagate according to the prevalent loading conditions. In stage II crack growth the crack propagates across other grains normal to the loading direction. This growth occurs not as a consequence of any structural damage but as a result of the stress concentration effect at the crack tip as it becomes sharp during unloading.

Stage I and stage II crack growth are often grouped together and the total fatigue life N_{tot} is characterised using equation 2.19.

$$N_{tot}=N_i+N_p \quad (2.19)$$

Where N_i is the number of cycles until crack initiation and N_p is the number of cycles to propagate the crack to fracture.

4. Ultimate failure

Failure of the material occurs when the crack extends in a rapid and unstable manner. The fracture toughness (K_c or K_{Ic}) of a material indicates the strength of the material in the presence of a defect or crack. The fracture toughness is also affected by thickness with thin sections having greater toughness than thick sections. The fracture surface of thin sections are generally characterised by shear lips as a result of the high energy fracture known as plane stress fracture. The fracture surfaces of thick section are flat and known as plane strain fractures.

Crack propagation rate depends primarily on crack length, the applied stress range (σ_{max} - σ_{min}) and the stress ratio (R = σ_{min} / σ_{max}). The stress intensity factor approach accounts for these parameters as demonstrated in equation 2.20 and 2.21.

$$\Delta K = K_{max} - K_{min} \quad (2.20)$$

$$R = \frac{K_{min}}{K_{max}} \quad (2.21)$$

The value of K_{max} is always dependent on σ_{max} in the form of equation 2.13. However the value of K_{min} can be influenced by other effects such as crack closure which will be discussed in more detail in section 2.3.

2.1.1 Models for Prediction of Fatigue Crack Growth Rate

Paris [12] was the first to report a relationship between the fatigue crack growth rate and the stress intensity factor range as shown in equation 2.22 below where C and n are material constants determined experimentally.

$$\frac{da}{dN} = C(\Delta K)^n \quad (2.22)$$

The formula describes the linear portion of the log-log plot of da/dN vs. ΔK as shown in Figure 2.3. This figure illustrates the typical fatigue crack growth behaviour of metals.

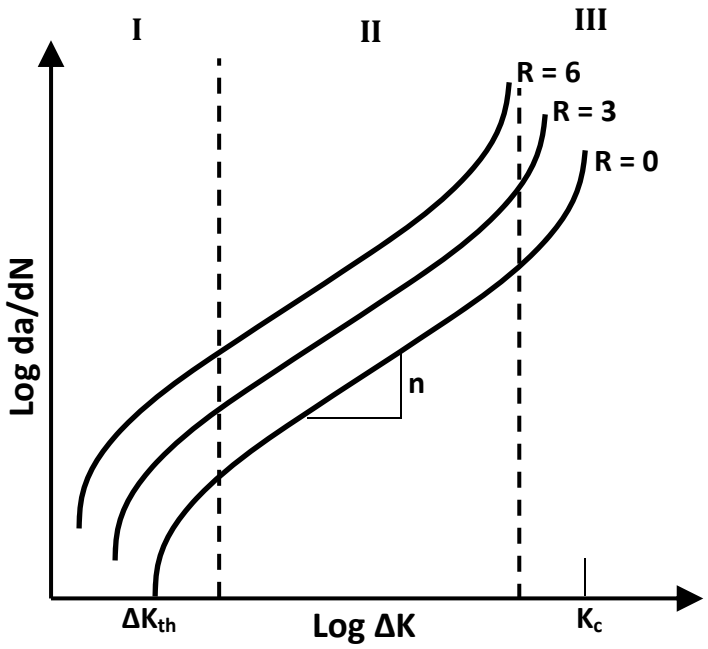

Figure 2.3: Typical fatigue crack growth behaviour in metals

The major limitation of the Paris equation is that the material constants must be determined for different load conditions. Under constant amplitude loading FCGR will only be influenced by the stress ratio R which cannot be taken into account by this law. Other researchers have developed equations which describe all or part of the da/dN vs. ΔK relationship. The Walker equation [13] was an enhancement of the

Paris equation that accounted for the effect of stress ratio on FCGR. The Walker equation is shown below where m is an exponent that controls the shift in the crack growth data.

$$\frac{da}{dN} = C\left(\Delta K(1-R)^{(m-1)}\right)^n \quad (2.23)$$

The Forman equation [14] is a further improvement on the Walker equation that accounts for the upper portion of the da/dN vs. ΔK curve. The Forman equation is shown below where K_c is the fracture toughness of the material as shown in Figure 2.3.

$$\frac{da}{dN} = \frac{C(\Delta K)^n}{\left((1-R)K_C - \Delta K\right)} \quad (2.24)$$

Klesmil & Lukas [15] modified the Paris equation to account for material threshold as shown in the equation below.

$$\frac{da}{dN} = C(\Delta K^n - \Delta K_{th}^n) \quad (2.25)$$

The NASGRO equation [16] accounts for the complete fatigue crack growth curve and is shown below where C and n are material constants and p and q control the slope of the threshold and failure regions respectively.

$$\frac{da}{dN} = C\left[\left(\frac{1-f}{1-R}\right)\Delta K\right]^n \frac{\left(1-\frac{\Delta K_{th}}{\Delta K}\right)^p}{\left(1-\frac{K_{max}}{K_C}\right)^q} \quad (2.26)$$

2.1.2 Short Crack Effects

It was first shown by Pearson [17] that short cracks propagate at a faster rate than long cracks when correlated against stress intensity factor range. Small cracks can also propagate below the threshold (ΔK_{th}) of long fatigue cracks. This behaviour is illustrated in Figure 2.4 for a given material under constant amplitude loading. Short crack behaviour is usually more pronounced at negative stress ratios.

There is still no general consensus on what fully constitutes a short crack. Ritchie & Lankford [18] defined a microstructurally short crack as one having length less than a critical microstructural dimension such a grain size. They described a mechanically short as having length less than the plastic zone size and a physically short as having length less than 1 mm. Because of the scales involved acquisition of short crack data is more difficult than long cracks. Characterisation of short crack growth behaviour is time consuming, tedious, and can be subject to large experimental scatter [7].

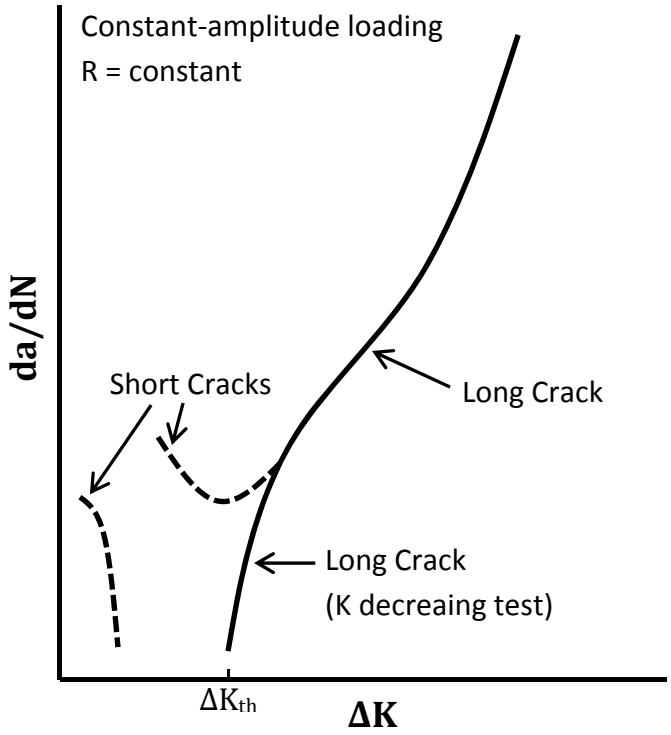

Figure 2.4: Illustration of fatigue crack rate data for long and short cracks

The crack growth behaviour of short cracks is further complicated if the crack is embedded in the stress field around a notch [7]. Due to the rapidly decreasing stress field around the notch the FCGR may decrease initially with increasing crack length. Then depending on the local stress conditions the FCGR could accelerate with increasing crack length or even arrest.

Experimental short and long FCGR data for 2024-T3 aluminium is compared in Figure 2.5 [19]. At constant amplitude loading with negative stress ratio of -2 (Figure 2.5 (A)) short FCGR was greater than long FCGR at the same stress intensity factor range. This is usually attributed to two factors: plastic zone size and crack closure [6]. For instance some authors successfully correlated FCGR data of long and short cracks down to ≈20 µm by correcting ΔK for crack closure effects (i.e. ΔK_{eff}) [20,21]. The short crack threshold in Figure 2.5 (A) is not clearly identifiable however it is apparent that it was less than long crack threshold. As seen in Figure 2.5 (A) there was a lot of scatter in the short crack data. This is normal behaviour for short cracks which are greatly influenced by microstructural features. The sporadic growth rate of short cracks is often attributed to microstructural barriers such as grain boundaries and second phase particles [22]. Short crack test results at a stress ratio of 0 (Figure 2.5 (B)) showed similar FCGR to long cracks at the same ΔK in the region above the long crack threshold. Fatigue tests performed [19] at a positive stress ratio of 0.5 (not

shown) found short cracks actually grew at a rate slightly slower than long cracks at the same ΔK above the long crack threshold.

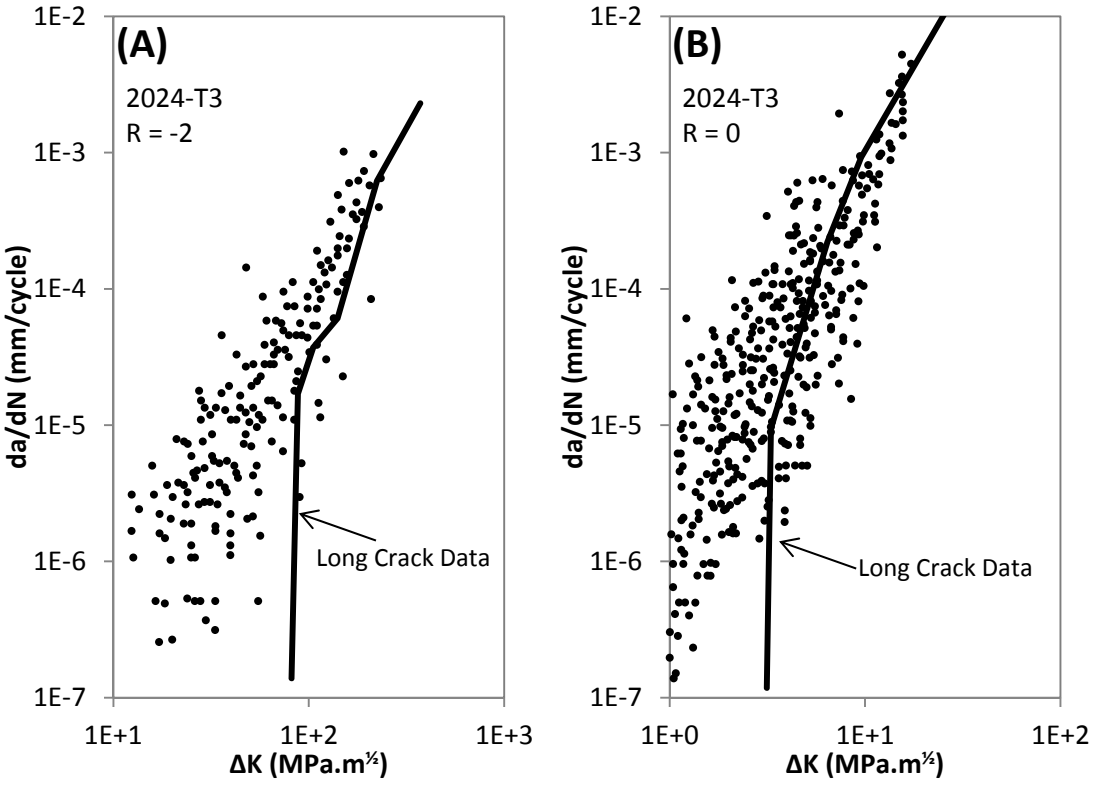

Figure 2.5: Comparison of short and long FCGR data for Al2024-T3 at (A) R = -2 and (B) R = 0 [19]

2.1.3 Fatigue Striations

An important characteristic of stage II fatigue crack growth is the formation of fatigue striations on the fracture surface. Under constant amplitude loading the striation spacing represents the increment of crack growth that occurs in one load cycle [10,23]. As such with the aid of scanning electron microscopy fatigue crack growth rates can be estimated from counting and measurement of striation spacings [24-27]. However not all engineering materials exhibit striations. They are clearly seen in pure metals and many ductile alloys such as aluminium. Striations are actually ripples on the fracture surface. The most commonly accepted mechanism [28,29] for the formation of striation marks is the successive blunting and re-sharpening at the crack tip with crack growth as illustrated in Figure 2.6.

Difficulties using striation counting to estimate FCGR may arise. Striation development is strongly influenced by ΔK, stress state, environment and alloy content [10]. Striations can get easily damaged due to rubbing, oxidation, corrosion or fretting. High cycles fatigue may produce a high density of striations on the fracture surface which cannot be clearly resolved making accurate counting difficult

[30]. Ideally striation counting should be done across a flat surface however most fracture surfaces are not entirely flat. Therefore striations measured on an angled surface may result in artificially shortening of the striation spacing [30].

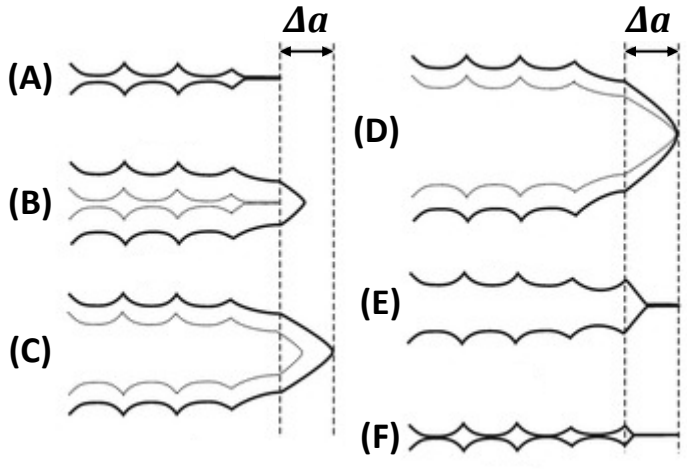

Figure 2.6: Mechanisms of striation formation in stage II propagation: (A) no load, (B) tensile load, (C) intermediate tensile load, (D) maximum tensile load, (E) load reversion and (F) no load

2.2 Effect on Fatigue Life of Scratches and Scribes

The effect of scratches on fatigue performance was first investigated by Nader [31]. He created rounded tip scratches of depths from 40 to 225 µm using a modified milling machine. Fatigue tests were performed using dogbone samples to a maximum stress of 345 MPa using a stress ratio of 0.1. As scratch depth increased fatigue life at any stress amplitude decreased. In the worst case fatigue life was reduced by up to 98% compared to pristine material. Observation of the root of the scratches revealed sub grain size micro crack formation. The micro cracks coalesced to form a single crack front that propagated in the through thickness direction. Deeper scratches resulted in earlier crack initiation as well as a greater number of nucleation sites along the scratch root.

Inchekel and Talia [32] studied the effect on fatigue life of scratches in aluminium lithium alloy 2090 F. They reported that fatigue life reduced as scratch depth was increased and also as the radius of the scratch root was reduced. Examination of fracture surfaces revealed crack initiation at multiple sites along the scratch root and that the cracks coalesced as they propagated through the material.

The effect on fatigue life of scratches in unclad 2024-T3 was investigated by Talia & Talia [33]. Scratches of depth 20, 50 and 100 µm were scribed in samples then tested under constant amplitude load at a stress ratio of 0.1. They observed that cracks initiated at the root of the scratches and initially propagated in mode I indicated by a

perpendicular fracture surface to loading direction. The fracture mode transitioned to shear evident by shear lips on the fracture surface. They reported that fatigue life decreased as the scratch depth was increased and that the fatigue crack growth rates were greater for the deeper scratches. The fatigue life of specimens with scribes 150 µm deep was 15× less than pristine samples. They also proposed [34] a semi-empirical method to predict crack propagation from the root of scratches as shown in equation 2.27.

$$\Delta K_{eff} = \beta K_t \Delta\sigma\sqrt{\pi a} \quad (2.27)$$

According to the proposed equation the scratch behaves like a notch i.e. it increases the local stress range and therefore the crack driving force by means of the elastic stress concentration factor K_t. Experimental long crack growth data for unscratched material was assumed valid for scratched samples

Everett *et al.* [35] evaluated the effect on fatigue life of scratches in 4340 steel 8.9 mm thick. The scratches, created using a milling machine, were of rounded V shape 51 µm deep created in dogbone shaped samples. Constant amplitude fully reversed (R = -1) fatigue tests were performed on scratched and unscratched material. The scratches reduced the fatigue limit by 40% compared to pristine material. The fatigue life of the scratched samples was 12× less than the pristine samples at an applied stress range of 550 MPa. A fatigue life prediction model was proposed that assumed the total life consisted of only crack propagation i.e. no initiation period. The software code FASTRAN was used to calculate the fatigue crack growth life and close agreement with experimental results were obtained.

Das *et al.* [4] observed scratches initiated at multiple sites along scratches in longitudinal and circumferential aircraft fuselage joints. The scratches coalesced during early crack growth and continued to propagate in the through thickness direction as one long continuous crack front. A damage tolerance methodology for scratches was developed. Stress intensity factors were calculated based on a constant geometric modification factor for fatigue cracks growing from scratches based striation spacing measurements. Stress intensity factor solutions were also empirically determined from crack growth data. The suggested method was validated against service data of aircraft fleets.

Kyle [36] assessed the effect on fatigue performance of scratches in clad 7075-T6 aluminium. The scratches were created using two methods, material removal by machining and plunging a tool into the material. Using these methods scratches 50 to 150 µm deep were created. The samples were tested in fatigue to a peak stress of 175 MPa at R = 0.1. He measured no difference in fatigue performance between

machined and plunged formed scratches. If the scratch root was inside the clad layer the fatigue life reduced by 40% compared to the pristine material. However if the root of the scratch was inside the substrate it reduced fatigue life only if it was deeper than 190 µm.

Morency [37] studied how scratch depth affected fatigue performance. The scratches were created using diamond tipped tools in 2024-T351 aluminium in clad and unclad conditions. He considered three scribe depths of 50, 100 and 200 µm. All scribes had root radius of 5 µm and wall angle of 60°. The samples were tested under cyclic loading to a maximum stress of 200 MPa at an R of 0.1. For unclad material fatigue cracks initiated at the root of all scribes however only the scribes of 200 µm depth fractured due to these cracks. For clad material the scratches of depth 50 and 200 µm caused fracture due to crack initiation at the root. The scratches 100 µm deep (similar depth of the clad / substrate interface) did not affect the fatigue life compared to baseline material.

The effect on fatigue performance of different scraping tools such as plastic scrapers, sharpened aluminium strips and Stanley blades was assessed [38,39]. Tests were performed on 2024-T351 aluminium 2 mm thick fatigued to 200 MPa maximum stress at an R = 0.1. The plastic scrapers did not damage the material sufficiently to affect fatigue life (note: these are the recommended tool for removal of sealant at fuselage joints). The aluminium strips produced irregular scratches. Fatigue cracks did initiate from these scratches but only if the scratch penetrated through the clad layer. The Stanley blade created sharp V shaped scratches that penetrated through the cladding. The scratches were similar in profile to the scribes created using diamond tools however the blades ploughed through the material leaving behind plastically deformed material.

The effect on fatigue life of the scratches created by sharp knives was explored further by Tizard [40]. He created scratches of various depths and found that the fatigue performance of scratched material was actually greater than the pristine material. The hardness and residual stress around the scratch root was measured using nanoindentation. The hardness around the scratches had increased whereas he measured the hardness around the diamond cut scribes to be equivalent to the baseline material. Compressive residual stress equal to the material's yield strength was measured at the root of the scratches. The combination of increased hardness and compressive residual stress was the reason for the increased fatigue performance of scratched material. Furthermore Tizard's fatigue results indicated a stress concentration threshold of K_t = 6 existed below which scratches did not affect fatigue life.

The residual stress field around machined and diamond cut scratches was measured using synchrotron X-ray diffraction [41]. Machined scratches with root radii of 5 µm induced tensile residual stress around the root. In fact the magnitude and extent of the residual stress field was twice that of the diamond cut scribes. However for scratches with root radii of 50 µm no residual stress was measured at the root.

Cini [42] accessed the sensitivity of 2024-T351 aluminium 2 mm thick to scribe damaged created using a diamond tipped tools He studied scribes of depth 25 to 185 µm with 60° wall angle and using different diamond tools he varied the scribe root radius from 5 to 50 µm. Dogbone shaped samples were scribed and tested in fatigue to a maximum stress of 200 MPa and at R = 0.1. The reduction of fatigue life was greater as the scribe depth was increased or as the root radius was reduced. The greatest decrease of fatigue life was 97.8% for a scribe 185 µm deep with 5 µm root radius. He found for scribes of K_t > 7.8 multiple cracks initiated along the root but coalesced during early propagation forming one long crack that then continued to propagate in the through thickness direction.

2.3 Crack Closure

A variety of different mechanisms can be involved in the development of crack closure such as: plasticity induced closure, roughness induced closure, crack filling closure, transitional closure, transformal-induced closure and grain boundary closure [43]. The focus of this section is plasticity induced crack closure first observed by Elber [44]. During cyclic loading residual plastic deformation is built up in the wake of an advancing fatigue crack. This plastic deformation induces a compressive stress that causes the crack faces to close prior to the minimum load being reached. Upon reapplication of the applied external load the crack faces do not separate at the minimum load but at a greater load termed the opening stress level (σ_{op}). The crack is no longer open at K_{min} but instead opens at K_{op} hence a new SIF range must be defined. This is termed the effective SIF range (ΔK_{eff}) and is calculated using equation 2.28.

$$\Delta K_{eff}=\left(\sigma_{max}-\sigma_{op}\right)\beta\sqrt{\pi a} \quad (2.28)$$

The crack closure concept is illustrated in Figure 2.7. The portion of the fatigue cycle below K_{op} does not contribute to crack growth since the crack is closed. Crack closure shields the crack tip from the full effects of the stress intensity factor range so that it only experiences the effective stress intensity factor range and so should have no net benefit on fatigue life.

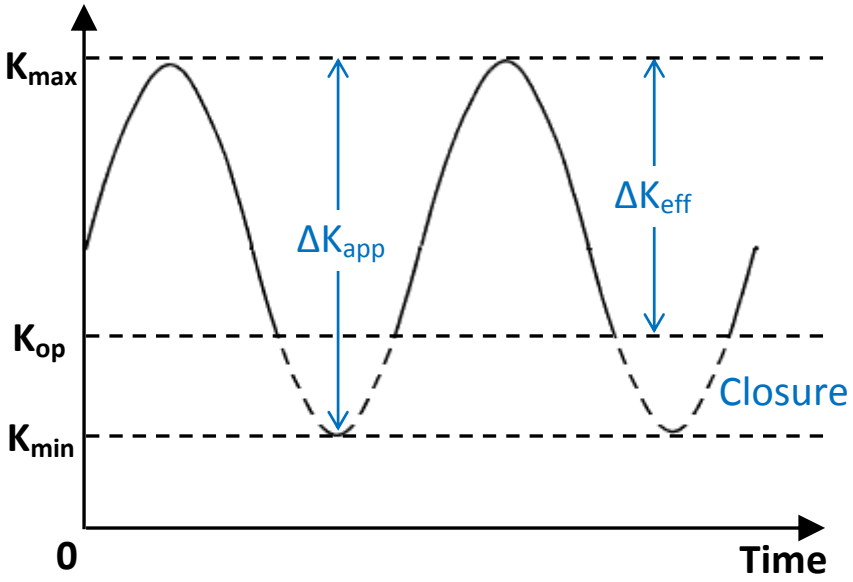

Figure 2.7: Definition of the effective stress intensity factor range

Experimental techniques to measure the crack opening stress level have a high associated cost and effort [45]. Deformation of the crack face is not uniform and it can be difficult to determine the exact opening location in order to consider the crack fully open [45]. Elber [46] proposed an empirical rule for 2024-T3 material to correlate the opening stress ratio with R ratio as shown in equation 2.29.

$$\frac{\sigma_{op}}{\sigma_{max}} = 0.5 + 0.1R + 0.4R^2 \quad (2.29)$$

Equation 2.29 is plotted in Figure 2.8 and results in unrealistic opening stress ratios at negative stress ratios. Schijve [47] proposed a new equation based on experimental observations:

$$\frac{\sigma_{op}}{\sigma_{max}} = 0.45 + (0.1 + \alpha)R + (0.45 - 2\alpha)R^2 + \alpha R^3 \quad (2.30)$$

where α is a constraint parameter. Equation 2.30 is plotted in Figure 2.8 for α = 0.1 to 0.15. De koning [48] developed the following equations based on experiments using 7075-T6:

$$For\ R > 0 \quad \frac{\sigma_{op}}{\sigma_{max}} = 0.45 + 0.2R - 0.15R^2 + 0.9R^3 - 0.4R^4 \quad (2.31)$$

$$For\ R \leq 0 \quad \frac{\sigma_{op}}{\sigma_{max}} = 0.45 + 0.2R \quad (2.32)$$

This is also plotted in Figure 2.8. Even though there are some differences between predicted opening stress ratios using these equations, it is clear that closure effects

are more pronounced at low and negative stress ratios. The stress opening level can also be determined using the finite element method and this is explored further in next sections.

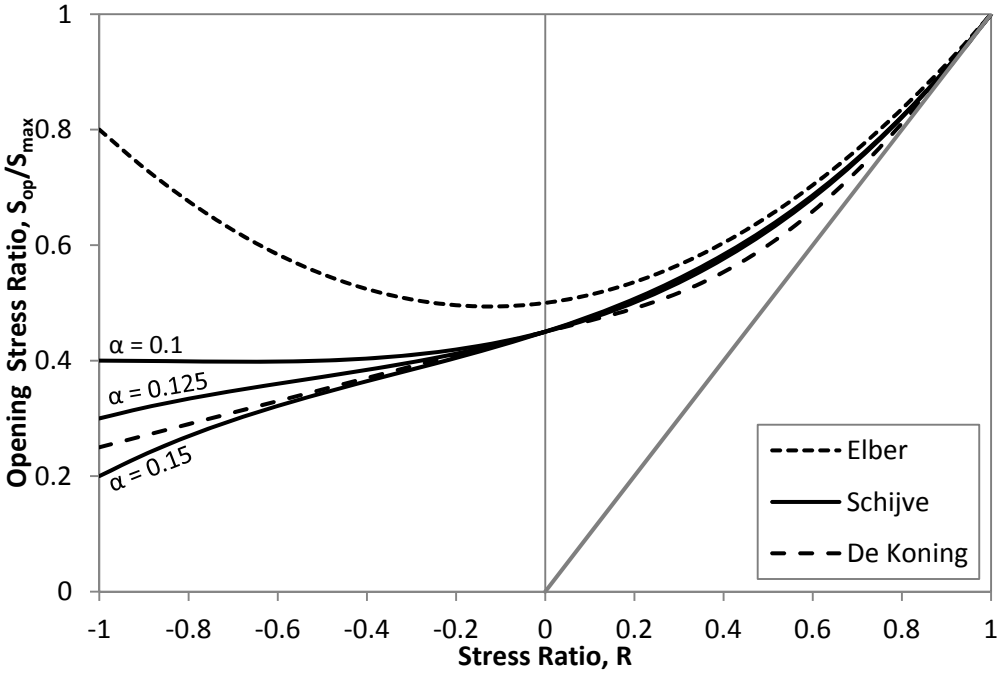

Figure 2.8: Crack opening stress ratio according to different empirical formulas

The growth and closure behaviour of plane strain short cracks in 2024-T351 aluminium alloy was studied [49]. The short cracks were created by machining off the major portion of specimens containing long cracks which resulted in cracks of length between 0.16 and 0.57 mm. Fatigue tests were performed in bend at six R ratios between 0.5 and -1.0. Fatigue crack growth rate and crack closure were measured using a compliance based technique. It was found that short cracks grew faster than long cracks at small ΔK and the FCGR of short and long crack merged with increasing ΔK. Also the difference in long and short FCGR reduced as the R ratio increased. The long and short crack growth rate behaviour plotted as a function of ΔK_{eff} is shown in Figure 2.9 (A) (note only the outer bounds of the long FCGR data is shown for clarity). There is good agreement between the data which implies that the difference in growth rate is mainly governed by crack closure. However as shown in Figure 2.9 (B) the closure behaviour of short cracks was significantly different than that of long cracks.

Kujawksi [50,51] has argued that crack closure is not the sole mechanism responsible for correlating the effect of load ratio, overloads and type of loading with the FCGR. He considered the case of partial crack closure, which is when the cracks face contact first behind the crack tip. This can occur particularly in the near threshold region of

crack growth when the fracture surfaces can be faceted and mismatched. He stated this can cause the crack shape to change from a blunt parabolic to a sharper wedge shape which can induce damaging strain ahead of the crack. He also states that FCGR is dependent on the interplay of two damaging processes at the crack tip namely K_{max} and the positive part of the SIF range ΔK^{+} and not just the effective SIF.

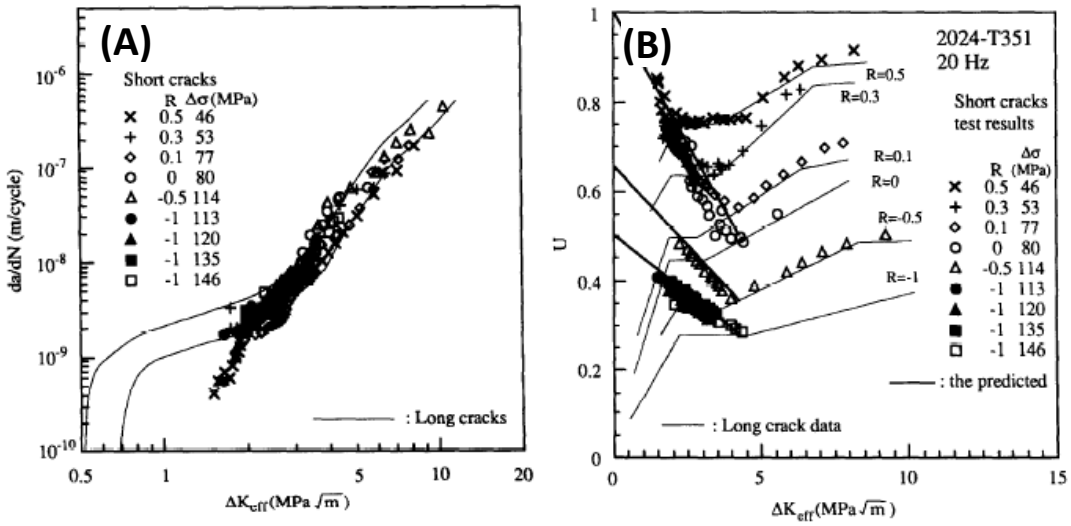

Figure 2.9: (A) Growth rate of short and long fatigue cracks in Al 2024-T351 and (B) variation of crack opening stress ratio with crack length

2.3.1 Comparison between Predictions and Measurements of Crack Closure

A detailed review of crack closure modelling techniques is contained in section 6.1. Reviewed in this section are published comparisons between crack closure predicted and measured under applied external loading only. The effect on crack closure of residual stress is reviewed separately in section 2.3.3.

In a recent paper crack closure was measured for long and short (0.1-2 mm) cracks in 304L steel [52,53]. The tests were performed using the compact tension specimens and crack closure was measured using compliance based methods. Excellent agreement was found between experimental results and numerical simulation as shown in Figure 2.10 (A) below. The simulation was based on 3D FE analysis of the compact tension specimen with a straight crack front. The model contained 8 node cubic elements. In the crack tip region the elements were $1/20^{th}$ the size of the forward plastic zone. A kinematic material model was used and crack tip node release was performed at the minimum applied load after 15 applied load cycles so as to achieve a steady state of stress and strain field near the crack tip. Closure occurred at the surface of the specimen but not in the centre. This was due to the plane strain state at the centre of the sample as will be described further in the next section.

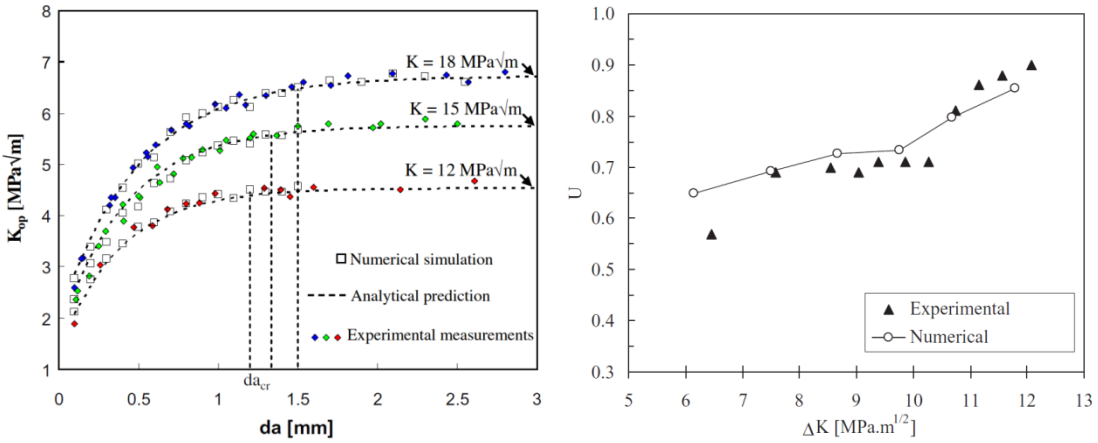

Figure 2.10: (A) Comparison between numerical and experimental results in the C(T) specimen for three values of applied ΔK [53] and (B) Comparison between numerical and experimental results in the M(T) specimen [56].

Similarly Sarzosa *et al.* [54] investigated crack closure in C(T) specimens of ASTM A516Gr70 steel of which some were welded along the crack plane. Residual stress was not included in the model since the welded samples were heat treated after welding which significantly relieved (though did not fully eliminate) the surface residual stress (measured using XRD). The base and weld material were differentiated in the model by applying different mechanical and hardening properties. FCGR was measured in the base and weld material and was then corrected to account for crack closure by calculation of ΔK_{eff}. Fatigue lives were estimated and found to be within a factor of 0.2 of experimental lives. The analysis would however have benefitted greatly had crack closure been measured during the experiments to allow direct comparison with the FE predictions. Similar findings were reported [55] for C(T) samples of Al 7075-T651. However in this work measurement of the opening load was undertaken experimentally using compliance techniques.

Numerical prediction of crack closure was compared to experimental measurements in the M(T) specimen of Al 6016-T4 1 mm thick [56]. The opening load level (P_{op}) was determined by monitoring the load-displacement curve using a pin micro gauge with the pins placed in two holes above and below the notch. Then from the load-displacement curves variations of P_{op} were derived using the "maximisation of the correlation coefficient technique" [56].3D FE analysis was utilised to determine the Pop. The load-displacement was monitored at a nodes placed at the same positions as the pin holes described above. Despite the small sample thickness (1 mm) far greater opening load was predicted on the sample surface that in the centre. A good agreement between experimental numerical results was found as shown in Figure 2.10 (B). Good agreement was reported [57] between experimental and numerical

FCGR in M(T) specimens of 2024-T351 14 mm thick when crack closure effects were included in the numerical prediction.

The propagation behaviour of microstructurally small cracks was simulated [58]. The approach combined a crack tip slip band model with Newman's crack closure model [59]. For a homogeneous material they found that crack closure increased with crack extension until it reached stabilised value due to the build-up of the plastic wake. This is consistent with other results described here. However when the plastic zone was constrained by an adjacent grain with a greater yield stress the stress opening value rapidly increased as the crack crossed the grain boundary. In situ SEM crack closure measurement of short fatigue cracks (0.05-0.5 mm) in Al 2024-T351 were compared to numerical predictions using 3D FE analysis [60]. The experimental measured crack closure level was consistently greater than values predicted. The FE analysis only considered the plastic wake effect on crack closure and the greater experimental crack closure was attributed to contact first behind the crack tip caused by asperities and mismatch of the fatigue crack surfaces.

2.3.2 Crack Closure in Plane Strain Conditions

There can be major differences in the closure behaviour of a fatigue crack depending on stress state. It is widely accepted that crack opening stress is greater for plane stress than plane strain [11] with some researchers even doubting the existence of PICC in the plane strain [61,62]. The plastic zone size in plane stress is generally regarded as being 3× bigger than in plane strain. Since PICC is dependent on the reversed plastic zone and hence the size of the forward plastic zone, it follows that PICC would be less prevalent in plane strain than the plane stress state. A series of experiments was performed [63] using 2024-T3 MCT specimens of thickness 10.2 mm. Fatigue cracks were grown and measurements of crack closure indicated the crack tip was open during 72% of the applied load cycle. The plate the thickness was reduced to 7.2 mm through layer removal on both sides. Crack closure was re-measured and it was found the crack tip remained open during 87% of the applied load cycle. The procedure was repeated. The sample thickness was reduced to 3.75 mm and the crack tip was measured open during 89% of the applied load cycle. It was concluded that crack closure was greater at the sample surface where plane stress conditions existed than in the centre of the plate where plane strain conditions existed.

Early FE work by McClung *et al.* [64] focused on the mechanics behind plane strain crack closure. They showed the plastic wake of a propagating plane stress fatigue crack was associated with material transfer from the thickness direction to the axial direction. In plane strain the plastic wake is associated with material transfer from the in-plane transverse direction to the axial direction (noting that in plane strain it is

only the out of plane displacements that must be zero). Material transfer in the plane strain state was investigated further by Riemelmoser & Pippan [65]. They stated that the entire plastic wake of a fatigue crack is sheared and that without the constraint of the surrounding elastic material the shear deformation would open the crack as shown in Figure 2.11 (A). However due to the surrounding elastic body the plastic shear opening must be balanced by elastic rotation. The effect of the elastic rotation is that material is transported in the crack direction instead of the longitudinal direction, Figure 2.11 (B). The transport of material leads to a wedge of material at the crack tip and hence crack tip closure.

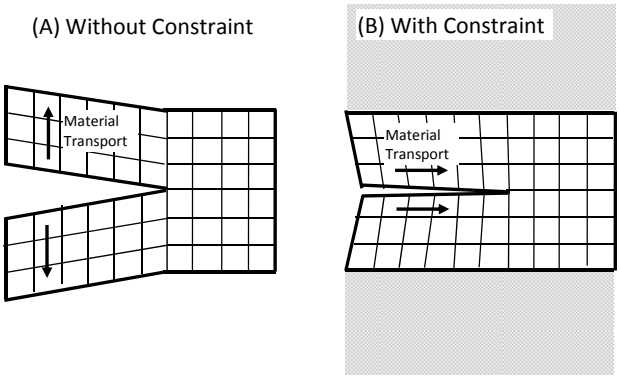

Figure 2.11: Plastic shear deformation in the wake of a fatigue crack (A) unconstrained and (B) constrained by elastic material

Antunes *et al.* [66] studied using FEA the effect of stress state on PICC in the M(T) specimen. They studied the effect on crack tip opening stress of maximum applied stress. As shown in Figure 2.12 (A) the crack tip opening load increased as the maximum applied load was increased in both plane stress and plane strain states. The level of PICC was 1.5-3× greater for plane stress than plane strain. They also studied the effect on the opening stress ratio in plane strain of three hardness models, the results are shown in Figure 2.12 (A). Isotropic hardening resulted in greater opening stress than the kinematic hardening model. A mixed hardening model was also studied and gave similar results to the isotropic model.

In a recent paper [67] plane strain PICC was not predicted for either DEN(T) or M(T) specimen geometries. Details on element sizing was missing from the paper however from the pictures of the mesh it is doubtful it was dense enough to properly characterise the reversed plastic zone and plastic wake necessary for PICC. Singh *et al.* [68] modelled PICC in the M(T) specimen under plane stress and plane strain states. They found remote crack tip closure occurred under both plane stress and plane strain conditions although it was more prevalent in plane strain. They attributed this to crack advance scheme and hardening model. They concluded that steady state crack opening stress level was not achieved under plane strain and the

closure that was observed was attributed to remote closure suggesting that that PICC may not be exist in plane strain.

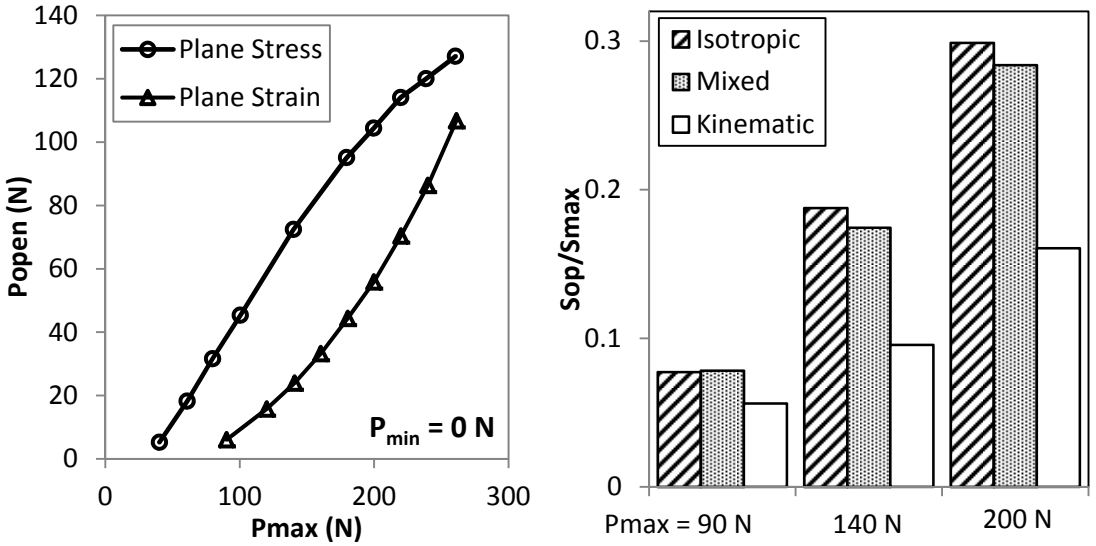

Figure 2.12: (A) The effect of maximum load on the opening load [195]

PICC in an M(T) sample were predicted de Alizadeh *et al.* [69] using 2D and 3D FE analysis. They found that 2D plane stress results agreed with 3D results at the surface and 2D plane strain results agreed with the mid-thickness of the 3D model provided the specimen thickness was sufficiently large.

De Matos & Nowell [70] studied the effect on PICC of the number of applied loads between release of the crack tip node boundary constraint. They found for plane strain that increasing the number of cycles had deceasing effect on the opening stress level. They suggested for plane stress that two cycles was sufficient but for plane strain the exact number of cycles was not established however more than eight had little effect on the predicted crack opening stress level. They did suggest however that the number of load cycles used is a compromise between numerical accuracy and computational cost of the analysis. They found that for 2D plane strain cracks under constant amplitude loading that crack closure existed only at the beginning of the crack growth process before decreasing to zero.

De Matos & Nowell [71] measured crack closure in compact tension specimens of thickness 3, 10 and 25 mm. Crack closure was measured using traditional compliance based methods and DIC. The experimental results were compared with predictions using 2D and 3D FE analysis. For the thin samples where the state of stress along the crack front would be in plane stress, good correlation between experimental results and predictions of opening stress load were made. However as the sample thickness increased a considerable difference between the experimental bulk measurements

and surface measurements was found. However it was found that the bulk measurements when used to predict an effective SIF provided better correlation with FCGR.

The effect of the T-stress on plane strain crack closure has been studied using FE analysis [72,73]. It was found by Fleck [73]. that PICC occurred provided the ratio T_{max}/σ_y is less than a critical value as shown in Figure 2.13. The crack closure response was insensitive to the material properties σy, E and ν. For a stress ratio of zero it was found that an initial wedge of material was left on the crack flanks at a location immediately ahead of the initial crack tip position that lead to the crack closing first behind the crack tip (referred to as remote closure). Remote closure was also reported by Lei [74] for compact tension specimens modelled in the plane strain state but not in plane stress (R = -2). He stated that remote closure may not be caused by the plastic wake but instead due to blunting of the crack tip and strain hardening of the material.

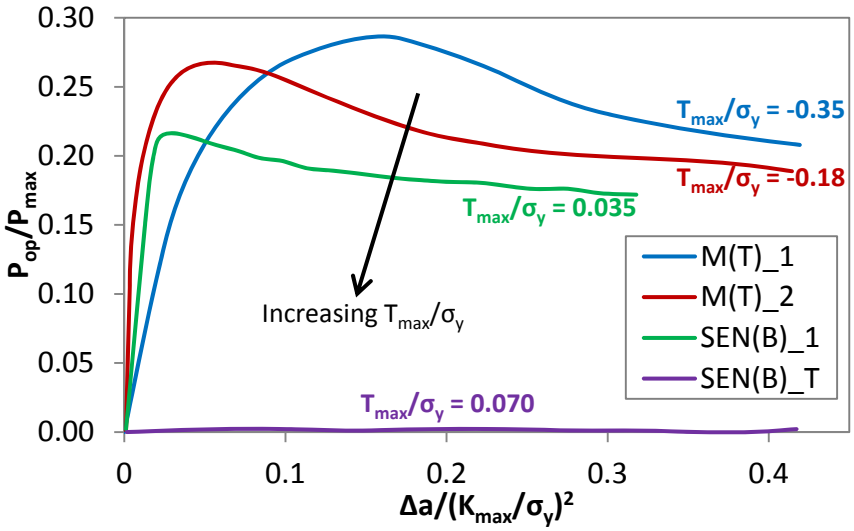

Figure 2.13: Effect of specimen geometry on closure response

Stress state can also have an effect on the stabilisation of the crack opening load. Antunes *et al.* [75] have shown that for plane stress conditions under constant amplitude loading the opening stress ratio will increase monotonically with increasing crack length until a stabilised value is reached. It was shown for plane stress conditions and constant amplitude loading that the crack must be advanced completely through the initial forward plastic zone to form a stabilized plastic wake and therefore stabilised stress opening values [76]. However Antunes *et al.* [75] also noted a peak opening stress ratio was observed for plane strain conditions after which the opening ratio decreased with increasing crack length. Similar observations were noted by other authors [61,77]. Lee & Song [78] concluded that in order to

obtain stabilised crack opening values the crack must be advanced approximately four times the length of the initial forward plastic zone.

2.3.3 Effect on Crack Closure of Initial Residual Stress Fields

Although there have been many studies on fatigue crack closure using experimental, numerical and FE approaches, few have considered the effects of an initial residual stress field. A distinction is made here between an initial residual stress field defined as a pre-existing stress field in the component prior to crack propagation and residual stress as a result of plasticity during crack propagation such as in the plastic wake or forward plastic zone. This section reviews the effects on crack closure of a fatigue crack propagating through an initial residual stress field.

A 2-D elastic-plastic FE element analysis of crack closure in an M(T) specimen was studied [79]. The model used 4 node plane stress elements and isotropic hardening. A compressive residual stress field was induced through application of an overload. A fatigue crack was advanced from the notch at the maximum applied load. Crack closure was simulated by monitoring the position of the nodes behind the crack tip. During unloading if the nodal position became negative relative to the crack tip a node fixity condition was applied. The compressive residual stress field increased the crack opening stress level by up to 3× compared to a residual stress free analysis. The crack was advanced through the residual stress field and ΔK_{eff} was calculated. a. The results were correlated well with experimental data. It was noted that prediction of closure level was highly dependent on the $da/dN = f(\Delta K_{eff})$ relationship used.

Berghini and Bertini [80] considered a residual stress field due to welding in 12 mm thick steel. Three distinct situations were recognized: (1) the crack is completely open at the minimum load, (2) the crack tip is open while crack surfaces are partially closed at minimum load and (3) the crack is completely closed at minimum load. Crack closure prediction using FE and weight function methods were compared to experimental results. Predicted K_{op} values compared well with predictions using FE and weight functions however it was noted that caution is required when dealing with partially open cracks.

Kang *et al.* [81] studied the behaviour of FCG and closure through a compressive residual stress field from electron beam welding in 6 mm thick steel. They found that depending on the type of residual stress field in the region of crack growth, the growth and closure of the crack show different behaviour in particular in the transition region from a compressive to tensile residual stress field. This was attributed to partial crack opening when the load was released i.e. it didn't close at the crack tip first. These findings are similar to those reported by Choi and Song [82]. Kang *et al.* [83] also studied the effect on FCG and closure level through a tensile

residual stress field under compressive applied loading. Comparison between experimental FCGR and predictions were made. They concluded that prediction based on the R_{eff} method and ΔK_{eff} method correlated well with FCGR measurements. However they also concluded that a version of the R_{eff} method where $\Delta K_{eff} = K_{max} + K_{res}$ and $R_{ef} = 0$ when $K_{min} < 0$ may lead to non-conservative estimates.

Schnubel and Huber [84] considered closure in a welded 5 mm thick C(T) specimen. An elastic FE model was used with and without hard contact of the crack faces to compare the superposition approach with a contact approach. A significant difference between calculated SIF with and without contact was found particularly in the transition region from compressive to tensile residual stress. This attributed to the effect of the contact condition on the local opening behaviour of the crack face near the crack tip.

Moshier and Hilberry [85] considered a 2.54 mm thick 2024-T3 SENT. A tensile overload was applied to induce a compressive residual stress field. They noted that when a crack grows in a component without compressive residual stress, it leaves plasticity in the wake of the crack. However when compressive residual stress is present, the residual stress acts as an external closing mechanism, opposite to the applied load, which forces the crack closed and reduces the amount of plastically deformed material. This results in an opening stress due to plasticity that is less than the original opening stress when residual stress was not present.

The effect of compressive residual stress on FCG from hole was modelled using elastic-plastic FE analysis [86]. Isotropic hardening and PICC was considered. Predicted FCGR compared well with experiment to within a factor of 5%.

Liljedahl *et al.* [87] considered a residual stress field from welding in 7mm thick 2024-T351 aluminium. They compared the ΔK_{eff} approach with superposition approach. Superposition compared well with experiment at lower load levels. In contrast ΔK_{eff} approach was better at greater load levels however it was noted that the reason for this may have been due to experimental measurement technique used.

Wang *et al.* [89] considered a compressive residual stress field from shot peening on etched 7075-T7451 dogbone samples (t = 6.35 mm). They extended the Newman PICC method by using CTOD. The predicted fatigue lives based on the closure model were within a factor of 2-3 of experimental lives.

Ma *et al.* [90] found good agreement between predicted and experimentally measured FCGR through a weld induced residual stress field. A crack closure based approach was used where crack opening levels were predicted using Newman's equations [59].

The effect of residual stress induced by shot peening on crack closure was measured by Zhu *et al.* [91]. Crack closure levels were found to increase with shot peening intensity and were on average 2× greater than for the unpeened condition. They noted the opening level initial increased prior to decreasing with crack extension, no residual stress measurements were made. A closure based model [FASTRAN] to predict FCGR from a machine like scratch in 4340 steel was used [91]. Crack growth was through a residual stress field induced by shot peening. Very good agreement between predictions and experimental measurements were reported. Differences between FCGR behaviour were accounted for by using the closure corrected effective stress intensity factor range in LSP treated titanium [92,93].

Hill and Kim [94] considered crack closure in a residual stress field induced by LSP. An elastic analysis was performed where crack closure occurred due to the strain fields locked in the material (i.e. the residual stress field) that altered the shape of the crack faces and caused contact. The contact pressure arising from a closed crack was calculated using the WFM and FE method for comparison are compared well. A number of FCGR prediction methodologies were compared to experimental measurements in 3.8 mm thick 7075-T6 aluminium C(T) specimens. It was found that prediction methodologies that included crack closure improved the accuracy of the results.

De Matos and Nowell [95] developed an analytical model based on PICC and considered an initial residual stress field from a cold expanded hole. They found that the opening stress level increased significantly in the presence of compressive residual stress. When the crack advanced through the field the opening stress level was similar to that in the absence of residual stress. Also compared was the effect on closure behaviour of remote applied stress level ($\sigma_{max}/\sigma_{yield}$). They found for low levels of remote applied stress the residual stress dominates the closure behaviour but at high levels ($\sigma_{max}/\sigma_{yield}$ = 0.8) the closure behaviour was similar to that in the absence of residual stress. FCGR was predicted using the analytical model and correlated well with experimental data.

2.4 Residual Stress and its Effect on Fatigue Performance

Residual stresses are self-balanced stresses in a material without any external forces present. They can be induced into the material unintentionally for example during welding processes or deliberately introduced into the material such as from laser shock peening. Residual stresses occur through a variety of mechanisms including plastic deformations, temperature gradients or structural changes.

In this section residual stress and its effect on fatigue performance will be reviewed. The first section describes briefly some of the various ways residual stress fields are

induced in components with laser shock peening dealt with specifically in section two. The methods used to measure residual stress fields are reviewed in section three. The fourth section reviews the effect on fatigue performance of residual stress fields induced during manufacturing processes and shot peening. The effect on fatigue performance of LSP is review in section five and in the sixth section specific applications to thin sheet material (<3 mm) of LSP are reviewed.

2.4.1 Causes of Residual Stress

Many manufacturing processes can induce as an inherent by-product residual stress in components such as welding, machining, forming, hardening, casting and forging. These stresses are generally unwanted and sometimes additional steps are added to the manufacturing process to induce beneficial compressive residual stresses at safety critical locations such as shot peening, laser shock peening, low plasticity burnishing, deep rolling, cold expanded holes and autofrettage of thick cylinders. Residual stress can also be induced from pre-service loading (such as proof testing) and in-service loading (such as maximum service load causing yielding at stress concentrations). In section 2.4.4 the effect on fatigue performance of residual stress reported in the literature is reviewed. For the majority of cases reviewed residual stress was induced created from shot peening or welding processes. A brief description of these two processes is given below. Laser shock peening is reviewed in detail in next section.

The shot peening technique was invented in the 1920's in Germany and the USA independently and has been widely used in industry since the 1950's [96]. It is often used for the specific purpose of improving the fatigue strength and fatigue life. During the process ceramic or metallic balls, called shot, are fired with force onto the surface to be treated. Each shot acts as a hammer and creates a dimple on the components surface plastically deforming the near-surface layer by stretching as illustrated in Figure 2.14 (A). The neighbouring material reacts against the stretching and a compressive residual stress field is formed, illustrated in Figure 2.14 (B). However other changes to the material can occur such as micro hardness, dislocation density, surface roughness, surface defects and phase composition [97].

Welding processes are most widely used in automotive and naval industries but have also been explored in the aerospace industry [99-101]. Welding joins the component pieces by melting the materials whilst adding a filler material. This forms a pool of molten material that then cools to become a strong joint. However the heat induced from welding may cause localised expansion of the components which then then filled with the molten metal. When the weld cools some areas may contract more than other causing residual stresses. Welding processes can also change the material

properties of the component. Microstructure and hardness changes are localized to the welded strip.

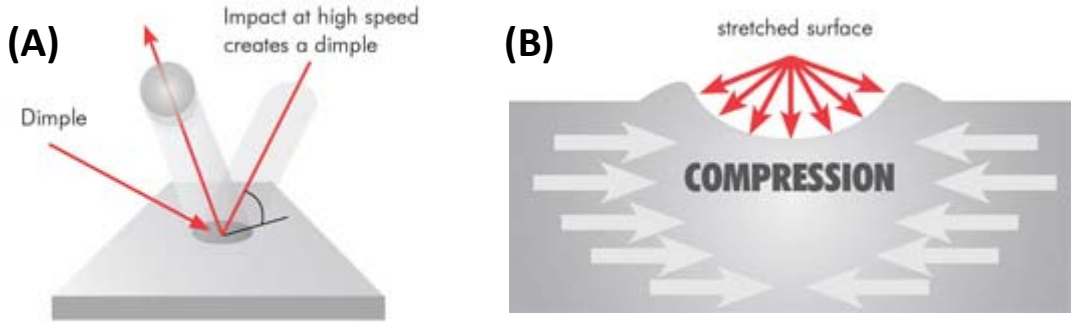

Figure 2.14: (A) Dimple creation on material surface during shot peening and (B) formation of compressive residual stress around dimple [98]

The residual stress field created by shot peening are generally referred to as cold worked residual stresses whereas from welding they are termed thermal residual stresses. It is interesting to note at this point that the residual stress field induced during laser shock peening is actually the result of cold working.

2.4.2 Laser Shock Peening

In this section an overview of the history and applications of Laser Shock Peening (LSP) is provided. A detailed description of how the treatment works and is performed is given. Finally a review of reported applications of LSP to enhance fatigue life in the literature is detailed.

Laser shock peening is a technique for the surface treatment of metallic materials. LSP is applied to improve the fatigue performance of the treated component by creating a layer of compressive residual stress at the surface. The first reported investigation on the effect of stress waves created by lasers and their effect on metals was by White in 1963 [102]. The first patent for an application of LSP was in 1974 [103]. Initially applications of LSP were limited due to the size and expense of the required laser systems. However over the last two decades its application has increased significantly as more suitable laser systems were developed. It has been used extensively in the aerospace industry for the treatment of gas turbine blades and discs, and more recently wing attachment lugs. Other applications of laser peening include treatment of steam turbine blades [104], forming of metals [105,106] with applications to aircraft wing panels, enhance service life of automotive springs [107], and as a preventative measure against SCC in nuclear power reactors [108]. The effect of LSP process variations on the induced residual stress fields have been assessed for a range of materials such as steel [109-111], titanium [112-114], and

aluminium [115-117]. Numerous researchers have developed models that attempt to predict the induced residual stress field from LSP with varying success [118-121].

An illustration of the typical LSP process is shown in Figure 2.15. When laser shock peening the surface of the component is normally first coated with a sacrificial ablative layer. The ablative layer used can be black paint, tape, or metallic foils. The ablative layer is primarily used to protect the surface of the component from thermal effects during the peening treatment [122]. However greater surface pressures have been reported when an ablative layer is used [123]. This was attributed to an ablative layer such as black paint absorbing more of the lasers energy. LSP can also be applied without an ablative coating. This is generally performed where application of paint or tape onto the component surface is difficult due to complex geometry or if the component is already in service and hard to access. When an ablative layer is absent the lasers used tend to be of less energy per pulse to minimise thermal effects on the target surface. It is generally regarded that there are now two variants of the LSP treatment [124]. The first uses high energy per pulse (>10 J), large laser spot size (>3 mm), and protective coating. The other uses lower energies per pulse, a smaller laser spot size, and no protective coating.

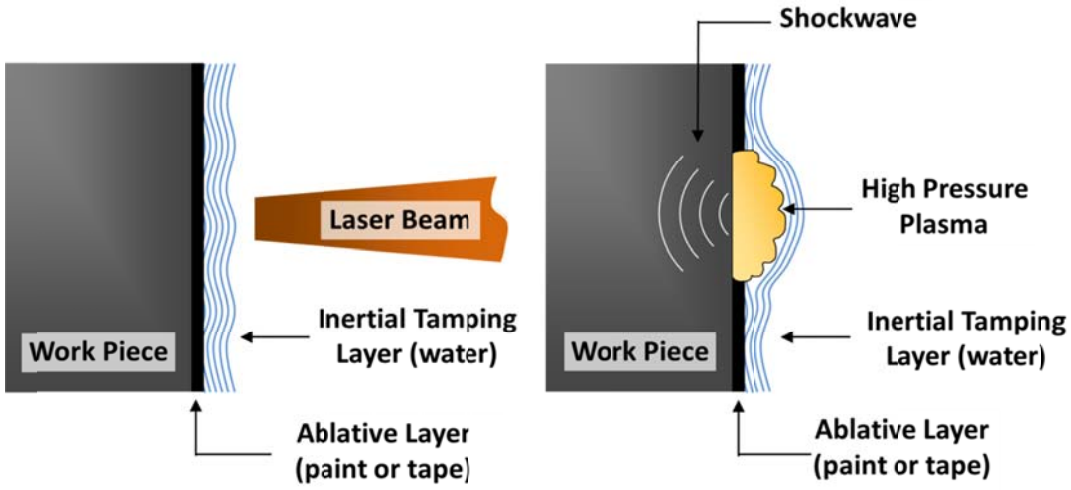

Figure 2.15: Illustration of typical laser shock peening process

After surface preparation a pulsed laser light is fired and delivered to the component surface by a series of mirrors. The ablative tape (if used) is vaporised by the extreme heat generated (> 10000 K [125]). High pressure plasma is created through ionisation and a shockwave is generated. To increase the efficiency of the process an inertial tamping layer is used. This confines the plasma and directs more of the generated pressure into the component. The tamping layer needs to be transparent to the laser light and so water or glass is normally used. The shockwave generated results in

plastic deformation of the near surface and it is this plastic deformation that creates the residual stress field.

The creation of the residual stress field (i.e. plastic deformation of the near surface layer) is comparable to how the residual stress field is created using the more traditional shot peening method (i.e. indentation of the component surface by bombardment using metal or ceramic balls as illustrated in Figure 2.14 (B).). However the residual stress field created using LSP generally extends further from the surface than after shot peening. This extent has been reported to be up 16 times greater [126]. The surface finish after LSP is generally better than after shot peening. For example Masse and Barreau [127] reported a surface roughness (R_a) of 0.17 after LSP and 5.67 after shot peening where untreated material roughness was 0.1. LSP also has the advantage of being more controllable than shot peening both in terms of the residual stress field produced but also the region of coverage. Improvement of the mechanical properties of aluminium 7075-T7351 was reported after LSP but not shot peening [128]. However LSP has the disadvantages of requiring a longer initial set up time and being more expensive.

For further details on the laser shock peening process consult the following review papers by Montross *et al.* [129], Clauer & Lahrman [124] and Peyre *et al.* [123, 130]. A brief description of the terminology used when describing and comparing laser systems is provided here.

Laser Type refers to the gain medium used in the laser system. It is used to amplify the laser from its source. Common types used for laser peening include Nd:YLF, Nd:YAG and Nd:Glass.

Wavelength of the laser light. Commonly used for laser peening applications are 355 nm (ultraviolet), 532 nm (green), and 1064 nm (infrared).

Laser Frequency refers to the number of laser pulses per second (i.e. how often the laser is fired) and is measured in hertz (Hz).

Application Time is the duration of a single laser pulse and is measured in nanoseconds (ns).

Laser Spot Geometry is the shape of the contact area between the laser beam and the targeted component. Square or circular spot geometries are commonly used.

Laser Spot Size refers to the diameter of a circular spot or the width of a square spot.

Energy in the laser beam and is measured in joules (J)

Power Density is the power per unit area of the laser beam and is calculated using equation 2.33. It is usually expressed with the units W/cm^2.

$$\text{Power Density} = \frac{\text{Energy (J)}}{\text{Pulse Time(s)} \times \text{Laser Spot Area(cm)}} \quad (2.33)$$

2.4.3 Measurement of Residual Stress Fields

There are several techniques that are used to measure residual stress fields. The measurement techniques are classified as destructive or non-destructive based on the nature of their damage to the material during measurement [131]. Destructive techniques are based on elastic stress relaxation and associated strain when a layer of material is removed from the sample. The non-destructive techniques rely on material characteristic features such as atomic d-spacing (distance between crystallographic planes) or the material response to magnetism or sound. Non-destructive techniques generally require measurement of the characteristic feature in the unstressed and stressed state.

The most widely used destructive techniques are surface X-ray diffraction (with surface layer removal), hole drilling, slitting (crack compliance), and the contour method. X-ray diffraction, synchrotron X-ray diffraction, neutron diffraction, ultrasonic and magnetic methods, and Raman spectroscopy are the most common non-destructive residual stress field measurement techniques.

The residual stress fields induced by LSP in the current work were measured by the by Toparli [132]. They used hole drilling, surface X-ray diffraction, synchrotron X-ray diffraction, neutron diffraction and the contour method for stress measurements. In all cases the stress fields were measured using hole drilling and at least one other method for comparison to increase confidence of the measurement data. The results used in the current work and presented in subsequent chapters are from the hole drilling method only. A brief description of the hole drilling method is given below.

The hole drilling method is one of the main destructive residual stress measurement techniques used in industry as it is simple, fast, and relatively inexpensive [132]. The method is based on the elastic stress relaxation after material removal. A hole is introduced to a sample with residual stress resulting in displacements around the hole as the stresses relax. A special strain gauge is used to measure the displacements and they used to back calculate the residual stress. The main requirement on the drilling is that no further residual stress should be induced in the material. An ASTM standard E837 [133] is available for the technique as well as an NPL good practice guide [134].

Toparli [132] used a variant of the hole drilling method termed incremental hole drilling. This method was used due to thin material (2 mm) being studied and expected high non-uniformity of residual stress through the depth induced by LSP. For this method the hole is introduced step by step and strains are recorded at each increment. A 2 mm diameter drill was used for material removal. As the strains are measured at the surface the sensitivity of the gauges decreases as the hole depth increases. At deeper depths larger increment steps are used to increase the amount of material removal therefore increasing the amount of strain relaxation. Finally due to the proportion of the hole depth (1.4 mm) to the thickness of the material (2 mm) a backing material (epoxy resin) was used during measurement of residual stress.

2.4.4 Effect on Fatigue Performance of Residual Stress

The fatigue performance of components is a function of their load history. A primary variable that influences fatigue performance is the amplitude of the applied cyclic load. Also of major influence is the mean (or maximum) value of the applied load during each cycle. Significant in fatigue are residual stress fields established in the component prior to service. Although residual stress fields do not directly influence the amplitude of cyclic loading they do alter the mean (or maximum) value of the load in each cycle and therefore can have a major influence on the fatigue performance. Residual stresses are self-equilibrating and so any region of compressive residual stress must be counterbalanced by tensile residual stress elsewhere in the component.

This is most evident of residual stress fields induced through welding processes. Tensile residual stress normally forms in the centre the weld with balancing compressive residual stress at the edges. Beghini *et al.* [135] studied the effect on FCGR of welding induced residual stress fields in C(T) specimens to. It was found that fatigue cracks propagated faster through the tensile residual stress and slower through the compressive residual stress field compared to in the baseline material. Crack propagation can also be influenced by changes to micro-hardness and microstructure in the weld heat affected zone however it has been found that residual stresses are the most important parameter influencing FCGR [136,137].

Shot peening is applied to components to enhance fatigue performance by inducing a compressive residual stress field. There has been extensive research on the effect on fatigue of shot peening [97]. Early research by Reed & Viens [138] found a 25% improvement of the endurance limit after shot peening of Ti-6Al-4V. The effect of shot peen induced residual stress on the fatigue performance of 7010 and 8090 aluminium alloys was studied by Mutoh *et al.* [139]. The found the crack initiation time after peening was shorter due to the rough peened surface. However the FCGR was significantly reduced by the compressive residual stress field and total fatigue life

was greater after peening. Hammond & Meguid [140] studied the effect of shot peening on the fatigue performance of 7075 aluminium and 080M40 steel. Shot peening enhanced the fatigue life of both materials and was attributed to the induced compressive residual stress field. They also noted peening treatment promoted subsurface crack initiation in the aluminium but not steel. Sridhar *et al.* [141] published results showing a decrease in fatigue life of the titanium alloys after shot peening at ambient and elevated temperatures. This was attributed to residual stress relaxation with applied cyclic loading and increased surface roughness.

The effect of shot peening on small fatigue crack growth has been studied [142]. De Los Rios *et al.* [143] found crack initiation and propagation behaviour completely changed after shot peening. Shot peening accelerated crack initiation and early crack growth but reduced crack propagation rate. Natkaniec-Kocanda *et al.* [144] found the number of cracks of length less than 50 µm was significantly lower after peening and attributed this to squeezed grains, high dislocation density, and compressive residual stress in the hardened layer. More recently Černý *et al.* [145,146] studied the effect of shot peening on short crack growth in 2.4 mm thick 7075 aluminium. They found that crack retardation was significant after peening particularly for cracks of length less than 2 mm.

The effect on the fatigue performance of scratched material after shot peening has been studied. Everett *et al.* [147] found that the fatigue life of shot peened samples that contained scratches 51 µm deep was equivalent to that of pristine samples however no measurement of the peening induced residual stress field was made. Shot peened 2024-T3 aluminium specimens with scratches 20 to 100 µm deep were studied [33]. Peening reduced the crack growth rates of scratched specimens and the crack growth rates were similar to that measured in pristine samples. However the samples were peened until the scratches were eliminated and therefore the beneficial effect on fatigue life of peening in this case may be more attributable to the removal of the stress concentration than induced residual stress field.

Claudio *et al.* [148] measured the fatigue lives of shot peened nickel based superalloy samples with scratches 50 and 100 µm deep. The fatigue lives of samples with scratches 50 µm deep was up to 1.8× greater after shot peening. The fatigue life of samples with scratches 100 µm deep did not change after shot peening. Considering the residual stress field measurements [148], the tip of the 50 µm scratch was within the compressive stress field whereas the tip of the scratch 100 µm deep was on the limit of the compressive stress field. The fatigue results were therefore consistent with residual stress fields measured.

2.4.5 Effect on Fatigue Performance of Laser Shock Peening

The first paper that reported the effect on fatigue performance due to LSP was published in 1979 [149]. Since then there have been many papers detailing the merits of LSP to fatigue performance of metallic components [150-155]. During the 1970's and 80's it was generally accepted that increase of material hardness after peening was the reason for improvement of fatigue life [123]. However it was demonstrated later that the improvement was possible without significant change to the material hardness [156] and it has been shown that the induced compressive residual stress field through the depth has the greatest effect on fatigue performance [157-163].

Since shot peening is the most conventional and widely used surface treatment to echance mechanical properies many authors have directly compared it to LSP [164-175]. Heckenberger *et al.* [126] compared the effect of LSP and shot peening on the induced residual stress field and fatigue performance in 7050-T7451 aluminium 28 mm thick. The magnitude of the induced compressive residual stress at the surface was simliar however LSP induced field extended 16× deeper from the surface. The fatigue strength after shot peening was 15% greater than the baseline material and 30% greater after LSP treatment. For the same material but 19.1 mm thick Luong & Hill [176] measured LSP induced compressive residual stress 10× deeper than after shot peening. The fatigue strength was 1.2× greater for LSP treated samples than shot peened samples.

The effect on crack initiation of LSP has been studied [177,178]. Peyre *et a.l* [170] claimed the main improvement in fatigue performance of Al7075 was observed during crack initiation. They concluded that the crack initiation stage increased by 700% whereas crack propagation stage increased by just 200%. Shot peening the increased the crack initiation and propagation stages by just 150% to 200% respectively. The effect on FCGR of LSP has been measured using the DCPD method [92,93,179]. In all instances LSP reduced the FCGR and this was attributed to the induced compressive residual stress fields.

LSP has been applied to welded joints to reduce the tensile residual stresses induced during the welding process [164-166]. Hatemlah *et al.* [167] studied the effect on the fatigue properties of friction stir welded (FSW) 7075-T651 aluminium M(T) specimens 1.25 cm thick after LSP (5 GW/cm^2). Measured FCGRs were lower after LSP and fatigue life was 1.3× and 2× greater compared to baseline and FSW specimens respectively. Sakino e*t al.* [180] found that the fatigue strength of 9 mm thick welded steel increased by a factor of 1.7 after LSP (energy of 200 mJ, laser spot diamter of 0.8 mm). Both authors above attributed the increased fatigue life increase to the induced compressive residual stress fields.

The effect on residual stress and fatigue performance in the compact specimen of LSP has been studied in the literature [181-184]. However the relationship between the induced residual stress field and the resultant change to the fatigue life has received little consideration. Hill *et al.* [185,186] considered the effect of one-layer and three-layer LSP on 7075-T6 aluminium 3.81 mm thick. The peening treatment had a square laser spot with a power density of 4 GW/cm^2, 18 ns pulse duration and was applied to both sides. The effect on the residual stress intensity factor of the position of the peened area was also studied, It was found that peening near the front face resulted in negative K_{res} whilst peening near the back face resulted in positive K_{res} (note: K_{res} was determined experimentally). Residual stresses measured using the contour method were compressive through the full thickness within the peened region.

Huang *et al.* [187,188] considered double sided peening on 6061-T6 aluminium 6 mm thick. They studied multiple peening treatments with laser energies of 3, 5 and 7 J, 5 mm diameter laser spot and 10 ns pulse duration. They found that fatigue life increased with greater laser energy. They also considered the shape of the LSP region. A square area (15×15 mm) ahead of the notch tip, a rectangular area (35×15 mm) that extended from the notch tip to the back face, and a rectangular area (15×60 mm) that extended from the bottom face to the top face. Compact specimens peened from the top to bottom face had fatigue lives approximately two times greater than the other two treatments.

The effect on residual stress and fatigue life of laser pulse density (900 to 2500 pul/cm^2) was studied [189,190]. Compact specimens 6.3 mm thick of 2205 stainless steel and 6061-T6 aluminium were peened at energies of 2.5 and 1.2 J respectively using a 1.5 mm diameter laser spot and pulse duration of 8 ns. The residual stresses were more compressive with increased pulsed density and this resulted in lower FCGR and longer fatigue lives.

The effect on the fatigue performance at elevated temperatures has been studied [191,192]. Altenberger *et al.* [193] found that residual stress field was almost fully relaxed at T = 450-550 °C in Ti-6Al-4V. However the fatigue life was still greater than the as machined condition due to reduced plastic strain amplitude by work hardening.

The effect on fretting fatigue of laser peening has been investigated [173,194]. Liu and Hill [195] reported fatigue lives up to three times greater after LSP treatment of Ti-6AL-4V coupons compared to as machined coupons. However fatigue lives of shot peened coupons was greater than laser peened coupons despite less surface roughness and deeper compressive residual stress. The shot peened samples failed due to fatigue crack initiation on the surface however the LSP samples failed due to

subsurface initiation. It was concluded that the LSP samples failed due to the greater magnitude of the balancing tensile residual stresses. It was noted by Srinivasan *et al.* [196] that whilst LSP increased fatigue life it did not mitigate fatigue crack initiation.

LSP applied to 2024 aluminium has been reported in a number of papers [147,149,174,175,197-199]. The fatigue life increased after LSP treatment of 2024-T3 specimens with corner cracks, centre holes, elliptical holes and crack-stop holes [91]. The peening pattern can influence the induced residual stress field and hence the fatigue life [200,201]. It was reported [168,202-204] that the compressive residual stress field induced by LSP increased the resistance of 300M steel and 304 stainless steel to stress corrosion cracking.

It has been noted by some authors that LSP can actually reduce fatigue life. This was attributed to internal cracking caused by the laser power density being above a critical level [205]. Surface damage caused by laser peening without surface coating was also reported as a cause [206]. Charderhai *et al.* [207] reported that balancing tensile stress field increased the FCGR enough to effectively wipe out the beneficial effect of the induced compressive residual stress field.

2.4.6 Application of LSP to thin sheet to improve fatigue properties

The applications of laser peening reviewed so far have been concerned with plate material of 5 mm thickness and greater. A review of the literature of investigations and theoretical predictions concerning laser peening of thin sheet (<3 mm) is contained below.

The effect of LSP on the fatigue performance of holes in thin sheet aluminium has been studied by Ivetic *et al.* [208]. They used a Nd:YAG laser (2.8 J, 9 ns, 1.5 mm spot) on 3 mm thick 6082-T6 aluminium and measured negative effects on fatigue lives if the hole was drilled prior to peening and positive effects if the hole was drilled post peening. They concluded that LSP needs to be optimised for the intended application specifically in thin sheet and that sequence of operation is crucial. However similar investigations [209,210] of LSP treatment (Nd:glass, 18 ns, 10 mm spot, 5 GW/cm2) on 2.5 mm thick 2024-T3 aluminium containing pre-existing fastener holes, multiple crack stop-holes, and single edge notch found beneficial effects on fatigue performance. Residual stress, -360 MPa, was measured at the surface that decreased with depth to about -60 MPa at 1 mm. Striation spacings on the fracture surfaces were measured and found to be smaller on peened than unpeened. It was also found that improvement in fatigue crack initiation life attributed to LSP decreased as the associated stress concentration factor of the notched samples increased.

Tang *et al.* [211] investigated LSP treatment of 2.5 mm 2024-T62 aluminium. The parameters of the Nd:glass laser used were a 30 ns pulse duration, 7 mm spot size,

and varied energy between 8-20J. An increase in surface hardness and residual compressive surface stress (average 30MPa) was measured. Fatigues lives increased by a factor of up to 9.8 after LSP treatment and this was attributed to the residual stress field.

The effect of repeated impacts (1 to 3) from a Nd:YAG laser (5J, 10ns, 3mm spot) on hardness, residual stress, and fatigue life of 2 mm thick 6061-T6 aluminium were studied by Zhou *et al.* [212]. They found that hardness increased with the number of impacts. The maximum compressive stress increased from 146 MPa to 213 MPa and depth of the compressive stress zone increased from 0.51 mm to 0.62 mm as the number of impacts increased from 1 to 3 respectively. The fatigue life compared to unpeened material also increased from 7% to 99% as the number of repeated impacts increased. Fatigue crack initiation moved subsurface after LSP treatment and fatigue striation spacings decreased.

Laser peening has been applied to friction stir welds in 3 mm thick 6061-T6 aluminium [213]. An Nd:YAG laser with parameters 60mJ, 8 ns, and 0.7 mm spot was used. Fatigue strength increased after LSP when compared to both baseline and FSW material. Hardness increased and surface tensile residual stress reduced in the welded zone after LSP. It was noted that further enhancement could be achieved if the LSP parameters were optimised for the application.

Residual strains were measured by Toparli & Fitzpatrick [214] in 1.8 mm thick 2024-T351 sheet peened with a Nd:YLF laser (5.8&11.6 J, 18ns, 8x8 mm spot). They found that the residual strains were greater as the power density and number of laser passes was increased however they noted a need to balance peen intensity to prevent “over-peening” that could reduce the strain field. They also found that the strains perpendicular to the peening direction were smaller than those parallel and this was attributed to distortion. Bhamare *et al.* [215] also noted in addition to careful selection of the peening parameters that the peening sequence should carefully considered. They noted that if the peening sequence is not proper tensile balancing stresses at the sample edges may result.

The effect of LSP on 2 mm thick steel was studied [216]. An increase in hardness after LSP (625-1695J, 4.3-25 mm spot) was found and tensile residual stress was measured on the peened surface that varied from tension to compression in a sinusoidal way with depth. A study using 1.3mm thick steel [217] also found that the hardness increased (30 to 80%) after LSP (100J, 3 mm spot). Compressive residual stress was measured from the surface (100 MPa) and the compression zone extended 75 µm from the surface. Yilbas *et al.* [218,219] studied the effect of an Nd:YAG laser (450mJ, 8ns, 2.5 mm spot) on 2 mm thick 316 steel and Ti-6Al-4V titanium. They found an

increase in hardness in the irradiated zone by a factor of 1.8 and 1.5 for steel and titanium respectively.

Residual stress fields induced by laser peening have been predicted using the finite element method for 2 mm thick 2024-T351 sheet by Ivetic [220] and on 1-3mm thick Ti-6AL-4AV sheet by Ding & Ye [221]. It was predicted [222] that as thickness increased from 3 to 6 mm the surface compressive stress on both the peened and non-peened faces decreased and for thin sheet the compressive stress on the non-peened side was actually greater. The effect of laser peening on mechanical properties and microstructural changes of steel and aluminium alloys ranging from 2-3mm thickness has also been studied [223-226].

In a paper by Dorman *et al.* [227] laser peening (0.5-3 GW/cm2) was applied to 2 mm thick 2024-T351 prior to introduction of scribes in the material. It was found that as the power density increased so too did the depth and magnitude of the maximum compressive stress. Fatigue lives after peening varied with a reduction of 10% to increases of up to 47%.

2.4.7 Predicting effect on Fatigue Crack growth of Residual Stress

Two methods have been widely used to predict the fatigue crack growth rate through residual stress fields. The first employs the superposition method and the other is based on the crack closure. The superposition method requires calculation of the stress intensity factor associated with the initial pre-existing residual stress field (K_{res}) [79]. The stress intensity factor due to residual stress is then superimposed on the stress intensity factor due to the external applied loading (K_{app}) to give a total resultant stress intensity factor as shown in equations 2.34 and 2.35 below.

$$K_{tot,max} = K_{app,max} + K_{res} \quad (2.34)$$

$$K_{tot,min} = K_{app,min} + K_{res} \quad (2.35)$$

The stress intensity factor range and stress ratio are then calculated using equations 2.36 and 2.37 below. It is interesting to note that for the superposition method ΔK is independent of the residual stress field and it is only the mean stress and stress ratio that are affected.

$$\Delta K_{tot} = K_{tot,max} - K_{tot,min} = K_{app,max} - K_{app,min} = \Delta K \quad (2.36)$$

$$R_{tot} = \frac{K_{tot,min}}{K_{tot,max}} \quad (2.37)$$

Fatigue crack growth rate can then be calculated using a correlation of the form shown in equation 2.38 below.

$$\frac{da}{dN} = f(\Delta K, R_{tot}) \quad (2.38)$$

The weight function method and elastic-plastic FE analysis can be used to calculate K_{res} and both have been found to produce similar results when applied to the same problem [228]. The advantage of the weight function method is that it provides fast reliable predictions however it does require a specific weight function for the specimen geometry being analysed. Also some authors [229-231] have questioned the validity of the weight function method to predict FCGR through residual stress fields since the initial residual field is used during the whole analysis only i.e. redistribution of the residual stress field with crack advance is not accounted for. However others have disagreed [232,233] and stated that superposition is still valid even without redistribution of the residual stress field. As stated the FE method can be used to calculate K_{res} and can applied directly to arbitrary geometries. The FE method naturally considers residual stress redistribution effects during crack advance.

Beghini & Bertini [80] proposed three distinct phases of crack opening state (1) the crack is completely open, (2) the crack tip is open while crack surfaces are partially closed and (3) the crack is completely closed. If the crack is fully open superposition principle applies. Since a compressive residual stress field will induce a negative K_{res} the superposition method is still valid [84] assuming no crack face closure occurs under the combined loading (i.e. $K_{tot,min}$ must be greater than 0). If the compressive residual stress field is great enough to induce crack face closure another method should be considered. A simple approach to deal with negative $K_{tot,min}$ is simply to set it equal to zero. This approach is known as the modified superposition method [84,233,234]. The stress intensity factor range and stress ratio can be calculated using equations 2.39 and 2.40 below

$$\Delta K_{tot} = \begin{cases} K_{tot,max} & , \quad if\ K_{tot,min} \leq 0 \\ K_{tot,max} - K_{tot,min} & , \quad if\ K_{tot,min} > 0 \end{cases} \quad (2.39)$$

$$R_{tot} = \begin{cases} 0 & , \quad if\ K_{tot,min} \leq 0 \\ \dfrac{K_{tot,min}}{K_{tot,max}} & , \quad if\ K_{tot,min} > 0 \end{cases} \quad (2.40)$$

If $K_{tot,min} < 0$ fatigue crack growth is calculated using a correlation of the form shown in equation 2.41 otherwise equation 2.38 is still valid.

$$\frac{da}{dN} = f(\Delta K_{tot}, 0) \quad (2.41)$$

The modified superposition method makes the assumption that crack opening occurs at $K_{tot,min}$. However as discussed in section 2.3 PICC can affect the opening stress level and so crack opening can occur above the $K_{tot,min}$ at K_{op}. An effective stress intensity factor range was defined in equation 2.28 along with a description of formulae for prediction of the stress opening value. However since the residual stress field will affect the crack tip plastic zone size, it will also affect the plastic wake left behind the advancing crack and so the K_{op} value. The effect of residual stress can be accounted for in the formulae by use of R_{eff} in place of R. Alternative the effect of residual on crack closure can be computed directly using elastic-plastic FE analysis.

The stress opening level of a fatigue crack advanced through a compressive residual stress field was studied using a 2D elastic-plastic FE analysis [79]. The stress intensity factor due to the maximum applied load was determined using weight function method. This was scaled using the predicted stress opening level to determine ΔK_{eff}. FCGR was also predicted using the modified superposition method. The stress intensity factor range was also calculated using the weight function method combined with modified superposition. FCGR were calculated based on experimental $da/dN = f(\Delta K_{eff})$ curves. Closure results compared well with experiment but the superposition was found to be non-conservative. It was noted that prediction of closure level are highly dependent on the relationship used. It was also noted that the initial residual stress and its redistribution with crack growth can result in final crack opening away from the crack tip where it normally occurs under constant amplitude loading. This can potentially complicate the methodology used to predict fatigue crack growth.

Beghini & Bertini [135] employed the weight function method to determine K_{res} in welded steel plates based on measured residual stress fields. They used the modified superposition method to determine ΔK_{tot} and R_{tot}. Predicted FCGR were within a factor 2.5 of measured data.

Jones & Dunn [88] considered residual stress fields from plastically bent 2024-T351 beams of 11 mm thickness. They compared measured FCGR to three LEFM approaches: (1) superposition method, (2) modified superposition and (3) superposition contact method using FE analysis. The superposition contact method resulted in the closest agreement with experimental to a factor of 2 to FCGR data and 1.2 to fatigue life. They concluded that crack growth through residual stress fields may be predicted provided the residual stress field is accurately known, the material properties are not changed by the introduction of the residual stress field, and the effect, if any, of partial crack closure is taken into account.

Predicted and measured FCGRs through a residual stress field in a welded M(T) sample were compared by Servetti [234]. Three prediction methodologies were assessed namely superposition, crack closure based on Newman's equations [59], and crack closure based on an FE contact model. He found that the closure method based on an FE contact model was in best agreement (within 20%) with experimental measurements. He noted that accurate measurement of the residual stress field, in particular the compressive region, was critical for accurate predictions.

The residual stress field induced via laser shock peening of 2 mm thick 6061-T6 aluminium was modelled by Zhao *et al.* [235]. Crack propagation was modelled from a hole through the predicted residual stress field using the fatigue analysis software MSC.Fatigue. The FCGR reduced and failure crack length increased due to the compressive residual stress field. However no comparison with measured residual stress field or FCGR was performed and therefore the predictions were not validated. Similarly the FE method was used to determine K_{res} due to a laser peen induced residual stress field [236]. The induced stress field was also predicted using the FE method. Predicted fatigue lives were within a factor of 1.2× of experimental lives however predictions were sensitive to the analysis parameters used. The SIF was calculated using J integral and related to K using LEFM. However J is path dependent for a crack advanced through a residual stress field in an elastic-plastic material [237,238]. Sherry *et al.* [239] used an in house post processer to determine J in a residual stress field in an elastic-plastic material. However their post processor has the limitation that in cannot account for crack face contact and so is unsuitable for cases incolving compressive residual stress fields.

3 Materials and Test Methods

In this chapter the methods used during experimentation are detailed. The material used is characterised in section 3.1 and in section 3.2 the geometry of the test samples is defined. The procedures used to recreate the scratch damage under laboratory conditions are outlined in section 3.3. The methods used to characterise the scratch damage is described in section 3.4. The laser shock peening treatment parameters are given in section 3.5 and the methods used to characterise the effect on the test samples of the LSP treatment are outlined in section 3.6. The tension-tension and four point bend fatigue test procedures are given in sections 3.7 and 3.8 respectively. Measurement of striation spacing on the fracture surface was performed after fatigue tests and the methodology followed is given in section 3.9. Finally an interrupted test method was used to study the effect of LSP on crack initiation and early crack growth and this is described in section 3.10.

3.1 Material Characterisation

The material was supplied by Airbus and sourced from Alcoa. It was supplied in 160 × 400 mm rectangular sheets and from these the required test specimen geometries were machined. The material was 2024-T351 series wrought aluminium sheet 2 mm thick clad on both sides. This is used commonly in the aerospace industry for aircraft fuselage panels and wing skins. 2000 series alloy uses copper as its major alloying element and the composition of 2024 aluminium as specified by Alcoa is given in Table 3.1. The clad layer is of soft unalloyed aluminium and constitutes nominally 2.5% of the thickness (i.e. 50 μm thick on each side).

Table 3.1: Specified alloy 2024 chemical composition limits (WT.%) [240]

Si . . .	0.5	Zn . . .	0.25
Fe . . .	0.5	Ti . . .	0.15
Cu . . .	3.8-4.9	Others, each . .	0.05
Mn . . .	0.3-0.9	Others, total . .	0.15
Mg . . .	1.2-1.8	Zn . . .	0.25
Cr . . .	0.1	Balance, Aluminium	
Note: Value maximum if range not show			

The T351 solution heat treatment requires heating the material to a temperature of 500°C followed by quenching to less than 40°C. After heat treatment it is stress relieved by controlled stretching (1-3%) and then aged naturally. There is no further straightening after stretching.

Using material from the same batch grain size was measured by Cini [42]. Samples were polished and chemically etched and grain size measured using the line counting

method. The substrate grain structure contained pancake shaped grains typical of rolled sheet. The grains were 150-200 µm in the longitudinal grain direction (L), 80-100 µm in the long transverse direction (T), and approximately 20 µm in the short transverse direction (S). No grain structure was observed in the clad layer. The thickness of the clad layer was measured using an optical microscope and found to be 70-80 µm.

The mechanical properties of the material were obtained by tensile test according to ASTM standard E8M [241]. The tensile tests were conducted parallel to the rolling direction. The tests were repeated five times and the average is reported in Table 3.2.

Table 3.2: Mechanical properties of Al 2024-T351

Material	Young's Modulus E (MPa)	Poisson's Ratio ν	Yield Stress (MPa)	Ultimate Tensile Stress (MPa)	Elongation at Fracture (%)
2024-T351	72000	0.33	360	481	19

3.2 Fatigue Test Specimen Geometry

The tension-tension fatigue test samples had dogbone shape with minimum section width of 80 mm as shown in Figure 3.1. The reduction in width was achieved by material removal to a 340 mm radius as shown in Figure 3.1. This large radius created a small stress concentration (K_t) predicted [242] using FEM as 1.01.

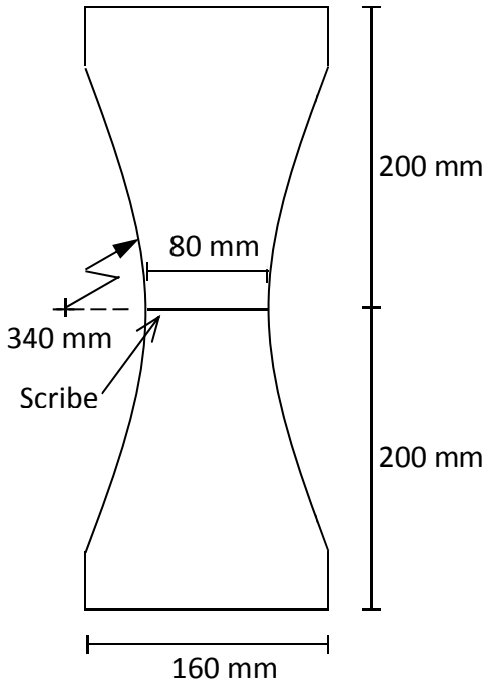

Figure 3.1: Dogbone shaped specimen used for tension-tension fatigue tests

The sample edges were rounded and polished using progressively finer grades of emery paper down to P4000 grit. Edge polishing decreased the cross sectional area (CSA) of the samples. The samples were 2 mm thick and so a maximum edge rounding radius of 1 mm can be assumed. The reduction in CSA increases the nominal stress at the section of minimum width by 0.5 %. Therefore to achieve the desired stress level a slight reduction in external applied loading would be required. However the edges were only slightly rounded and material removal was minimal. Therefore no correction factor on applied external load was used. The combination of a large material removal radius and polished edges minimised the potential for crack initiation at the sample edges.

The scribes were machined at the mid length of the samples corresponding to the section of minimum width and thus the highest stress. Details of the scribing procedure are given in Section 3.3.

There is no applicable ASTM standard for four point bend fatigue test sample geometry and so the sample was designed to fit an available four point bend test jig (details of jig are given in section 3.8). The sample geometry used is shown in Figure 3.2 and was rectangular in shape with dimensions 80 mm wide by 210 mm long. As for the tensile samples the samples edges were rounded and polished using emery paper to inhibit fatigue crack initiation at the edges. The scribe was machined at the mid length of the sample as shown in Figure 3.2.

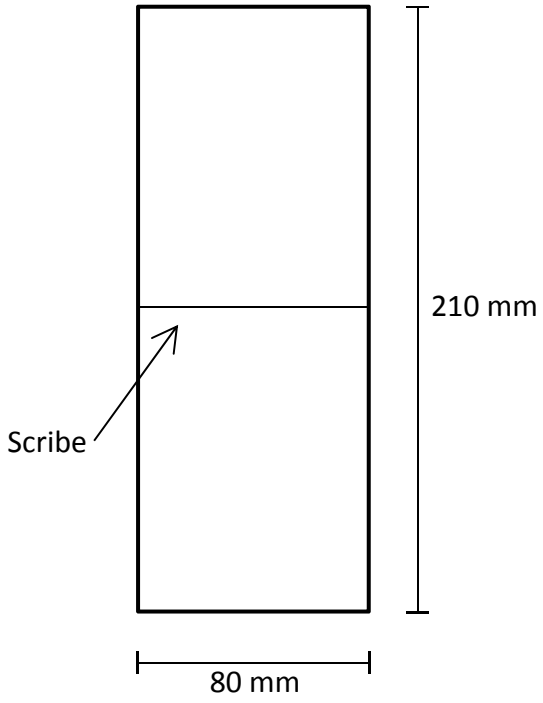

Figure 3.2: Rectangular specimen used for four point bend fatigue tests

3.3 Scribing of Test Samples

As noted in section 2 the scratches found in service were created using blunt metal objects such as blades. Recreating these types of scratches in a repeatable and controlled manor is difficult. Therefore to replicate scratches in the laboratory a diamond tipped tool was used to scribe the material. In contrast to the ploughing nature of blunt tools the diamond tipped tool cut and removed material to create the scratch and resulted in less plastically deformed material. The diamond tool created a rounded tip V notch in the material as illustrated in Figure 3.3. Using the diamond tool allowed precise control of notch depth (d), root radius (ρ), and wall angle (θ). The notch root radius was 5 µm and the wall angle was 60° for all scribes. Scribe of depth 50 µm and 150 µm were created in samples.

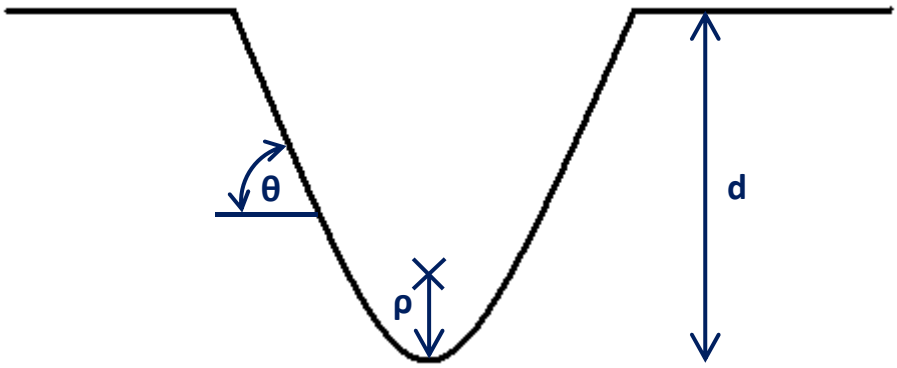

Figure 3.3: Schematic of rounded tip V notch created using diamond tipped tool

A modified milling machine was used for the scribing process, shown in Figure 3.4. The machine consisted of a backing plate with four suction ports and a moveable stage that held the diamond tipped tool. The stage could be moved manually in the Y direction, it could be set to travel automatically in the X direction and was fixed in the Z direction. The sample was constrained to the backing plate by the four suction ports and was orientated lengthwise in line with the Z axis. As mentioned the position of the stage and hence the diamond tipped tool was fixed in the Z direction. To align the tool with the sample midpoint metal shims were placed underneath the sample.

The notch root radius and wall angle were controlled by the shape of the diamond. The third notch variable depth required detailed measurement of flatness across the sample surface. A Mahr 1303 LVDT inductive probe (Figure 3.5) was placed on the stage using a magnetic jig. The probe was connected to a MAHR 1200 IC compact amplifier. The probe was positioned at one edge of the sample surface close to the midpoint of the sample. The stage was then traversed in the X direction so the probe travelled across the sample face and sample flatness was monitored on the amplifier.

A flatness of +/-5% of the desired notch depth was required to ensure that the depth of the notch was relatively constant along the scribe length. If the sample fell outside this tolerance plastic shims were placed between the sample and the backing plate to adjust flatness. Once sample flatness was within tolerance the diamond tipped tool was placed in the stage as shown in Figure 3.6.

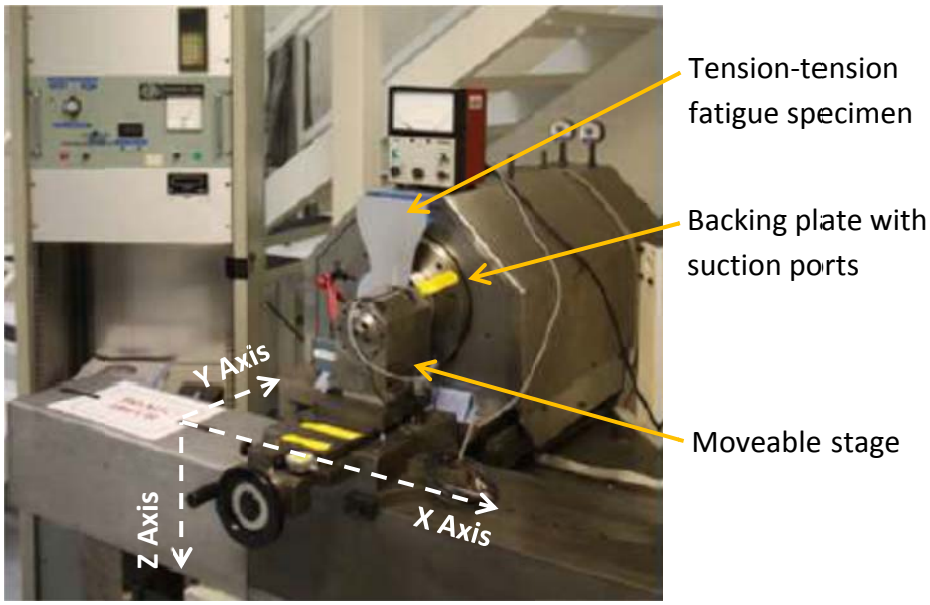

Figure 3.4: Scribing equipment

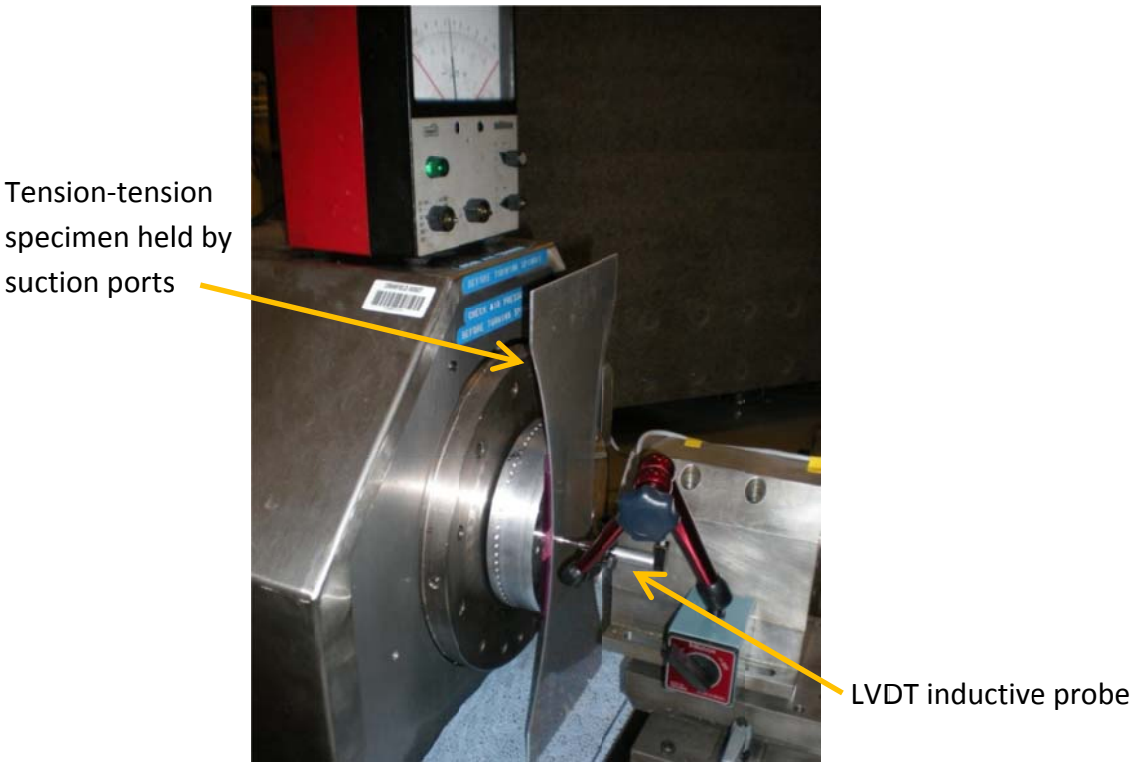

Figure 3.5: Measurement of sample flatness using LVDT probe

The stage was then gradually moved in the Y direction until the diamond tool was approximately 20 µm from the sample surface. It was important not to contact the tool with the sample face as to do so could damage the diamond. The diamond tool was first located adjacent the sample face and traversed automatically in the X direction at a travelling speed of 100 mm/min. If no contact was made with the sample face the diamond was then moved 3 µm closer in the Y direction and the procedure was repeated. Once first contact of the diamond and the sample was made this was considered the initial zero position, contact between the diamond and sample was obvious by the build-up of swarf on the diamond. The probe was then repositioned on the stage and the diamond was initially moved 5 µm in the Y direction and traversed across the sample face. This was followed by repeated cuts incrementing the depth by 10 µm on each cut, until the final 5 µm cut to reach the required 50 µm or 150 µm scribe depth. Using this procedure ensured constant scribe depths to within +/-3 µm across the width of the sample. After every three to four scribing operations, the diamond tool was checked using an optical microscope for damage and if found it was returned to the manufacturer for repair.

Figure 3.6: Scribing of sample surface using diamond tipped tool

Some samples had the sample face near the edge regions polished using emery paper to remove the scribe. The extent of the region where the scribe was removed was between 5 mm and 15 mm. When edge rework was performed it is noted along with the test results in chapter 4.

3.4 Measurement of the Depth of the Scribes

The depth of the scribes was measured using an Olympus OLS3100 confocal laser scanning microscope (LEXT). Using the LEXT a 3D map of the scribe at up to 100× magnification was created. The LEXT software allowed quantitative measurements on

the acquired 3D map to be taken and this was used to measure the depth of the scribe. Due to the variation of flatness across the sample surface, as mentioned in section 3.3, depth was not uniform along the scribe. Therefore measurements were taken at three positions. For each fatigue test configuration samples were chosen randomly for depth characterisation. The measured depths are listed in Table 3.3.

Table 3.3: Measured scribe depths

Sample No.	Target Notch Depth (μm)	Measured Notch Depth (μm)		
		Location 1	Location 2	Location 3
T003	50	48	49	48
T004	150	152	154	153
T005	50	50	50	52
T007	50	47	49	51
T008	150	151	152	152
T016	50	53	51	50
T021	150	153	153	152
T024	150	146	150	152
T027	50	50	51	53
T030	150	155	153	151
B001	50	51	52	51
B003	150	147	148	151
B005	50	50	53	51
B006	150	151	147	149
B008	50	48	47	48
B011	150	151	154	153
SN07	50	51	52	47
SN09	50	52	48	50
SN13	150	153	150	149
SN17	150	149	146	149
CI02	150	150	148	149
CI05	150	153	152	150
CI08	50	52	51	52

3.5 Laser Shock Peening Treatments

Laser peening treatment from three providers was used. These were Metal Improvement Company (MIC), Universidad Politecnica de Madrid (UPM), and the Toshiba Corporation. The laser system parameters as set during the peening procedures are compared in Table 3.4. Toshiba provided two treatments with different spot sizes. Laser peening was performed after cutting of the scribes in the sample surface.

Table 3.4: Comparison of laser peening parameters used

Parameter	MIC	UPM	Toshiba	
Laser Type	Nd:glass	Nd:YAG	Nd:YAG	
Wavelength (nm)	1064	1064	532	
Laser Spot Geometry	Square	Circle	Circle	
Laser Spot Diameter (mm)	7.5	1.5	0.4	0.7
Application Time (ns)	18	10	8	8
Energy (J/pulse)	15.2	2.8	0.02	0.06
Peak Intensity (GW/cm^2)	1.5	15.72	1.99	1.95

The MIC system used a Nd:glass laser with a 7.5 mm wide square spot. Two variants of the MIC treatment were used and are termed 1 Row and 3 Row. The 1 row peening pattern is illustrated in Figure 3.7. It consisted of three laser peening layers offset by 30% resulting in a total treated area width of approximately 15 mm. The laser tracking direction was parallel to the scribe line and an overlap of approximately 2% was used between each spot in the row. The 3 row peening was similar but consisted of nine peening layers in total. Again an offset of 30% between layers was used and this resulted in a total treated area width of approximately 30 mm. Both treatments used a water jet tamping layer with aluminium foil ablative tape. The sample surface after treatment is pictured in Figure 3.8

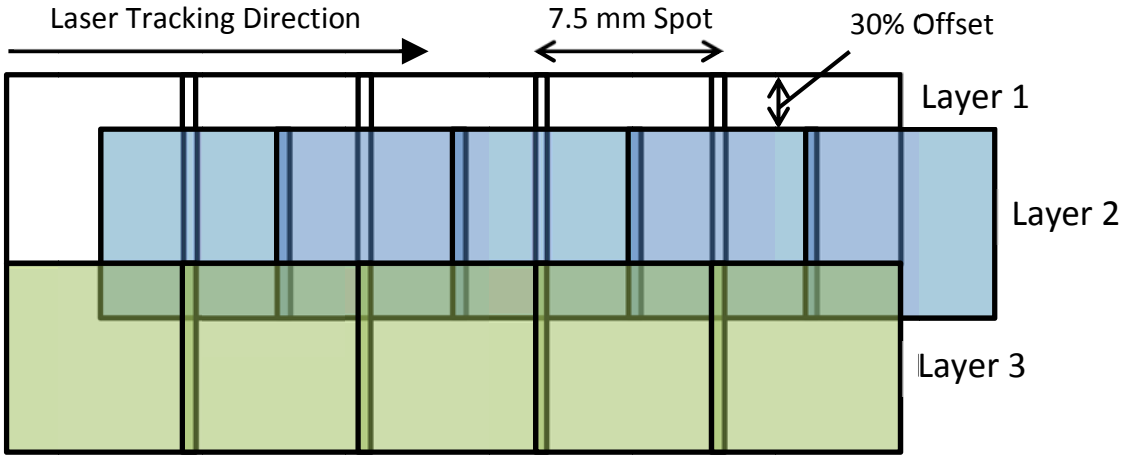

Figure 3.7: MIC 1 Row peen pattern consisting of three laser peening layers

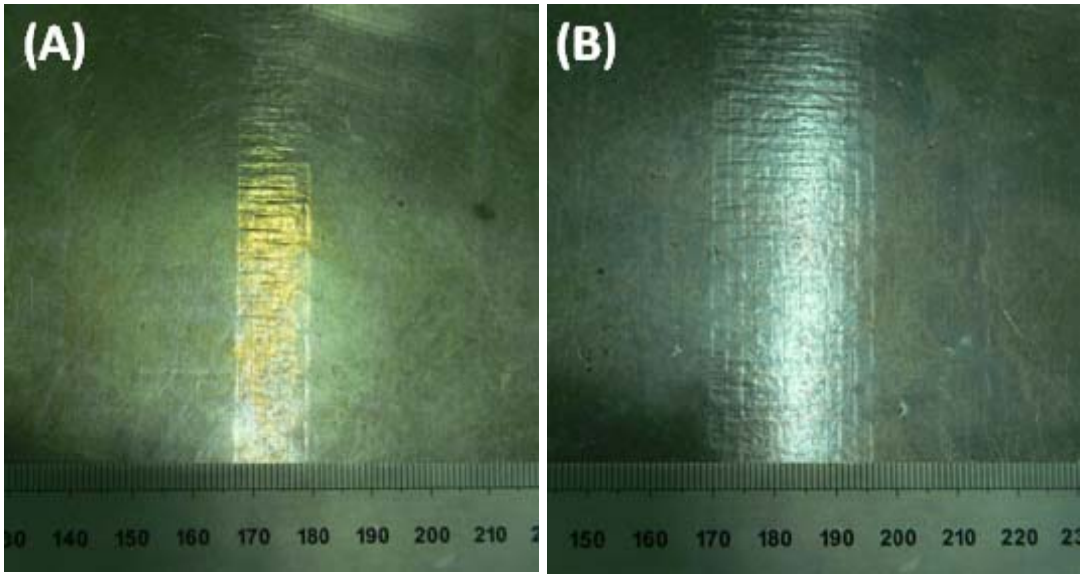

Figure 3.8: Sample surface after (A) MIC 1 row LSP treatment and (B) MIC 3 row LSP treatment

The UPM treatment used a Nd:YAG laser with a 1.5 mm diameter circular spot. A water jet tamping layer was used but no ablative tape. The peening pattern is illustrated in Figure 3.9. The treated area was approximately 5 mm wide and extended across the full 80 mm width of the specimens. The laser tracking direction was parallel to the scribe line with an overlapping pitch of 0.75 mm. The surface finish after UPM peening is shown in Figure 3.10.

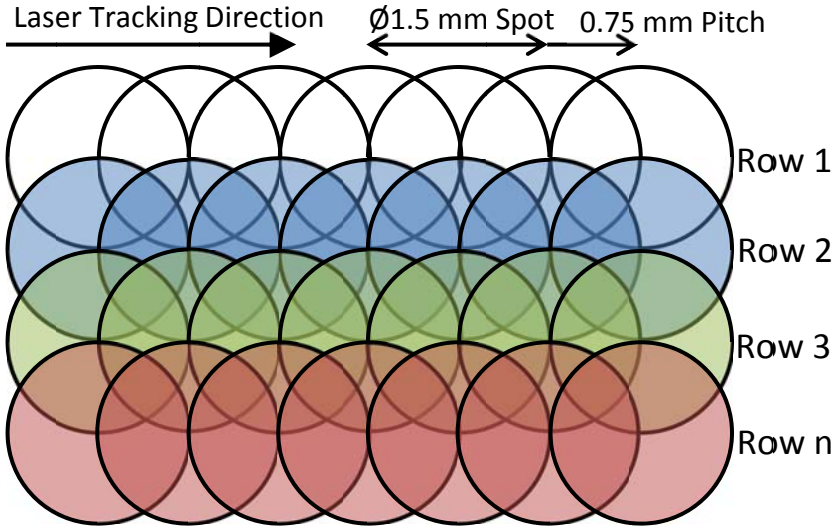

Figure 3.9: Illustration of UPM laser peening pattern

Figure 3.10: Sample surface after UPM LSP treatment

Toshiba also used a Nd:YAG laser for the peening treatment. It had a circular spot and two diameters were used of 0.4 mm and 0.7 mm. During peening the specimens were submerged in a water tank and no ablative tape was used. The treated area was approximately 5 mm wide and extended across the full 80 mm width of the specimens. Three variations of the treatment were used to study the induced residual stress field. The first variant used a 0.4 mm diameter laser with 18 pulses per mm^2. The laser tracking direction was parallel to the scribe line and an overlapping pitch of 0.236 mm was used as illustrated in Figure 3.11. The overlapping pitch between peening rows was also 0.236 mm. The second variant again used a 0.4 mm diameter laser but with 54 pulses per mm^2. The overlapping pitch was 0.136 mm. Finally the third variant used a 0.7 mm diameter laser with 18 pulses per mm^2. The overlapping pitch was 0.236 mm. The treatments are referred to as 0.4Ø-18, 0.4Ø-54, and 0.7Ø-18 respectively.

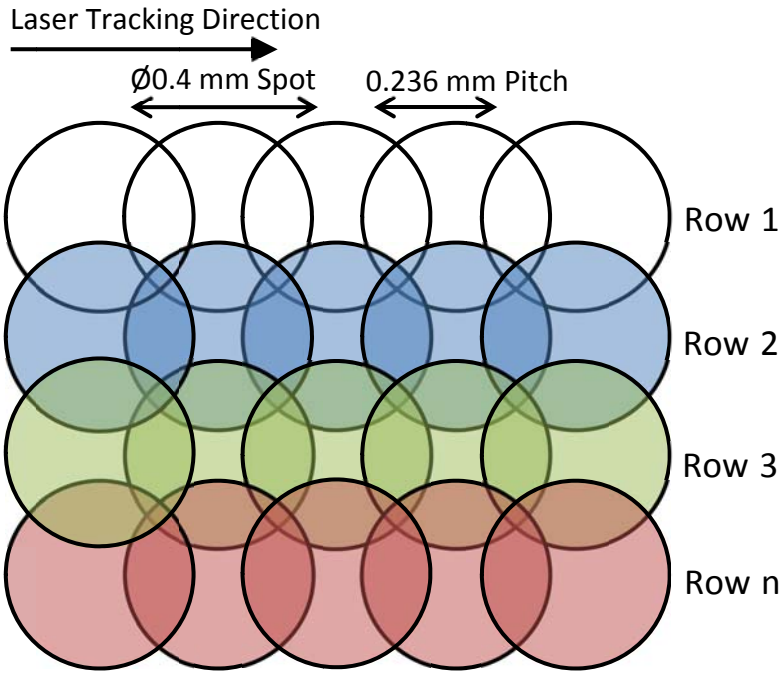

Figure 3.11: Illustration of Toshiba 0.4Ø-18 peening pattern

For fatigue tests two variants of Toshiba treatment were used for fatigue testing and are compared in Figure 3.12. The first variant used a combination of the 0.4Ø-18 and 0.4Ø-54 treatments. The 0.4Ø-54 treatment extended 20 mm across the face from both edges and the 0.4Ø-18 treatment was applied to the central 40 mm of the sample. The second variant for fatigue testing applied the 0.4Ø-18 treatment across the entire 80 mm width.

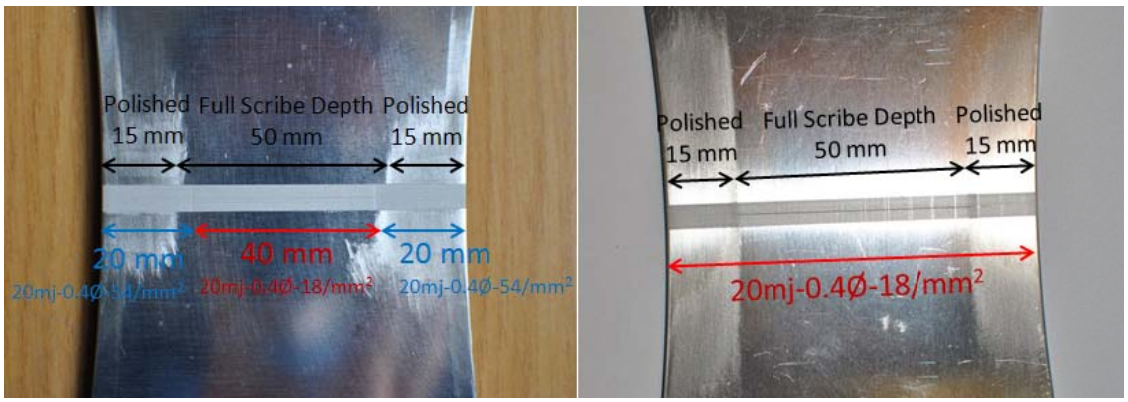

Figure 3.12: Surface after (A) Toshiba type 1 and (B) Toshiba type 2 LSP treatments

3.6 Characterisation of LSP Effects on Test Specimens

The effect of laser shock peen induced plastic deformation of the scribes was studied using an Olympus OLS3100 confocal laser scanning microscope (LEXT). Pre and post

peening 3D maps of the scribe geometries were created for comparison. Also topographic images of the planar surface were created post peening with the LEXT. The results are given in section 4.1.

After laser shock peening the fatigue samples were visibly distorted. To characterise the distortion the sample geometries were measured using a coordinate measurement machine (CMM) [The system had a specified accuracy of 1.7+3L/1000 µm where L is the measured length]. Measurements were taken in lines along the length of the samples i.e. perpendicular to the peening direction. For the UPM peened samples the measurements consisted of seven lines spaced 10 mm apart with a measurement interval of 25 mm along each line. For Toshiba peened samples the measurements consisted of 15 lines 5 mm apart with a measurement interval of 1 mm along each line. No measurements were taken on MIC peened samples. The measurement data was used to create 2D line plots of the sample geometry and are shown with the experimental results in section 4.1.

The test samples characterised using CMM measurements were strain gauged prior to fatigue testing using TML strain gauges of type FLA-5-23. These have a gauge length of 5 mm, resistance of 120 ohms, and a gauge factor of 2.16. Prior to installation the samples were cleaned using acetone. The gauges were bonded using adhesive to the peened face and placed 15 mm from the scribe line along the central axis. Strain gauges were also placed at the opposing position on the non-peened face. Gauge lead extensions were soldered to the gauges. This allowed measurement of tensile applied strain and the strain induced by out of plane bending.

3.7 Tension-Tension Fatigue Tests

Tension-tension fatigue tests were conducted using servo hydraulic machines with maximum load capacities of 100 kN (shown in Figure 3.13) and 250 kN. The machine that was used for each test is detailed with the results in Section 4.3. Strain gauged specimens were connected to a National Instruments CompactDAQ modular data acquisition system to record strain, load, and displacement. The dogbone fatigue specimens were then hydraulically clamped into the 100 kN machine or clamped using bolted grips into the 250 kN machine. In both cases the test specimens were aligned centrally along the load path.

An R ratio of 0.1 was used for the fatigue tests. A maximum stress of 200 MPa at the section of minimum width of the dogbone specimens was desired. This required a maximum applied load of 32 kN. The fatigue tests were conducted at room temperature. Fatigue tests using the 100 kN machine were done at 10 Hz whilst those using the 250 kN machine were at 5 Hz. The tests were run until sample fracture.

Figure 3.13: Tension-tension fatigue test using 100 kN servo hydraulic machine

A series of fatigue tests were done to develop an S-N curve. These tests were performed using both the 100 kN and 250 kN test machines. Three samples configurations all without LSP treatment were studied: non-scribed, scribed to 50 µm depth, and scribed to 150 µm depth. An R ratio of 0.1 was used with the applied stress range reduced after each test until a sample run out was achieved. For these S-N tests the run out was set as 10×10^6 cycles.

3.8 Four Point Bend Fatigue Tests

Four point bend fatigue testing was done using a servo hydraulic machine with a maximum load capacity of 20 kN, pictured in Figure 3.14. A schematic of the four point bend test jig is shown in Figure 3.15. The jig consisted of two outer 31 mm diameter contact rollers attached to a lower mounting plate and two inner 37 mm diameter contact rollers attached to an upper mounting plate. The gauge section (i.e. the distance between the centres of the inner rollers) was 80 mm. The distance between the centre of the inner and outer rollers was 50 mm. The upper rollers were free to rotate and kept in place by use of rubber O-rings whilst the lower rollers were fixed. Lateral movement of the test sample was prevented by lips on the extremities of the lower rollers and longitudinal movement was restrained by two plates fixed at

the ends of the test sample. The test samples were placed in the jig scribed face downward.

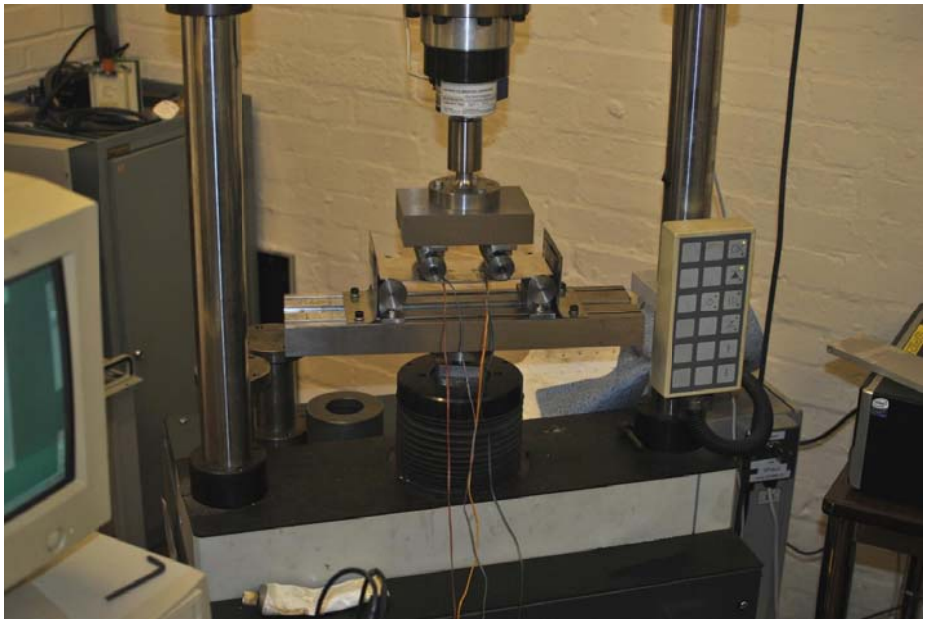

Figure 3.14: Four point bend fatigue test using 20 kN servo hydraulic machine

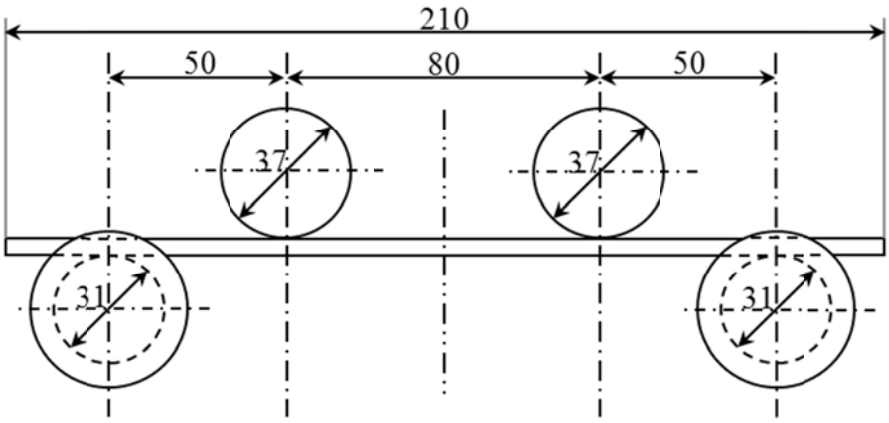

Figure 3.15: Schematic of four point bend test jig (dimensions in mm)

As for the tension-tension fatigue tests the R ratio was 0.1 and maximum desired stress was 200 MPa. Four point bending induces a pure bending load and therefore if a tensile stress of 200 MPa is induced on the scribed face a compressive stress of -200 MPa will be induced on the back face. The tests were conducted at a frequency of 1 Hz at room temperature. Sample failure was defined as fracture of the specimens. Fatigue tests were initially performed in displacement control as the 20 kN load cell was not capable of maintaining the small applied loads required. Subsequent tests were performed in load control using a 1.5 kN load cell and also using a 500 N load cell that were attached above the upper mounting plate.

To measure the required stresses all test specimens were strain gauged using TML strain gauges of type FLA-5-23. Gauges were bonded 15 mm on each side of the scribe and at the opposing locations on the back face. External load was applied to the samples until a strain corresponding to surface stresses of 20 MPa and 200 MPa was achieved on the scribed face (278 με and 2778 με respectively) The displacement or load at these strains was noted and used for the cyclic test.

3.9 Measurement of Striation Spacings

After completion of tension-tension and four point bend fatigue tests the distance between fatigue striation marks on the fracture faces were measured using a Philips XL30 SFEG scanning electron microscope (SEM). The fractured samples were first cut to fit within the SEM chamber. After cutting the fracture faces were placed in alcohol solution and cleaned using in ultrasonic bath.

To minimise measurement error, striation spacings were measured in bands of five to ten. In addition five to ten bands at each position were measured. As discussed in section 2.1.3 the relationship between fatigue striation marks and load cycles is a topic of debate however the assumption was made in this work that the distance between each striation mark accounted for the increment of crack growth that occurred in one load cycle. The distance was measured from the scribe root of each striation spacing measurement and therefore local fatigue crack growth rates at each distance (i.e. crack length) was estimated. By measurement of striation spacing at various distances from the scribe root an estimated of the FCGR against crack length was established. Measurements of striation spacing were taken on both peened and unpeened samples to allow comparison of the effect on FCGR of various LSP treatments. The results of this study are given section 4.5.

This method was used to estimate FCGR because conventional methods were not practical. Direct observation and measurment of crack length was not possible due to the direction of crack growth. Some success has been reported using DCPD to measure FCGR rate of short cracks 0.2 mm greater [145]. The replica method has also been used with some success [42] however for it deemed unapproapriate for the current work due to the possibility of high level of crack closure induced by the compressive residual stress fields.

3.10 Measurement of Fatigue Crack Growth

Striation marks were not visible on the fracture faces in the region near the scribe root. The closest striation marks visible were located approximately 50 μm away. The distance measured between striation marks increased with crack length. Therefore in the first 50 μm of crack growth the resolution required to observe striation marks exceeded that achieved using the SEM.

A series of fatigue tests was performed to solely study the effect of laser shock peening on the crack growth region not observable using striation spacing measurements. This was done by first cycling dogbone fatigue specimens to a pre-determined number of cycles under the same test conditions as used for the tensile fatigue tests (see Section 3.7). Once the required number of cycles was achieved the cycling was stopped and the external applied load was increased linearly until sample fracture. The fracture faces were then cleaned and crack length was measured using an SEM. This test procedure was repeated for different cycle counts.

The samples scribed to 150 µm all statically fractured at the scribe location. However not all samples scribed to 50 µm fractured at the scribe. This was attributed to the scribe and fatigue crack having not penetrated through the soft cladding layer. Also for the samples that did break at the scribe greater amounts of plastic necking was observed compared to samples scribed to 150 µm. The necking affects the accuracy of the crack length measured. To alleviate this problem unclad samples were used to study the effect of LSP on fatigue crack initiation for samples scribed to 50 µm.

4 Experimental Results

In the first section of this chapter physical effects on the experimental samples caused by the peening are described. This includes the effect of peening on the scribe geometry, sample surface, and sample distortion. The residual stress fields induced by laser peening are presented in section 4.2. In section 4.3 and 4.4 the results of tension-tension and four point bend fatigue tests are listed respectively. In section 4.5 fracture characteristics of the fatigued samples are described. Also listed are measured of striation spacings made on fracture surfaces. The results of interrupted fatigue tests are presented section 4.6. And finally a summary of the chapter is provided in section 4.7.

Throughout this and subsequent chapters the following terminology is used to refer to the LSP treatments. MIC1 is the 1 row peening performed by Metal Improvement Company and MIC3 is the 3 row peeing. UPM is peening performed by the Universidad Politecnica de Madrid. Two peening treatments were performed by Toshiba and these are referred to as TOSH #1 and TOSH #2. TOSH #1 was a combination of 0.4Ø-18 and 0.4Ø-54 peening and TOSH #2 used only 0.4Ø-18 peening. For full details of the peening treatments refer to section 3.5.

4.1 Effect on Sample Geometry and Surface Finish of Laser Peening

The effect of laser peening on the surface finish at a scribe 50 μm deep is shown in Figure 4.1. These images were created using a confocal laser scanning microscope. An unpeened scribe is shown in Figure 4.1 (A). This scribe was created using a diamond tipped tool as described in section 3.3. The diamond tipped tool removed material from the sample to create the scribe and minimal plastically deformed material was left behind in its wake. In contrast using blunt tools (refer to section 2.2) the scribes were formed by ploughing / plastically deforming the material. It cannot be quantifiably stated that the diamond tipped tool induced no residual stress as the scribes were formed however any residual stress induced would be less than that induced using blunt tools.

Shown in Figure 4.1 (B) is a scribe after peening by MIC. The MIC peening treatment used a square laser spot 7.5 mm wide. The confocal image was square shaped 0.254 mm wide and at this scale the LSP treatment qualitatively had little effect on the surface finish compared to the unpeened surface in Figure 4.1 (A). The nominal scribe root radius created by the scribe was 5 μm. After the MIC LSP the root radius was 3.5 μm determined using the confocal imaging data.

Scribes after UPM and TOSH LSP treatment are shown in Figure 4.1 (C) and (D) respectively. The UPM and TOSH laser spots were circular with a diameter of 1.5 and

0.4 mm respectively. The lasers induced visibly greater plastic deformation than the MIC laser. The root radius of the scribes was 12 and 6 µm after UPM and TOSH LSP treatments respectively.

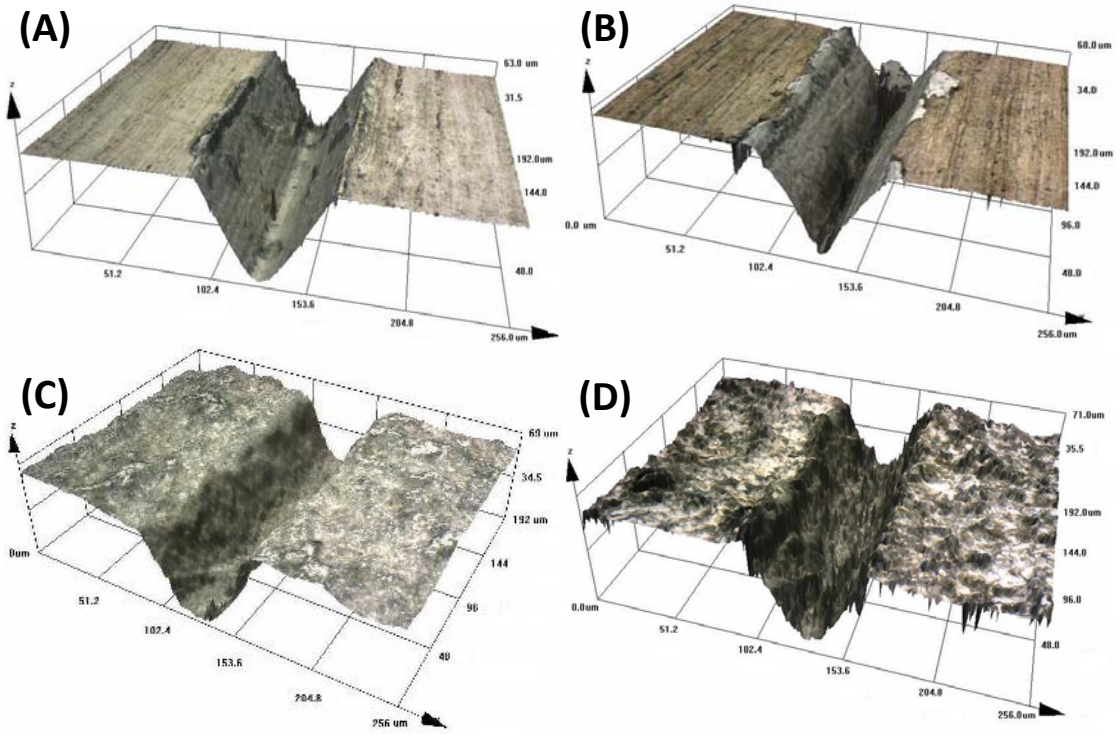

Figure 4.1: Surface finish of 50 µm deep scribes with (A) no peening, (B) MIC LSP, (C) UPM LSP and (D) TOSH LSP

The surface of a TOSH peened sample is shown in Figure 4.2. The location of individual laser hits as the system tracked across the sample was clearly identifiable on the surface as shown in Figure 4.2 (A). A topographic image created using the laser confocal microscope of the LSP treated surface is shown in Figure 4.2 (B). The image has been overlaid with circles that represent to scale the Ø0.4 mm laser spots. The centres of the spots are approximately 20 µm higher than at the edges where the spots have been overlapped up to 400%. The image also indicates that one of the peening lines was out of sync with the other lines.

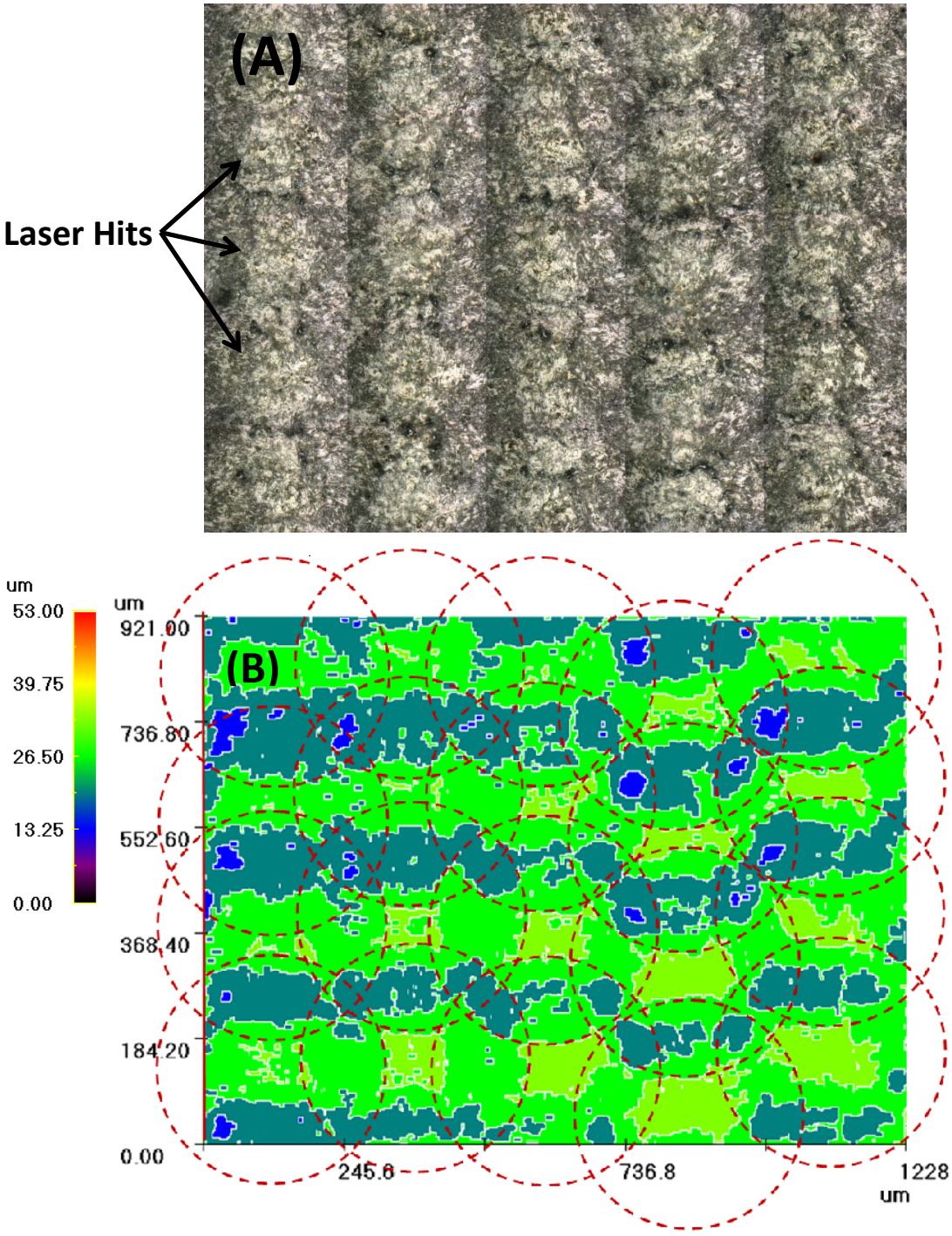

Figure 4.2: (A) Sample surface after TOSH LSP treatment and (B) surface topography overlaid with circles to scale of 0.4 mm laser spots

4.1.1 Residual Stress Induced Distortion

The LSP treatment was applied to one surface of the samples only. Distortion of test samples then occurred to maintain equilibrium of the elastic stress field generated following the laser induced plastic deformation. The distortion induced a balancing

stress field as illustrated in Figure 4.3. This shows that the compressive residual stress field on the peened face actually reduced due to sample distortion.

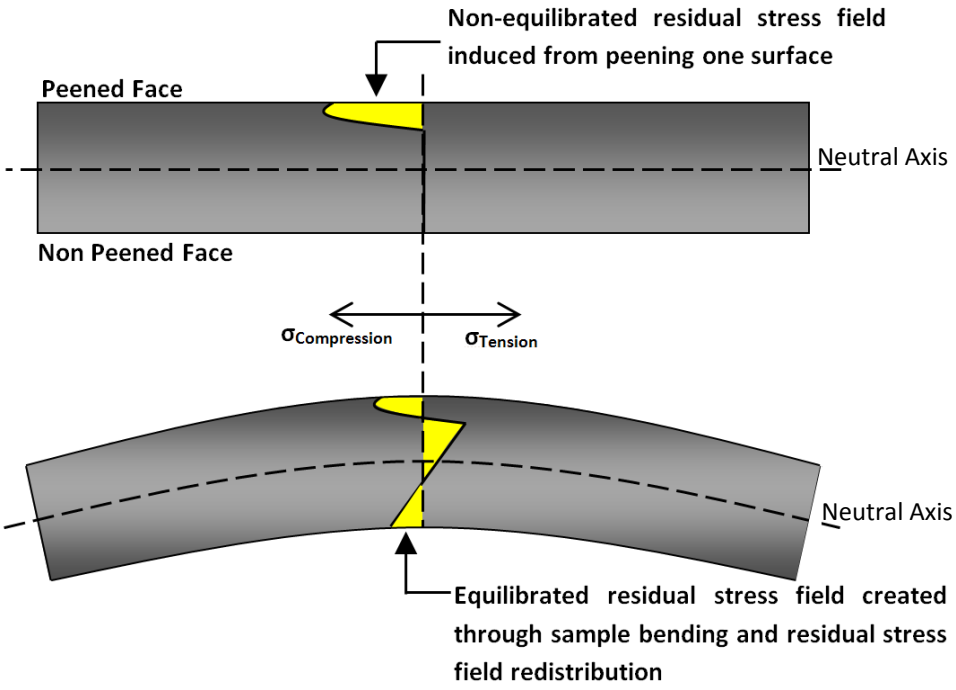

Figure 4.3: Effect of a non-equilibrated residual stress field on distortion and resulting residual stress redistribution

The distortion after peening was measured using a Coordinate Measurement Machine (CMM). In Figure 4.4 the surface profile of a sample without LSP treatment is compared to samples with LSP treatment. No measurements of distortion were taken on MIC treated samples. The untreated samples had initial distortion that was attributed to the machining of the test specimens. After UPM and TOSH LSP treatments the distortion increased.

The induced LSP distortion is confined to the peened area only which effectively acts as a “hinge” with the ends of the sample following the line of the deflected region at the edge of the peened area. A distortion angle was defined as the angle created by the material flanking the peened region, as illustrated in Figure 4.4. The deflection of the sample was defined as the difference in height between the position of the sample ends and the position of the sample mid-point. The samples deflection is a combination of the distortion angle created in the peened region and the overall length of the sample, i.e. a bigger angle or longer sample will result in greater deflection. The measured deflection and distortion angles are given in Table 4.1. The UPM LSP treatment induced sample deflection of up to 3.2 mm. The TOSH LSP induced sample deflection of up to 2.4 and 1.6 mm for treatment type 1 and 2 respectively.

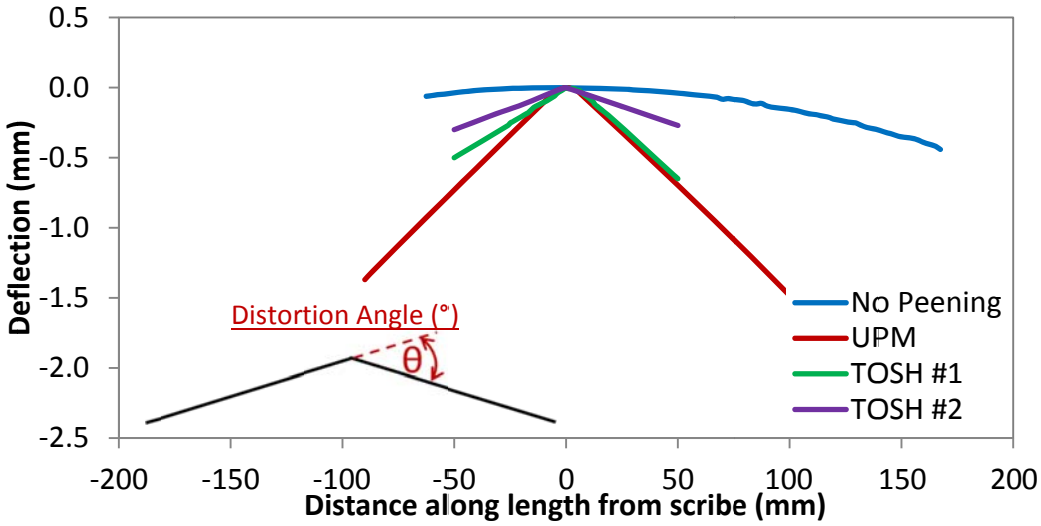

Figure 4.4: Illustration of CMM measured distortion of fatigue samples with and without LSP treatment

Table 4.1: Effect on sample distortion of LSP treatment

Sample No.	Treatment	Length (mm)	Angle (deg)	Defection (mm)
T016	UPM	400	1.8	3.2
T017	UPM	400	1.8	3.2
T019	UPM	400	1.8	3.2
T020	UPM	400	1.5	2.6
T021	UPM	400	1.5	2.6
T023	TOSH #1	400	1.4	2.4
T024	TOSH #1	400	1.2	2.1
T028	TOSH #2	400	0.7	1.2
T030	TOSH #2	400	0.7	1.2
B009	TOSH #2	210	0.6	0.3
B010	TOSH #2	210	0.9	0.8

4.1.2 Effect on Applied Loading of LSP induced Sample Distortion

Due to sample distortion induced by laser peening, the stress induced by the applied load during the tensile fatigue tests was not uniaxial tension but tension combined with out of plane bending. A bending component was induced at zero tension load when the sample was first clamped in the grips as illustrated in Figure 4.5. A further bending component is produced as the tensile load is ramped and the bent sample becomes straightened. To measure the true surface strain, gauges were bonded on both the peened and non-peened faces as illustrated in Figure 4.5. The surface strains

were measured throughout the fatigue load cycle. Surface stresses were calculated and are plotted in Figure 4.6.

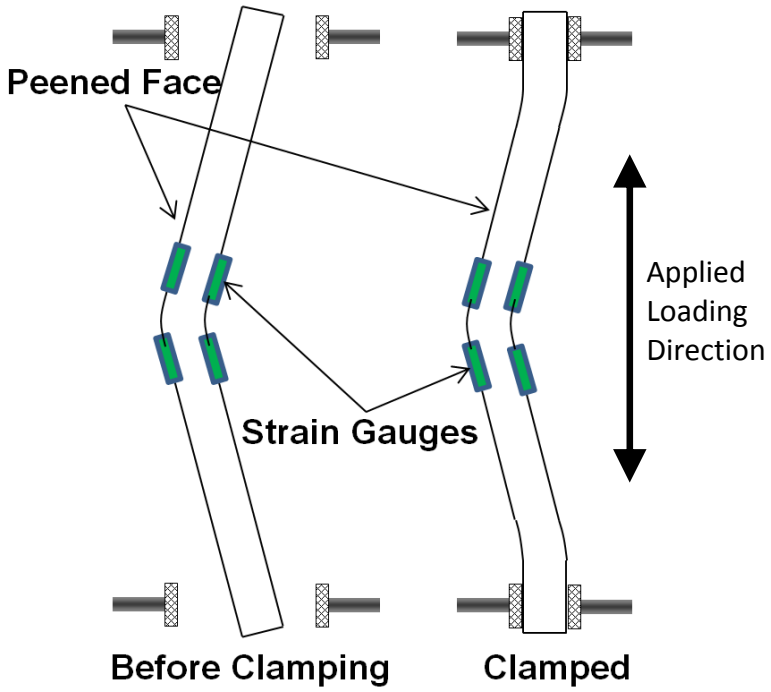

Figure 4.5: Illustration of clamping distorted fatigue specimen

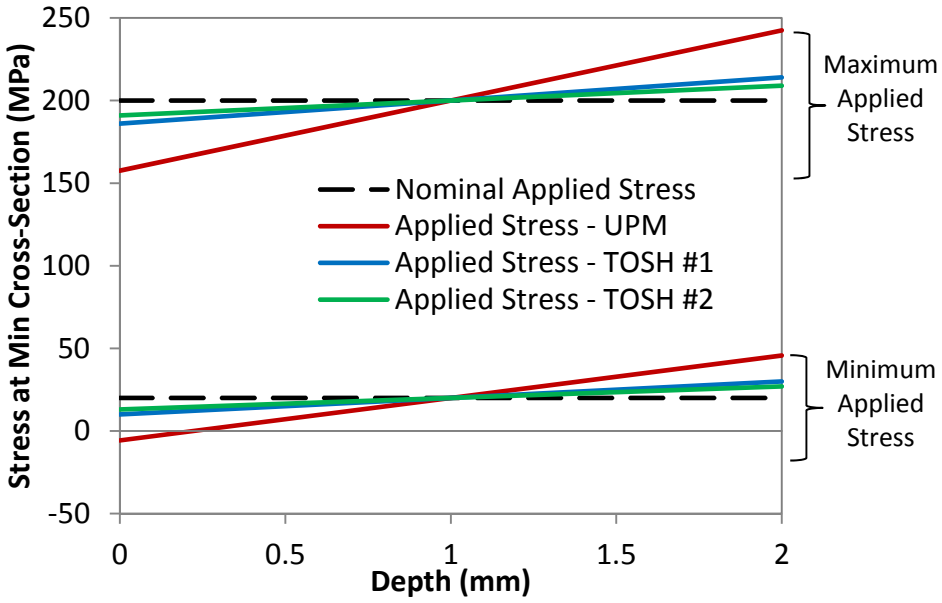

Figure 4.6: Surface stress applied during tension-tension fatigue tests determined using in situ strain gauges

On the peened face of the samples treated by UPM the surface stress was less than the nominal tensile stress and greater than nominal on the non-peened face. At the maximum applied load the nominal stress is 200 MPa however the surface stresses

were 158 MPa and 242 MPa on the peened and non-peened faces respectively. At the minimum applied load the nominal stress is 20 MPa however the surface stresses were -6 MPa and 46 MPa on the peened and non-peened faces respectively. These values give an R ratio and stress range of -0.04 and 163 MPa on the peened face and 0.19 and 197 MPa on the non-peened face (nominal values were 0.1 and 180 MPa).

The TOSH treatment 1 induced less distortion than the UPM treatment and therefore the effect on the applied load induced nominal stress was less. On the peened face the maximum and minimum surface stresses were 186 MPa and 10 MPa. On the non-peened face they were 214 and 30 MPa. This implied an R ratio of 0.05 and a stress range of 176 MPa on the peened face and on the non-peened face 0.14 and 184 MPa.

The TOSH treatment 2 induced the least distortion. On the peened face the maximum and minimum surface stress was 191 MPa and 13 MPa and on the non-peened face was 209 and 27 MPa. This implied an R ratio of 0.07 and a stress range of 178 MPa on the peened face and on the non-peened face 0.13 and 182 MPa.

When fatigue lives of unpeened and peened samples are compared, increases in life produced by the peening will require interpretation in the light of the fact that the stress range on the peened surface has been reduced and that on the unpeened surface increased with respect to the nominal tensile value of 180 MPa.

4.2 Residual Stress Fields induced by Laser Shock Peening

The residual stress fields induced by laser shock peening were measured using the incremental hole drilling method by Toparli [132]. A brief description of the results is provided in this section to aid understanding of the fatigue results that follow in subsequent sections.

The incremental hole drilling technique was described in chapter 2 however reminding that residual stress is measured in two perpendicular directions depending on the alignment of the strain gauge and that residual stress is measured in increments through the depth. The alignment of the strain gauges by Toparli [132] provided stress measurement parallel and perpendicular to the scribe as illustrated in Figure 4.7. Throughout the current work the direction parallel to the scribe line is termed S1 and perpendicular to the scribe line (i.e. the applied loading direction) is termed S2. Only residual stress measured in the S2 direction is presented in this section. A detailed description of the complete residual stress fields measured by Toparli is provided in appendix A.

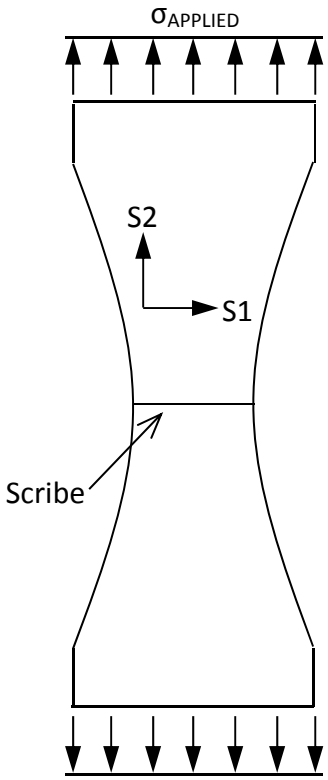

Figure 4.7: Direction of residual stress field measurements in relation to fatigue specimens

The residual stress fields that were measured by Toparli [132] in the S2 direction are compared in Figure 4.8. For comparison the depth of the 50 µm and 150 µm deep scribes is illustrated. The TOSH LSP treatment induced the greatest compressive residual stress of the four LSP treatments. The peak compressive stress was 204 MPa and was located approximately 100 µm from the peened surface. In comparison the UPM LSP treatment induced a peak compressive stress of 106 MPa and was located 112 µm from the peened surface. The compressive residual stress field induced by the UPM LSP extended further from the surface (0.7 mm) than field induced by TOSH LSP (0.35 mm) however the UPM LSP induced tensile residual stress near the surface.

The MIC1 and MIC3 LSP treatments also induced residual stress fields that were in tension near the peened surface. The MIC3 LSP treatment induced the deepest compressive stress field that extended 0.8 mm from the peened surface. However the MIC3 LSP treatment also induced the largest tensile region that extended 90 µm from the peened surface. The MIC1 LSP treatment induced comparatively little residual stress.

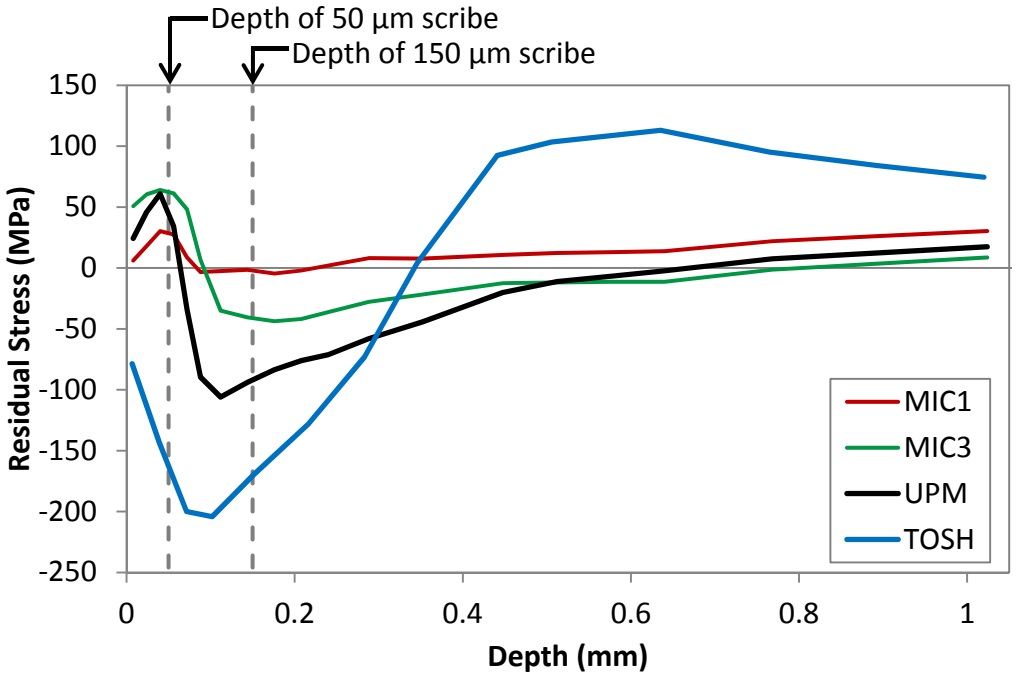

Figure 4.8: Comparison LSP induced residual stress fields in the S2 direction measured by Toparli [132]

4.3 Tension-Tension Fatigue Tests

A description of the tension-tension fatigue test procedures was given in Section 3.7. A total of 30 fatigue life tests were performed and are detailed in Table 4.2 with the results provided in Table 4.3. Baseline fatigue tests of unpeened material in the pristine condition, and with scribe defects of 50 µm and 150 µm were performed initially. The results are compared with those of Cini [42] in Figure 4.9 whom used the same test methods. The difference between the results was attributed to the normal scatter associated with fatigue testing. In the current work the majority of tests used material from the same batch however in a small number of cases material from a second batch was used as highlighted in Table 4.2. In addition to material characterisation of this batch (section 3.1) fatigue testing showed no discernible difference in fatigue performance i.e. the pristine fatigue life for batch 1 was on average 430297 cycles and for batch 2 was 424,240 cycles. The unpeened fatigue results gathered in the current work were combined with those from Cini [42] to increase sampling size. The fatigue performance of unpeened material with and without scribe defects is reported in Table 4.4. It was found that a scribe 50 µm deep reduced the fatigue life to 16% of the pristine life whilst a scribe 150 µm deep reduced the life to just 5%.

Table 4.2: Description of tension-tension fatigue tests

Test No.	Test Description
T001	No notch, Clad, Baseline test
T002	No notch, Clad, Baseline test
T003	50 µm notch, Clad, Baseline test
T004	150 µm notch, Clad, Baseline test
T005	50 µm notch, Clad, MIC 3 row LSP
T006	50 µm notch, Clad, MIC 1 row LSP
T007	50 µm notch, Clad, MIC 1 row LSP
T008	150 µm notch, Clad, MIC 3 row LSP
T009	150 µm notch, Clad, MIC 3 row LSP
T010	150 µm notch, Clad, MIC 1 row LSP
T011	150 µm notch, Clad, MIC 1 row LSP
T012	50 µm notch, Clad, UPM LSP
T013	50 µm notch, Clad, UPM LSP
T014	150 µm notch, Clad, UPM LSP
T015	150 µm notch, Clad, UPM LSP
T016	50 µm notch, Clad, UPM LSP, Edge rework after LSP
T017	50 µm notch, Clad, UPM LSP, Edge rework after LSP
T018	150 µm notch, Clad, UPM LSP, Edge rework after LSP
T019	150 µm notch, Clad, UPM LSP, Edge rework after LSP
T020	150 µm notch, Clad, UPM LSP, Edge rework
T021	150 µm notch, Clad, UPM LSP, Edge rework
T022	50 µm notch, Clad, TOSH #1, Edge rework
T023	50 µm notch, Clad, TOSH #1, Edge rework
T024	150 µm notch, Clad, TOSH #1 , Edge rework
T025	150 µm notch, Clad, TOSH #1, Edge rework
T026	No notch, Clad Batch 2, Baseline test
T027	50 µm notch, Clad Batch 2, TOSH #2, Edge rework
T028	50 µm notch, Clad Batch 2, TOSH #2, Edge rework
T029	150 µm notch, Clad Batch 2, TOSH #2, Edge rework
T030	150 µm notch, Clad Batch 2, TOSH #2, Edge rework

Table 4.3: Tension–tension fatigue test results

Test No.	Notch Depth (µm)	Peening Treatment	Fatigue Life (Cycles)	% of Pristine Sample Life	% Change in Fatigue Life
T001	0	n/a	403212	n/a	n/a
T002	0	n/a	528923	n/a	n/a
T003	50	n/a	84947	20	n/a
T004	150	n/a	21852	5	n/a
T005	50	MIC 1 Row	63340	16	-3
T006	50	MIC 1 Row	72391		
T007	150	MIC 1 Row	20576	6	24
T008	150	MIC 1 Row	28243		
T009	50	MIC 3 Row	107106	25	53
T010	150	MIC 3 Row	30484	8	81
T011	150	MIC 3 Row	40740		
T012	50	UPM	103927	27	66
T013	50	UPM	127488		
T014	150	UPM	32808	8	79
T015	150	UPM	37684		
T016	50	UPM	182934[(1)]	51	216
T017	50	UPM	258246[(1)]		
T018	150	UPM	51347	12	167
T019	150	UPM	54038		
T020	150	UPM	68371	16	243
T021	150	UPM	66953		
T022	50	TOSH #1	234449[(1)]	53	229
T023	50	TOSH #1	224596[(1)]		
T024	150	TOSH #1	272912[(1)]	61	1231
T025	150	TOSH #1	252087[(1)]		
T026	0	n/a	424240	n/a	n/a
T027	50	TOSH #2	316589[(1)]	74	352
T028	50	TOSH #2	315435[(1)]		
T029	150	TOSH #2	306093[(1)]	69	1409
T030	150	TOSH #2	289153[(1)]		

[(1)] Fracture not at scribe

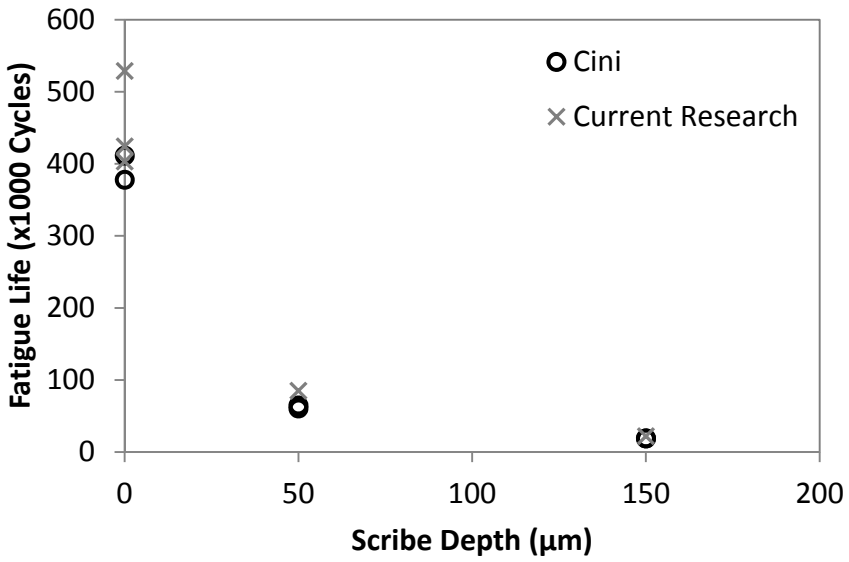

Figure 4.9: Comparison of baseline tension-tension results with Cini [42]

Table 4.4: Average fatigue lives of unpeened specimen

Scribe Depth (µm)	Average Fatigue Life (cycles)	% of Pristine Sample Life
0	429085	n/a
50	69867	16
150	19728	5

The effect of the laser peening treatments on the fatigue performance of samples scribed to 50 and 150 µm depths is illustrated in Figure 4.10 and Figure 4.11 respectively. Considering the MIC1 and MIC3 LSP treatments, tests were performed using 50 and 150 µm scribed samples with no edge rework. The fatigue life of samples scribed to 150 µm depth increased by 24% after MIC1 LSP treatment but actually reduced by 3% for samples scribed to 50 µm depth. MIC3 LSP treatment increased the life of samples with 50 µm and 150 µm deep scribes by 81% and 53% respectively. The longer fatigue lives of samples after MIC3 LSP treatment than after MIC1 LSP treatment could be due to the greater compressive residual stress field induced (see Figure 4.8).

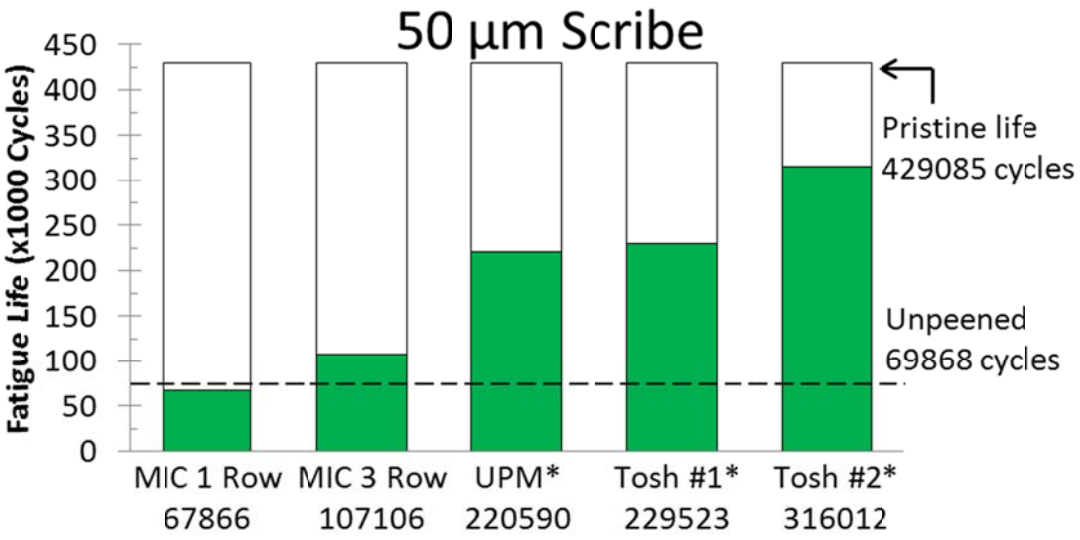

Figure 4.10: Comparison of fatigue lives tested in tension-tension after LSP treatments using 50 µm scribed samples

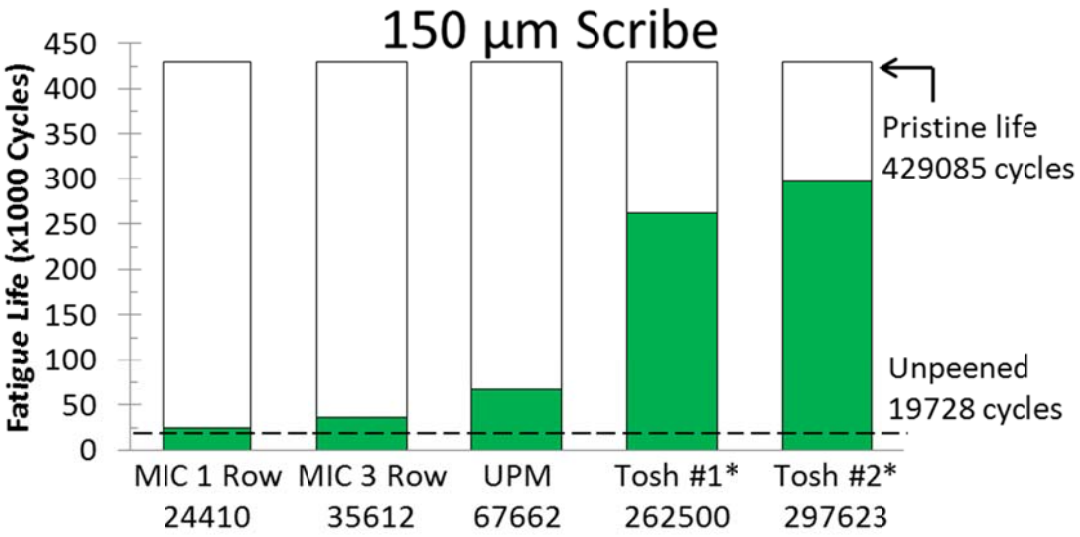

Figure 4.11: Comparison of fatigue lives tested in tension-tension after LSP treatments using 150 µm scribed samples

In total ten fatigue tests were perfomed using samples scribed and then peened with UPM LSP treatment as shown in Table 4.3. The first four tests were performed using samples scribed to 50 and 150 µm depths with no sample edge rework (test no. T012 to T015). The fatigue lives increased by 66% and 79% respectively compared to unpeened scribed samples. In all tests fatigue failure was due to crack initiation at the root of the scribes.

The next four tests used samples scribed to 50 and 150 µm depth with reworked sample edges (test no. T016 to T019). The rework extended 5 mm from the edge and was performed after LSP treatment. The fatigue life of peened samples with scribes

50 and 150 µm deep increased by 216% and 167% respectively compared to unpeened scribed samples. The sample scribed to 50 µm depth fractured due to crack initiation on the non-peened face directly opposite the peened region. However the samples scribed to 150 µm depth fractured due to crack initiation at the root of the scribe. Large thumbnails were evident on the fracture surface near the reworked region/scribe run out. It was considered that edge rework would have relieved the LSP induced compressive residual stress in the reworked region since it was performed after peening. Therefore two tests were performed using samples scribed to 150 µm depth with edge rework performed before LSP treatment (test no. T020 and T021). Indeed the fatigue was greater than when edge rework was performed post peening. The fatigue life increased by 243% compared to the unpeened scribe material. Both samples fractured due to crack initiation at the toot of the scribe.

A total of eight samples were tested using TOSH LSP treatments. As described in Section 2.4.6 two variants of TOSH treatment were used for the fatigue trials. The first variant referred two as TOSH #1 used a combination of the 20mj-0.4Ø-54/mm^2 and 20mj-0.4Ø-18/mm^2 peening treatments. The second variant referred to as TOSH #2 used solely the 20mj-0.4Ø-18/mm^2 peening treatment across the entire scribe length. All samples had edge rework extending 15 mm from the sample edges that was performed before LSP treatment.

Firstly consider the TOSH #1 peening treatment. The fatigue life of 50 and 150 µm deep scribed peened samples increased by 229% and 1231% respectively compared to unpeened scribe samples. In this case the fatigue crack that caused fracture did not initiate at the root of the scribes 50 and 150 µm deep but instead on the non-peened face. In contrast to the 50 µm deep scribed samples with UPM peening the fatigue crack that caused failure did not initiate on the surface directly opposed to the peened area but instead remote from the peened area completely.

The greatest improvement in fatigue life was after the TOSH #2 LSP treatment. Both 50 and 150 µm deep scribed samples resulted in similar fatigue lives with improvement of up to 1409% measured compared to unpeened scribe samples. As for the TOSH #1 case, the fatigue cracks that caused failure initiated on the non-peened face and remote from the opposing peened area. As reported in section 4.1 the TOSH #2 treatment induced less distortion than the TOSH #1 treatment. Therefore the improved fatigue performance is attributed primarily to the reduced stress range on the non-peened face.

The stress ranges measured on the peened face during fatigue testing was reported in section 4.1 after UPM and TOSH treatments. The fatigue lives are plotted against measured stress range in Figure 4.12 and Figure 4.13 for the 50 and 150 µm deep

scribed samples respectively. The reference fatigues lives at stress ranges of 180 MPa and 160 MPa were from fatigue tests whilst the reference data at stress ranges of 175 MPa and 178 MPa were interpolated from the other points.

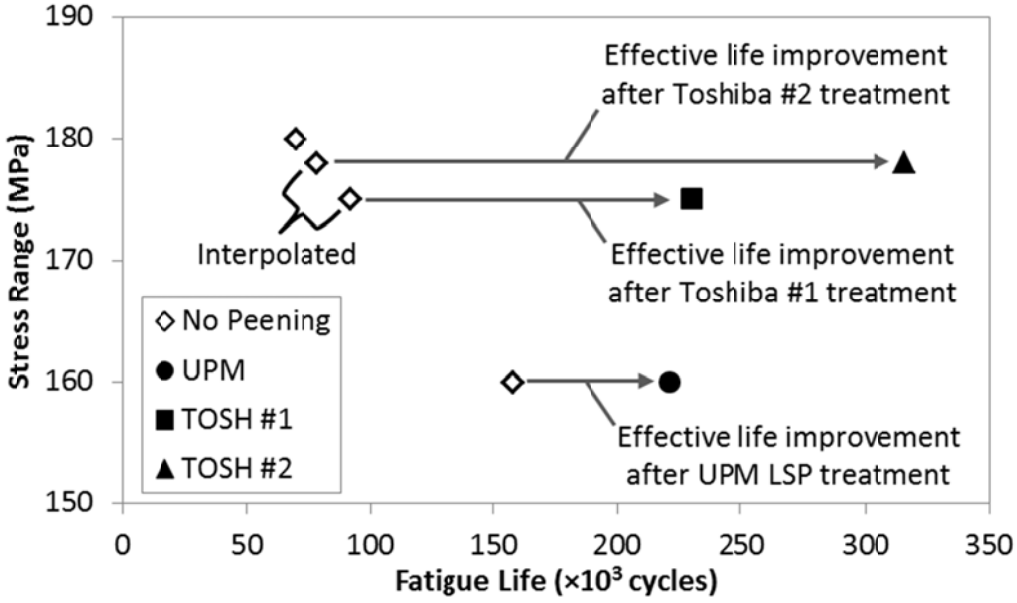

Figure 4.12: Effective life improvement considering effects of reduced stress range on the peened surface of 50 µm scribed samples

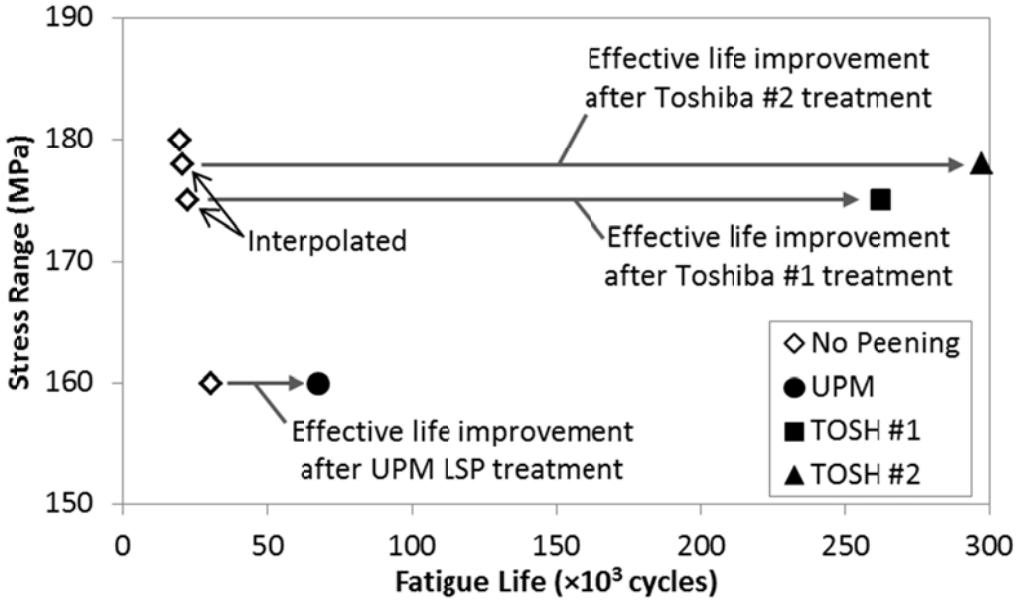

Figure 4.13: Effective life improvement considering effects of reduced stress range on the peened surface of 150 µm scribed samples

For the samples scribed to 50 µm depth (Figure 4.12) the reduced stress range resulted in a significant increase in fatigue life. Therefore the percentage fatigue life improvement as stated in Table 4.3 is corrected for in Table 4.5 considering effects of

distortion. The effect of the reduced stress range was not as significant in the case of the 150 µm scribed samples as shown in Figure 4.13 . A marginal increase in fatigue life was found at the 160 MPa stress range compared with the nominal stress range of 180 MPa. However the percentage fatigue life improvements are also updated in Table 4.5.

Table 4.5: Improvement in fatigue life based on stress range

LSP Treatment	Scribe Depth (µm)	Life improvement based on nominal stress range (%)	Life Improvement based on measured stress range (%)
UPM	50	+216	+40
	150	+243	+121
TOSH #1	50	+229	+150
	150	+1231	+1069
TOSH #2	50	+352	+302
	150	+1409	+1330

4.3.1 Tension-Tension Fatigue Tests at reduced Stress Range

A series of fatigue tests were performed at reduced stress ranges using unpeened clad material, see Section 3.7 for details of the test procedure. These tests were performed to determine the endurance limit of the baseline material and investigate the effect on the endurance limit of the scribes Samples were tested in three conditions namely unscribed, scribed to 50 µm depth and scribed to 150 µm depth. The stress range was reduced after each test until a sample run out was achieved (10^7 cycles). The samples tested are listed in Table 4.6 together with details of the stress range used and the number fatigue cycles applied at the end of the test. The majority of the samples were tested using a 100 kN test frame however some samples were tested using a 250 kN test frame as noted in Table 4.6.

The results are plotted in Figure 4.14. Included are fatigue test results at a stress range of 180 MPa from Table 4.3. Also included are tests at reduced stress ranges for samples containing 185 µm scribes from [42]. The results marked with an arrow note a test run out. The endurance limit of the pristine material was 145 MPa. This reduced to 125 MPa for material with a scribe 50 µm deep and 80 MPA for material with a scribe 150 µm deep. These results will be explored further in the discussion section.

Table 4.6: Details of tension-tension tests at reduced stress range and results

Test No.	Notch Depth (µm)	Stress Range (MPa)	Fatigue Life (Cycles)
SN01	0	170	500851
SN02	0	160	731779[(2)]
SN03	0	150	3152313[(2)]
SN04	0	145	3272839[(2)(3)]
SN05	0	145	952059[(4)]
SN06	0	145	12916043[(1)]
SN07	50	160	164830
SN08	50	160	150555
SN09	50	140	563703
SN10	50	130	2777037
SN11	50	125	10088036[(1)]
SN12	150	160	30517
SN13	150	160	30770
SN14	150	140	47525
SN15	150	120	82694
SN16	150	100	335206
SN17	150	90	483433
SN18	150	80	11483388[(1)]

[(1)] Run out, [(2)] Test on 250 kN machine, [(3)] Failure at grip, [(4)] Bonded tabs

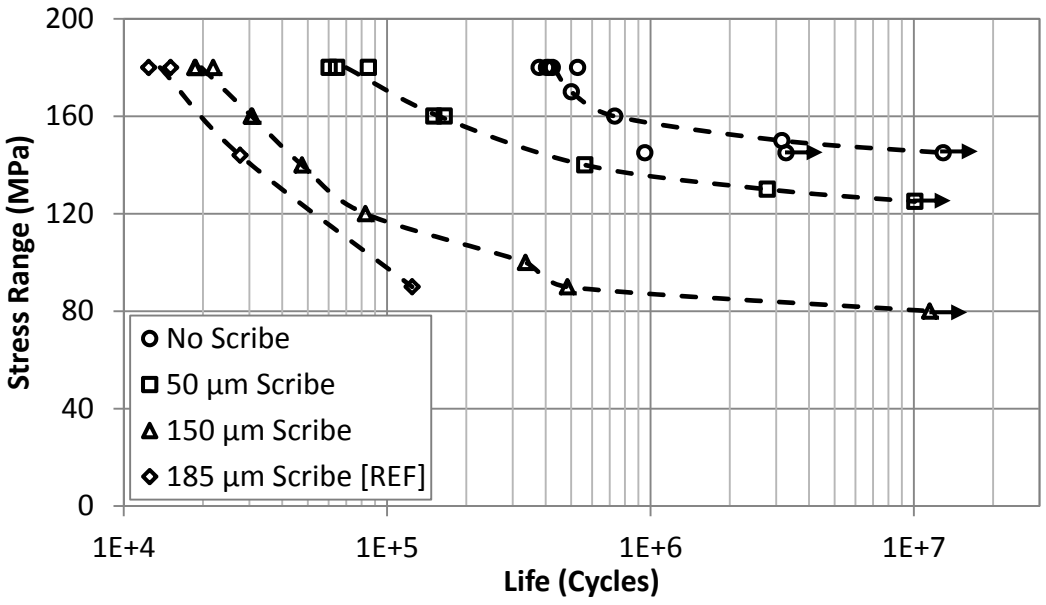

Figure 4.14: S-N curve for pristine and scribed samples at R = 0.1

4.4 Four Point Bend Fatigue Tests

Four point bend tests were performed to avoid the distortion related effects encountered during tension-tension testing. A description of the four point bend test procedures was given in section 3.8. In total 12 tests were performed and are outlined in Table 4.7. Samples were tested in the pristine condition and with scribe defects of depth 50 and 150 µm with and without LSP. Laser peening treatment was applied after scribing. As described in section 3.8 four point bend tests were initially performed in displacement control due to limitations with the available load cell however later during the project tests were performed in load control with the availability of a lower capacity load cell.

Table 4.7: Four point bend fatigue tests

Test No.	Scribe Depth (µm)	Test Control	Treatment
B001	50	Displacement	Unpeened
B002	150	Displacement	Unpeened
B003	150	Displacement	Unpeened
B004	50	Displacement	UPM no edge rework
B005	50	Displacement	UPM no edge rework
B006	150	Displacement	UPM no edge rework
B007	150	Displacement	UPM no edge rework
B008	50	Displacement	TOSH w/ edge rework
B009	50	Load	TOSH w/ edge rework
B010	150	Load	TOSH w/ edge rework
B011	150	Load	TOSH w/ edge rework
B012	0	Load	Unpeened

The fatigue test results are provided in Table 4.8. The fatigue life of the pristine sample tested in bending was 1.28× greater than the pristine life observed in tension-tension. Failure of the sample in bending occurred due to fretting between the sample / contact roller interface. The fatigue life of samples scribed to depths of 50 and 150 µm was 1.01× and 1.22× greater than samples tested in tension-tension respectively. These samples fractured due to crack initiation at the root of the scribes.

Four scribed samples with UPM peening were tested. The samples did not have reworked edges. The fatigue life of samples scribed to 50 µm depth with UPM LSP was 39% greater than the unpeened fatigue lives. The fatigue life of samples scribed to 150 µm depth with UPM LSP was 65% greater than the unpeened fatigue lives. Again these samples fractured due to crack initiation at the root of the scribes.

Table 4.8: Four point bend clad material fatigue test results

	Test No.	Scribe Depth (µm)	Peening Treatment	Fatigue Life (Cycles)	% Improvement in Fatigue life
Displacement Control	B001	50	n/a	70012	n/a
	B002	150	n/a	23452	n/a
	B003	150	n/a	24897	
	B004	50	UPM	91717	39
	B005	50	UPM	102512	
	B006	150	UPM	43936	65
	B007	150	UPM	35678	
Load Ctrl	B008	50	TOSH #2	587904(2)	666
	B009	50	TOSH #2	484560(2)	
	B010	150	TOSH #2	579494(2)	1997
	B011	150	TOSH #2	434224(2)	
	B012	0	n/a	550144(2)	n/a

(1) Run out, (2) Failed at roller

Scribed samples were tested that has TOSH #2 LSP treatment and 15 mm of edge rework (note: the same as used in the tension-tension tests). These samples were manufactured from a different material batch than the other tests. The fatigue life of the 50 and 150 µm deep scribed samples was 666% and 1997% greater than the unpeened fatigue lives respectively. For these samples fracture occurred due to fretting between the sample / contact roller interface. A pristine sample (i.e. no scribe and unpeened) from the same material batch was also tested. Fracture again occurred at the point of roller contact. The fatigue life was comparable to that measured for the scribed samples with TOSH LSP treatment.

4.5 Fractography and Fatigue Crack Growth Rate

The fracture surfaces of the fatigue samples were examined optically. The MIC1 and MIC3 LSP treated samples fractured at the scribe and exhibited similar failure characteristics. The fracture surface of a sample scribed to 50 µm depth and with MIC peening is illustrated in Figure 4.15. It had a single large thumbnail at one end and small thumbnails along the root of the scribe that were not fully coalesced. The fracture surface of a 150 µm deep scribed sample with MIC peening is illustrated in Figure 4.16. The fracture surface was similar to the 50 µm scribed sample however the fatigue crack propagating from the root of the scribe had coalesced before sample fracture.

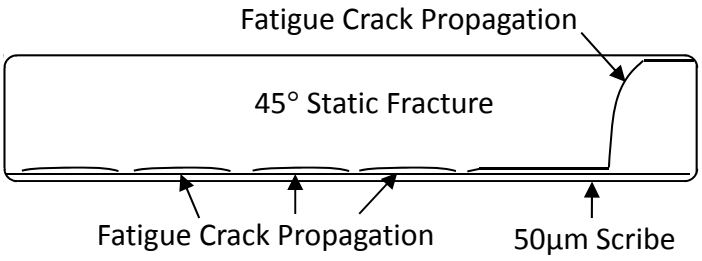

Figure 4.15: Illustration of fatigue crack development on fracture surface of 50 µm deep scribed sample with MIC peening treatment

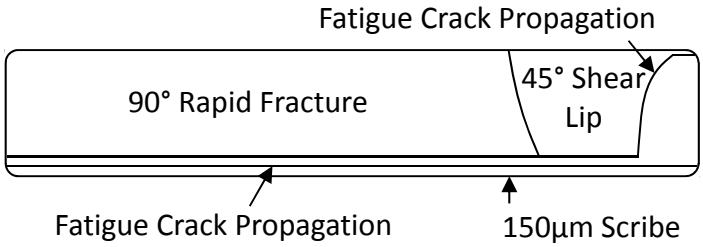

Figure 4.16: Illustration of fatigue crack development on fracture surface of 150 µm deep scribed sample with MIC peening treatment

Samples scribed to 50 µm depth and with UPM LSP treatment displayed similar failure characteristics to the MIC peened samples. As shown in Figure 4.17 it had a single large thumbnail at one end and smaller thumbnails along the root of the scribe that had not fully coalesced.

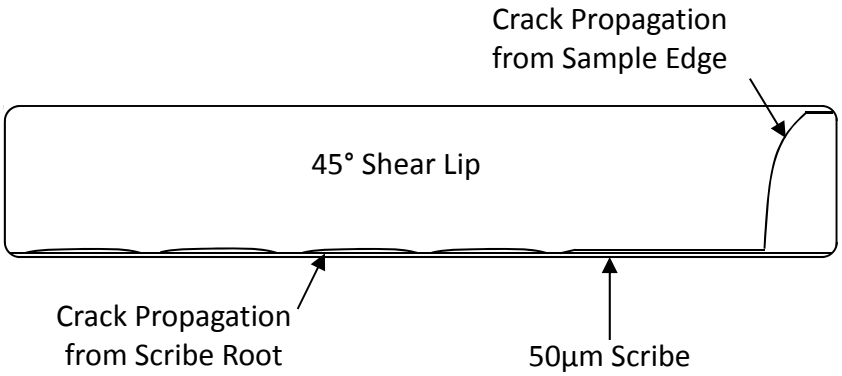

Figure 4.17: Illustration of fatigue crack development on fracture surface of 50 µm deep scribed sample with UPM peening treatment and without edge rework

However UPM peened samples scribed to 50 µm depth with edge rework did not fracture at the scribe but instead due to fatigue crack initiation on the non-peened face. The initiation location was directly opposite the peened area and the samples fracture within the peened region as shown in Figure 4.18. Fatigue crack initiation on the back face was attributed to the distortion induced through peening and the associated increase in applied surface stress on the non-peened face. It is also

possible that tensile balancing residual stress existed on the non-peened face that would encourage early crack initiation compared to non-peened samples however stress on the back face was never measured. A fatigue crack had initiated at the root of the scribe as observed using SEM and shown in Figure 4.19.

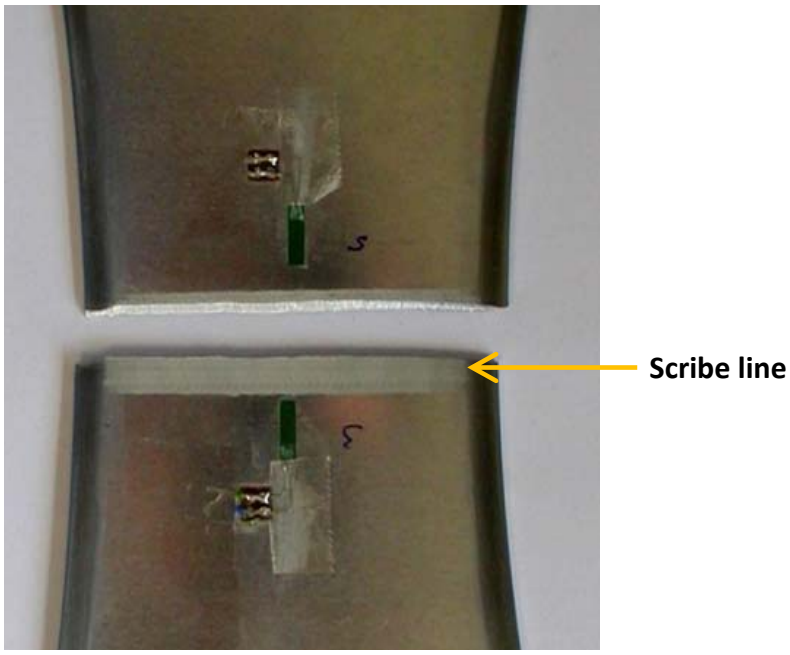

Figure 4.18: Fracture location on 50 µm deep scribed sample with UPM peening and edge rework

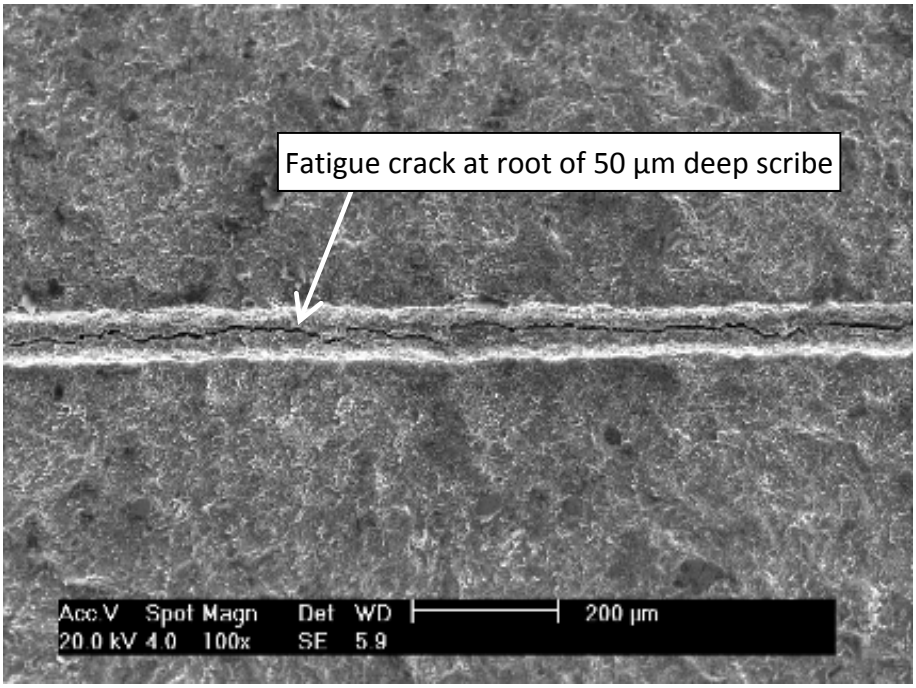

Figure 4.19: Fatigue crack initiation at root of 50 µm deep scribed sample with UPM LSP treatment after fatigue fracture remote from scribe

The UPM peened samples scribed to 150 µm depth with and without edge rework all fractured at the scribe and displayed similar failure characteristics on the fracture surfaces which are illustrated in Figure 4.20 below. A large thumbnail was observed at the one sample edge and a fully coalesced fatigue crack had propagated from the root of the scribe as shown in Figure 4.21.

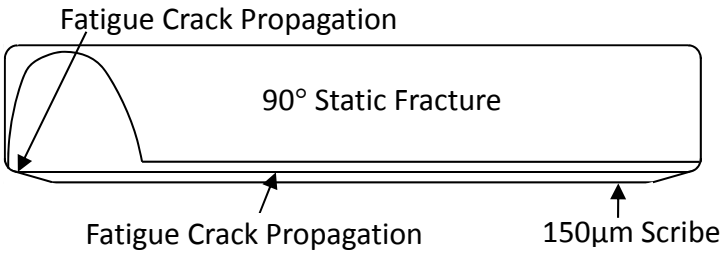

Figure 4.20: Illustration of fatigue crack development on fracture surface of 150 µm deep scribed sample with UPM peening treatment

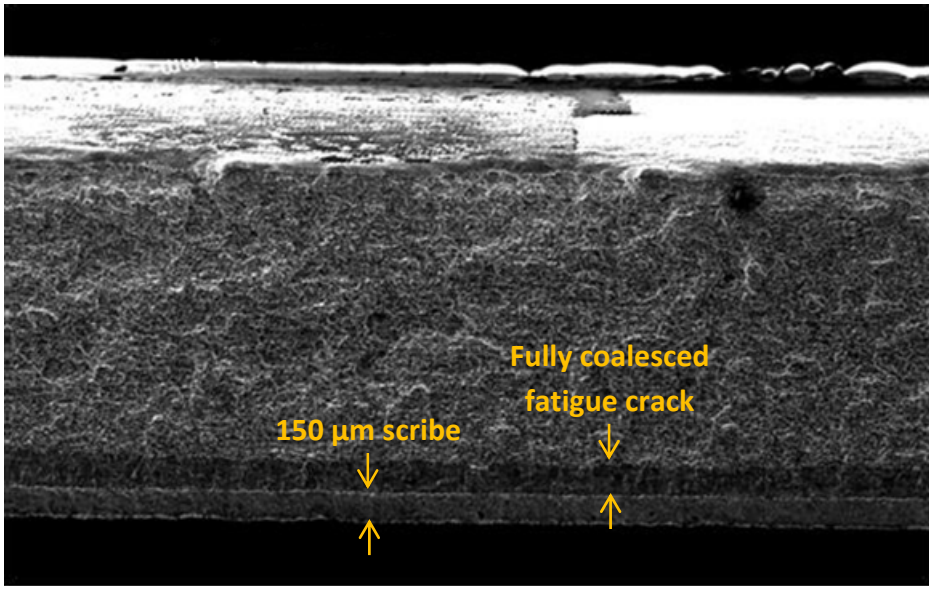

Figure 4.21: Fully coalesced fatigue crack advancing from root of 150 µm deep scribe in sample peend using UPM treatment

All of the TOSH peened samples fractured due to fatigue crack initiation on the non-peened face which was again attributed to the LSP induced distortion and resultant increased applied stress range on the back face. However unlike the UPM peened samples for the TOSH peened fatigue crack initiation on the back face occurred remote from the peened area. Fatigue cracks were observed to have initiated at the root of the scribes 50 µm and 150 µm deep as shown in Figure 4.22 and Figure 4.23. The fatigue crack at the root of the 150 µm deep scribe was clearly visible along the entire length of the scribe which indicated full crack coalescence before fracture.

Distinct but separate fatigue cracks were visible along the length of the 50 µm which indicated that crack coalescence had not happened before fracture.

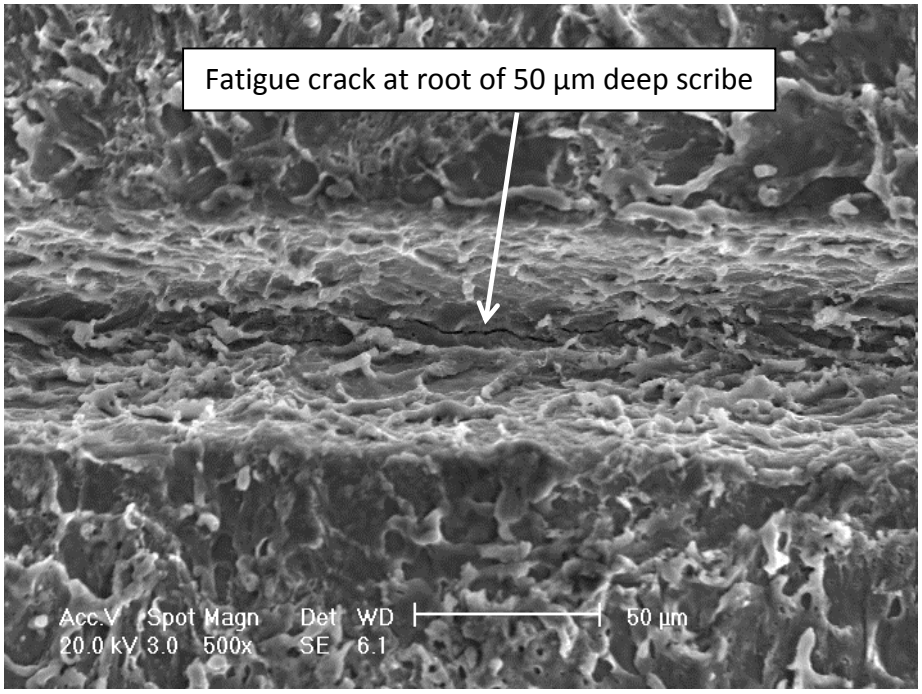

Figure 4.22: Fatigue crack visible at root of 50 µm deep scribe in sample peened using TOSH LSP treatment after fracture remote from scribe

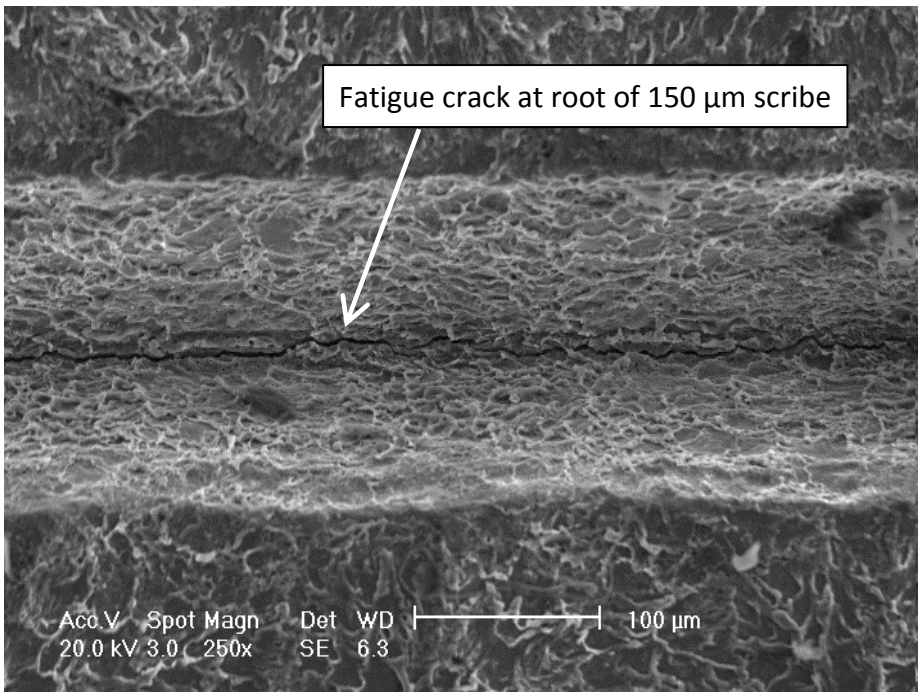

Figure 4.23: Fatigue crack visible at root of 150 µm deep scribe in sample peened using TOSH LSP treatment after fracture remote from scribe

Striation spacings on the fracture surfaces of unpeened and UPM peened samples were measured for samples tested in tension-tension and four point bend. The procedures followed were described in section 3.9. The measured striation spacings were converted to an estimate of da/dN as described in section 3.9. Crack length was calculated into effective stress intensity factor range using FE models as will be described over subsequent chapters. Shown in Figure 4.24 is ΔK_{eff} plotted against da/dN calculated from measurements taken on 50 µm deep scribed samples tested in tension-tension. The measurements implied that the peening treatment had little to no effect on the FCGR compared to unpeened samples at least over the crack length range measured. Shown in Figure 4.25 is ΔK_{eff} plotted against da/dN calculated from measurements taken on 150 µm deep scribed samples tested in tension-tension. In this case there does appear to be reduction in the FCGR in peened samples compared to unpeened samples.

Shown in Figure 4.26 is ΔK_{eff} plotted against da/dN calculated from measurements taken on 50 µm deep scribed samples tested in four point bend and for 150 µm scribed samples in Figure 4.27. Again the measurements imply that peening had little to no effect on the FCGR compared to unpeened samples. However it should be noted that striations were not visible on the fracture surface close to the root of the scribe. It is likely that the residual stress field had greatest effect on FCGR in this region when the crack length is short and the applied stress intensity range was low.

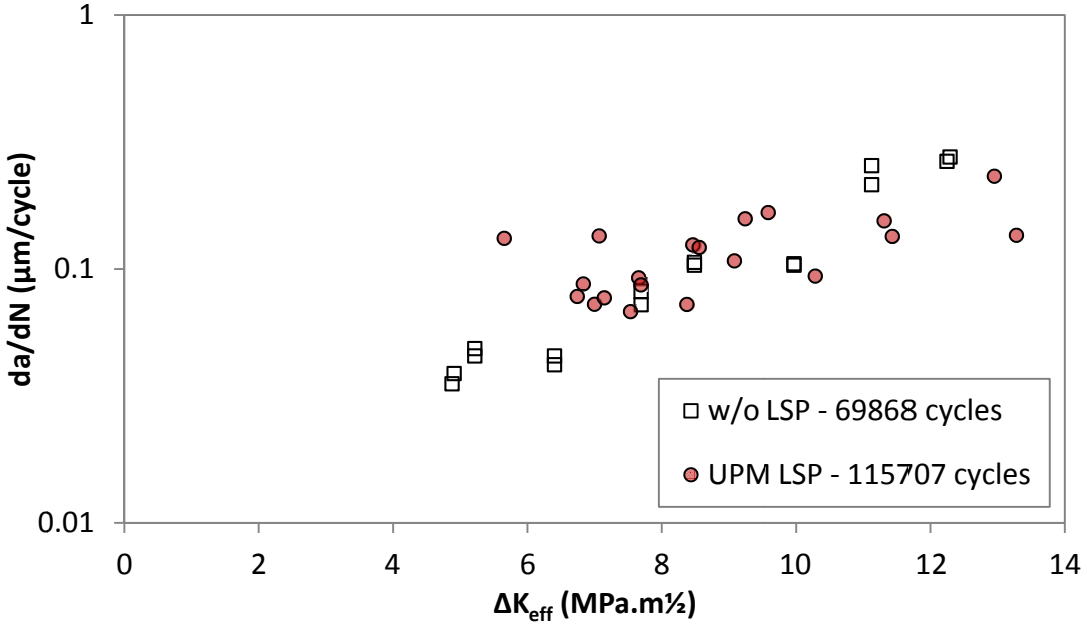

Figure 4.24: FCGR data calculated from measurements of striation spacings on the fracture surface of 50 µm deep scribed samples tested in tension-tension

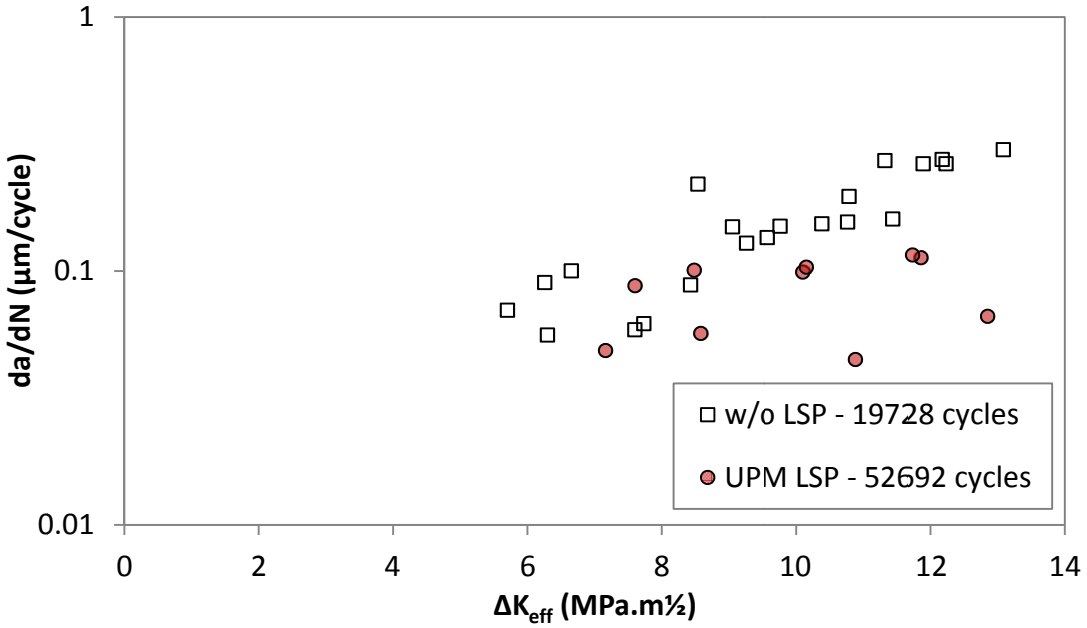

Figure 4.25: FCGR data calculated from measurements of striation spacings on the fracture surfaces of 150 µm deep scribed samples tested in tension-tension

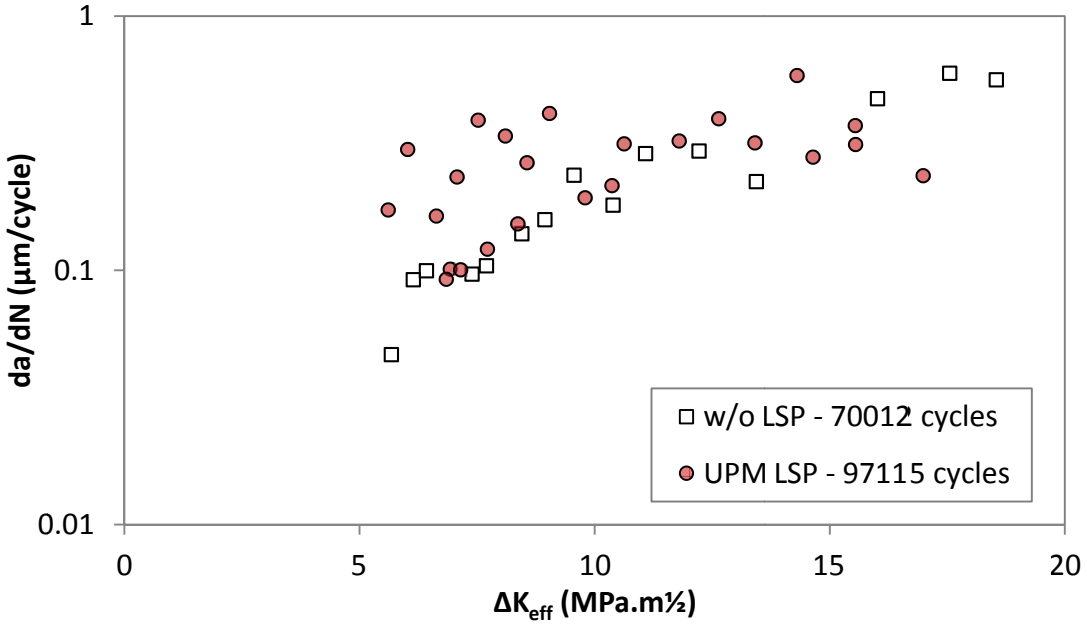

Figure 4.26: FCGR data calculated from measurements of striation spacings on the fracture surfaces of 50 µm deep scribed samples tested in four point bend

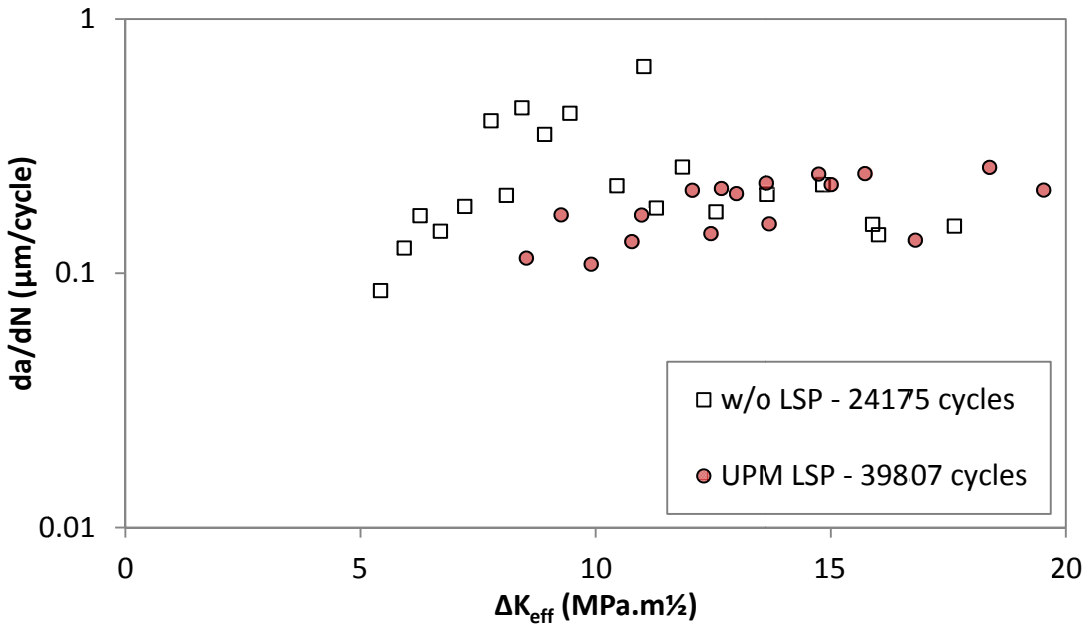

Figure 4.27: FCGR data calculated from measurements of striation spacings on the fracture surfaces of 150 µm deep scribed samples tested in four point bend

4.6 Fatigue Crack Growth Measurements

The FCGR data gathered from measurement of striation spacings on fracture surfaces could only account for approximately 10% of total fatigue life (estimated from back calculation using the acquired da/dN vs 'a' data) . To study the effect on crack initiation and early fatigue crack growth of laser peening a series of interrupted fatigue tests was performed. A description of the test procedures was given in section 3.10. The tests performed are listed in Table 4.9. Only TOSH LSP treatment was used to peen the samples and the samples edges were reworked to 15 mm.

Four unpeened samples scribed to 150 µm depth were fatigued to 15006, 10029, 2508, and 501 cycles noting that the expected fatigue life was 19728 cycles (Figure 4.11). Therefore this represents approximately 76%, 51%, 12.5%, and 2.5% of the expected fatigue life respectively. After reaching the required number of cycles the applied load was ramped until sample fracture. The fracture faces were then studied using an SEM and fatigue cracks were observed to have initiated and propagated from the root of the scribes in all cases. The crack length was then measured on the SEM at locations along the scribe length. Figure 4.28 shows fatigue cracks that had initiated and propagated from the the root of the scribes in the four test cases studied. The tests showed that after 501 cycles the fatigue crack length averaged 9 µm although full crack coalescence was not achieved. In the other three cases the fatigue cracks had fully coalesced.

Table 4.9: Interrupted fatigue crack growth tests

Test No.	Notch Depth (µm)	Test Description	Fatigue Cycles	Av. a (µm)
CI01	150	Clad, unpeened	15006	97
CI02	150	Clad, unpeeded	10029	60
CI03	150	Clad, unpeened	2508	19
CI04	150	Clad, unpeened	501	9
CI05	150	Clad, TOSH #2	200005	24
CI06	150	Clad, TOSH #2	100005	20
CI07	150	Clad, TOSH #2	10009	19
CI08	50	Clad, unpeened	10003	9
CI09	50	Clad, unpeened	5006[(1)]	n/a

(1) Fracture not at scribe

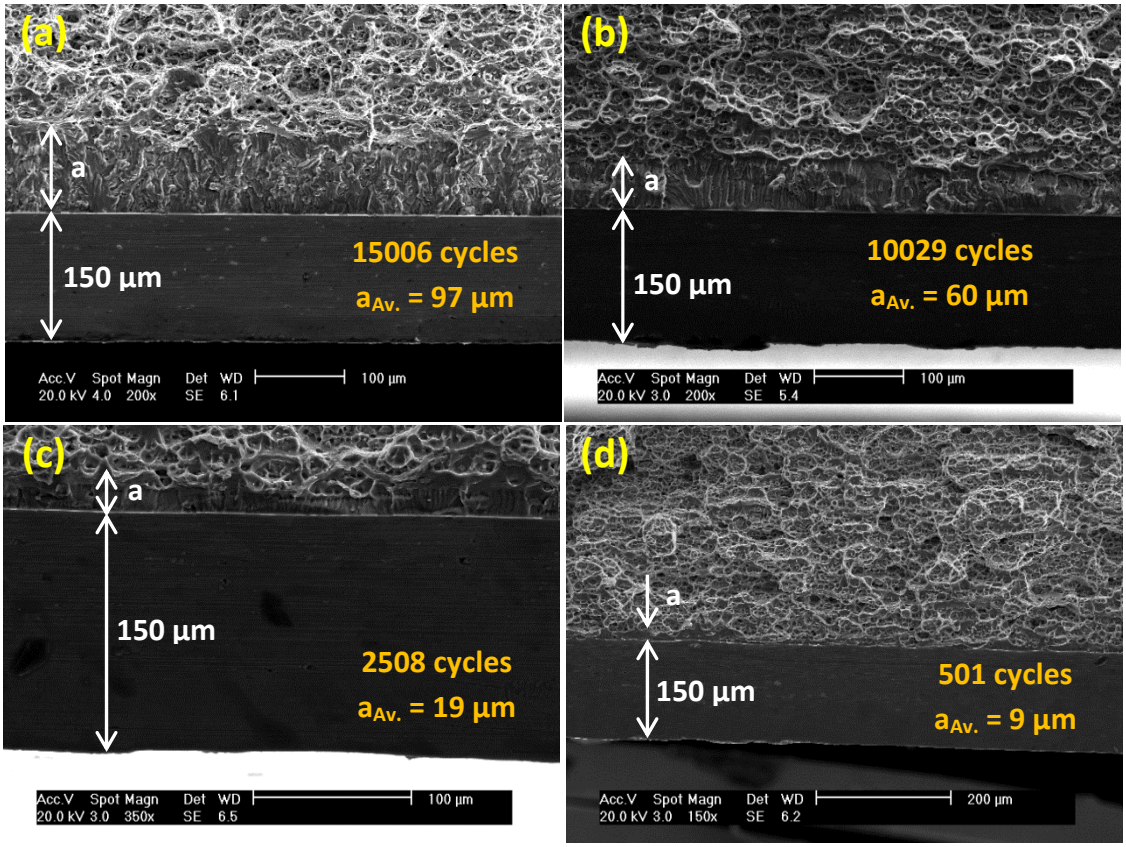

Figure 4.28: Fatigue cracks at root of 150 µm scribes after (a) 15006 cycles, (b) 10029 cycles, (c) 2508 cycles, and (d) 501 cycles

The average crack length measured is plotted against the number of load cycles applied before fracture in Figure 4.29. Also plotted is FCGR date calculated for the striation spacing measurements of section 4.5. The results indicated that fatigue crack

initiation occurred very soon after the first applied load and maybe even on the first applied load. The four interrupted test measurements indicated that crack length then increased linearly with the number of applied load cycles. The striation spacing measurements indicated that crack growth rate increased rapidly during the final 10% of the fatigue life before final fracture.

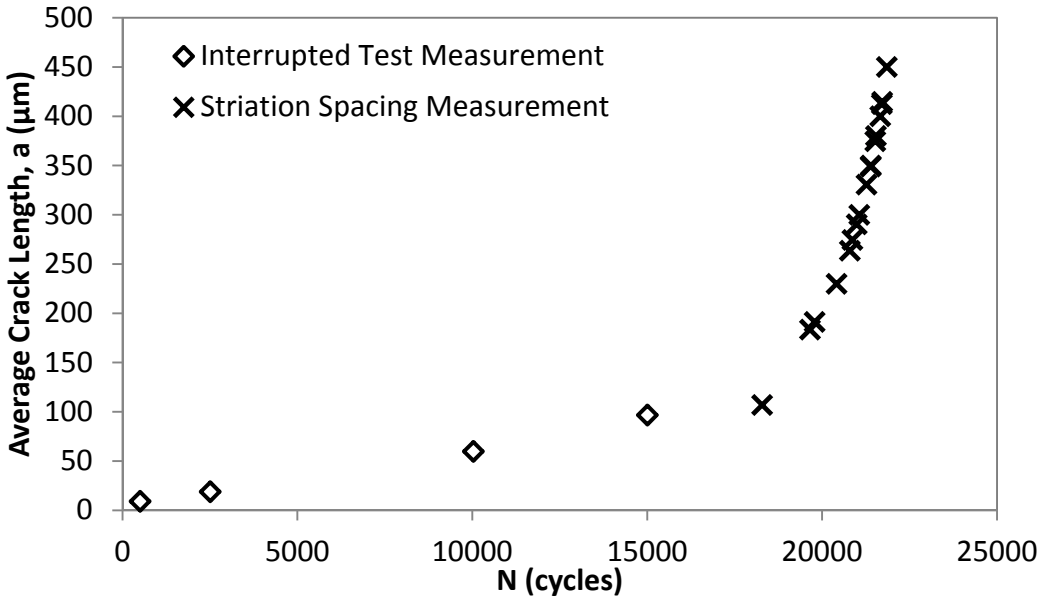

Figure 4.29: Comparison of measured crack length in 150 µm deep scribed samples from interrupted tests and measured striation spacings

Three 150 µm deep scribed samples were peened with TOSH LSP treatment and used for interrupted test. These were fatigued to 200005, 100005, and 10009 load cycles before static fracture. This represented 67%, 34%, and 3% of the expected fatigue life of 297623 cycles (Figure 4.11). The fracture faces were studied using an SEM. The length of the fatigue cracks was measured and is plotted in Figure 4.30. Also a fatigue specimen scribed to 150 µm depth with TOSH LSP treatment was studied (test no. T030). As described in section 4.5 although this specimen failed due to crack initiation on the unpeened face, the fracture revealed a partial section along the scribe line that allowed for direct measurement of crack length at failure, as shown in Figure 4.30 (A). The measured fatigue crack length for the four samples is plotted in Figure 4.31 along with the measurement data gathered from the unpeened specimens. The plot implied that after an initial period of crack growth the compressive residual stress induced via peening was sufficient to arrest fatigue crack propagation from the root of the scribe.

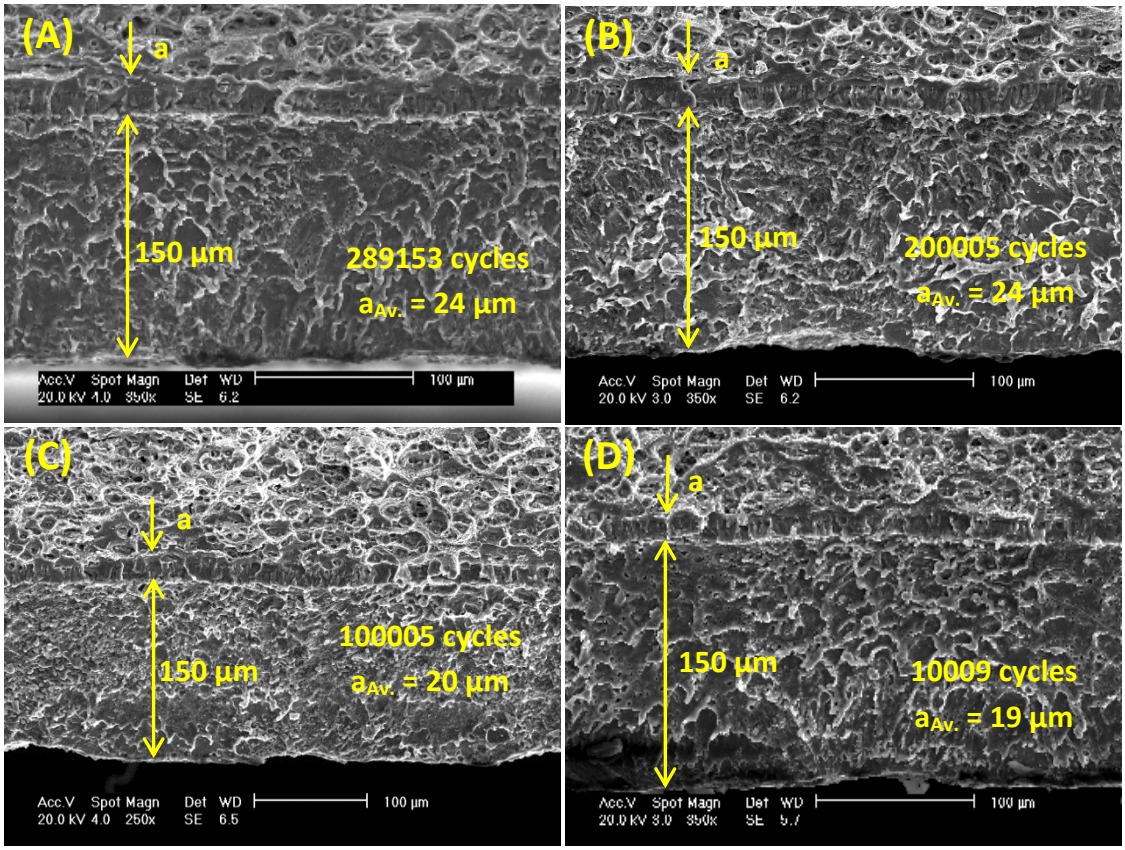

Figure 4.30: Fatigue cracks at root of 150 µm deep scribes in peened clad material after (a) 289153 cycles, (b) 200005 cycles, (c) 100005 cycles, and (d) 10009 cycles

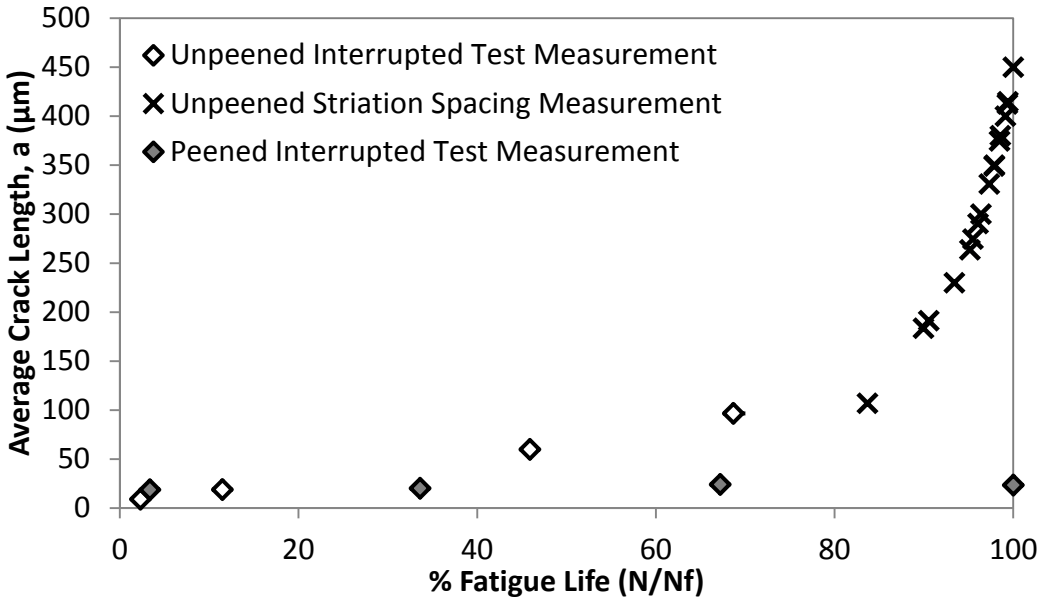

Figure 4.31: Comparison of measured crack lengths for peened and unpeened clad material containing 150 µm deep scribes

Two tests were conducted on unpeened clad material with 50 µm scribes. These were cycled to 10003 and 5006 cycles. The first sample (10003 cycles) statically fractured at the scribe however a large amount if plastic necking was observed. The fracture face is pictured in Figure 4.32. The fatigue crack at the root was not fully coalesced and averaged 9 µm in length. The sample cycled to 5006 cycles did not fail at the scribe line. The clad layer is approximately 70 µm thick and therefore the scribe / initiated crack do not penetrate into the substrate. As the clad layer has low yield strength (approximately 120 MPa) the stress concentration is low and the effect on tensile strength is minimal. However the scribe was studied using a SEM and cracks were observed to have initiated at the root but no measurement of length was possible.

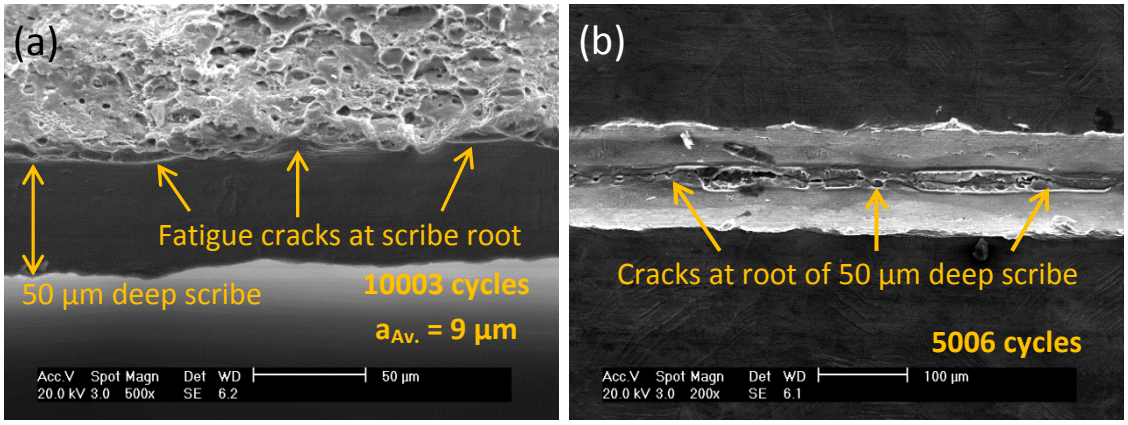

Figure 4.32: Fatigue cracks at root of 50 µm scribed clad material after (a) 10003 cycles and (b) 5006 cycles

4.7 Summary of Results

It was found that residual stress induced via LSP can affect the fatigue life of scribed samples tested in tension-tension. This ranged from a further 3% decrease up to a 15 times increase of the fatigue life compared to unpeened scribed material. Care should be taken when peening on one sample side only as the unbalanced stress field induced can cause significant sample distortion particularly in thin sections. The distortion caused out of plane bending in tension-tension fatigue tests that altered the applied surface stress experienced by the sample. This caused premature crack initiation on the unpeened surface compared to unpeened samples. Therefore fatigue tests were performed under four point bend and the fatigue life was measured equivalent to that of the pristine material. However in this case failure was due to crack initiation caused by fretting between the sample and the loading rollers. Through a series of interrupted tension-tension fatigue tests it was found that LSP did not stop crack initiation at the root of the scribes but that the residual stress field arrested crack propagation after an initial period of crack growth. This implied that the fatigue life of the scribed material could be restored to that of pristine material even in tension-tension but only if distortion was minimised.

5 Effect of Residual Stress on Stress Intensity Factor

In this chapter the effect on stress intensity factor of residual stress fields induced by LSP is considered. A FE model representative of the fatigue specimens was developed and is described in section 5.1. FE modelling was an efficient method to systematically study the effect on SIF of the measured residual stress fields combined with the external applied loading. The method to calculate SIFs using the FE approach is described in section 5.2. In section 5.3 SIFs are calculated for the case of external applied loading only. Fatigue crack propagation was not modelled explicitly however a crack was advanced from the root of the scribe and the SIF at different length cracks is reported. Note that in this section the length of fatigue cracks is defined as the distance from the crack tip to the peened surface i.e. in reference to a crack of length 500 µm the crack tip would be 500 µm from the peened surface.

The measured residual stress fields were not completely through thickness and this caused problems of global stress balancing in the FE model. A method was developed to balance the measured residual stress fields prior to inclusion in the FE model and the steps involved are described in section 5.4. As described in section 2.4.7 the residual stress fields were measured in samples that did not contain scribes. The residual stress field input to the FE model was redistributed around the scribe in the first step of the FE analysis. The redistribution of the measured residual stress fields in the presence of the scribe is reported in section 5.5. The redistribution of the residual stress field due to crack advance from the root of the scribe is reported in section 5.6. The effect on the SIF, the SIF range and the stress ratio of the different residual stress fields is reported in section 5.8.

The abbreviations used to refer to the four measured residual stress fields induced by LSP are as used in previous sections i.e. MIC1, MIC3, UPM and TOSH.

5.1 Description of Elastic FE Model used for Calculation of SIFs

The Abaqus software version 6.11 [243] was used for FE analysis including both pre and post processing and equation solving. As described in Section 3.2 a radius of 340 mm was used to reduce the width of the dogbone fatigue specimens from 160 mm to 80 mm at the gauge section. The reduction of area induced a stress concentration (K_t) and hence a stress variation across the sample width under external applied loading. However the K_t was predicted using FEM to be minimal (1.01 [242]) and the stress variation will be minimal also. Therefore the fatigue test specimens were modelled as a two-dimensional cross section.

A schematic of the two-dimensional geometry modelled in the FE analysis is shown in Figure 5.1. In this orientation the sample width is 2 mm and the thickness is 80 mm

(at the scribe line). Since the thickness was 80 mm and the width was 2 mm plane strain conditions were assumed. The fatigue test specimens are symmetrical about the scribe root and therefore symmetrical boundary conditions were used with only half the geometry modelled. The external applied loading was across the top surface of the model as depicted in Figure 5.1 and it was possible to implement either tensile or pure bending external applied load. The external loading in tension was 32 kN and equated to a nominal stress of 200 MPa at the gauge section, excluding the scribe area. For pure bending the stress on the notched face was 200 MPa in tension and reduced linearly to 200 MPa in compression on the back face. It was deemed unnecessary to model the full sample length (200 mm assuming symmetry about the scribe root) since the only stress concentration is at the scribe. An elastic stress decay distance of 10 times the defect size is generally accepted [244]. The largest scribe depth modelled was 150 µm and therefore the elastic decay distance was 1.5 mm however the geometry as modelled had a height of 3 mm as shown in Figure 5.1. The scribe was modelled as a rounded tip V notch with a root radius of 5 µm and a wall angle of 60 degrees. Two notch depths were modelled, 50 µm and 150 µm.

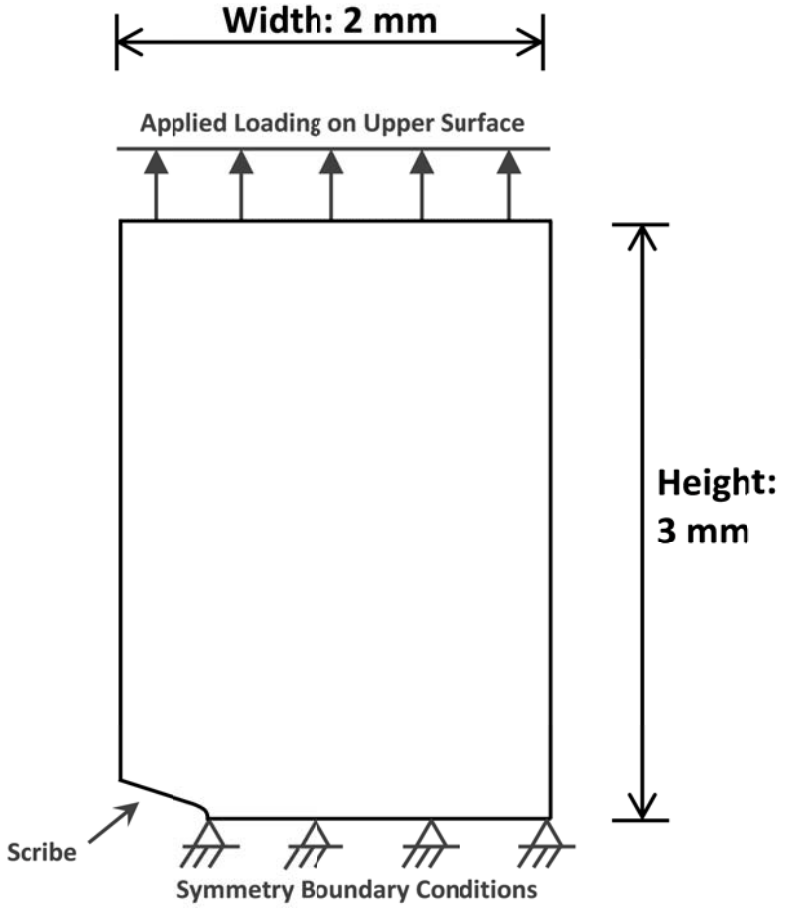

Figure 5.1: Schematic of FE model geometry showing dimensions, boundary conditions and applied loading

Elements of type CPE4R were used to mesh the geometry. These are four noded plane strain quadrilateral elements with reduced integration. A mesh sensitivity analysis to determine the appropriate element size at the scribe root was performed. The σ_{22} stress at the scribe root was chosen as the control parameter for mesh refinement. The FE mesh was refined until further accuracy increment of the calculated σ_{22} stress at the scribe root was less than 0.1%. A meshed geometry that contained a scribe 50 µm deep is shown in Figure 5.2 for reference. Element size along the crack path was progressively increased from 0.1 µm at the scribe root to a maximum element size of 37.9 µm. The FE model that contained the scribe 150 µm deep used the same maximum and minimum element sizing to maintain consistency.

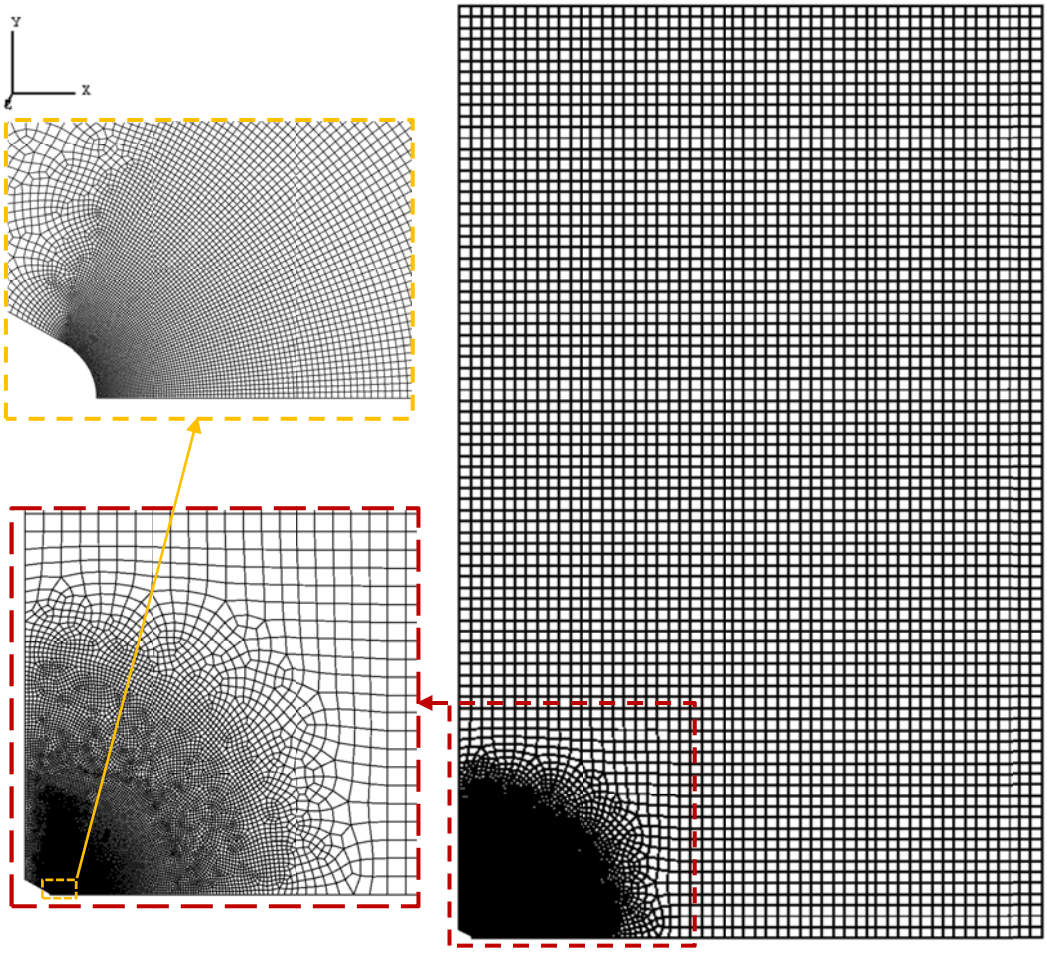

Figure 5.2: Finite element mesh used to model sample scribed to 50 µm

Linear elastic material properties were used in the FE model. These were Young's modulus of 72 GPa and Poisson's ratio of 0.33 (reference section 3.1). In linear elastic conditions there is no distinction between the cladding and substrate material. Crack advance was modelled using a node release scheme. To advance the crack the symmetry boundary conditions applied to individual nodes ahead of the crack tip

were removed. The minimum increment of crack advance is therefore determined by the element size ahead of the crack tip. However to reduce computational effort, nodes were released in groups to increase the increment of crack advance.

5.2 Method of Calculation of Stress Intensity Factor

The stress intensity factor (K) can be calculated for plane stress and plane strain conditions using equations 5.1 and 5.2 respectively,

$$K = \sqrt{GE} \quad \text{(Plane Stress)} \quad (5.1)$$

$$K = \sqrt{\frac{GE}{1-\nu^2}} \quad \text{(Plane Strain)} \quad (5.2)$$

where E is Young's modulus, ν is Poisson's ratio and G is the Strain Energy Release Rate (SERR). The SERR was evaluated using the modified Virtual Crack Closure Technique (VCCT) [245]. For VCCT the mode I component of SERR is calculated for four node finite elements using equation 5.3 below and illustrated in Figure 5.3,

$$G = \frac{1}{2\Delta a} Z_i \left(W_j - W_{j*}\right) \quad (5.3)$$

where Δa is the length of the element behind the crack tip and Z_i is the force at the crack tip (nodal point i in Figure 5.3). The relative displacements behind the crack tip were calculated from the nodal displacement at the upper crack face W_j (nodal point j) and the nodal displacement W_{j*} at the lower crack face (nodal point $j*$).

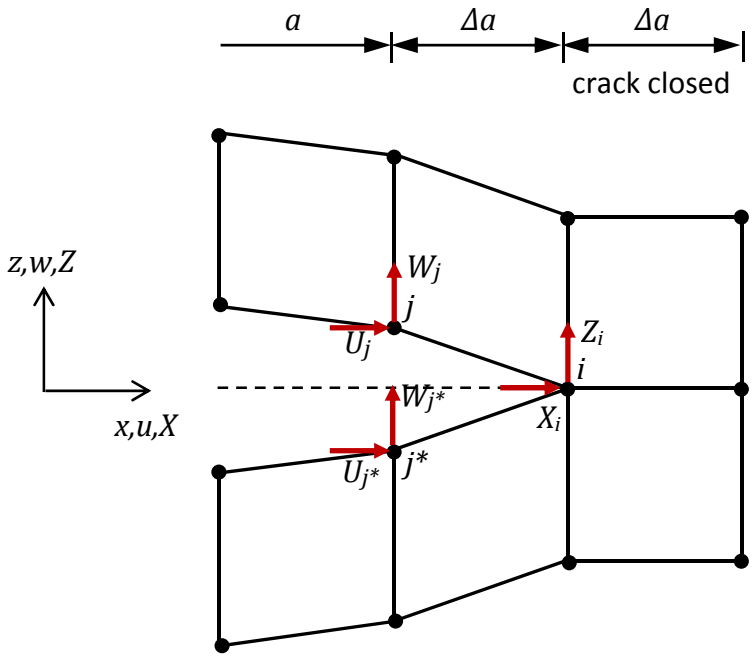

Figure 5.3: Virtual crack closure technique for four-node elements

To check the accuracy of the FE modelling methodology and VCCT, SIFs were calculated for a geometry that contained an initial crack 50 µm deep (no scribe). The results are shown in Figure 5.4. Two load conditions were considered, tension-tension and pure bending. SIFs were also calculated using equations 5.4 and 5.5 from Anderson [6] for tension-tension and pure bend applied load respectively. The SIFs predicted using the FE method compared well with those predicted using equations 5.4 and 5.5.

$$f\left(\frac{a}{W}\right) = \frac{K_I B\sqrt{W}}{P} = \frac{\sqrt{2tan\frac{\pi a}{2W}}}{cos\frac{\pi a}{2W}}\left[0.752 + 2.02\left(\frac{a}{W}\right) + 0.37\left(1 - sin\frac{\pi a}{2W}\right)^3\right] \quad (5.4)$$

$$f\left(\frac{a}{W}\right) = \frac{K_I B W^{3/2}}{M} = (\frac{6\sqrt{2tan\frac{\pi a}{2W}}}{cos\frac{\pi a}{2W}}\left[0.923 + 0.199\left(1 - sin\frac{\pi a}{2W}\right)^4\right] \quad (5.5)$$

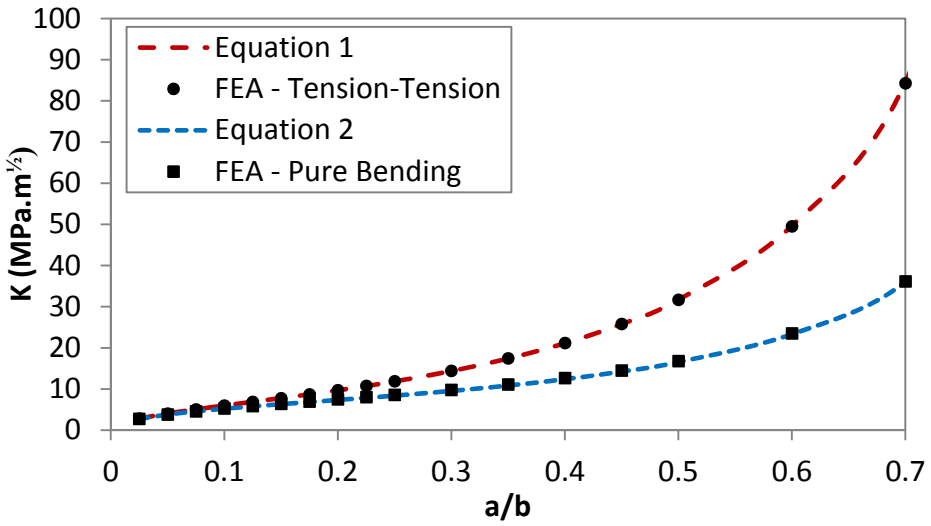

Figure 5.4: SIF calculated using the FE method and analytical method for tension-tension and pure bend applied load

5.3 SIFs Calculated for External Applied Loading Only

The SIFs at the minimum ($K_{app,max}$) and maximum ($K_{app,min}$) nominal applied stresses (20 and 200 MPa) were calculated using the methods described in the previous section and the results are shown in Figure 5.5. A crack was advanced from the root of scribes 50 µm and 150 µm deep. Crack advance from the scribe root was simulated using a node release scheme and SIFs were calculated at increments of crack advance. SIFs calculated using a FE model of an unscribed sample are also shown in Figure 5.5, in this study the crack was advanced from the sample surface and SIFs

were again calculated at increments of crack advance noting that the element size used in this model was equivalent to the element size used at the notch tip.

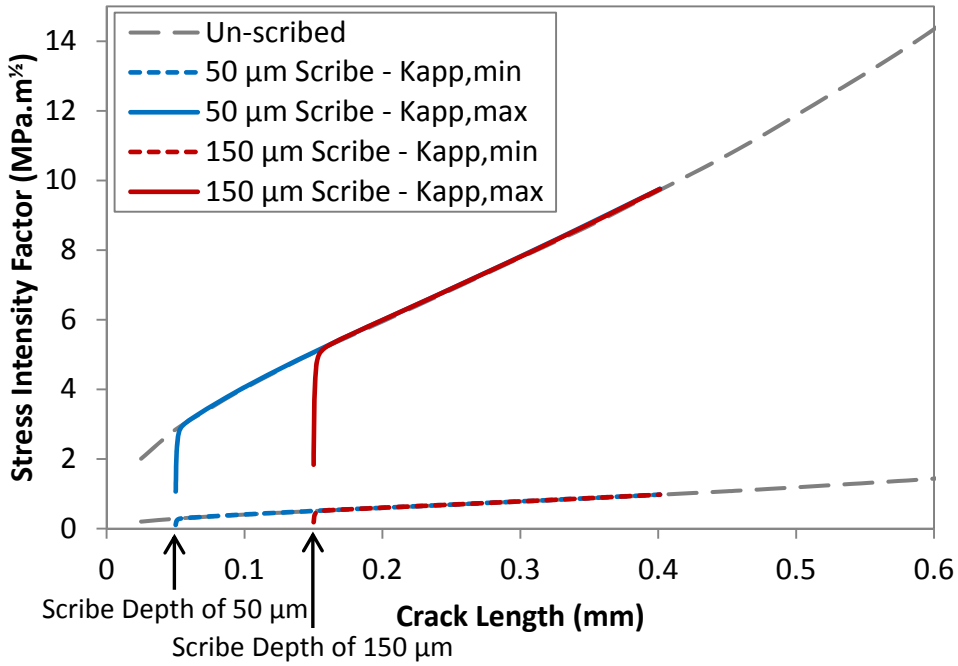

Figure 5.5: SIFs at crack tip at maximum and minimum nominal applied stress

The SIFs at the minimum nominal applied stress were a factor 10 smaller than at the maximum nominal applied stress i.e. simply a function of the applied stress ratio R = 0.1. The SIFs at the root of the scribes of 50 µm and 150 µm depth were less than at a crack tip of 50 µm and 150 µm length respectively. When the crack was advanced approximately 7 µm from the root of the scribe 50 µm deep and 15 µm from the root of the scribe 150 µm deep the calculated SIFs were equivalent at a crack of the same length i.e. 57 µm and 165 µm respectively.

Elastic S22 stress contours at the root of the scribes of 50 µm and 150 µm deep at the maximum nominal applied stress (200 MPa) is shown in Figure 5.6 (A) and (B) respectively. The stress concentration at the root of the scribe 150 µm deep (K_t = 13.2) is greater than are the root of the scribe 50 µm (K_t = 7.9). The effect of the greater stress concentration is clearly evident with larger area of material in excess of the material yield stress (360 MPa), coloured red in the figures.

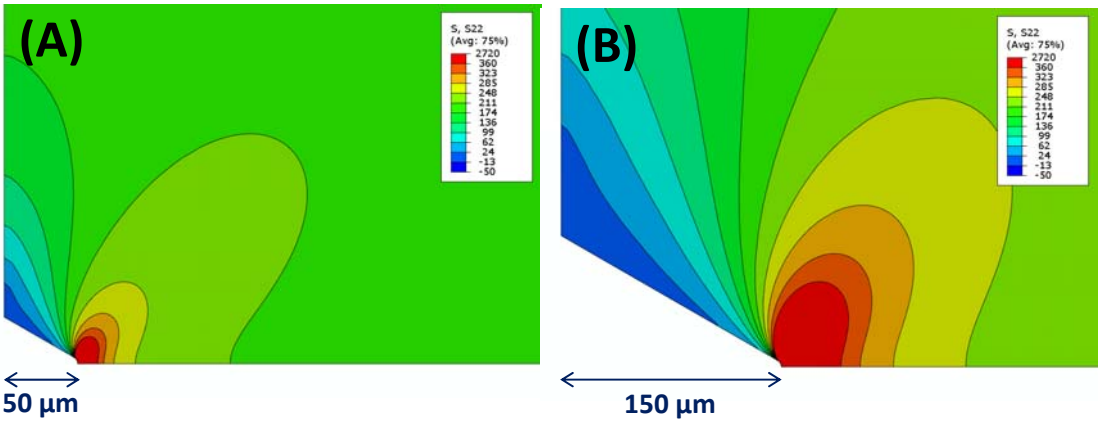

Figure 5.6: Elastic S_{22} stress contours at root of scribe (A) 50 µm and (B) 150 µm deep

The elastic S22 stress distribution along the crack path from the root of scribes 50 µm and 150 µm deep at maximum nominal applied stress (200 MPa) is shown Figure 5.7. The maximum residual stress at the root of the scribe 150 µm deep was 1.7× greater than at the root of the scribe 50 µm deep (ratio of the K_t of each scribe i.e. 13.2 / 7.9). However is should be noted that as the analysis used elastic material properties the maximum stress at the root of the scribes is a function of the minimum element size.

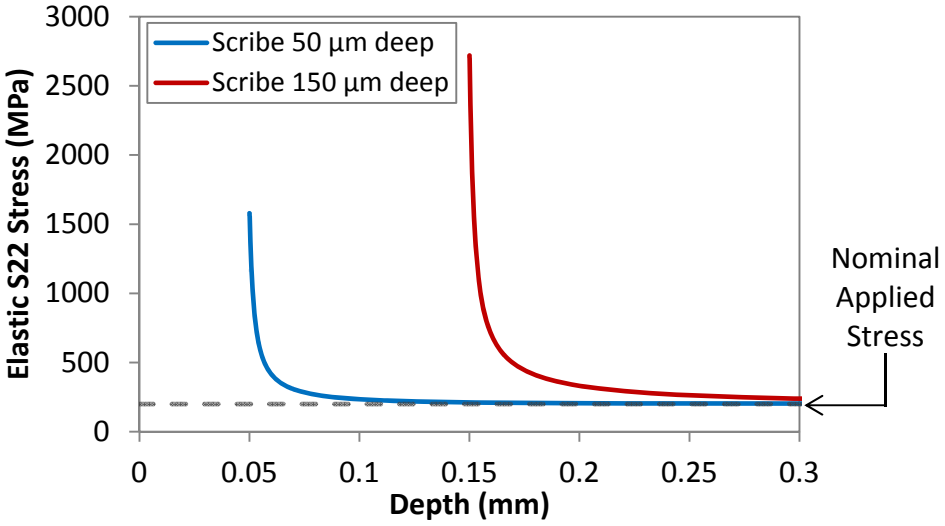

Figure 5.7: Elastic S22 stress along crack path from root of scribes 50 µm and 150 µm deep at maximum nominal applied stress

5.4 Inclusion of Residual Stress Fields Induced by LSP in FE Models

This section details the method used to include residual stress fields induced by LSP in the FE models. One approach is to model the LSP treatment using FE analysis and to predict the induced residual stress field directly however this was deemed outside the scope of the current work. An alternate approach, and that used in the current

work, is to input to the FE model a stress field as an initial condition. The stress fields input as initial conditions were the residual stress fields induced by LSP and measured using hole drilling [132] as presented in section 4.1. The residual stress fields were measured in increments from the peened surface to approximate depth of 1 mm. A total of 20 increment steps were made during measurement of the MIC1, MIC3, and UPM residual stress fields and 14 increment steps were made during measurement of the TOSH residual stress field. Measurement of residual stress was in two directions, parallel to the laser tracking direction (S1 direction) and perpendicular to the laser tracking direction (S2 direction). The S2 direction is the applied loading / crack opening direction and only the residual stress measured in this direction was input to the FE model.

The initial condition (i.e. residual stress field) was input to the FE model using the Abaqus user subroutine Sigini [243]. The measured residual stress fields are plotted in Figure 5.8 (A), (B), (C) and (D) for MIC1, MIC3, UPM and TOSH LSP respectively. In the written subroutine the residual stress at element integration points located between two measurement points was interpolated linearly. When using an initial condition in Abaqus a command step is required named 'Unbalanced Stresses'. If the initial condition is not in a state of global equilibrium, this command will determine equilibrium through either elongation or shortening and bending of the modelled geometry. The distortion will impose tensile and bending balancing stresses and alter the initial residual stress field as demonstrated in Figure 5.9. The measured residual stress fields were not in global equilibrium since the measurements were to only partial depth. Therefore distortion of the FE models occurred. The residual stress fields after FE model distortion (termed Abaqus balanced) are plotted in Figure 5.8 (A) to (D) for the MIC1, MIC3, UPM and TOSH residual stress fields respectively.

The Abaqus balanced residual stress fields are significantly different than the measured residual stress fields, shown in Figure 5.8. For example the maximum compressive stress for the UPM LSP treatment is 33% less after balancing. It has been noted [88, 234] that the accuracy of predicted FCGR through residual stress fields is highly dependent on the accuracy of the residual stress field data. Therefore it is important that the residual stress fields used in the FE analysis are equivalent to those measured.

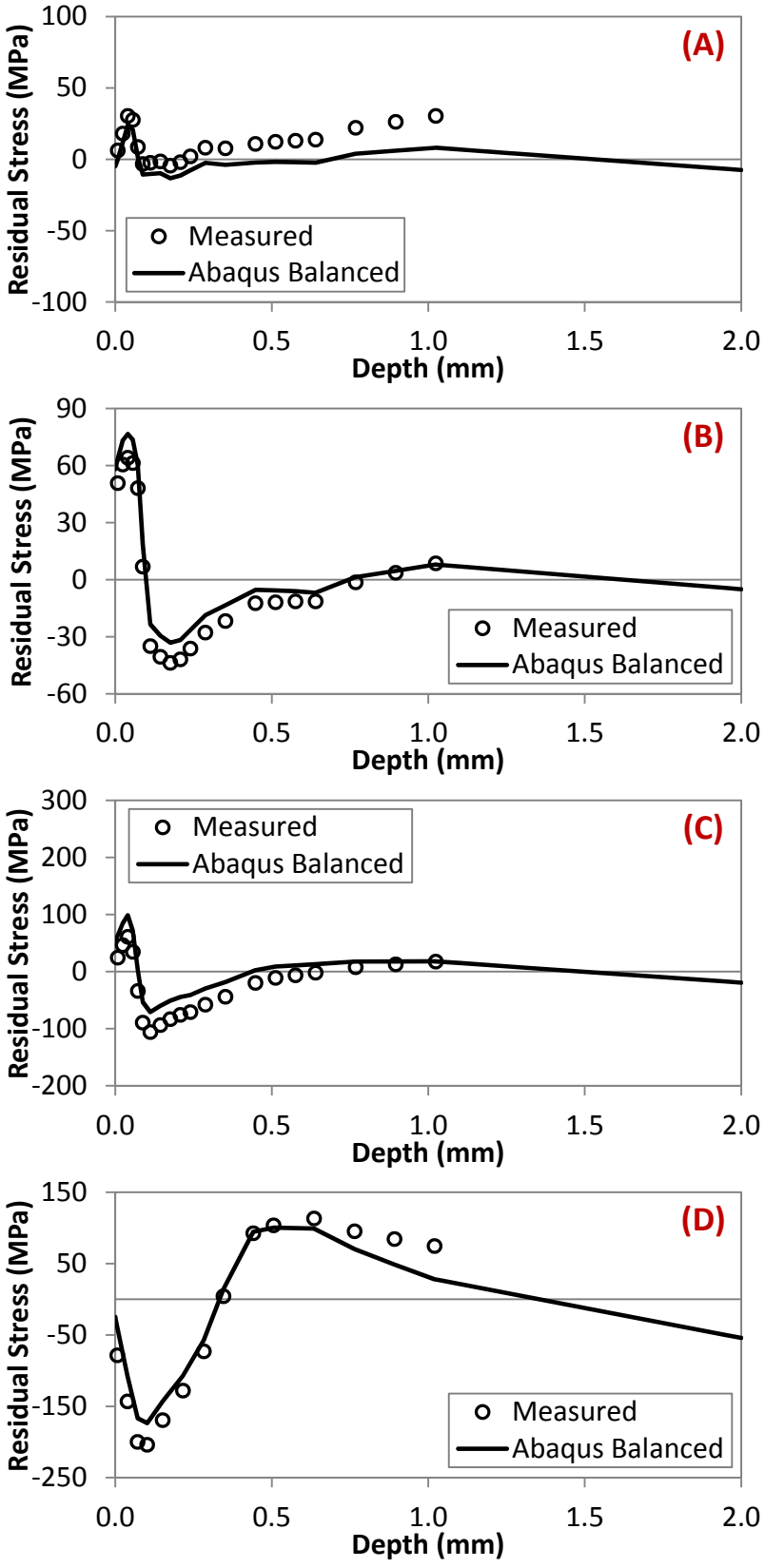

Figure 5.8: Comparison of measured and Abaqus balanced residual stress fields for (A) MIC1, (B) MIC3, (C) UPM and (D) TOSH LSP treatments

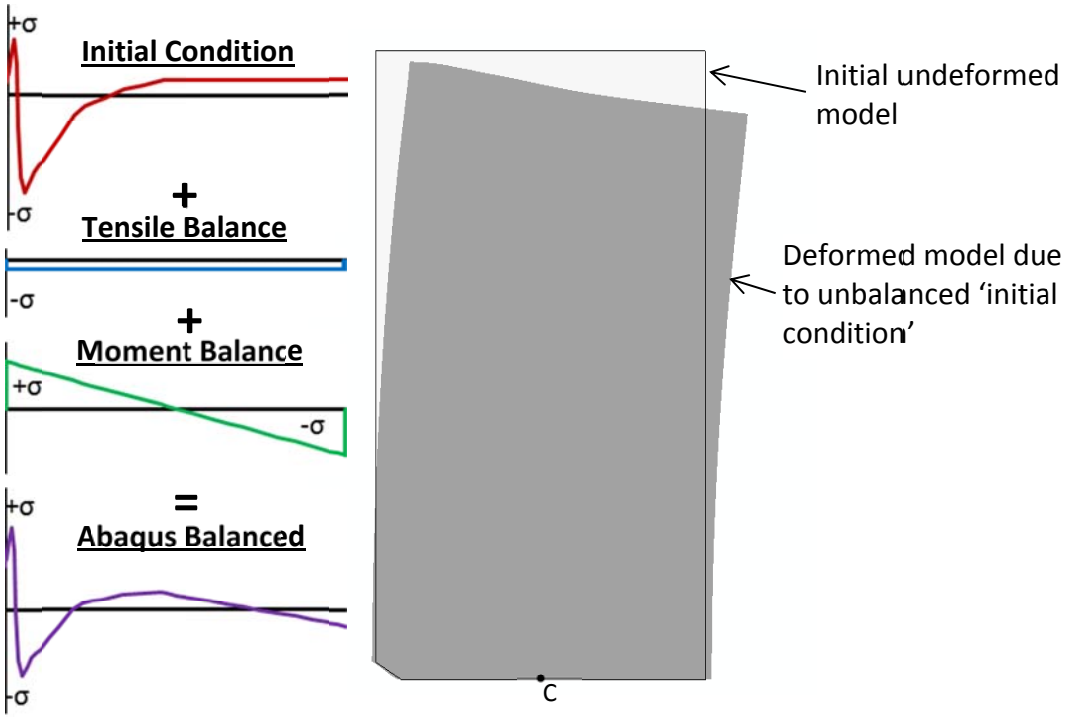

Figure 5.9: Distortion of modelled geometry due to unbalanced initial condition

To retain the initial conditions after the 'unbalanced stress' command, the initial condition (i.e. residual stress field) must satisfy equations 5.6 and 5.7 below.

$$\sum \sigma_{Tension} + \sum \sigma_{Compression} = 0 \quad (5.6)$$

$$\sum M_{C} = 0 \quad (5.7)$$

where c is the midpoint of the model width as shown in Figure 5.9. The measured residual stress fields extended approximately 1 mm from the peened surface. A balancing residual stress was introduced over the remaining length (i.e. from 1 to 2 mm) to maintain the measured residual stress field. To develop the balancing stress field the first step was to determine the level of imbalance of the measured residual stress field. Equations 5.8 and 5.9 were used to calculate the force and moment imbalance respectively.

$$A = \int_0^a \sigma^m(x)dx \quad (5.8)$$

$$M = A \times \left(a - \frac{1}{A}\int_0^a x \cdot \sigma^m(x)dx\right) \quad (5.9)$$

Where σ^m is the measured stress field and a denotes the depth residual stress field measurement. The balancing stress field consisted of two components: first a pure tensile / compressive stress field to satisfy equation 5.6 and second a pure bending stress field to satisfy equation 5.7, as illustrated in Figure 5.10. The magnitude of the balancing tensile / compressive stress field (σ^f) was determined using equation 5.10.

$$\sigma^f = \frac{A}{t-a} \quad (5.10)$$

Where t is the sample thickness (i.e. 2 mm). The balancing bending stress field (σ^b) was evaluated using equation 5.11.

$$\sigma^b = \frac{M(y)}{t-a} \quad (5.11)$$

Where y is the distance from $(t\text{-}a)/2$. Finally an equilibrated residual stress field (σ^e) was defined. This was a combination of the measured residual stress field and the balancing tensile / compressive and bending residual stress fields and was determined using equation 5.12.

$$\sigma^e = \sigma^e_{(0\rightarrow a)} + \sigma^e_{(a\rightarrow t)} \quad (5.12)$$

where $$\sigma^e_{(0\rightarrow a)} = \sigma^m \quad (5.13)$$

and $$\sigma^e_{(a\rightarrow t)} = \sigma^f + \sigma^b \quad (5.14)$$

The MIC1, MIC3, UPM and TOSH measured residual stress fields are compared to the derived equilibrated residual stress fields in Figure 5.11 (A), (B), (C) and (D) respectively.

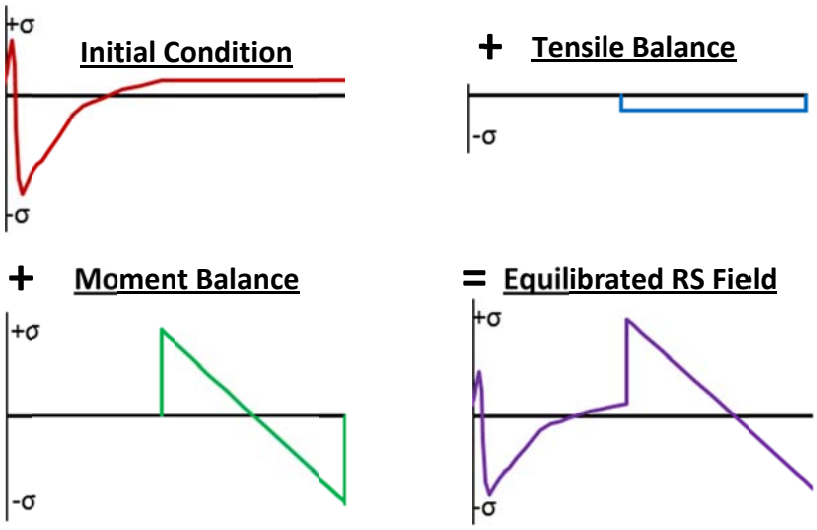

Figure 5.10: Development of equilibrated residual stress field

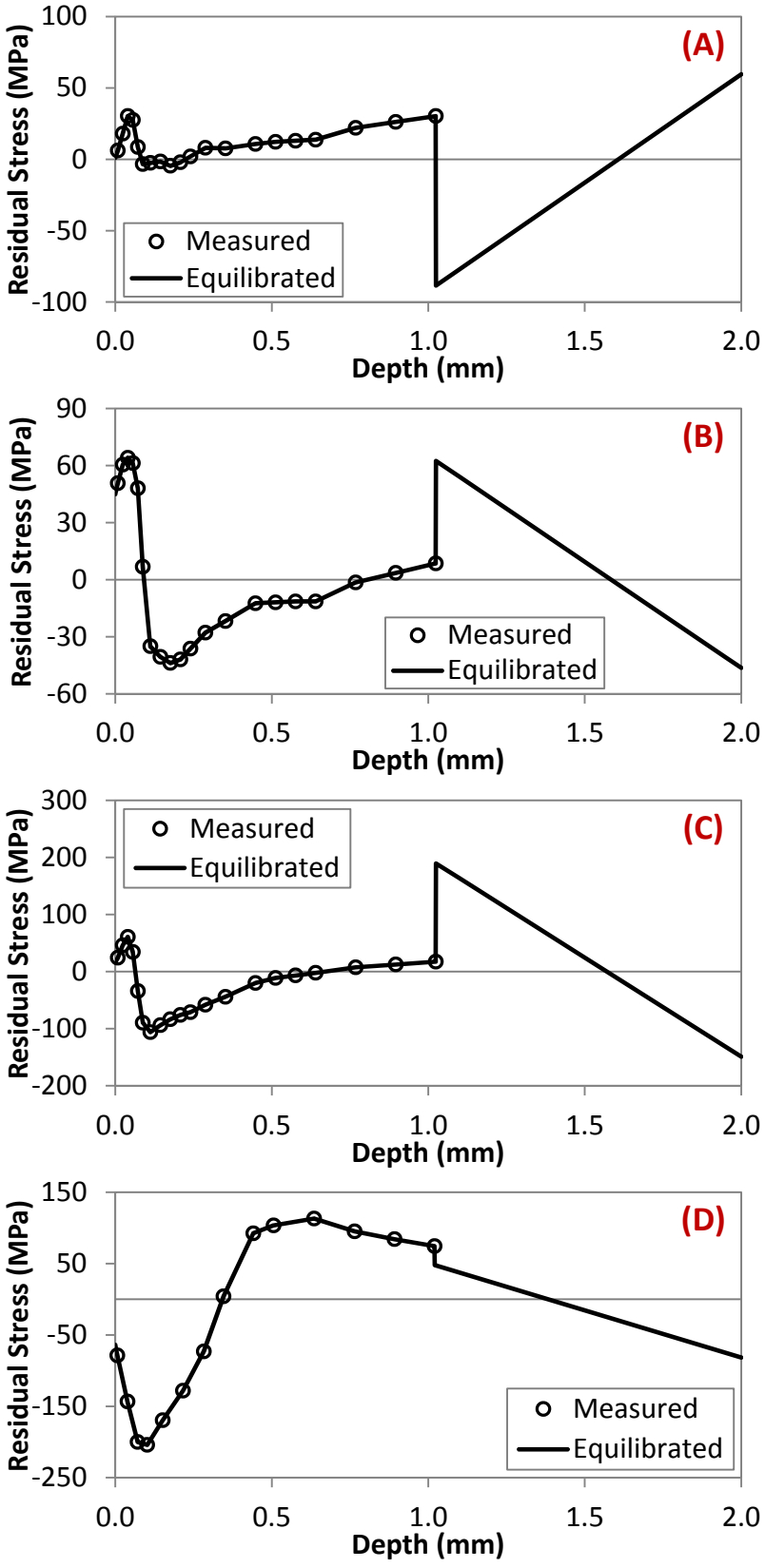

Figure 5.11: Comparison of measured and equilibrated residual stress fields for (A) MIC1, (B) MIC3, (C) UPM and (D) TOSH LSP treatments

It has been stated by Bao *et al.* [228] that SIFs calculated at crack lengths within the measured residual stress field are not affected by the balancing residual stress and that SIFs calculated at crack lengths outside the measured residual stress field are not meaningful. The following study was performed to validate this statement. Two hypothetical residual stress fields were created for the study and are referred to as field 1 and field 2, these are plotted in Figure 5.12.

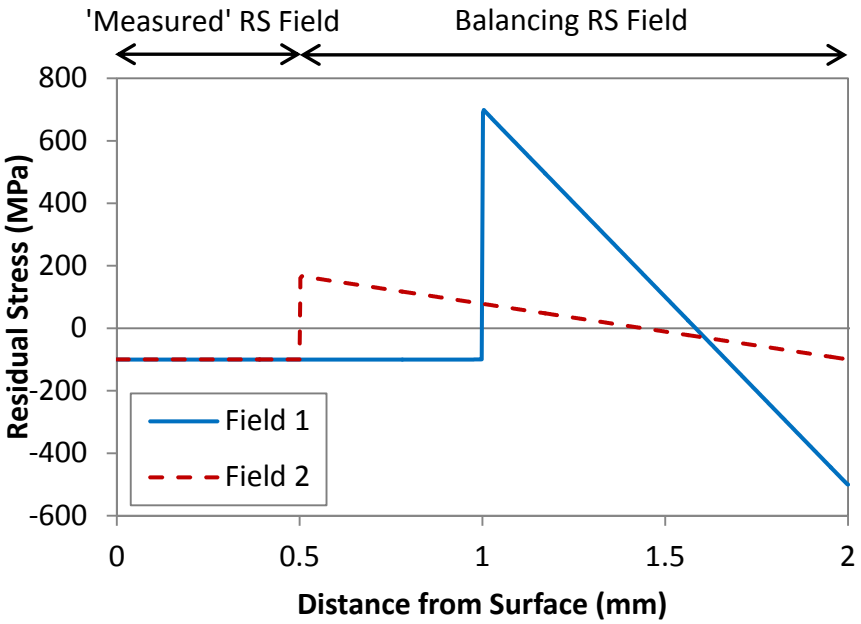

Figure 5.12: Residual stress fields used to validate use of equilibrated measured stress fields in FE analysis of SIFs

The two fields had residual compressive stress of magnitude -100 MPa that extended 0.5 mm from the surface and for the purpose of this study represent the 'measured' residual stress field. For field 1 the compressive stress of -100 MPa continued 1 mm from the surface and the region between 1 mm and 2 mm was used for residual stress field balancing. For field 2 the region between 0.5 mm and 2 mm was used for stress field balancing. This results in two very different balancing residual stress profiles as shown in Figure 5.12 noting however that both are in global equilibrium.

A crack was advanced 1 mm from the surface in the FE model. The residual stress intensity factor K_{res} was calculated at crack lengths increments and is plotted in Figure 5.13. The K_{res} were equivalent until a crack length of 0.5 mm i.e. within the 'measured' residual stress field. At crack lengths greater than 0.5 mm the K_{res} differed due to the two different balancing residual stress fields.

The analysis validated that SIFs calculated at crack lengths within the measured residual stress field are independent of the balancing residual stress and that SIFs

calculated at crack lengths outside the measured residual stress field would not be meaningful, as has been stated by Bao *et al.* [228].

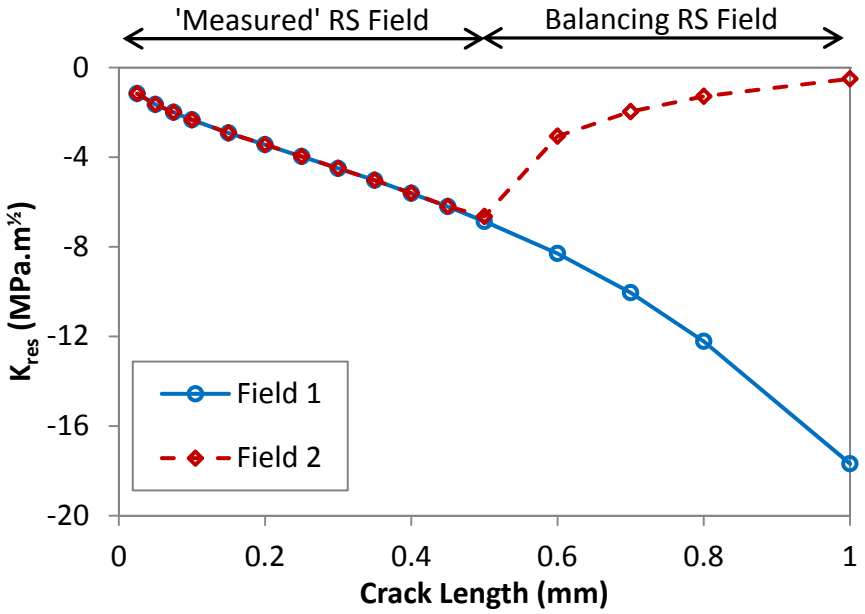

Figure 5.13: Comparison of K_{res} for two residual stress fields with equivalent 'measured' but different balancing residual stress

5.5 Redistribution of Residual Stress at Scribe Root

The LSP induced residual stress fields were measured using incremental hole drilling in unscribed samples. Equilibrated residual stress fields were developed in section 5.5 that maintained the measured residual stress fields in FE models of unscribed geometries. Residuals stress fields were not measured in the vicinity of scribes. In this section the redistribution of the equilibrated residual stress field around the scribed geometries using FE analysis is reported.

The MIC1, MIC3, UPM and TOSH residual stress fields in the area around the scribes is shown in Figure 5.14, Figure 5.15, Figure 5.16 and Figure 5.17 respectively where (A) is a plot of the original and redistributed residual stress field along the crack path from the root of scribes 50 µm and 150 µm deep and (B) and (C) are contour plots of the elastic S22 stress at the root of scribes 50 µm and 150 µm deep respectively.

Considering the MIC1 LSP treatment in Figure 5.14, the residual stress at the root of both scribes was in tension. The stress at the root of the scribe 150 µm deep (78 MPa) was less than the stress at the root of the scribe 50 µm deep (179 MPa). In fact the residual stress along the crack path from the root of the scribe 150 µm deep was fully

tensile. The residual stress ahead of the scribe 50 µm deep was in compression between 145 to 215 µm from the peened surface.

The root of the scribe 150 µm deep was located in a compressive region of the equilibrated residual stress field (located 80 to 220 µm from the peened surface). However after rebalancing the residual stress at the scribe root is in tension. This implied that the tensile residual stress near the peened surface affected the residual stress at the scribe root.

Consider the MIC3 LSP treatment shown in Figure 5.15. The root of the scribe 50 µm deep was located in a tension region of the equilibrated residual stress field and after rebalancing the residual stress at the root was in tension. The root of the scribe 150 µm deep was located in a compression region of the equilibrated residual stress field however after rebalancing the residual stress at the scribe root was in tension. Again this implies that the tensile residual stress near the peened surface affected the residual stress at the root of the scribe 150 µm deep. The magnitude of the tensile stress at the scribe root is lower for MIC3 (5 MPa) than MIC1 (78 MPa) despite the greater magnitude of the MIC3 equilibrated stress field this was because the tension / compression residual stress behind the scribe root was more balanced for MIC3 than MIC1 i.e. for MIC3 the ratio of tension stress behind the scribe root was 2.6× greater than the compression stress behind the root whereas for MIC1 it was 9.3× greater (this is a ratio of the area between the residual stress curve and neutral axis).

The root of the scribe 50 µm deep was located in a tension region of the UPM equilibrated residual stress field, shown in Figure 5.15. After rebalancing the residual stress at the root was in tension. The root of the scribe 150 µm deep was located in a compression region of the equilibrated residual stress field and after rebalancing the residual stress at the root was in compression. In this instance compression stress behind the scribe root 150 µm deep was 3× greater than the tension stress.

The TOSH equilibrated residual stress field was in compression from the peened surface to a depth of approximately 340 µm. Therefore the stress at the root of both scribes after rebalancing was in compression. The residual stress at the root of the scribe 150 µm deep was greater than at the root of the scribe 50 µm deep.

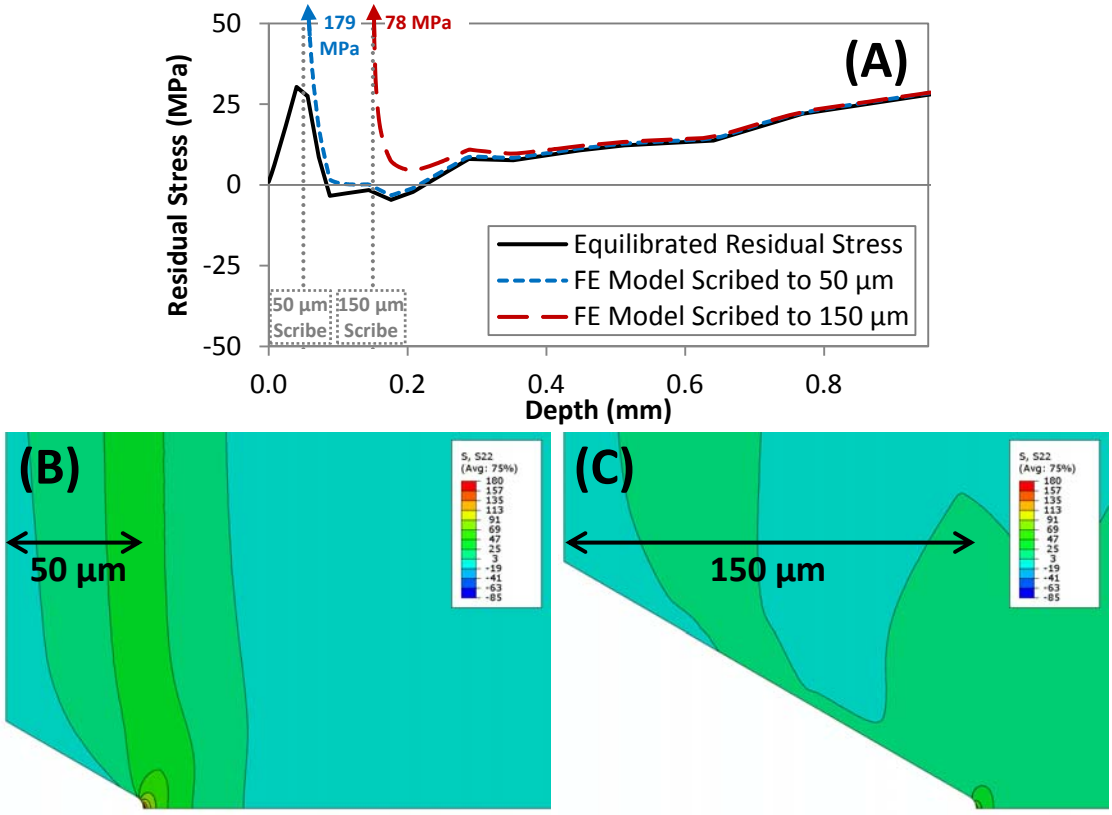

Figure 5.14: MIC1 residual stress field induced stress concentration at root of (B) 50 µm and (C) 150 µm scribe

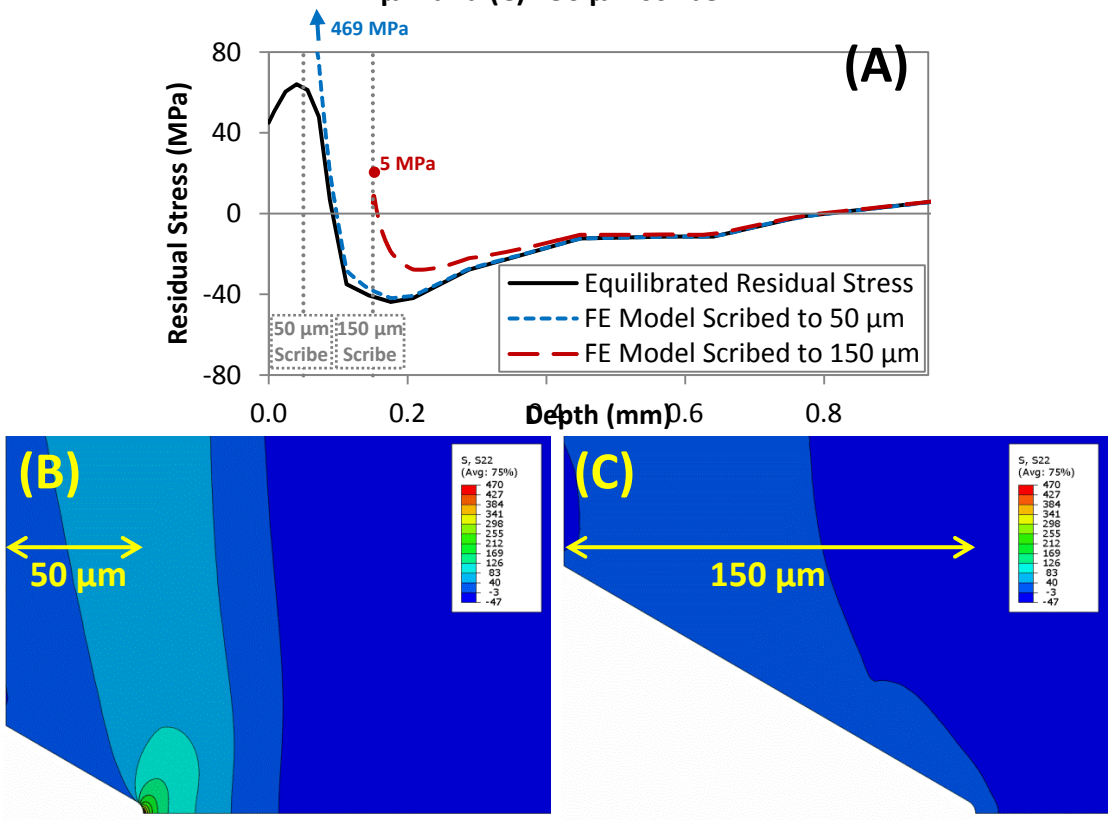

Figure 5.15: MIC3 residual stress field induced stress concentration at root of (A) 50 µm and (B) 150 µm scribe

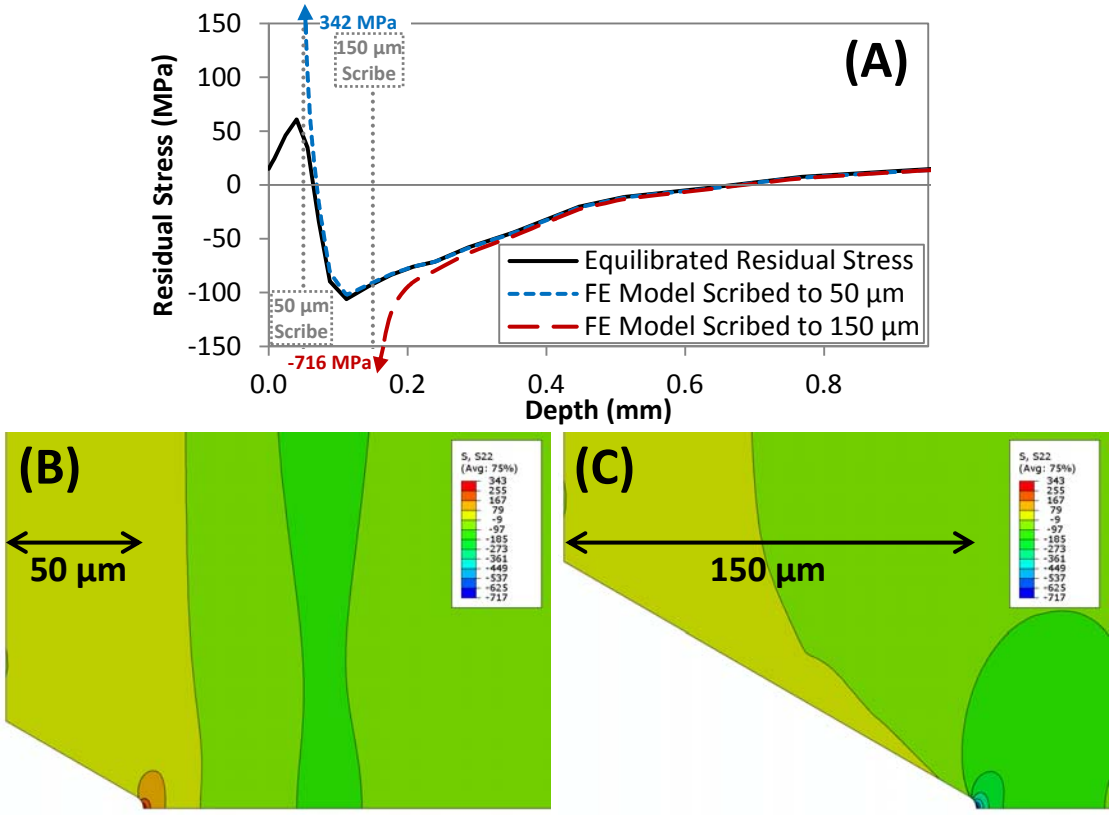

Figure 5.16: UPM residual stress field induced stress concentration at root of (A) 50 µm and (B) 150 µm scribe

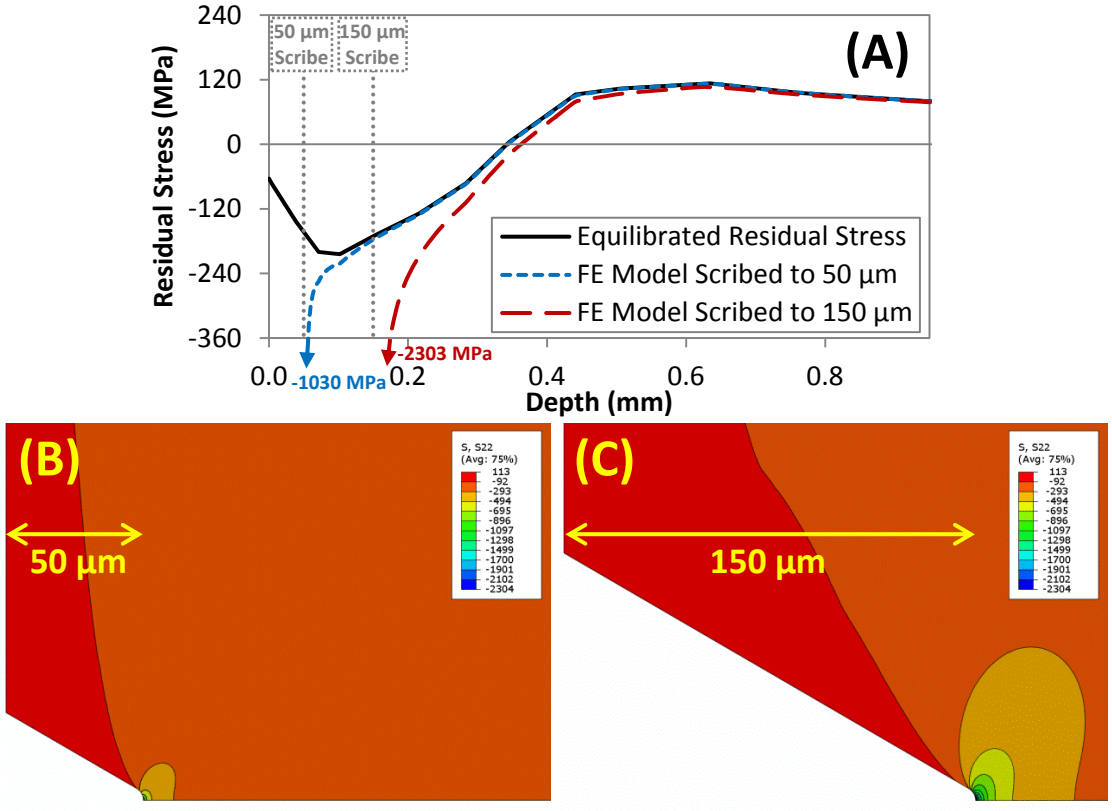

Figure 5.17: TOSH residual stress field induced stress concentration at root of (A) 50 µm and (B) 150 µm scribe

5.6 Redistribution of Residual Stress with Crack Advance

The redistribution of the equilibrated residual stress fields at the scribe root was reported in section 5.5. In this section a crack was advanced from the root of the scribes and the resultant redistribution of the residual stress fields is reported.

The effect of crack advance through the MIC1, MIC3, UPM, and TOSH residual stress fields is shown in Figure 5.18, Figure 5.19, Figure 5.20 and Figure 5.21 respectively. The crack was advanced from the root of scribes 50 µm and 150 µm deep using a node release scheme and the residual stress field ahead of the crack tip is shown in the figures. From the scribe 50 µm deep crack lengths of 100, 150, 250 and 400 µm are reported (note: crack length is measured from the peened surface) and from the scribe 150 µm deep crack lengths of 250 and 400 µm are reported.

First consider the MIC1 residual stress field in Figure 5.18. The rebalanced residual stress at the crack tip is in tension at all crack lengths reported. The stress at the tip of cracks advanced from the scribe root 150 µm deep was greater than the stress at the tip of cracks advanced from the scribe root 50 µm deep. In the FE models the element size increases from the scribe root along the crack path. For examples the element size at the crack tip of length 250 µm advanced from a scribe 50 µm deep was 4.1 µm whereas advanced from a scribe 150 µm deep the element size at the crack tip was 2.1 µm. Since elastic conditions were assumed the stress at the crack tip approaches infinity and therefore a smaller element size at the crack tip will result in a greater stress. However it can be observed in Figure 5.18 that the stress distribution ahead of the crack tip is equivalent for cracks advanced from scribes 50 µm and 150 µm deep.

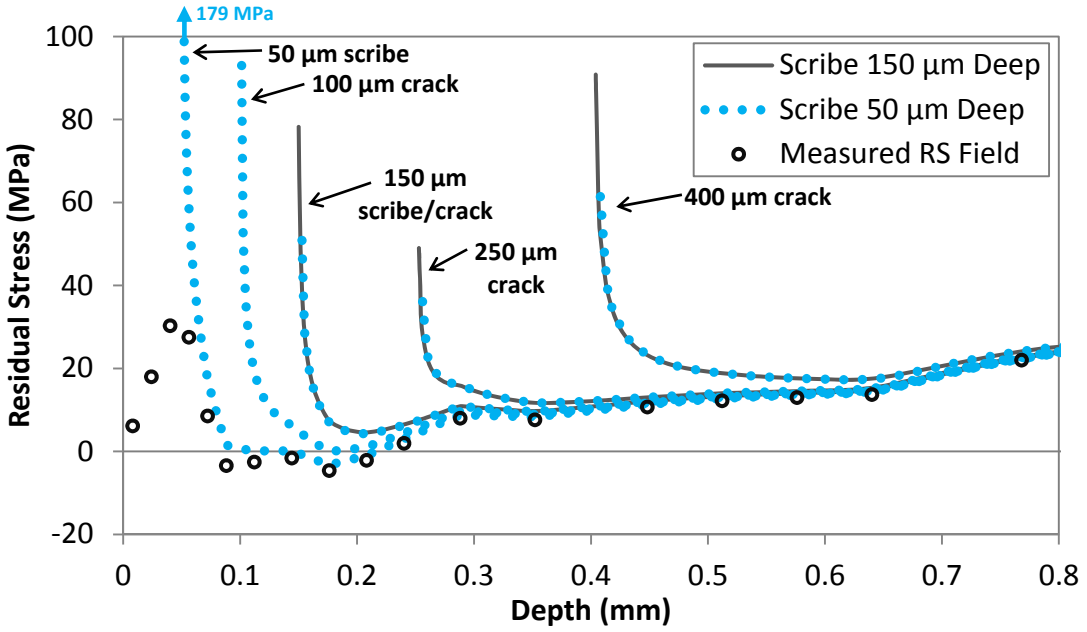

Figure 5.18: MIC1 residual stress field redistribution with crack extension

The effect of crack advance through the MIC3 residual stress field is shown in Figure 5.19. The measured residual stress field was tensile at the surface and became compressive a distance 92 µm from the surface and it remained in compression until 805 µm from the surface. The stress at the root of the scribe 50 µm deep was in tension. The tip of the crack of length 100 µm was located in a compressive region of the measured residual stress field but the stress at the crack tip was in tension. This implied that the tensile residual stress behind the crack tip affected the stress at the crack tip. At tip of cracks of length 250 and 400 µm the residual stress was in compression. The transition from tensile to compressive residual stress at the crack tip occurred at a length of approximately 150 µm.

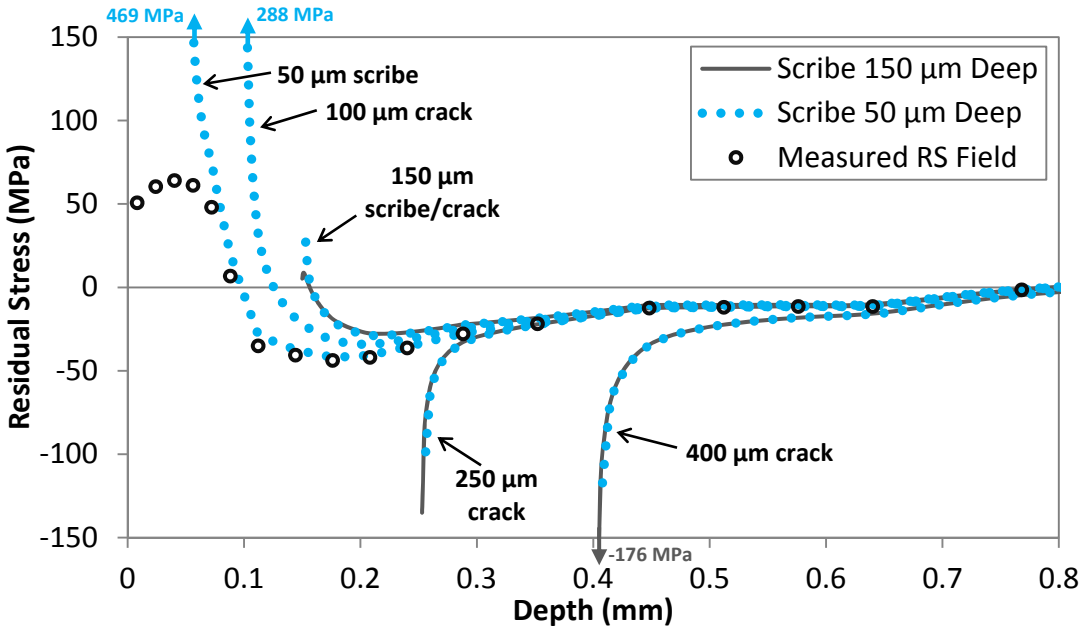

Figure 5.19: MIC3 residual stress field redistribution with crack extension

The effect of crack advance through the UPM residual stress field is shown in Figure 5.20. The measured residual stress field was tensile at the surface and became compressive a distance 64 µm from the surface. At the root of the scribe 50 µm deep the residual stress is tensile. The stress at the tip of cracks of length 100 µm and greater was compressive.

Shown in Figure 5.21 is the effect of crack advance though the TOSH residual stress field. The measured residual stress was compressive at the surface and transitioned to tension a distance 342 µm from the surface. The stress was in compressive at the tip of the cracks reported in Figure 5.21. The tip of the crack of length 400 µm was located in a region of the measured residual stress field that was in tension. However after rebalancing the stress at the tip was in compression. Again this implied that the residual stress behind the crack tip affected the stress at the crack tip.

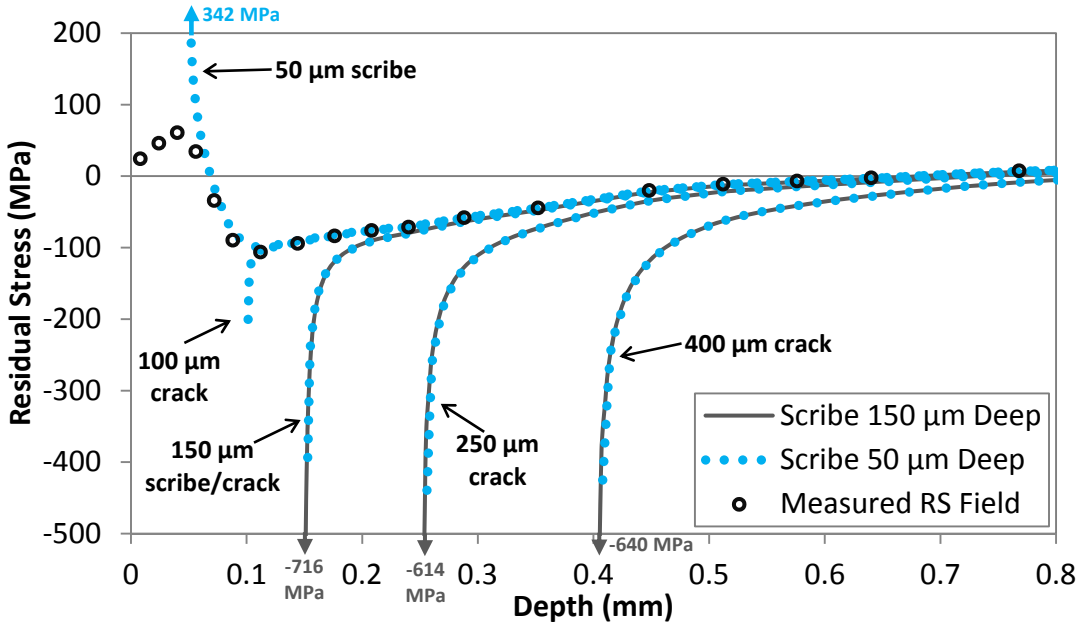

Figure 5.20: UPM residual stress field redistribution with crack extension

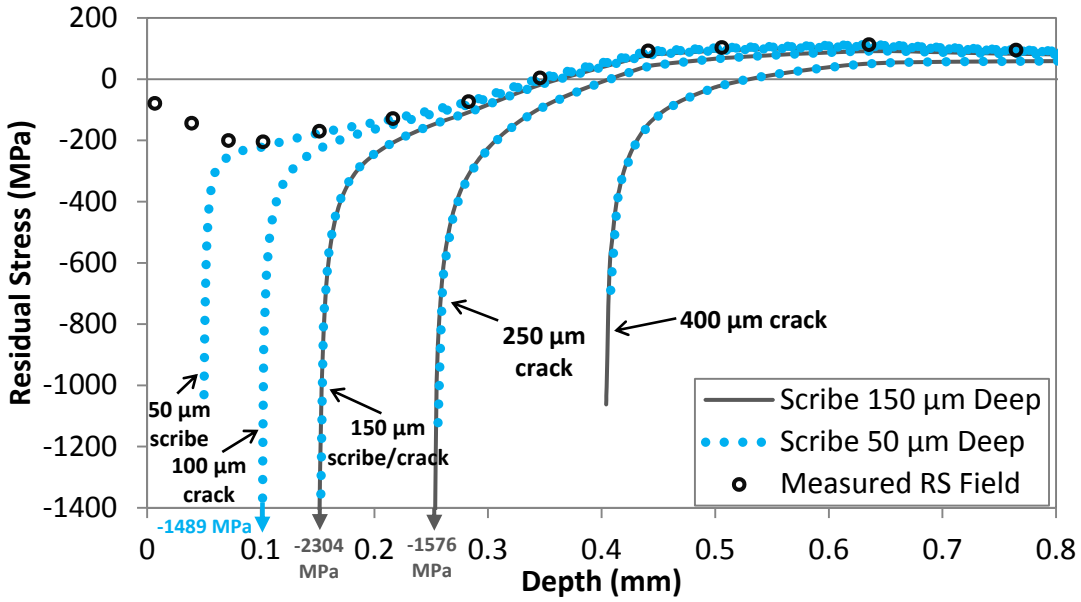

Figure 5.21: TOSH residual stress field redistribution with crack extension

The stress field at the tip of a crack of length 150 µm is compared to the stress field at the root of the scribe of depth 150 µm in Figure 5.22 (A) and (B). The crack of length 150 µm was advanced from a scribe root of depth 50 µm. In the figure stress greater than the compressive yield stress (-360 MPa) is coloured dark blue. The length of the region in excess of the yield stress was measured along from the crack tip / scribe root along the crack path. It was measured as 23.9 µm in length ahead of the 50 µm crack and 24.5 µm in length ahead of the 150 µm scribe.

A similar comparison is made in Figure 5.23 however in this case a crack of length 250 µm that was advanced from a scribe root of depth 50 µm and 150 µm is compared. The length of the region in excess of the yield stress was measured as 26.4 µm in length ahead of the 50 µm crack and 27.7 µm in length ahead of the 150 µm scribe.

The difference in area of material in excess of the yield stress may be a function of the different element sizes in these regions only with further FE analysis required.

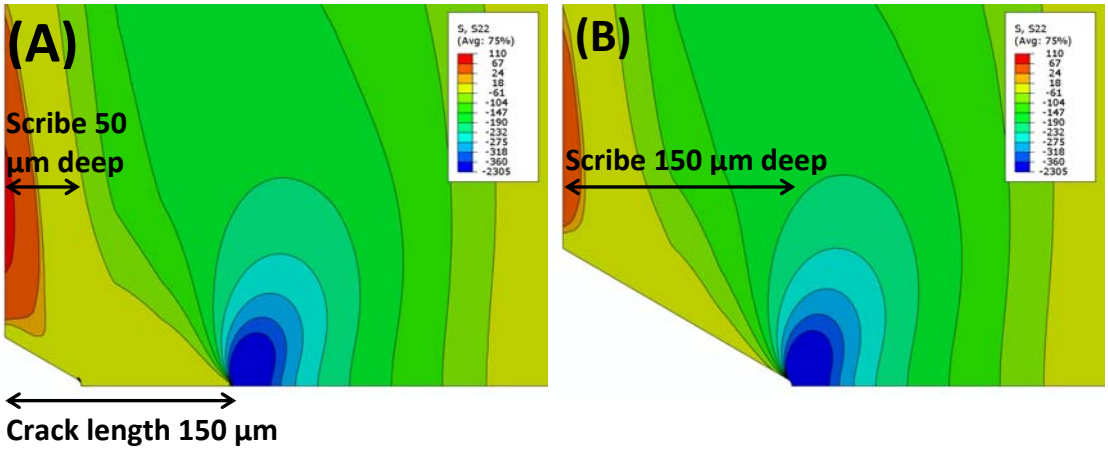

Figure 5.22: TOSH S_{22} stress contours at (A) crack tip of length 150 µm and (B) root of scribe of depth 150 µm

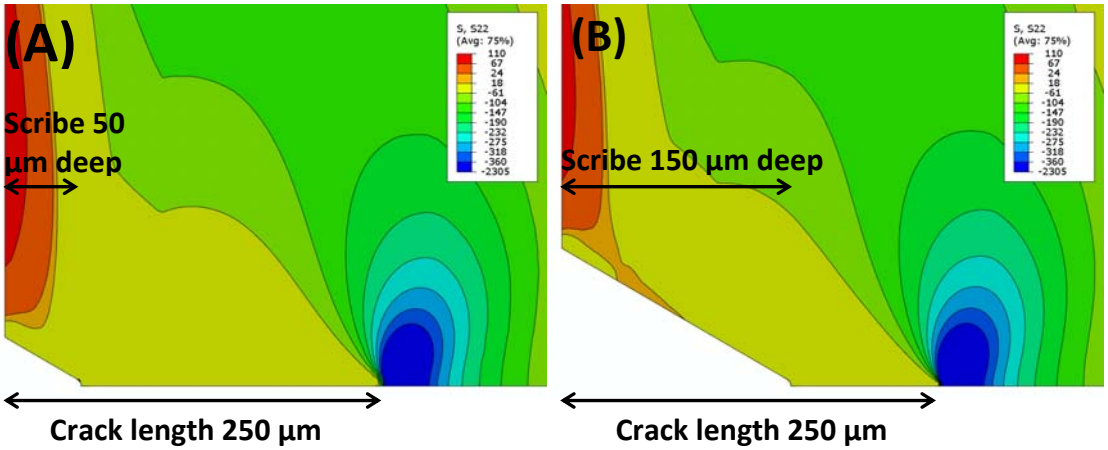

Figure 5.23: TOSH S_{22} stress contours at crack tip length 250 µm of (A) advanced from scribe 50 µm deep and (B) advanced from scribe 150 µm deep

5.7 Calculated Residual Stress Intensity Factors

The MIC1, MIC3, UPM and TOSH residual stress field induced stress intensity factors (K_{res}) are reported in Figure 5.24. K_{res} was calculated at crack advance increments from the root of scribes 50 µm and 150 µm deep. It was reported in Figure 5.18 that the MIC1 rebalanced residual stress at the crack tip was in tension at all crack lengths reported and in Figure 5.24 below it is shown that the MIC1 residual stress field induced K_{res} is fully positive. The UPM and MIC3 residual stress field induced K_{res} is

positive at the scribe root 50 µm deep and transitioned to negative at a crack tip approximately 85 µm and 166 µm from the peened surface respectively. The transition of K_{res} from positive to negative occurred at the same depth as the crack tip stress transitioned from tension to compression as reported in Figure 5.19 and Figure 5.20. Finally it was reported in Figure 5.21 that the TOSH rebalanced residual stress at the crack tip was in compression at all crack lengths and in Figure 5.24 below it is shown that the TOSH residual stress field induced K_{res} is fully negative.

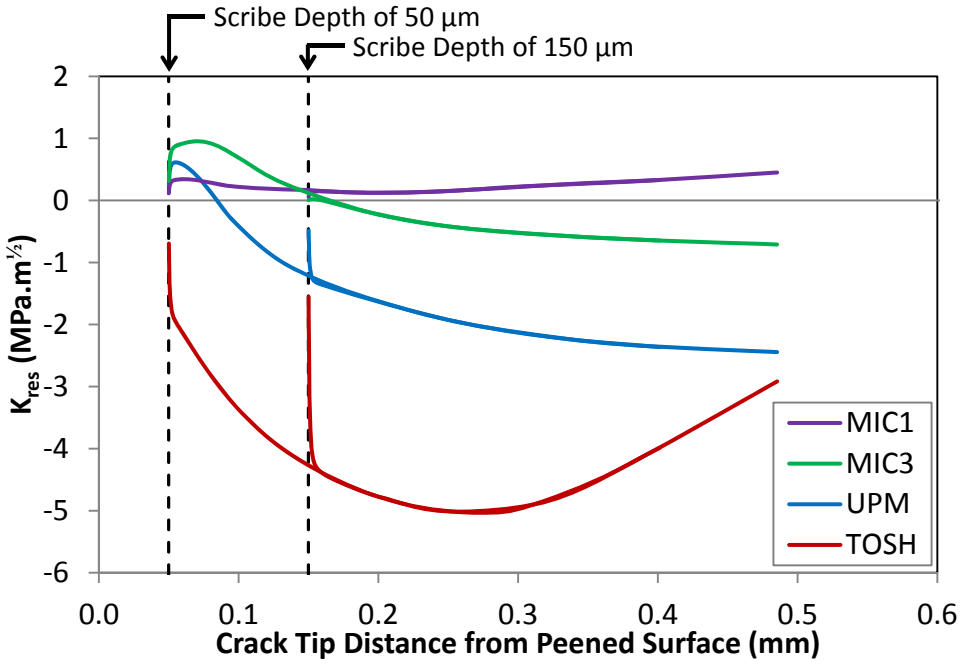

Figure 5.24: Comparison of residual stress intensity factors

5.8 Effect of Residual Stress on Applied SIF Range and Stress Ratio

The effect on the applied SIF range and stress ratio of the MIC1, MIC3, UPM, and TOSH residual stress fields is reported in Figure 5.25, Figure 5.26, Figure 5.27 and Figure 5.28 respectively. In these figures part (A) reports the stress intensity factor due to the maximum ($K_{app,max}$)and minimum ($K_{app,min}$) nominal applied stress from section 5.3 and the residual stress intensity factor (K_{res}) from section 5.7. Also shown in part (A) of the figures is the maximum total stress intensity factor ($K_{tot,max}$) calculated using equation 5.15 below.

$$K_{tot,max} = K_{app,max} + K_{res} \quad (5.15)$$

Part (B) of the figures report the minimum total stress intensity factor ($K_{tot,min}$). Two methods were used to calculate $K_{tot,min}$. The first method is named the superposition

method (SP) where $K_{tot,min}$ was calculated using equation 5.16 below. This method ignores crack face contact and can result in negative values of $K_{tot,min}$.

$$K_{tot,min} = K_{app,min} + K_{res} \quad (5.16)$$

The second method is called the modified superposition method (M.SP) where $K_{tot,min}$ was calculated using equation 5.17 below. This method is equivalent to superposition if $K_{tot,min}$ is greater than zero. However the modified superposition method accounts for crack face contact by setting values of $K_{tot,min}$ less than zero as equal to zero.

$$K_{tot,min} = if\left(K_{app,min} + K_{res}\right)\begin{cases} \leq 0, & 0 \\ > 0, & K_{app,min} + K_{res} \end{cases} \quad (5.17)$$

Part (C) of the figures report the stress intensity factor range (ΔK). For the superposition method K_{res} has no effect on ΔK_{app} as demonstrated in equations 5.18 to 5.20 below.

$$\Delta K_{tot} = K_{tot,max} - K_{tot,min} \quad (5.18)$$

$$\Delta K_{tot} = \left(K_{app,max} + K_{res}\right) - \left(K_{app,min} + K_{res}\right) \quad (5.19)$$

$$\Delta K_{tot} = K_{app,max} - K_{app,min} = \Delta K_{app} \quad (5.20)$$

Equation 5.18 above was also used to calculate ΔK_{tot} for the modified superposition method. At values of $K_{tot,min}$ greater than zero, ΔK_{tot} and ΔK_{app} are equivalent to values calculated using the superposition method. However at values of $K_{tot,min}$ less than zero ΔK_{tot} is equal to $K_{tot,max}$.

Another method [N.EQ] to calculate the stress intensity factor range was also considered. This was based on a crack closure approach and the equations by Newman [59] were used to calculate an effective stress intensity factor range (ΔK_{eff}). A crack opening stress ratio was calculated using equations 5.21 or 5.22.

$$\frac{\sigma_{op}}{\sigma_{max}} = A_0 + A_1 R + A_2 R^2 + A_3 R^3 \quad for\ R \geq 0 \quad (5.21)$$

$$\frac{\sigma_{op}}{\sigma_{max}} = A_0 + A_1 R \quad for\ R < 0 \quad (5.22)$$

where

$$A_0 = (0.825 - 0.34\alpha + 0.05\alpha^2)[cos(\pi\sigma_{max}/2\sigma_0)]^{1/\alpha} \quad (5.23)$$

$$A_1 = (0.415 - 0.071\alpha)\,\sigma_{max}/\sigma_0 \quad (5.24)$$

$$A_2 = 1 - A_0 - A_1 - A_3 \quad (5.25)$$

$$A_3 = 2A_0 + A_1 - 1 \quad (5.26)$$

For plane stress conditions α = 1 while for plane strain conditions α = 3. The flow stress (σ_0) is defined as the average of yield stress and the ultimate tensile strength of the material. An effective SIF range (ΔK_{eff}) was then calculated using equation 5.27.

$$\Delta K_{eff} = \left[\frac{1 - \sigma_{op}/\sigma_{max}}{1 - R}\right] \Delta K_{app} \quad (5.27)$$

For residual stress bearing materials the stress ratio R in equations 5.21, 5.22 and 5.27 above were replaced with the effective stress ratio R_{eff}. The effective stress ration (R_{eff}) was calculated using equation 5.28.

$$R_{eff} = \frac{K_{tot,min}}{K_{tot,max}} \quad (5.28)$$

Part (D) of the figures show the effect of residual stress on the nominal stress ratio (R = 0.1). For the modified superposition approach when $K_{tot,min} \leq 0$ the R_{eff} = 0. The R_{eff} used in the superposition and the Newman crack closure approach are equivalent.

The effect on SIF range and stress ratio of the MIC1 residual stress field is considered in Figure 5.25. The MIC1 residual stress field induced a fully positive K_{res}, as described in section 5.7, and therefore $K_{tot,max}$ was greater than $K_{app,max}$ as shown in figure (A). Since K_{res} was greater than zero, the calculated $K_{tot,min}$ using the superposition and modified superposition methods were equivalent, shown in figure (B). Again because K_{res} was greater than zero ΔK_{tot} calculated using superposition and modified superposition methods were equivalent as shown in figure (C). The calculated ΔK_{eff} using Newman's equations is also shown in figure (C) and is less than ΔK_{tot} due to the presence of crack closure. Finally the R_{eff} was equivalent for all three methods as shown in figure (D).

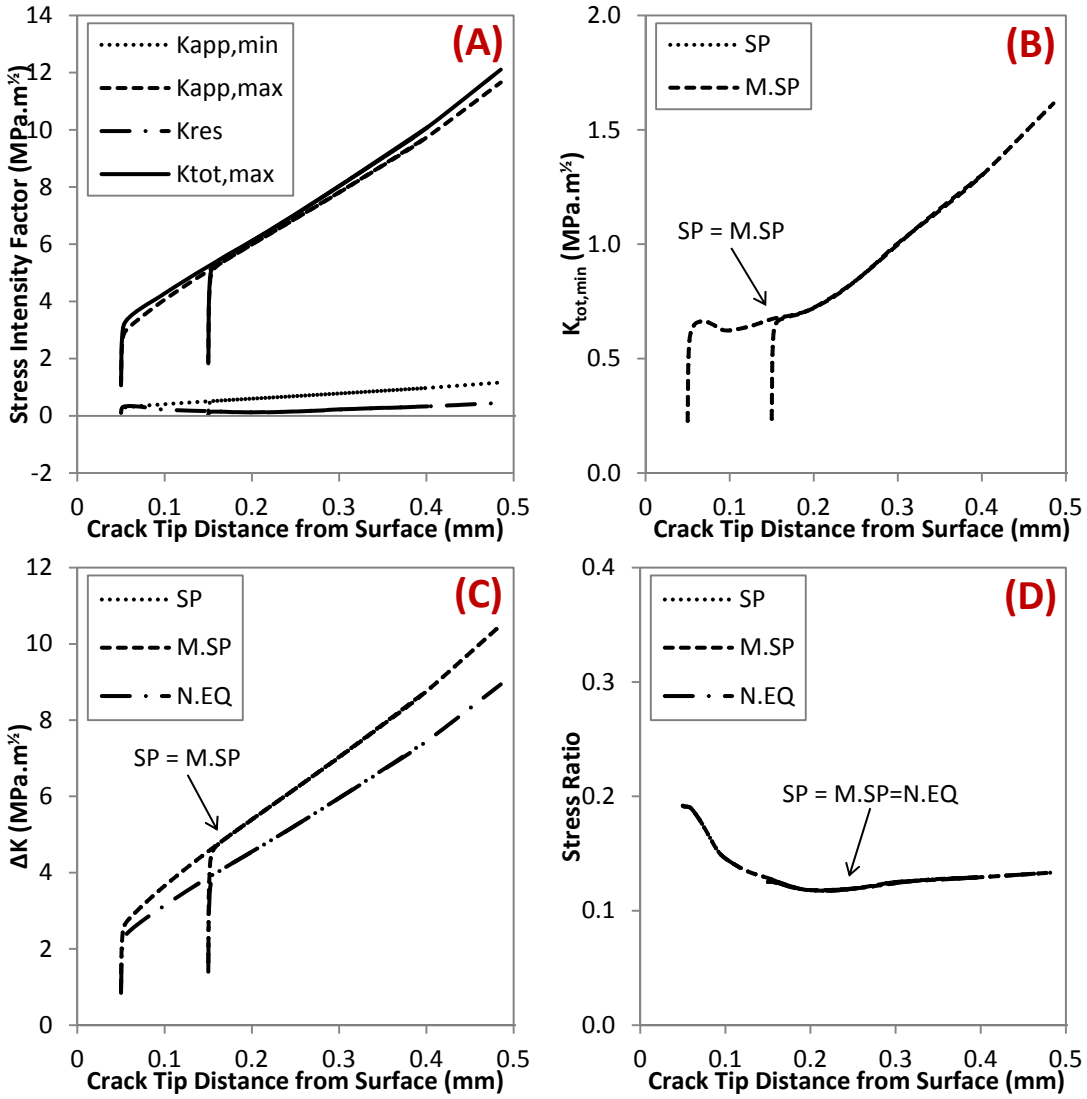

Figure 5.25: Results for MIC1 (A) stress intensity factors, (B) $K_{tot,min}$ for all methods, (C) ΔK for all methods and (D) stress ratio for all methods

The effect on SIF range and stress ratio of the MIC3 residual stress field is considered in Figure 5.26. The MIC3 residual stress field induced a K_{res} that was positive at the peened surface but became negative 166 µm from the peened surface, as described in section 5.7. Therefore $K_{tot,max}$ was greater than $K_{app,max}$ at crack tip positions less than 166 µm from the peened surface as shown in figure (A). At crack tip positions greater than 166 µm from the peened surface $K_{tot,max}$ was less than $K_{app,max}$. However the negative K_{res} values were not great enough to create negative $K_{tot,min}$ values. Therefore $K_{tot,min}$ calculated using the superposition and modified superposition methods was again equivalent as shown in figure (B) and therefore ΔK_{tot} was also equivalent for the two methods as shown in figure (C). The ΔK_{eff} is also shown in figure (C) and was less than ΔK_{tot}. Finally the R_{eff} was equivalent for all three methods as shown in figure (D).

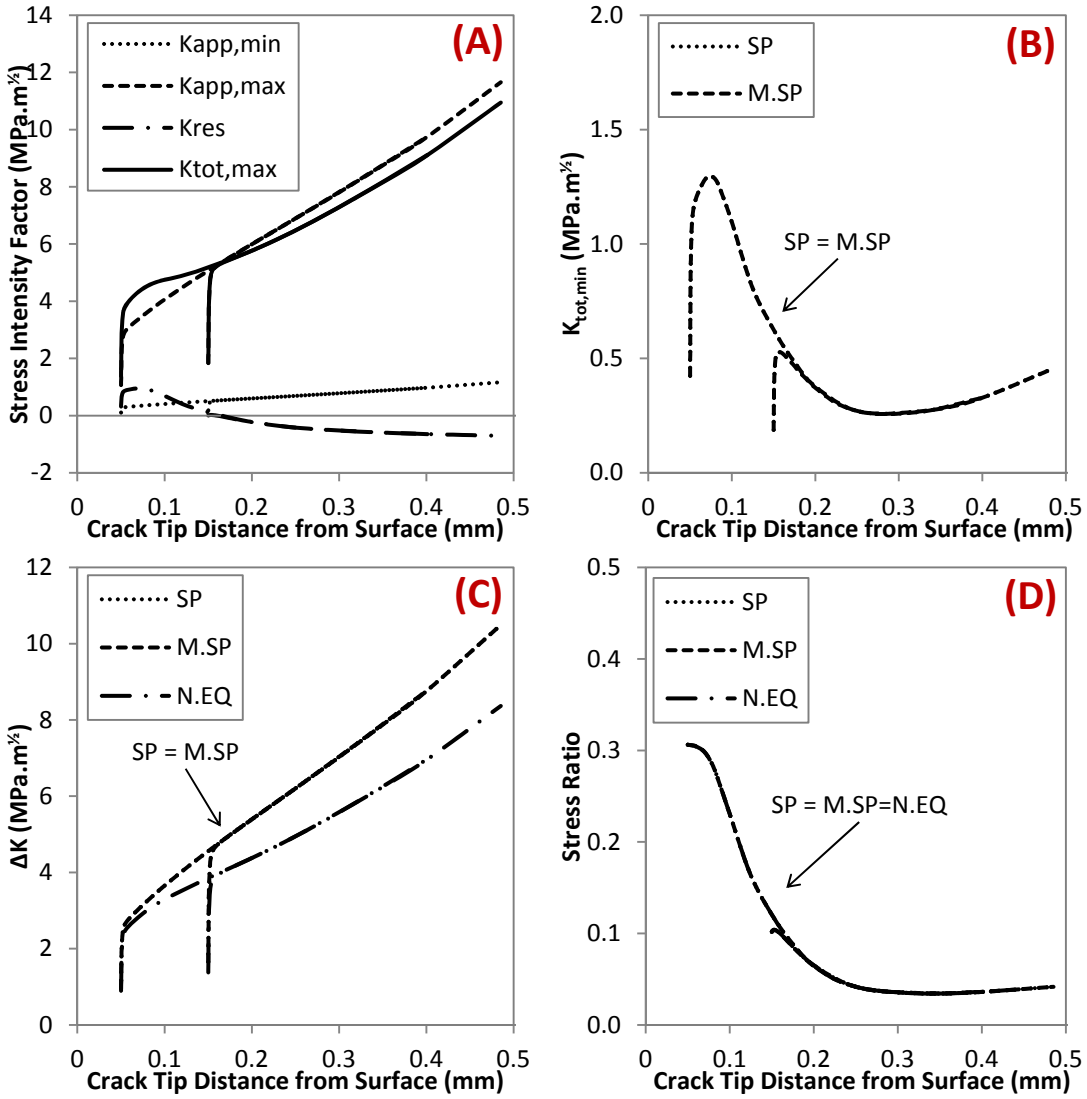

Figure 5.26: Results for MIC3 (A) stress intensity factors, (B) $K_{tot,min}$ for all methods, (C) ΔK for all methods and (D) stress ratio for all methods

The effect on SIF range and stress ratio of the UPM residual stress field is considered in Figure 5.27. The UPM residual stress field induced a K_{res} that was positive at the peened surface and became negative 85 µm from the peened surface as described in section 5.7. Therefore $K_{tot,max}$ was greater than $K_{app,max}$ at crack tips less than 85 µm from the peened surface as observed in figure (A). $K_{tot,max}$ was less than $K_{app,max}$ for crack tips greater than 85 µm from the peened surface. In this case the negative K_{res} was great enough to equate in negative $K_{tot,min}$ values at crack tips greater than 100 µm from the peened surface as shown in figure (B). Therefore ΔK_{tot} calculated using modified superposition was less than ΔK_{tot} calculated using superposition at crack tip positions greater than 100 µm from the peened surface as shown figure (C). The ΔK_{eff} was again less ΔK_{tot} due to predicted crack closure using Newman's equations. Finally R_{eff} was zero for modified superposition when $K_{tot,min}$ was zero as shown in figure (D).

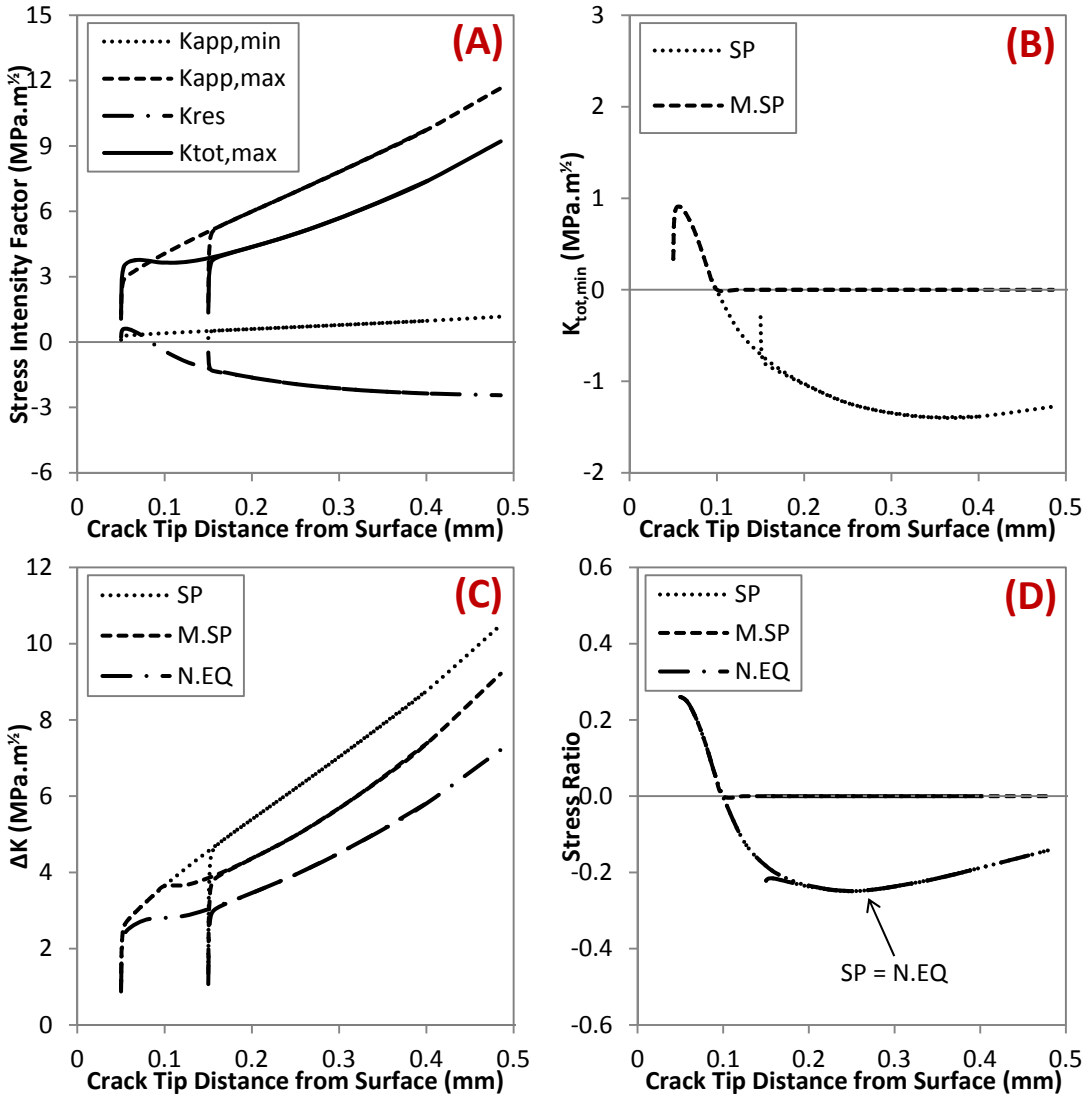

Figure 5.27: Results for UPM (A) stress intensity factors, (B) $K_{tot,min}$ for all methods, (C) ΔK for all methods and (D) stress ratio for all methods

The effect on SIF range and stress ratio of the TOSH residual stress field is considered in Figure 5.28. The TOSH residual stress field induced a negative K_{res} at all crack lengths calculated as described in section 5.7 and therefore $K_{tot,max}$ was less than $K_{app,max}$ as shown in figure (A). The negative K_{res} was great enough to create negative $K_{tot,min}$ at all crack tip distances from the peened surface as shown in figure (B). ΔK_{tot} calculated using modified superposition was less than ΔK_{tot} calculated using the superposition method as observed in figure (C). The ΔK_{eff} is also shown in figure (C) and was less than ΔK_{tot} due to the presence of crack closure. Finally R_{eff} was zero for modified superposition since $K_{tot,min}$ was zero as shown in figure (D).

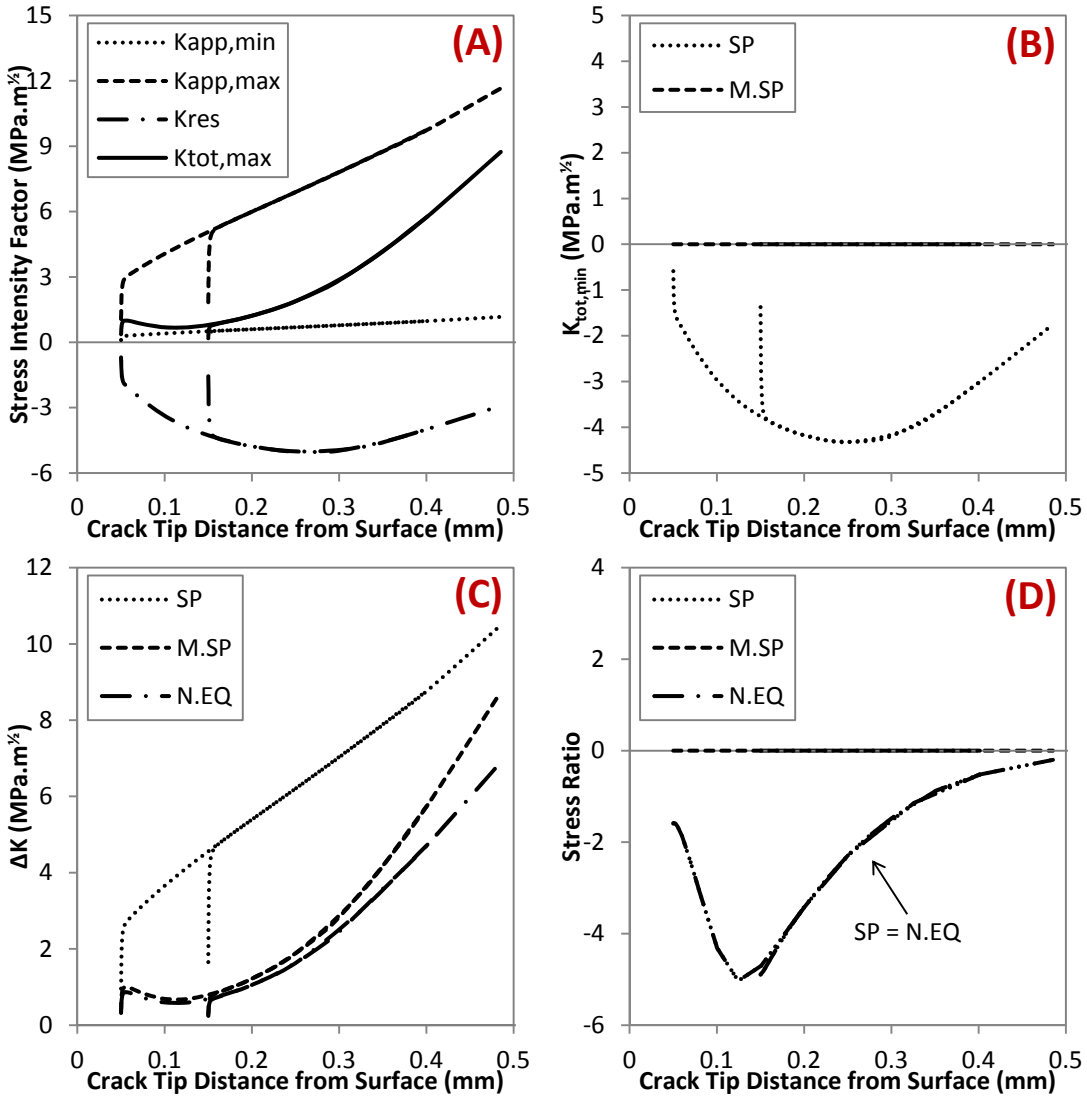

Figure 5.28: Results for TOSH (A) stress intensity factors, (B) $K_{tot,min}$ for all methods, (C) ΔK for all methods and (D) stress ratio for all methods

6 Effect of Residual Stress on Crack Closure

In this chapter the effect on fatigue crack closure of the LSP induced residual stress fields is investigated. In chapter 5 crack tip stress opening values were predicted using an elastic FE model combined with equations by Newman [59]. In this chapter an elastic-plastic FE model is developed that allows for direct calculation of applied stress opening values in a geometry representative of the dogbone shaped test specimens. In section 6.1 the methodology used to model crack closure using FE analysis is described. In section 6.2 the effect on the crack closure of the external applied loading only is reported. Finally the effect on crack closure of LSP induced residual stress combined with external applied loading is reported in section 6.3.

6.1 Crack Closure Finite Element Modelling Methodology

In this section modelling of PICC using the FE method is considered. FE analysis of PICC requires generation of a mesh containing an initial crack. The mesh is cycled between the maximum and minimum external applied stress. During the cyclic loading the crack is advanced in some fashion leading to the formation of a plastic wake behind the crack tip. Although conceptually simple there is however several issues related to FE modelling of PICC. These include: element choice, mesh refinement, material model, contact model, crack advance scheme, stabilisation of crack opening load and crack opening criteria. These issues are summarised and discussed in this section.

6.1.1 Element Selection

One of the first considerations of modelling of PICC is element selection. Higher order elements are generally considered to best capture the stress and strain field near the crack tip. However higher order elements demand greater computational effort and require many load steps due to the non-linearity of the analysis and therefore many early researchers used constant strain triangular elements (CST) [246-250]. With advances in computational power quadrilateral elements are now mainly used and good agreement has been found by many researchers [45,69,76,251,252,]. Some have even used higher order eight node elements to better capture the stress field around the crack tip [62,253-256]. Dougherty *et al.* [62] concluded the high gradient stresses induced in 8 node elements create an inaccurate opening displacement that may result in inaccurate opening stress levels.

When implementing plane strain conditions some additional element selection issues need to be considered. As stated most researchers used either CST elements, 4-noded quadrilateral elements, or higher order elements. Under in the plane-strain stress state these elements generally do not satisfy incompressibility requirements and are susceptible to plane-strain locking [257]. Element locking causes the stress to

oscillate from one element to the next. To avoid this issue constant strain triangular elements can be arranged in a union-jack configuration [257]. Alternatively simply using a reduced integration scheme for quadrilateral or CST elements can avoid plane-strain locking.

In the current analysis four node plane strain elements with reduced integration (CPE4R) were used. The mesh contained a total of 37960 elements. A comparative study between PICC in plane strain and plane stress is reported in subsequent sections. For the plane stress study four node plane stress elements with reduced integration (CPS4R) were used.

6.1.2 Mesh Refinement

Two types of crack tip plastic zone are generated by a propagating fatigue crack namely the forward plastic zone and the reversed plastic zone. The forward plastic zone is the material at the crack tip undergoing plastic yielding at the maximum applied load. The reversed plastic zone is the material near the crack tip undergoing compressive plastic yielding at the minimum load.

The mesh along the crack path must be sufficiently refined to capture the stress concentration at the crack tip and must be even finer to capture the reverse plastic zone size produced when unloading [258]. However extreme mesh refinement would lead to a large stiffness matrix and many degrees of freedom demanding long run times [259]. Furthermore, as the mesh size reduced the number of node release increments to advance the crack increases and so makes crack propagation studies more computationally intensive.

It has been found that for applied cyclic load the reversed plastic zone size is approximately ten times smaller than the forward plastic zone size formed during the loading [45,76]. Therefore a common parameter to determine appropriate mesh size is the ratio between element size and forward plastic zone size. The mesh refinement study was conducted for the external applied loading case only i.e. no residual stress was included in the model. The 50 µm notched geometry was used for the study as this would have the smallest plastic zone size. The minimum element size used was 0.002 mm.

6.1.3 Material Model

The elastic–perfect plastic material model has been used extensively in FE analysis of PICC. The effect of material hardening has also been considered assuming with kinematic and isotropic hardening used. Material hardening affects the crack tip plastic zone size and will therefore affect mesh refinement requirements.

Antunes *et al.* [254,260] studied isotropic, kinematic and combination models under plane stress conditions. Greater levels of closure were predicted using isotropic hardening models than for kinematic hardening models and was attributed to more significant plastic deformation for the isotropic hardening model. Predicted closure levels were closer to experimental values when the kinematic hardening model was used. Conversely Kamp *et al.* [261] reported no significant difference in predicted crack opening for an aluminium alloy using kinematic, isotropic or elastic-perfectly plastic models. Based on the results Kamp noted that hardening might not be the primary factor in PICC at least for the materials studied.

To reduce computational time it was desirable to use a single load cycle between crack advance steps. An elastic perfectly-plastic material model stabilises after one loading cycle whereas other material models can require further load cycles. For the current study an elastic-perfectly plastic material model was chosen and effects of material hardening on PICC were not considered. The following material properties of 2024-T351 aluminium were used in the analysis. Yield strength, σ_{yield} = 360 MPa, modulus of elasticity, E = 72 GPa, Poisson's ratio, ν = 0.3. No distinction between the clad and unclad material layers was made.

6.1.4 Crack Face Contact

To improve modelling efficiency it is often possible to model only half the geometry (or less) due to symmetry conitions. However this poses a problem since crack closure inherently requires two faces behind the crack tip to make contact as the minimum load is approached. Therefore some mechanism must be implemented into the FE analysis to simulate crack face contact. This can be achieved by attaching spring elements along the crack face, removing / imposing nodal constraints along the crack face, or by using contact based approach.

To model the contact boundary conditions using the spring element approach, spring elements are connected to the nodes along the crack path. At nodes where the crack is open the spring element stiffness is set equal to zero. At nodes where crack is closed the spring element stiffness is assigned a large value. However numerical difficulties were encountered by some researchers using this approach and was attributed to the large stiffness values imposed [45,262,263].

A more direct approach to simulate crack face contact has also been used [264-266]. During unloading the displacement of nodes along the crack face are monitored. If the displacement of the node becomes negative, relative to the crack tip the node, it is locked in position using boundary condition thus simulating contact. Conversely during loading the force acting on the nodes along the crack face are monitored and if it becomes positive the nodal boundary condition is released.

The use of contact elements probably offers a more realistic idealisation of PICC evolution however some authors have experienced convergence problems and long execution times [76]. Contact modelling involves implementing a hard contact boundary condition on the crack faces so as to avoid penetration.

The contact element approach was used for the current study. This was chosen as it was readily available and implemented using Abaqus. Although it has been reported to require more processing time than the other methods, the analysis can be run unmonitored until completion and was deemed the most suitable when a residual stress field is present.

The scribed test samples are symmetrical about the crack path and to increase modelling efficiency and reduce processing time one half of the geometry was modelled by use of symmetry boundary conditions. However for PICC to exist, two opposing crack surfaces are required. The approach used considered two surfaces called the slave surface and the master surface as depicted in Figure 6.1. The slave surface consisted of the nodes of the elements along the crack face i.e. on the modelled geometry. The master surface is an analytic surface created using 2D rigid shell elements. The master surface represents the opposing crack face i.e. the crack face of the geometry half that was not modelled. The master surface was non-deformable and therefore penetration of the master surface by the slave surface is not possible.

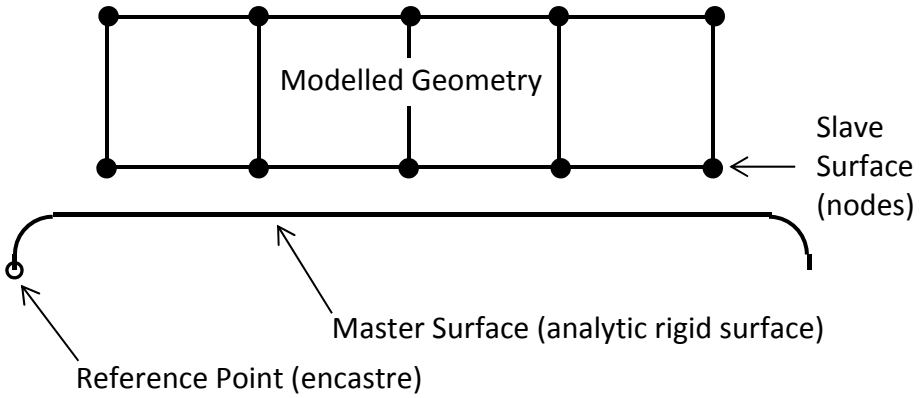

Figure 6.1: Schematic of contact model used in FE analysis

6.1.5 Crack Advance Scheme

To model the build up of a plastic wake behind the crack tip, the crack must be advanced incrementally using node release under the applied cyclic loading. There is no consensus on the appropriate FE mechanism for crack advance and various schemes are reported in the literature. Some authors release the node at the

maximum applied load [77,255,264,265], some at the minimum applied load [77,246,247,265] whilst others release nodes at some intermediate value [267,268]. Some researchers have concluded that crack advance scheme has no bearing on the predicted crack opening value [64,265] whilst other researchers have shown significant differences [45,77,262].

The influence of the number of cycles applied before node release has also been investigated [70]. For a 2D plane stress analysis the influence is small while for plane strain closure increased with increased cycles before crack advancement. The optimum number of cycles before node release was not determined however it was shown that after 8 cycles the change in opening stress level was minimal.

For the current research a node release scheme was implemented to advance the crack length and crack advance occurred at the maximum applied load. When the maximum applied load was reached, the symmetry boundary condition at the crack tip node was removed. The symmetry condition was replaced with a contact condition to prevent penetration of the new crack surface with the opposing crack surface (i.e. the master surface) during unloading.

Because contact boundary conditions were implemented in the FE model and LSP induced compressive residual stress fields may be present, crack advancement at the maximum load when the crack was most likely to be fully open was deemed the most suitable for the current work to avoid convergence problems. One load cycle was implemented between crack advance steps. Only the boundary conditions of the crack tip node were removed for each crack increment to allow the plastic wake to develop sufficiently.

The crack advanceme distance after each cycle was therefore equal to the crack tip element size. Modelling crack advanceme using a node release scheme bears no resemblance to fatigue crack growth i.e. no consideration of the physics of fatigue crack growth were made.

6.1.6 Crack Opening Assessment

Determination of precise crack opening or closing level has been debated [70,77,264]. Since the crack tip is normally the last point to open along the crack face most researchers use the first node behind the crack tip to assess the crack opening load [45,246-248,255,269] although others have used the second node behind the crack tip [264,270]. Using the second node can avoid the high stress gradient which can influence the first node during FE analysis. The crack tip itself was used to determine the crack opening value by Wu and Ellyin [77]. They monitored the stress at the tip node and deemed the crack open once the stress changed from compression to tension.

For the current research the second node behind the crack tip was chosen to compute the crack opening stress level although the first node was also monitored for reference. The criterion used to determine when the crack was open was to monitor the force acting on the node as the external applied tensile load was increased. Once the force acting on the node became zero the crack was considered open.

To assess the exact percentage of the applied load at which the crack can be considered fully open, the external load must incrementally applied and hence a high computational cost results. The applied external loading was increased from the minimum stress (20 MPa) to the maximum stress (200 MPa) in thirty increments of 6 MPa.

6.2 Plasticity Induced Crack Closure due to Applied Loading

In this section the model described in section 6.1 was used to study the plasticity induced crack closure that developed as the FE model was cycled between the maximum and minimum external applied stress. A fatigue crack was advanced at the maximum applied stress level using a node release scheme. Note: The effect of an initial residual stress field is not considered until section 6.3.

Shown in Figure 6.2 (A), (B), (C) and (D) is the crack opening displacement (COD) at the minimum applied stress (20 MPa) at cracks of length 100, 150, 200 and 250 µm respectively. A comparison was made between the COD profiles with and without crack face contact included in the FE model. Crack face contact clearly affected the COD profile. The COD profiles without contact indicate the crack was fully open at all lengths at the minimum applied stress and therefore throughout the entire applied load cycle. In the FE model with contact the crack was closed at minimum applied stress behind the tip of cracks of length of 100, 150 and 200 µm indicating PICC. However the crack was open at the minimum applied stress at a crack length of 250 µm as shown in Figure 6.2 (D).

As stated in section 6.1 for the crack to be considered open the force acting on the 2^{nd} node behind the crack tip must be zero. A crack was advanced from the root of scribe 50 and 150 µm deep using a node release scheme. The force on the 2^{nd} node behind the crack tip was monitored as the external applied stress was increased from the minimum (20 MPa) to the maximum (200 MPa).

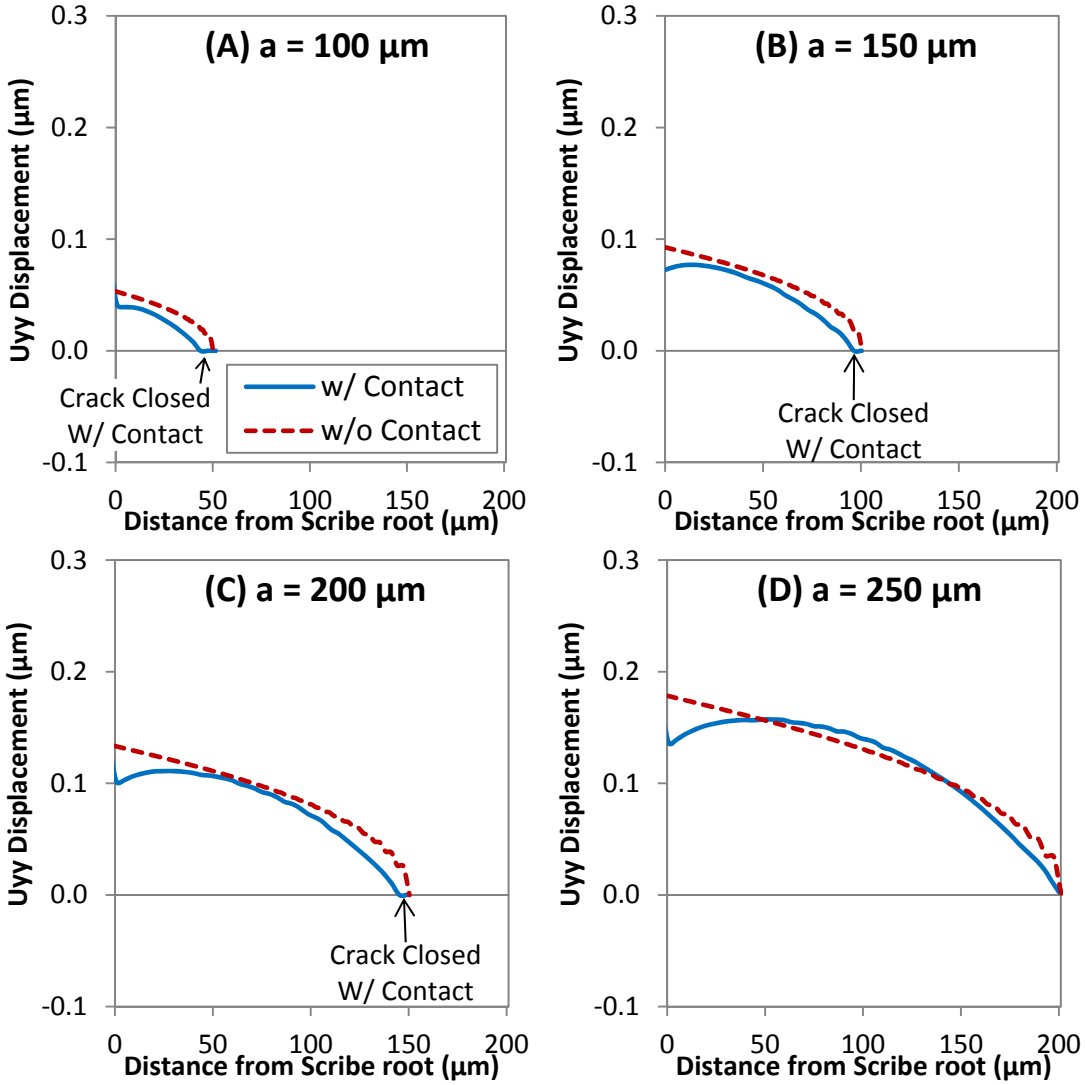

Figure 6.2: Crack opening displacement at minimum applied stress for cracks of length (A) 100 µm, (B) 150 µm, (C) 200 µm and (D) 250 µm

The crack closure level is plotted in Figure 6.3 as a percentage of the applied stress range that the crack is open i.e. 100% indicates that the crack is open during the entire applied load cycle whereas 0% indicates that the crack is closed for the entire load cycle. Firstly consider crack advanced from the scribe root 50 µm deep. Initially the crack was fully open throughout the entire load cycle. At crack lengths greater than 94 µm the closure level began to increase and between crack lengths of 115 and 139 µm the crack was open for 93% of the load cycle only. The closure level decreased at crack lengths greater than 139 µm and was open throughout the entire load cycle at crack lengths greater than 238 µm.

Now consider crack advance from the scribe 150 µm deep. The level of closure initially increased and the crack was open for only 83% of the load cycle at crack lengths between 154 and 170 µm. At crack lengths greater than 170 µm the closure

level reduced and at crack lengths greater than 195 µm the closure level predicted was equivalent to that predicted for crack advance from the scribe root 50 µm deep.

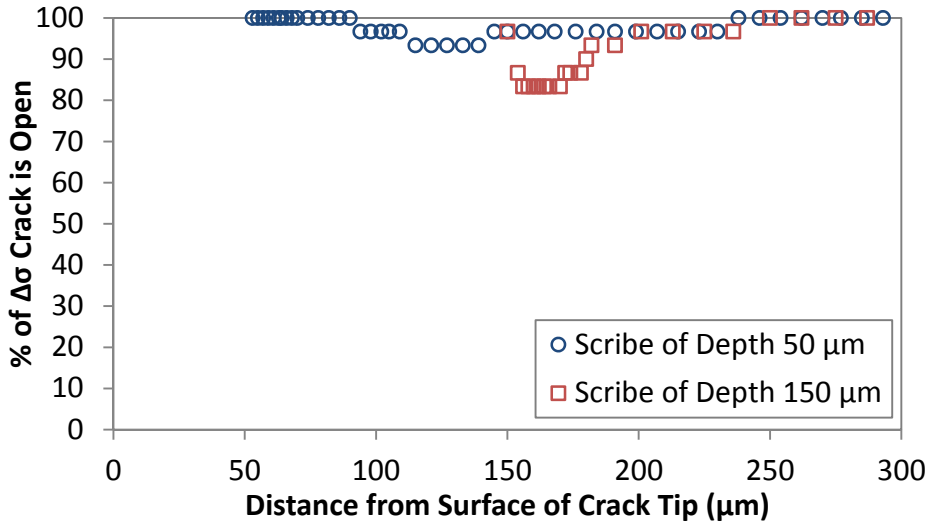

Figure 6.3: Predicted crack closure level of crack advanced from scribe root of depth 50 and 150 µm

6.2.1 Effect on PICC of Plane Strain and Plane Stress State

A comparison of the crack closure level under plane strain and plane stress conditions is shown in Figure 6.4. For the study a crack was advanced from a scribe of depth 50 µm. The crack closure level predicted for plane strain was less than for plane stress. This was expected as it has been well established that crack closure levels are less in plane strain than plane stress conditions, see section 2.3. It was predicated that the crack would remain open for 93% of the load cycle (at the peak closure level) in plane strain conditions whereas it would be open for only 63% of the load cycle in plane stress conditions.

The effect on the crack tip plastic zone of stress state at the maximum applied stress (200 MPa) is shown in Figure 6.5. Plastic zones at crack lengths of 50, 150 and 300 µm are shown. The plastic zone size is defined as the length of the plastic zone measured along the crack path. The plane stress plastic zone was approximately 9, 36 and 103 µm greater in length than the plane strain plastic zone at the tip of cracks of length 50, 150 and 300 µm respectively. A large forward plastic zone will induce a greater reversed plastic zone [271,272] hence why the crack remains closed through more of the applied load cycle in plane stress.

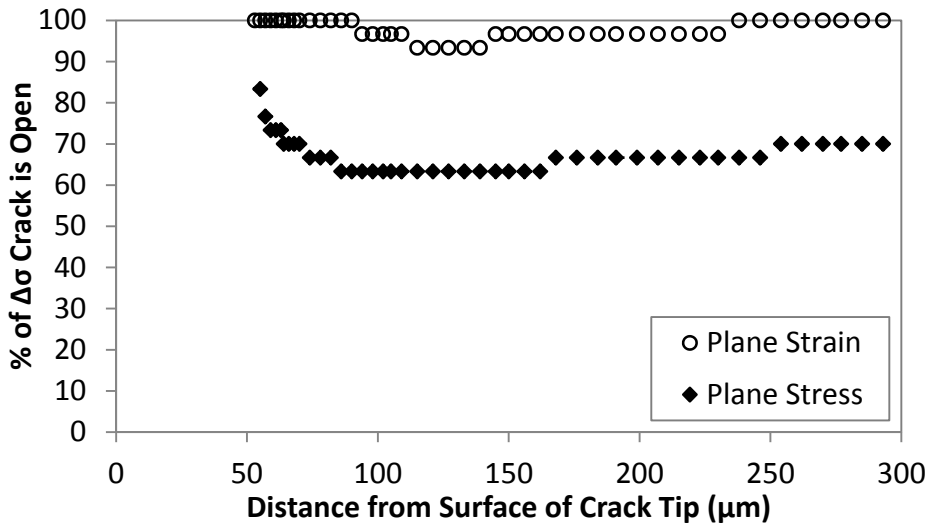

Figure 6.4: Predicted PICC using plane strain and plane stress elements in FE model

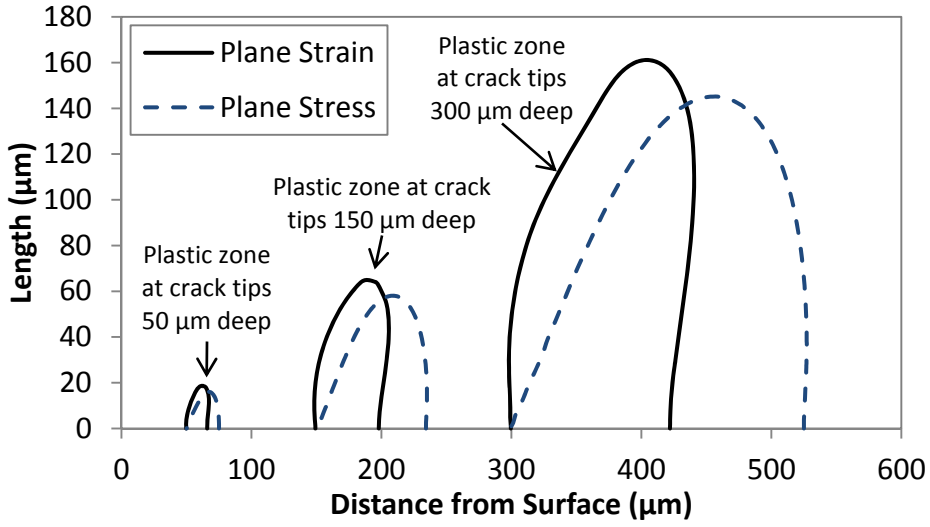

Figure 6.5: Comparison of plastic zone size for 2 mm and 5 mm thick geometries with a 50 µm crack length using plane strain and plane stress elements

6.2.2 Effect on PICC of Remaining Ligament Length

The predicted plane stress crack opening values in Figure 6.4 show a similar trend to those published in the literature [273,274]. During the initial crack length increments the crack closure level increased as the plastic wake built up due to cyclic plasticity. At a crack length of 86 µm the crack closure stabilized at 37% of the applied load cycle. However a notable feature of the predicted crack closure values in the current study are that the crack closure began to decrease at crack lengths greater than 156 µm (i.e. at a crack length of 250 µm the crack was closed for only 30% of the applied load cycle). This was most apparent for plane stress but can also be observed in Figure 6.4

for plane strain conditions where the crack closure level decreased at crack lengths greater than 139 µm.

It was envisaged that the reduction of crack closure at the longer crack lengths was due to the reducing ligament length (the ligament length is defined as the distance from the crack tip to the back surface). The effect on the plane strain and plane stress plastic zone size of remaining ligament length is shown in Figure 6.6 (A) and (B) respectively. In this study 2 mm wide geometry was compared with 5 mm wide geometry. The crack tip plastic zone at the maximum applied stress (200 MPa) at cracks of length 50, 150 and 300 µm is reported. The remaining ligament length was therefore 1.95, 1.85 and 1.7 mm for 2 mm wide geometry and 4.95, 4.85 and 4.7 mm for 5 mm wide geometry.

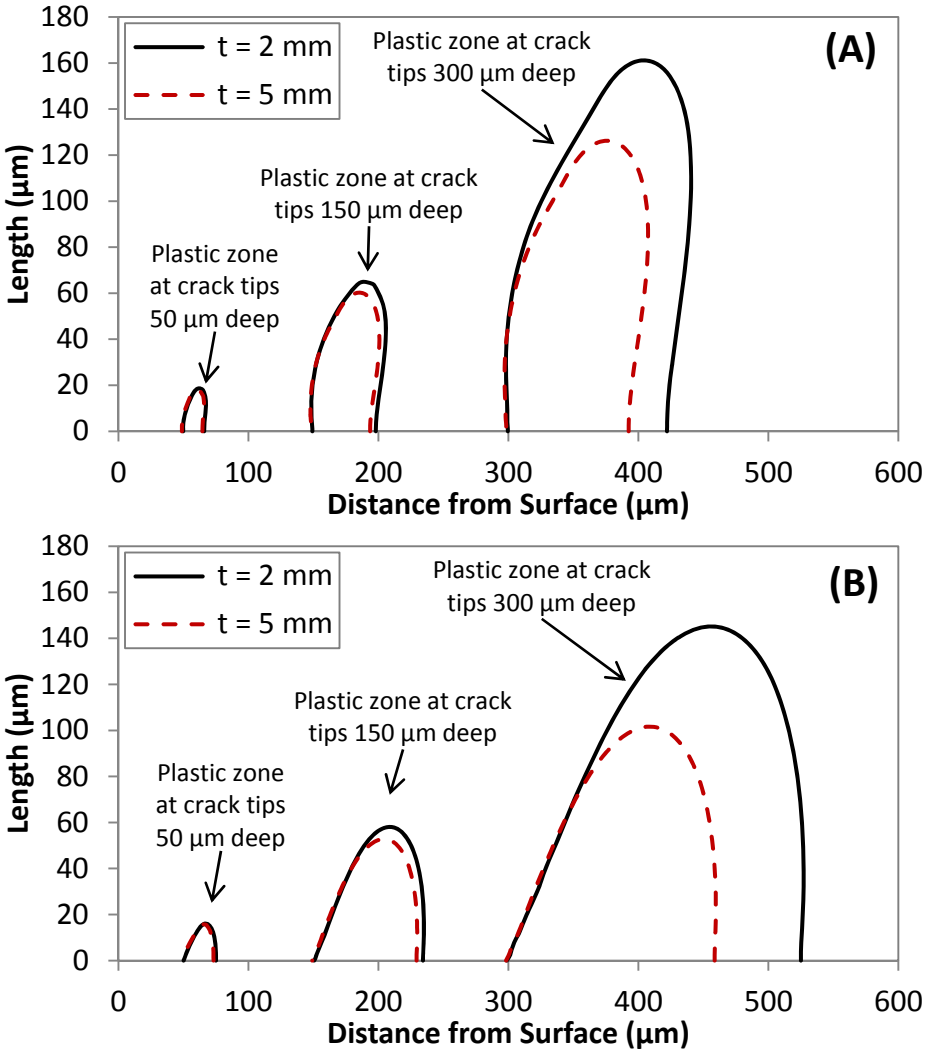

Figure 6.6: Crack tip plastic zones in 2 and 5 mm thick geometries for (A) plane strain and (B) plane stress states

The plane strain plastic zone at the tip of a crack of length 50 µm was 1 µm larger in 2 mm wide geometry than 5 mm wide geometry. The effect on the crack tip plastic zone of remaining ligament length increased at longer crack lengths. The plastic zone was 5 and 30 µm larger at the tip of cracks of length 150 and 300 µm respectively in the 2 mm wide geometry than in 5 mm geometry. Similarly the plane stress plastic zone was larger for the 2 mm wide geometry than the 5 mm wide geometry.

The effect on PICC of sample thickness is shown in Figure 6.7. It was found in both stress states that the crack closure level does not reduce at longer crack lengths in the 5 mm wide geometry. This demonstrates that the closure drop off observed for the 2 mm thick geometry was as a result of the remaining ligament length. Also observed in Figure 6.7 is that the crack closure level increased to it maximum at a shorter crack length in the 2 mm thick geometry than in the 5 mm wide geometry. In plane stress the maximum closure level was reached after 36 µm of crack advance in the 2 mm thick sample compared to 60 µm in the 5 mm wide sample. In plane stress the maximum was reached after 65 µm of crack advance in the 2 mm thick sample compared to 100 µm in the 5 mm wide sample. This may be caused by the larger forward plastic zone in the thinner samples thus a larger reversed plastic zone / plastic wake.

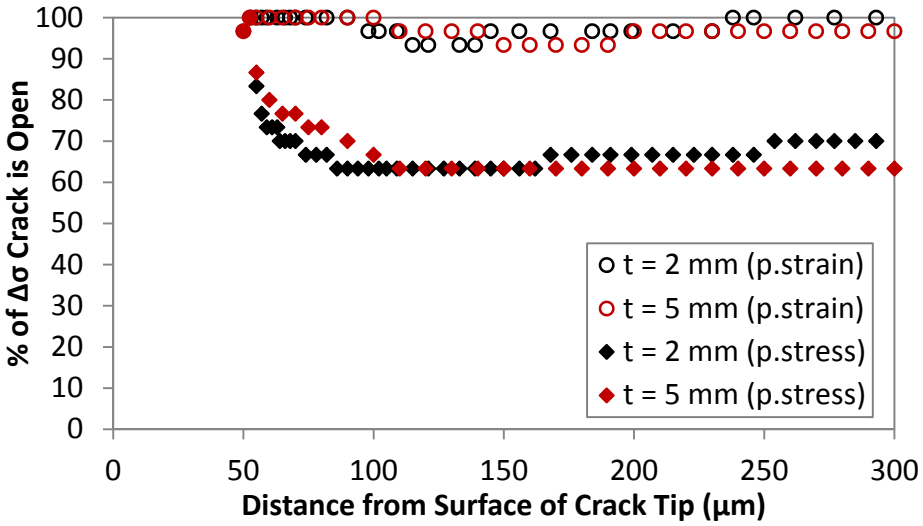

Figure 6.7: Comparison of the effect on PICC of specimen thickness

6.3 Effect on Crack Closure of Residual Stress Fields

The effect on crack closure of the measured residual stress fields is reported in this section. The FE contact model for the analysis without initial residual stress from section 6.2 was used but this time with the inclusion of residual stress fields. The residual stress fields were input to the FE model during the first analysis step prior to boundary and load conditions as described in section 5.4.

The effect on the crack opening displacement (COD) of the MIC1 residual stress field at the minimum applied stress level (20 MPa) is shown in Figure 6.8 (a), (b), (c) and (d) at cracks of length of 100, 150, 200 and 250 µm respectively. A comparison between the COD with and without crack face contact is shown in Figure 6.8. For the case without contact the crack was open at all crack lengths studied. With contact the crack was closed behind the crack tip at a crack length of 150 µm as shown in Figure 6.8 (b). At the the other crack lengths studied the crack was open at the minimum applied load.

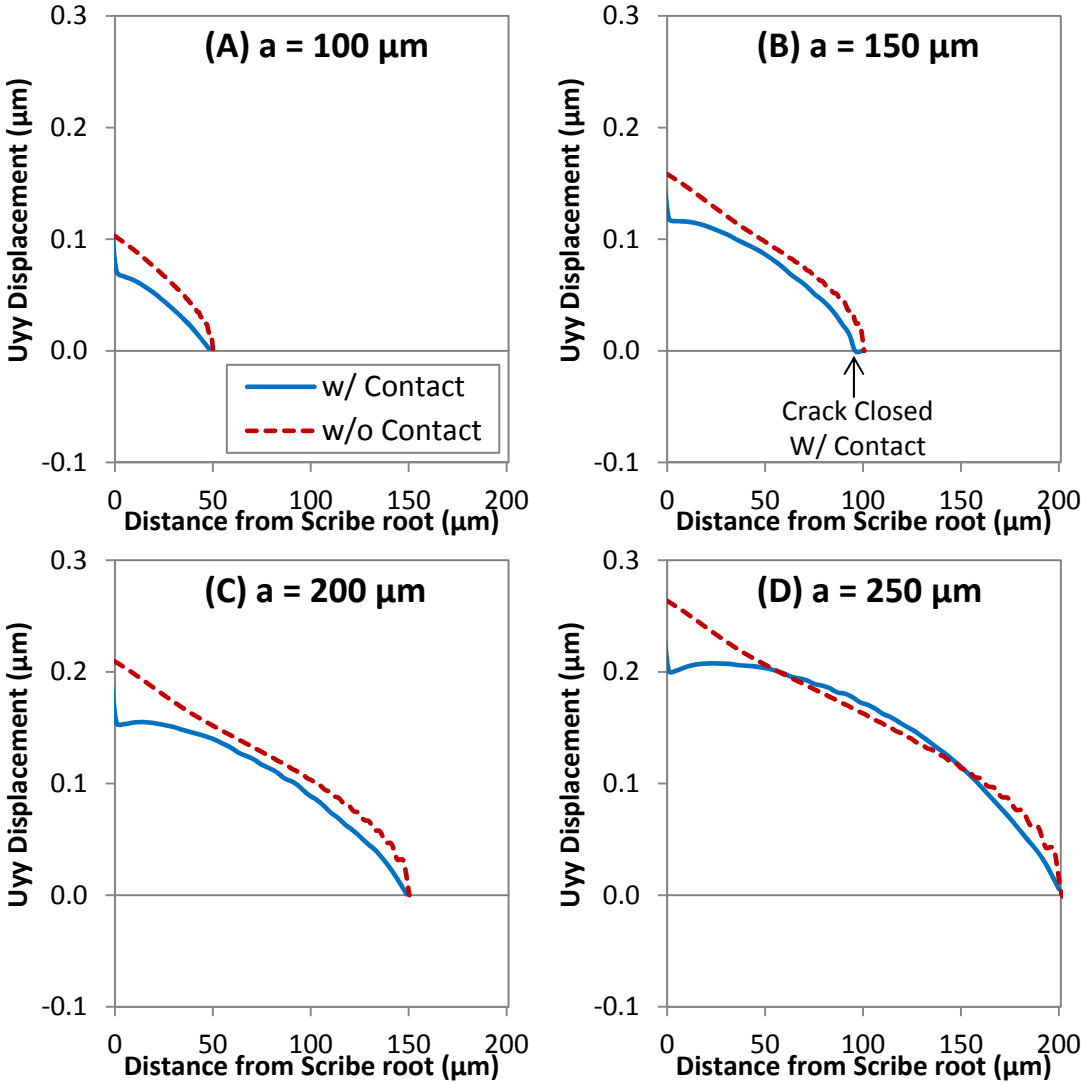

Figure 6.8: Effect on COD of MIC1 residual stress field at minimum applied stress at cracks of length (A) 100 µm, (B) 150 µm, (C) 200 µm and (D) 250 µm

The percentage of the applied stress range that the crack was open is shown in Figure 6.9 again noting that 100% indicates the crack is fully open during the entire applied load cycle whereas 0% indicates the crack is fully closed throughout the load cycle. The MIC1 measured residual stress field is also shown in the figure for comparison.

Firstly considering the crack advanced from the scribe root 50 µm deep, initially the crack was fully open however at crack lengths greater than 115 µm the closure level increased and the crack was open for 97% of the load cycle only. The level of closure decreased at crack length of 156 µm and was fully open throughout the applied load cycle at crack lengths greater than this. The crack advanced from the scribe root 150 µm deep was fully open throughout the load cycle at all crack lengths studied.

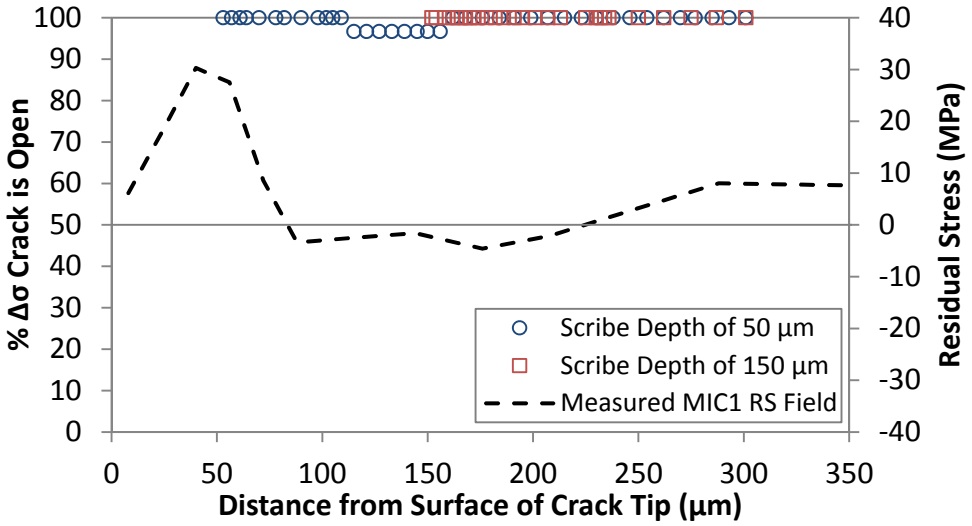

Figure 6.9: Effect on crack closure of MIC1 residual stress field

The effect on the crack opening displacement (COD) of the MIC3 residual stress field at the minimum applied stress level is shown in Figure 6.10. The effect of crack face contact in the FE analysis was compared at four crack lengths: 100, 150, 200 and 250 µm. At the four crack lengths studied, the crack was fully open at the minimum applied stress with and without contact. However the COD was less with contact included in the FE analysis than without. The percentage of the applied stress range that the crack was open is shown in Figure 6.11. The cracks advanced from the scribe roots 50 and 150 µm deep were fully open throughout the entire load cycle i.e. no closure existed.

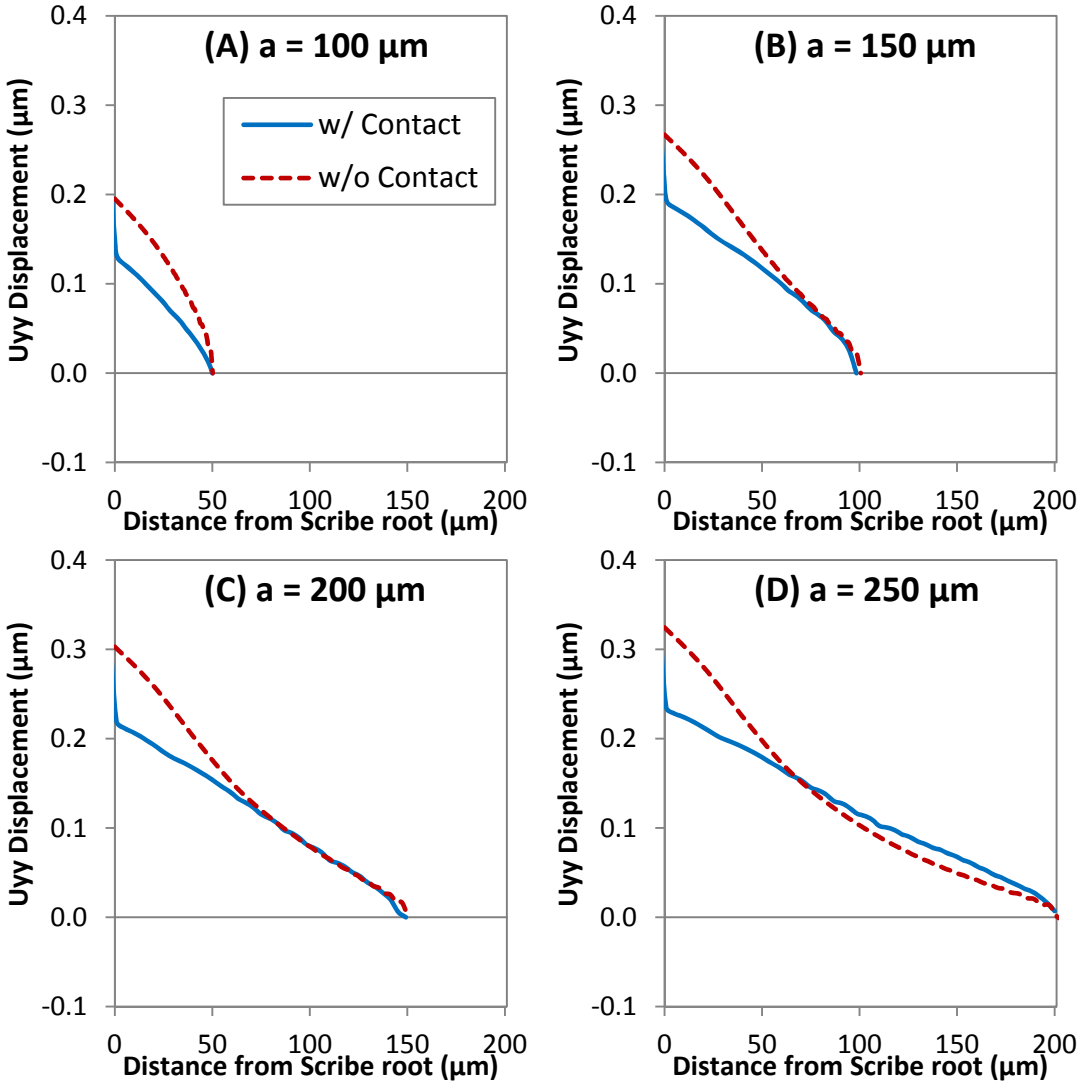

Figure 6.10: Effect on COD of MIC3 residual stress field at minimum applied stress at cracks of length (A) 100 µm, (B) 150 µm, (C) 200 µm and (D) 250 µm

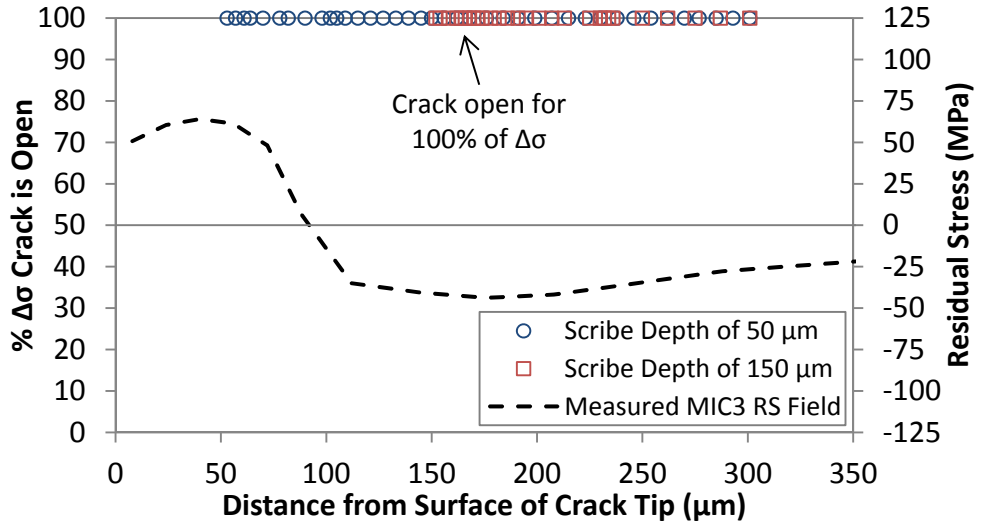

Figure 6.11: Effect on crack closure of MIC3 residual stress field

The effect on COD of the UPM residual stress field at the minimum applied stress level is shown in Figure 6.12 (a), (b), (c) and (d) at crack lengths of 100, 150, 200 and 250 µm respectively. The effect of crack face contact in the FE analysis was compared. For the case without contact the crack faces overlap, this is most noticeable in 150, 200 and 250 µm however also occurred at a crack length of 100 µm. For the case with contact the crack is closed directly behind the crack tip but open in the region near the scribe root. The UPM residual stress field had near surface tensile residual stress and this caused the crack to remain open near to the surface.

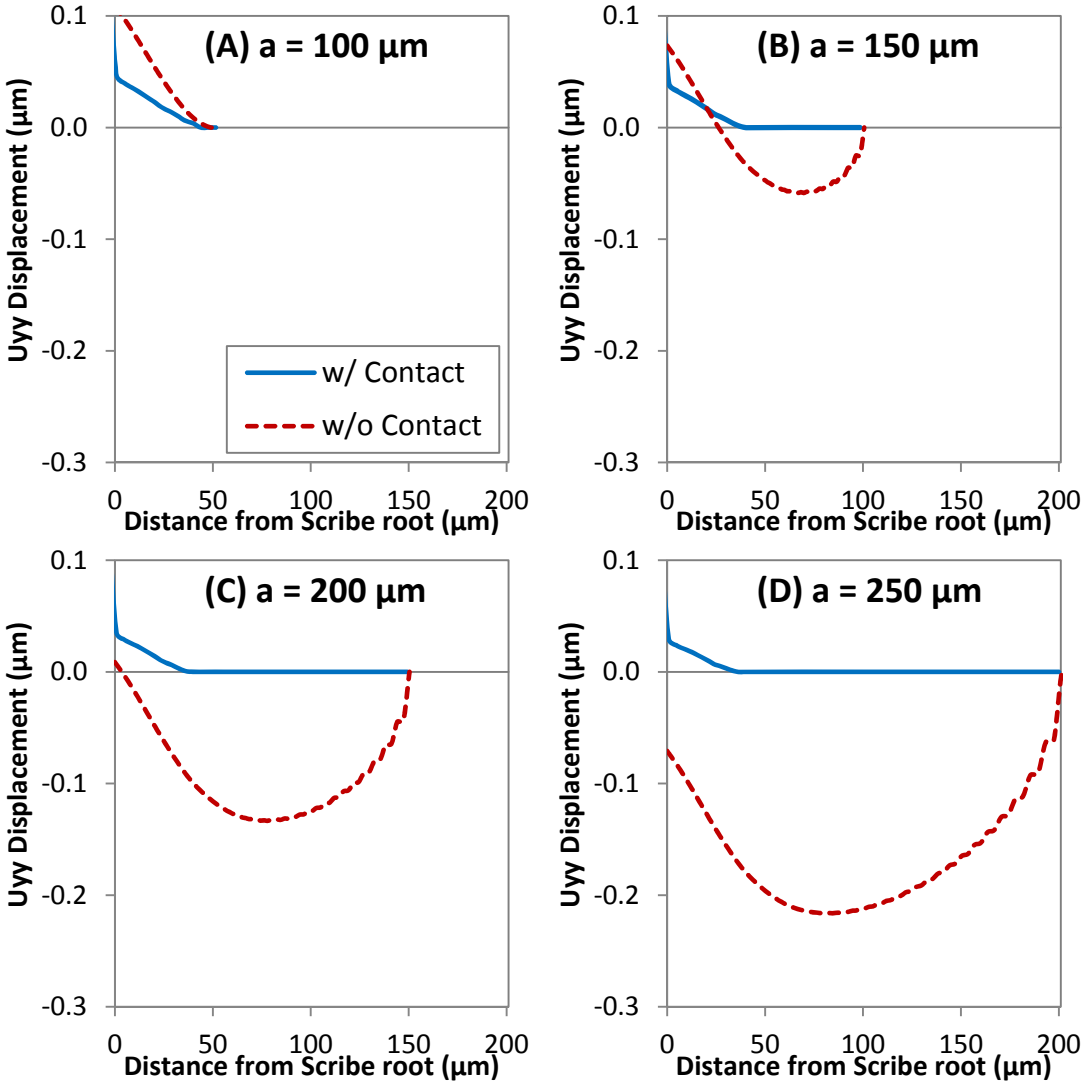

Figure 6.12: Effect on COD of UPM residual stress field at minimum applied stress at cracks of length (A) 100 µm, (B) 150 µm, (C) 200 µm and (D) 250 µm

The COD at the applied stress to cause the crack to open behind the tip is shown in Figure 6.13 (a), (b), (c) and (d) at crack lengths of 100, 150, 200 and 250 µm respectively. The COD profiles are for the FE model with contact only. The percentage of the applied stress range that the crack was open is shown in Figure 6.14. The UPM

measured residual stress field is also shown in the figure for comparison. Firstly considering the crack advanced from the scribe root 50 µm deep, initially the crack was fully open throughout the applied load cycle due to the near surface tensile residual stress. For crack length greater than 90 µm the closure level increased due to the compressive residual stress field. At a crack length of 162 µm the crack was open for 77% of the applied loading cycle and remained approximately at this level as the crack was advanced. The closure level of the crack advanced from the scribe root 150 µm deep increased quickly due to the compressive residual stress field and at a crack length of 158 µm the crack was open for 73% of the load cycle. At a crack length of 176 µm the closure level decreased marginally and the closure behaviour of the cracks advanced from the 50 µm and 150 µm scribe root was equivalent.

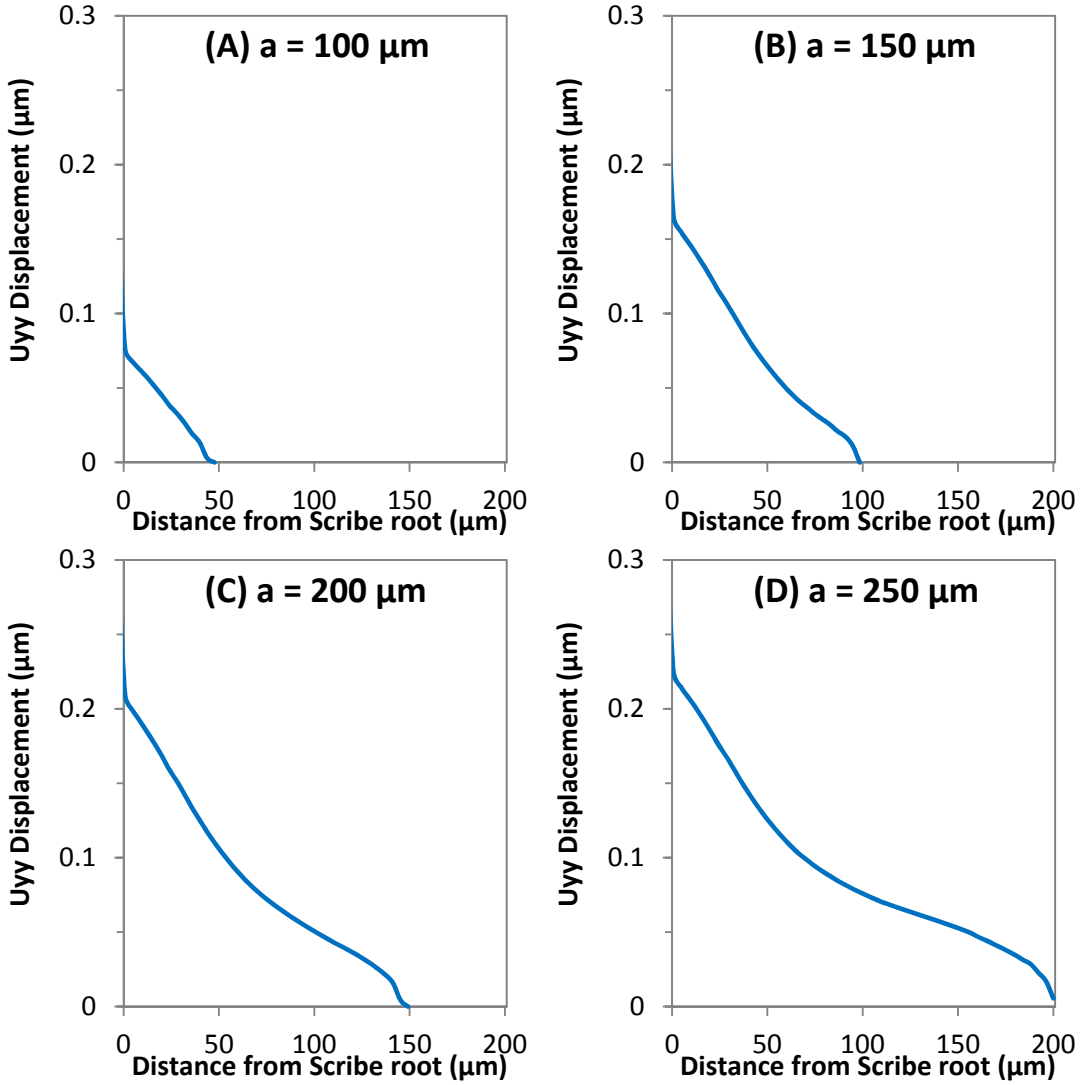

Figure 6.13 Effect on COD of UPM residual stress field at minimum applied stress to open crack behind tip at lengths (A) 100 µm, (B) 150 µm, (C) 200 µm and (D) 250 µm

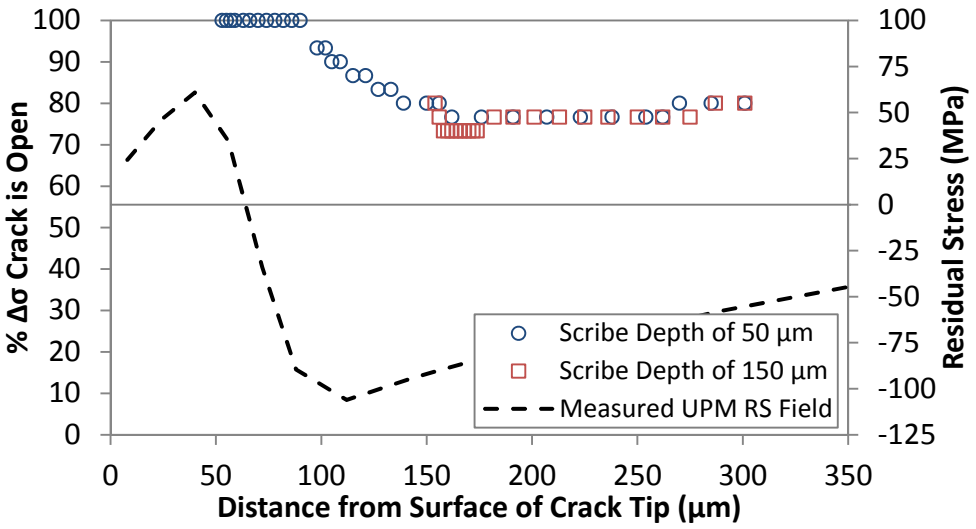

Figure 6.14: Effect on crack closure of UPM residual stress field

The effect on COD of the TOSH residual stress field at the minimum applied stress level is shown in Figure 6.15 (a), (b), (c) and (d) at crack lengths of 100, 150, 200 and 250 µm respectively. The effect of crack face contact in the FE analysis was compared. For the case without contact the crack faces overlap. For the case with contact the crack is fully closed behind the crack tip noting that the TOSH compressive residual stress field extended 340 µm from the surface where it then became tensile.

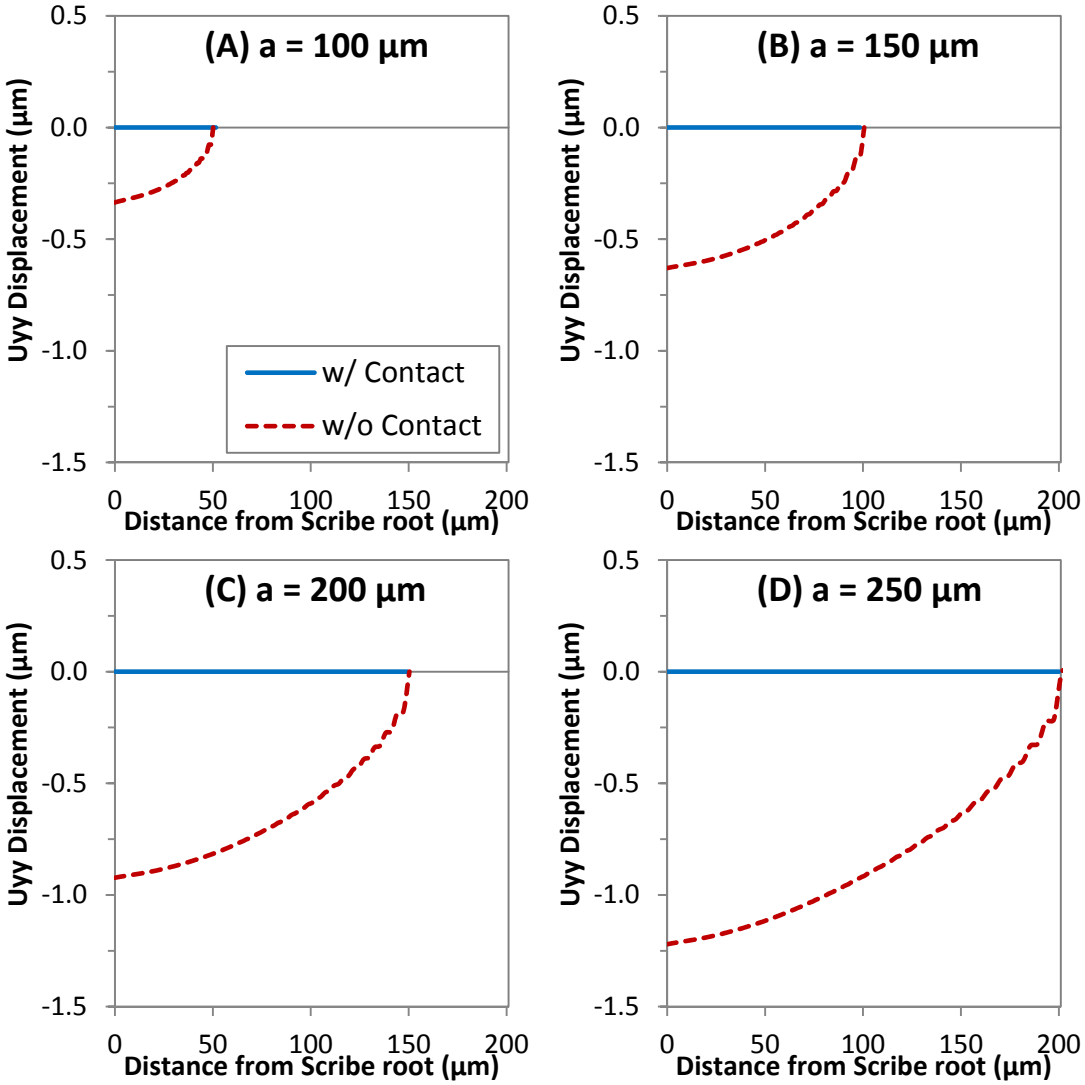

Figure 6.15: Effect on COD of TOSH residual stress field at minimum applied stress at cracks of length (A) 100 µm, (B) 150 µm, (C) 200 µm and (D) 250 µm

The at the applied stress required to first open the crack behind the tip is shown in Figure 6.16 (a), (b), (c) and (d) at crack lengths of 100, 150, 200 and 250 µm respectively. The COD is from the FE analysis with contact. At lengths of 100 and 150 µm the crack was fully open behind the crack tip, shown in (a) and (b). However at lengths of 200 and 250 µm the crack was open at the crack tip but closed remote from the tip and open again near the scribe root. This remote crack closure was caused by the profile of the compressive residual stress field as shown in Figure 6.17. The magnitude of the residual compressive stress increased from the surface to a maximum at 100 µm.

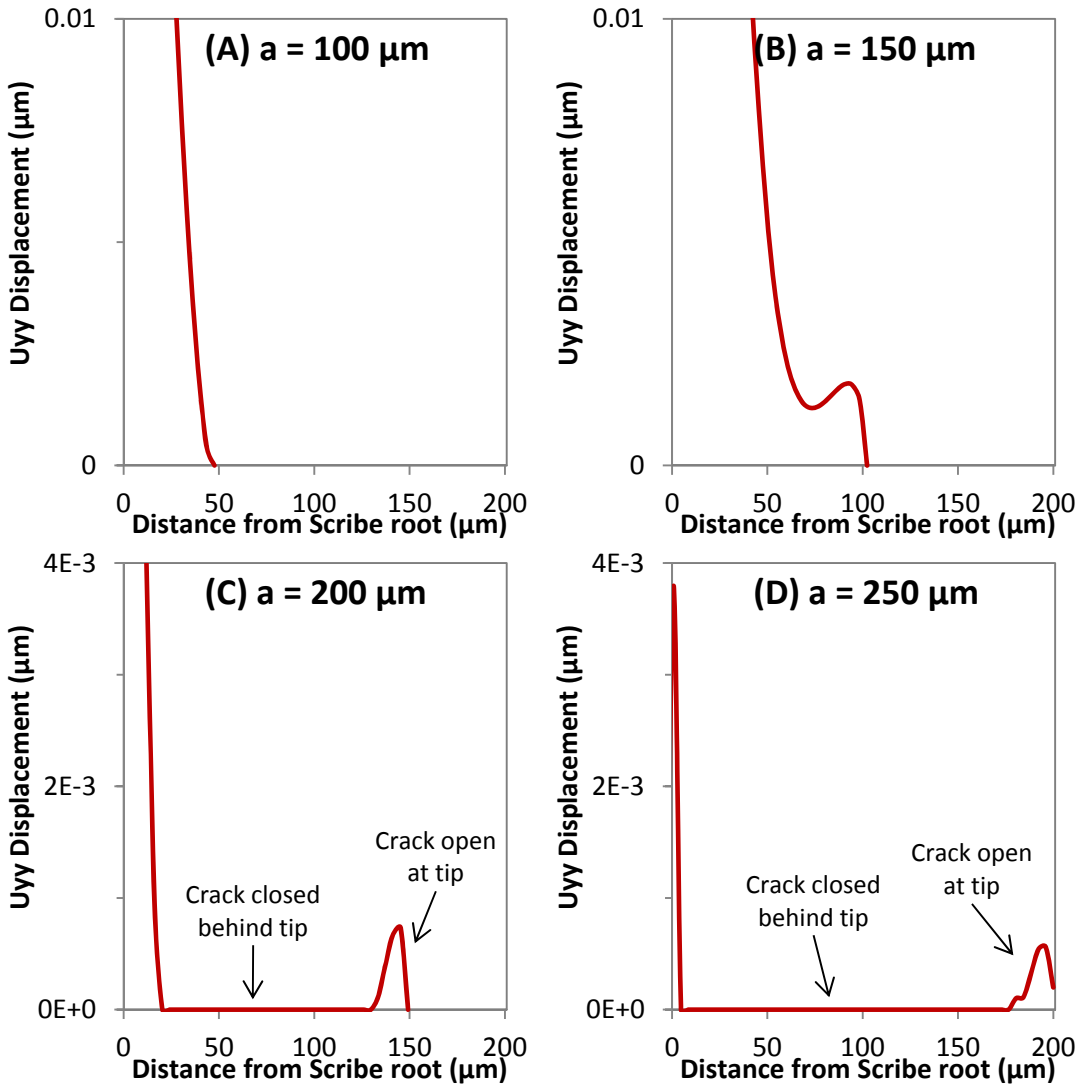

Figure 6.16: Effect on COD of Tosh residual stress field at minimum applied stress to open crack behind tip at lengths (A) 100 µm, (B) 150 µm, (C) 200 µm and (D) 250 µm

The percentage of the applied stress range that the crack was open is shown in Figure 6.17. A crack was advanced from the root of scribes of depth 50 µm and 150 µm. For both scribes as the crack was advanced from the root the closure level initially increased, peaked and then decreased. It can be seen in the Figure 6.17 that the closure level followed a similar trend to that of residual stress field. However an interesting feature is the delayed response of crack closure to the changing residual stress field. For example the maximum compressive residual stress was located 100 µm from the surface but the closure level reached a maximum approximately 145 µm from the surface where the crack was open for only 17% of the applied load cycle. The maximum closure level reached for the crack advanced from the scribe 150 deep 30% of the applied load cycle at a crack length of 186 µm. At crack length greater than this the closure level was equivalent for cracks advanced from both 50 and 150 µm deep scribes.

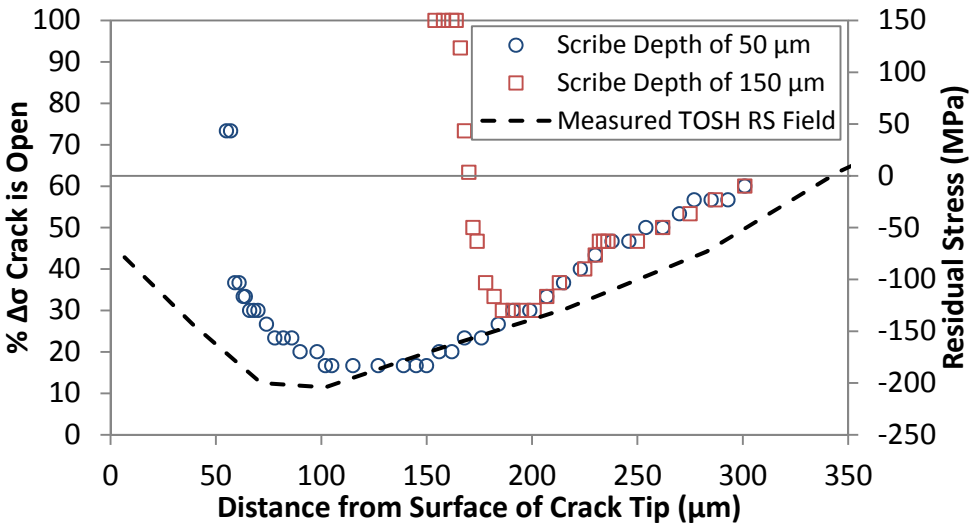

Figure 6.17: Effect on crack closure of TOSH residual stress field

6.3.1 Crack Closure caused by Plasticity or Residual Stress

To study whether the crack closure was caused by plasticity or the residual stress field, a crack closure analysis that used elastic material properties in the FE model was developed. Since the material was elastic no plastic wake can build up behind the crack tip with crack advance and therefore there is no PICC. Shown in Figure 6.18 is the percentage of the applied stress range that the crack was open at the minimum applied stress where (A) is a crack advanced from a scribe 50 µm deep and through the UPM residual stress field and (B) is a crack advanced through the TOSH residual stress field. The result of analyses with elastic and elastic-plastic material properties is compared.

Crack closure was present even in the analysis that used elastic material properties. In this instance crack closure is solely due to the compressive residual stress field. Considering the crack advanced through the UPM residual stress field shown in figure (A), the crack closure level was greater when elastic-plastic material properties were used and this was attributed to the plastic wake. At the maximum closure level the crack was open for 77% of the load cycle in elastic-plastic material and 80% of the load cycle in the elastic material.

The crack advanced through the TOSH residual stress field is shown in figure (B). At crack lengths less than 238 µm the closure level in elastic and in elastic-plastic material was identical. This indicated that crack closure was solely due to the compressive residual stress field even in the elastic-plastic material. The reason no PICC existed was because the compressive residual stress was great enough keep the crack closed and reduce the amount of plastically deformed material left behind the advancing crack. At crack lengths greater than 238 µm where the compressive

residual stress was significantly less, the closure level was greater in elastic-plastic material than in elastic material.

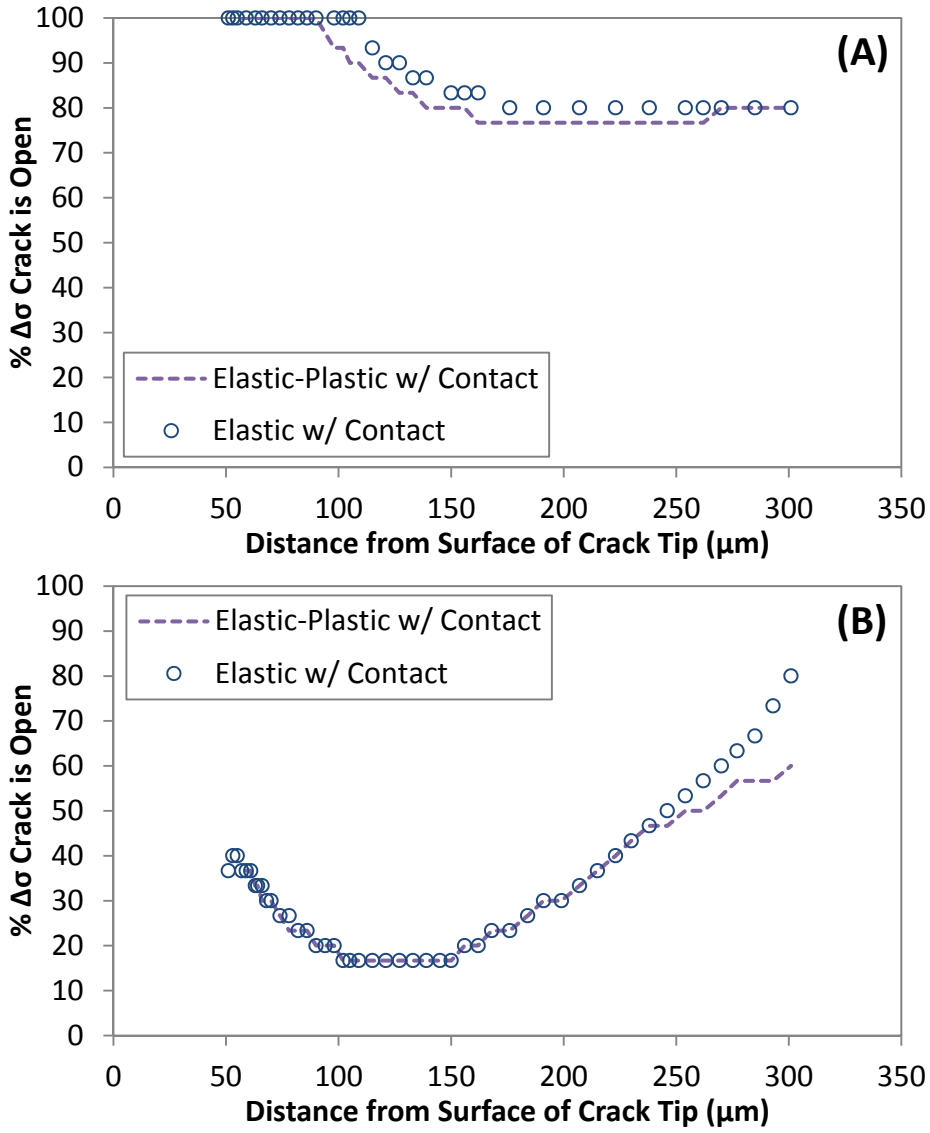

Figure 6.18: Effect on crack closure of elastic and elastic-plastic material properties in (A) UPM RS field and (B) TOSH RS field

6.3.2 Effect on Crack Closure of Tension and Bending Applied Loading

The effect on crack closure of pure bending external applied loading was considered. In pure bending at the maximum applied load the stress on the notched / peened surface was 200 MPa in tension and reduced linearly to 200 MPa in compression on back surface. The stress ratio was 0.1. Shown in Figure 6.19 is the percentage of the applied stress range that the crack was open at the minimum applied stress where (A) was the case of external applied loading only, (B) was crack advance through the UPM residual stress field and (C) was crack advance through the TOSH residual stress field.

Firstly consider the case without residual stress in figure (A). The crack closure level was slightly less under pure bending than tensile applied stress. In bending the applied stress range experienced at the crack tip will reduce as the crack is advanced. Therefore the forward plastic zone will be smaller in bending than tension and so the build-up of the plastic wake behind the crack tip is less.

In contrast crack closure was greater in bending than tension applied loading when the crack was advanced through the UPM and TOSH residual stress fields as shown in figure (B) and (C) respectively. This is because of the lower stress intensity factor at the crack tip induced by bend applied loading than tension. Since the stress intensity factor is less the compressive residual stress had a greater effect on increasing crack closure.

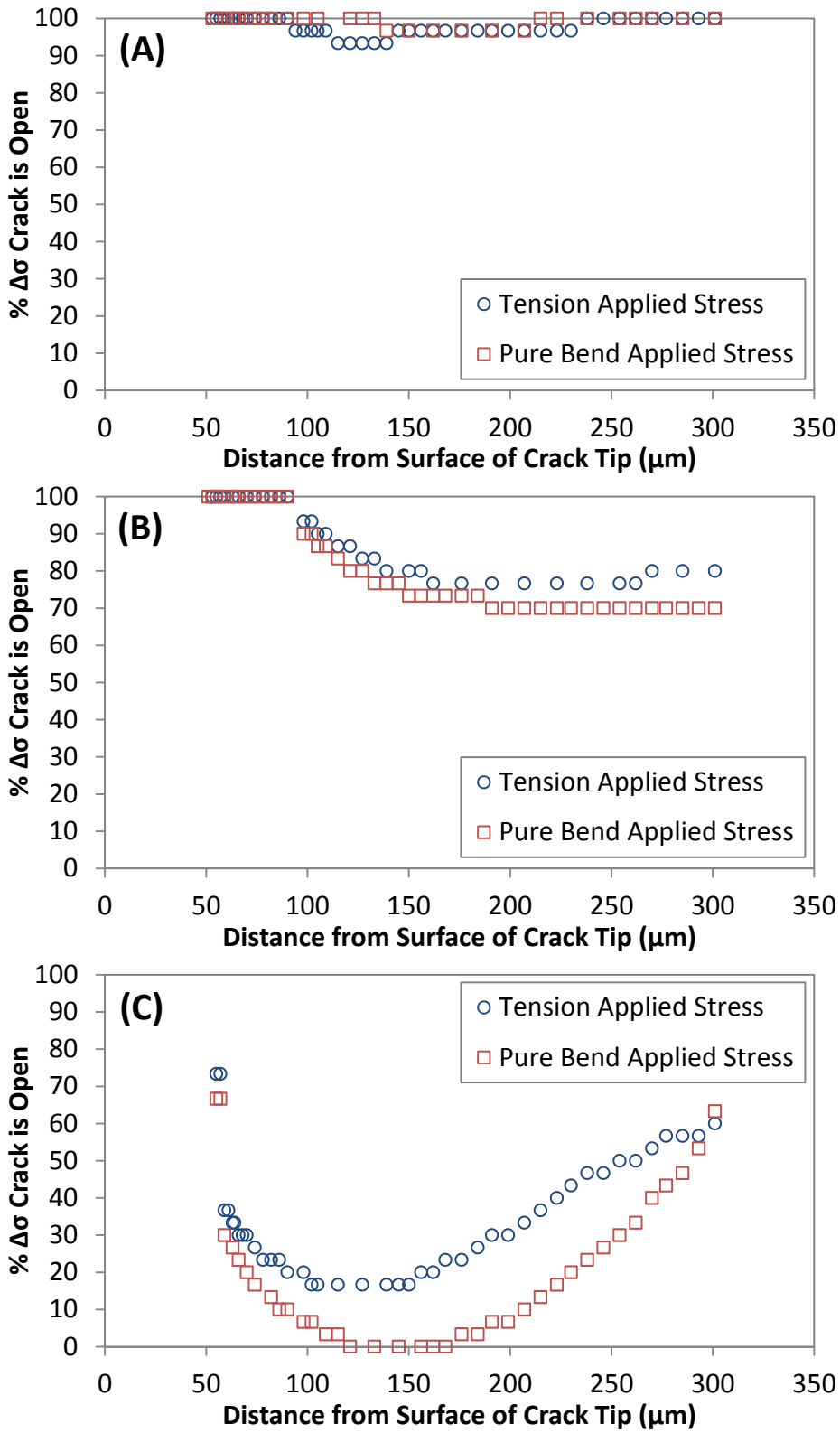

Figure 6.19: Effect on crack closure of (A) bend external applied stress only, (B) bend applied stress and UPM RS field and (C) bend applied stress and TOSH RS field

7 Effect on Fatigue Life of Residual Stress Fields Induced by LSP

The effect on fatigue life of the LSP induced residual stress fields is reported in this chapter. The stress intensity factors and stress ratios calculated using the FE method in chapter 5 were used as input to FCGR equations. Fatigue lives were predicted for scribed models unpeened and with MIC1, MIC3, UPM and TOSH residual stress fields. Also the fatigue crack closure ratios predicted using an elastic plastic FE model in chapter 6 were used to modify the Newman crack closure equations and predict fatigue lives. Predicted fatigue lives are compared to the fatigue lives measured experimentally from chapter 4.

In section two the methodology used in a sensitivity study on fatigue life of residual stress is described. The sensitivity study defined characteristic features of the residual stress fields and investigated the effect of these characteristics on predicted lives. In section three the results of the sensitivity study are reported and recommendations are given for the required residual stress field to restore the fatigue of scribed samples back to that of pristine material.

7.1 Fatigue Life Predictions

In this section the fatigue lives predicted for unpeened and peened samples containing scribes 50 µm and 150 µm deep are reported. In section 5.8 three methodologies to determine the stress intensity factor range (ΔK) and the stress ratio (R) were defined namely the superposition method, the modified superposition method, and the Newman crack closure approach. The calculated ΔK and R values using the three methodologies are reported here again for convenience respectively in Figure 7.1, Figure 7.2 and Figure 7.3. The fatigue lives predicted in this section were based on these calculated ΔK and R values.

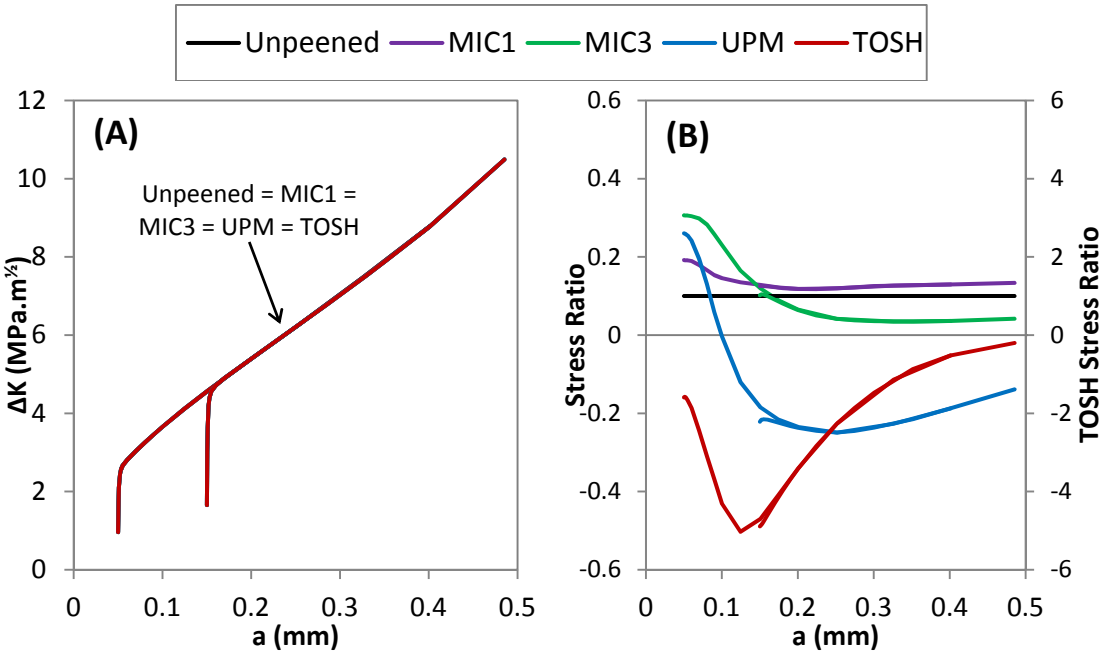

Figure 7.1: (A) Stress intensity factor range and (B) stress ratio calculated using the superposition method

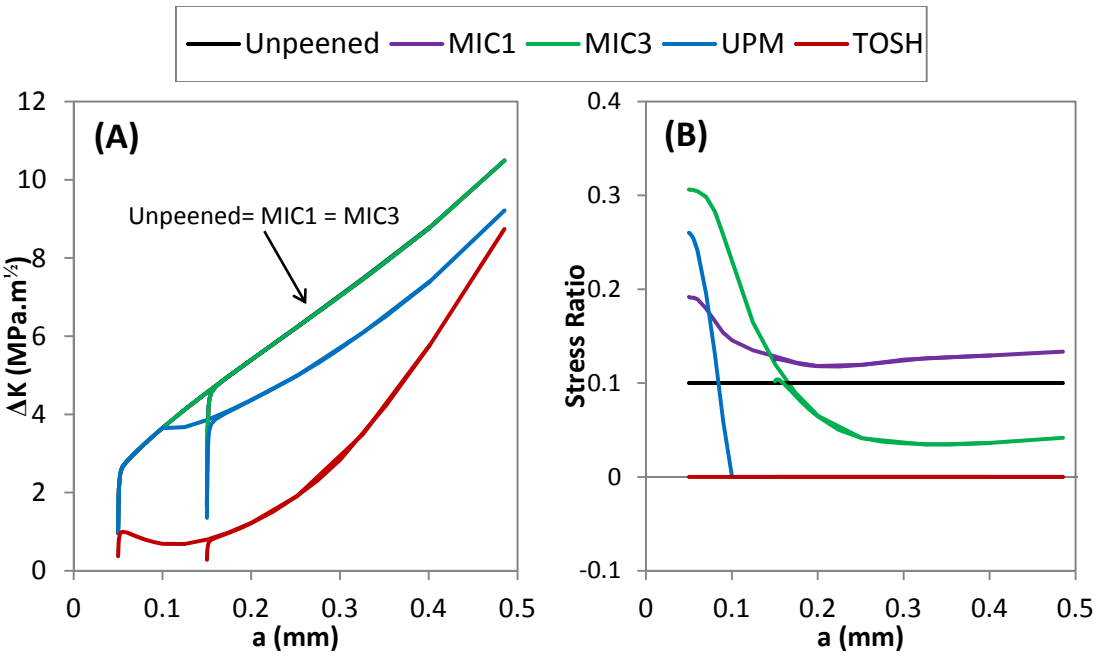

Figure 7.2: (A) Stress intensity factor range and (B) stress ratio calculated using the modified superposition method

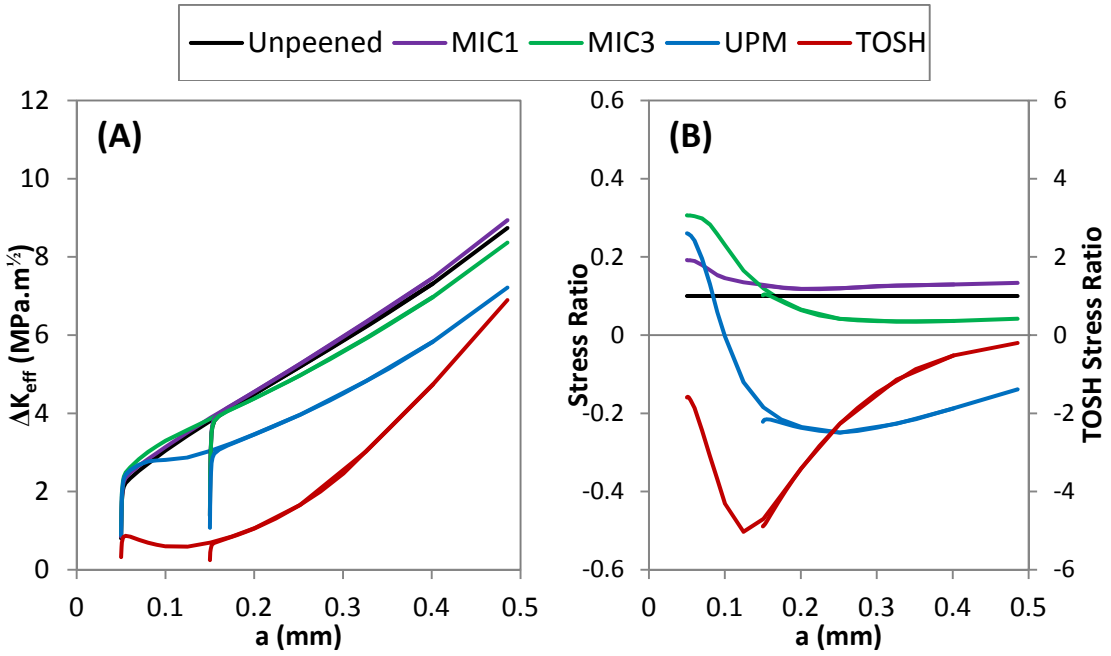

Figure 7.3: (A) stress intensity factor range and (B) stress ratio calculated using the Newman crack closure approach

To calculate fatigue lives using the superposition and modified superposition methods the Walker fatigue crack growth equation was used as shown below where C and n are the Paris law material constants that define the fit and m determines the shift between stress ratios.

$$\frac{da}{dN} = C(\Delta K(1-R)^{m-1})^n \quad (7.1)$$

To calculate the number of fatigue cycles for a given fatigue crack increment equation 7.1 was rearranged as shown in equation 7.2. For more detail on the walker equation refer to section 2.1.1.

$$dN = \frac{da}{C(\Delta K(1-R)^{m-1})^n} \quad (7.2)$$

The material constants for 2024-T351 plate and sheet from the NASMAT material database [275] were used where C = 4.8 ×10^{-11}, n = 3.2 and m = 0.6937. The ΔK and R values were taken from Figure 7.1 and Figure 7.2.

For the Newman crack closure approach FCGR data [275] for 2024-T351 in the L-T direction at stress ratios of -2, -1, -0.5, 0, 0.5 and 0.7 was used. This data is reproduced in Figure 7.4.

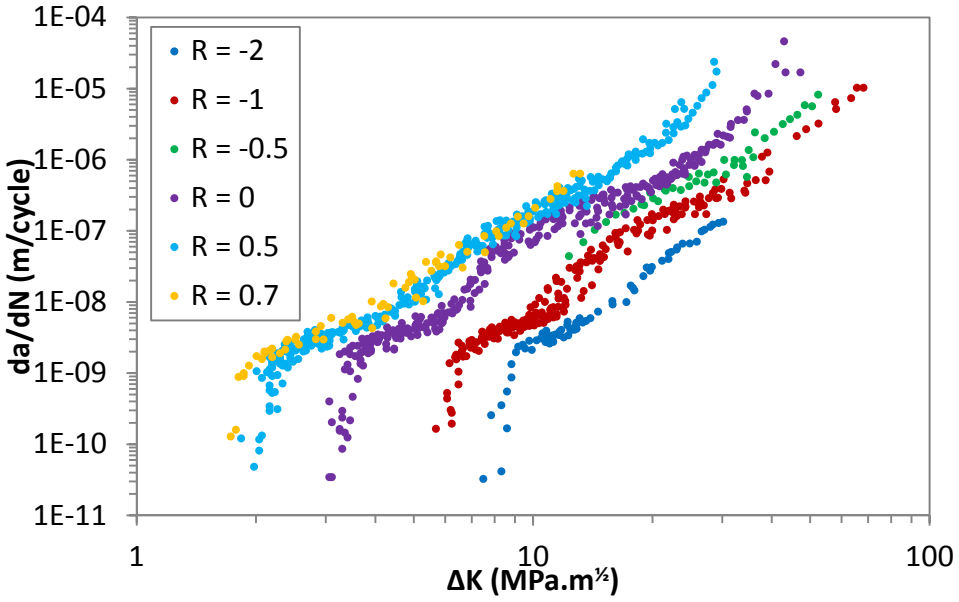

Figure 7.4: FCGR rate curves for 2024-T351 L-T [275]

The ΔK values in Figure 7.4 were converted to ΔK_{eff} using equation 7.3 below and a master curve was calculated as shown in Figure 7.5.

$$\Delta K_{eff} = \left[\frac{1 - \sigma_{op}/\sigma_{max}}{1 - R}\right]\Delta K_{app} \quad (7.3)$$

The relationship between FCGR and ΔK_{eff} was characterised using the Paris relationship as shown in equation 7.4.

$$\frac{da}{dN} = C\left(\Delta K_{eff}\right)^{n} \quad (7.4)$$

A power trendline was fitted to the linear portion of the data in Figure 7.5 and the walker equation constants C and n equal to 5.49 $\times 10^{-11}$ and 3.45 were obtained. To calculate fatigue lives equation 7.4 was rearranged to form equation 7.5 and the ΔK and R values were taken from Figure 7.3.

$$dN = \frac{da}{C\left(\Delta K_{eff}\right)^{n}} \quad (7.5)$$

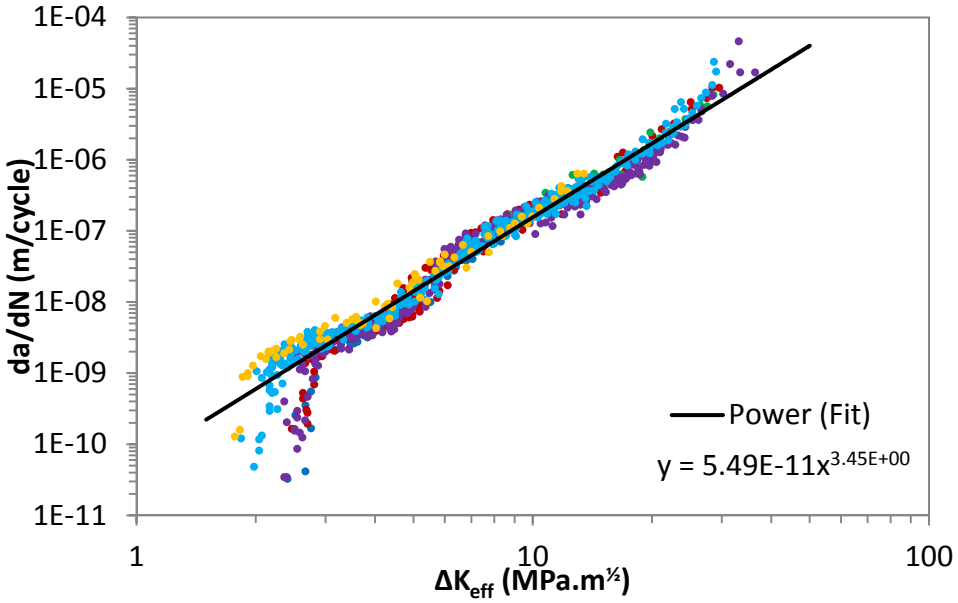

Figure 7.5: Material master curve derived from Figure 7.4 data (α = 3)

Shown in Table 7.1 are the predicted fatigue lives using the superposition method (SP), the modified superposition method (M.SP) and the Newman crack closure method (N.EQ). Predicted fatigue lives for samples scribed to 50 and 150 µm depths unpeened and with MIC1, MIC3, UPM and TOSH LSP treatments are shown in Table 7.1. Also shown for comparison are the experimentally measured tension-tension fatigue lives from section 4.3.

Table 7.1: Predicted fatigue lives based on 2024-T351 L-T FCGR data

LSP	Depth of Scribe (µm)	Fatigue Life (cycles)			
		Measured	SP	M.SP	N.EQ
None	50	69868	54384	54384	70507
	150	19728	14659	14659	17369
MIC1	50	67868	49207	49207	61834
	150	24410	14309	14309	16485
MIC3	50	107106	45289	45289	56364
	150	35612	15198	15198	19069
UPM	50	220590*	55031	68084	93772
	150	69662	21398	31515	42178
TOSH	50	316012*	226912	6.6×10^6	10×10^6
	150	297623*	66164	1.9×10^6	5.4×10^6

* Note fracture of fatigue sample was remote from scribe

The ΔK_{tot} calculated using superposition method is not affected by K_{res} i.e. negative $K_{tot,min}$ values are used to calculate ΔK_{tot} and crack face contact is not considered. Therefore the effect on predicted fatigue lives of residual stress is a function of R_{eff} only. Predicted fatigue lives based on the superposition method were highly conservative when the compressive residual stress field was great enough to create negative $K_{tot,min}$ values. For example the predicted lives for UPM and TOSH LSP were on average 3.6× and 2.9× less than the measured lives respectively. For tensile residual stress fields the superposition method is suitable since crack face contact should be less. The predicted fatigue lives for the unpeened, MIC1 and MIC3 were 1.3×, 1.5× and 2.3× less than the measured fatigue lives.

Now consider the modified superposition method which does consider crack face contact. For the cases where $K_{tot,min}$ was positive (i.e. unpeened, MIC1 and MIC3) the predicted fatigue lives using the superposition and modified superposition methods were equivalent since there is no contact. Predicted fatigue lives for the UPM residual stress field were again conservative and on average 2.7× less than the measured lives. Predicted fatigue lives for the TOSH residual stress field were non-conservative and were at least 6× greater than the measured fatigue lives. However note that the TOSH peened fatigue samples did not fracture at the scribes and therefore the developed prediction model is not capable of predicting these lives. This topic is discussed further in the discussion chapter.

Of the three methods studied the predicted fatigue lives using the Newman crack closure approach were most similar to the fatigue lives measured experimentally. The unpeened fatigue lives were 1.1× less than measured fatigue lives. The predicted MIC1, MIC3 and UPM fatigue lives were on average 1.3×, 1.9× and 2.0× less than the measured fatigue lives respectively. The predicted TOSH fatigue lives were non-conservative however again note that the experimental fatigue samples did not fracture at the scribes.

Based on values of ΔK and R using the modified superposition method FCGRs from scribe roots 50 µm and 150 µm deep were predicted and are shown in Figure 7.6 (A) and (B) respectively. The predicted FCGRs through MIC1 and MIC3 residual stress field are almost equivlenet to the FCGRs for the unpeened case and note that the predicted fatigue lives were all within a factor of 1.2. The predicted FCGR through the UPM residual stress field was greater than in the unpeened case up to a crack length of approximately 100 µm due to the tensile residual stress near the peened surface. As the crack was advance through the compressive residual stress field the predicted FCGRs reduced and were less than unpeened.

The FCGR of the crack at the root of the scribe 50 µm deep increased for the first 5 µm of crack advance through the TOSH residual stress field. The FCGR then reduced for the next 70 µm of crack advance as the residual stress field became more compressive at this depth. As the residual stress field became less compressive the FCGR increased i.e. at depths greater than 125 µm from the surface.

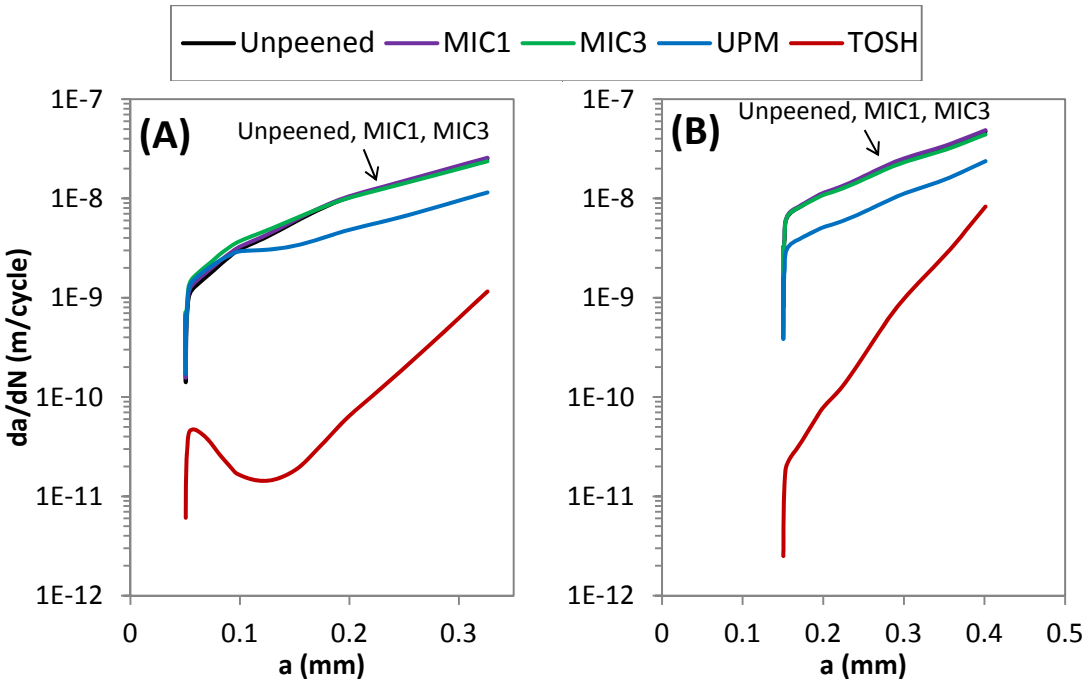

Figure 7.6: Predicted FCGRs from scribes of depth (A) 50 µm and (B) 150 µm using the modified superposition approach

7.1.1 Effect on Predicted Fatigue Life of LSP induced Samples Distortion

It was shown in section 4.1 that due to distortion induced by LSP the stresses imposed on the test samples were not uniaxial tension but were combined tension with out of plane bending. Surface stresses on the peened and unpeened face of the UPM treated samples were 158 MPa and 242 MPa respectively at the maximum applied loading and –6 MPa and 46 MPa at the minimum applied loading. An FE analysis was performed where the measured stresses were used in place of the nominal applied stresses. Values of ΔK and R were calculated using the superposition, modified superposition and Newman crack closure methods. Shown in Figure 7.7 (A) and (B) are the ΔK and R values calculated using modified superposition. Also shown for comparison are the ΔK and R values calculated for the unpeened case and for UPM with nominal applied stress.

The UPM with measured applied stress resulted in ΔK values on average 1.3× less than UPM with nominal applied stress as shown in Figure 7.7 (A). Since the minimum applied stress on the peened face was negative the R ratio was negative (0 for

modified superposition as shown in Figure 7.7 (B)). Fatigue lives for UPM with measured applied stress were calculated and are shown in Table 7.1.

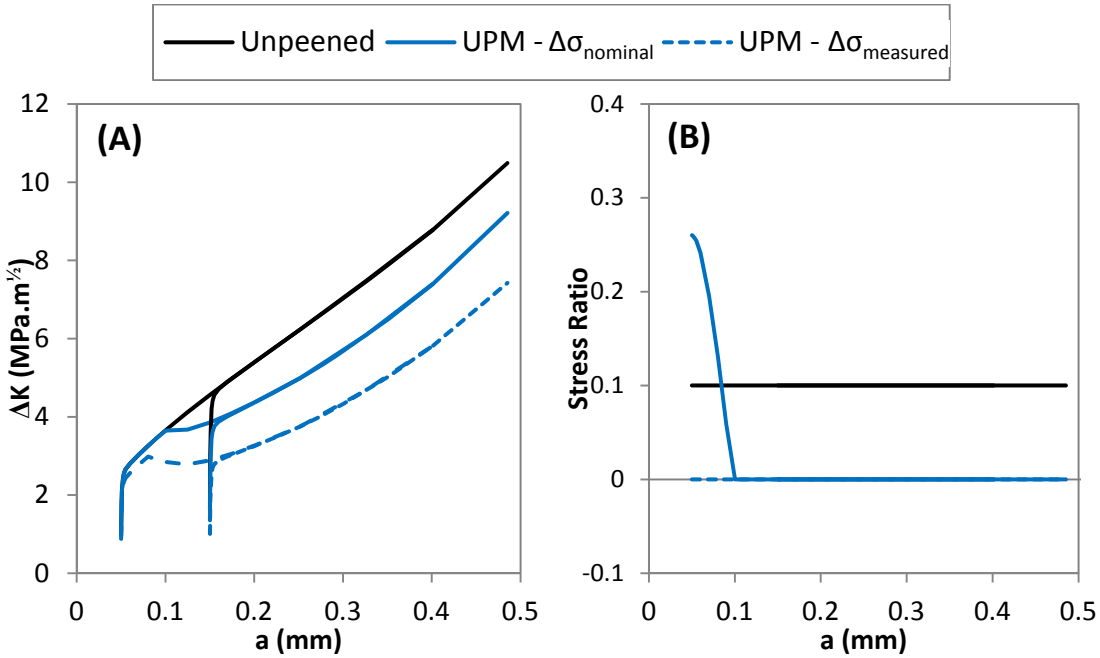

Figure 7.7: Comparison of (A) ΔK and (B) R using the modified superposition method for UPM residual stress field with nominal and measured $\Delta\sigma$

Table 7.2: Predicted fatigue lives based on 2024-T351 L-T FCGR data

LSP	Depth of Scribe (µm)	Fatigue Life (cycles)			
		Measured	SP	M.SP	N.EQ
UPM ($\Delta\sigma_{nominal}$)	50	220590*	55031	68084	93772
	150	69662	21398	31515	42178
UPM ($\Delta\sigma_{measured}$)	50	220590*	84075	149367	199086
	150	69662	31515	78499	100739

* Fracture of fatigue sample remote from scribe

Predicted fatigue lives based on the measured applied stress range were greater than predicted fatigue lives based on the nominal applied stress range due to the lower ΔK and R values. Again fatigue lives predicted using the superposition method was conservative, on average of 2.4× less than the measured fatigue lives. Fatigue lives for scribes 50 µm deep using the M.SP and N.EQ methods were 1.5× and 1.1× less than the measured lives respectively. However predicted fatigue lives for scribes 150 µm deep using the M.SP and N.EQ methods were non-conservative, 1.1× and 1.4× greater than the measured lives respectively.

Surface strain was not measured on MIC1 and MIC3 treated samples. Surface strain data was available for the TOSH treated samples however since the fatigue samples did not fracture at the scribes, a modified fatigue life analysis was deemed unnecessary.

7.1.2 Prediction of Fatigue Life based results of FE Crack Closure Model

In this section fatigue lives of scribed samples were predicted based on results of the PICC analysis in chapter 6. Shown in Figure 7.8 is the ratio of the opening stress at the crack tip to the maximum applied stress predicted using the Newman equation and FE PICC model. It was predicted using the Newman equation that the crack would open at the tip at 0.25 of the maximum applied stress. This did not vary with crack avdvance since the Newman equation is a function of R ratio, maximum applied stress and flow stress only. Using the FE method it was predicted that the opening stress of a crack advanced from a scribe 50 µm deep peaked at 0.16 of the maximum applied stress. For a crack advanced from a scribe 150 µm deep the opening stress reached the same level predicted using the Newman equation however it decreased with continued crack advance.

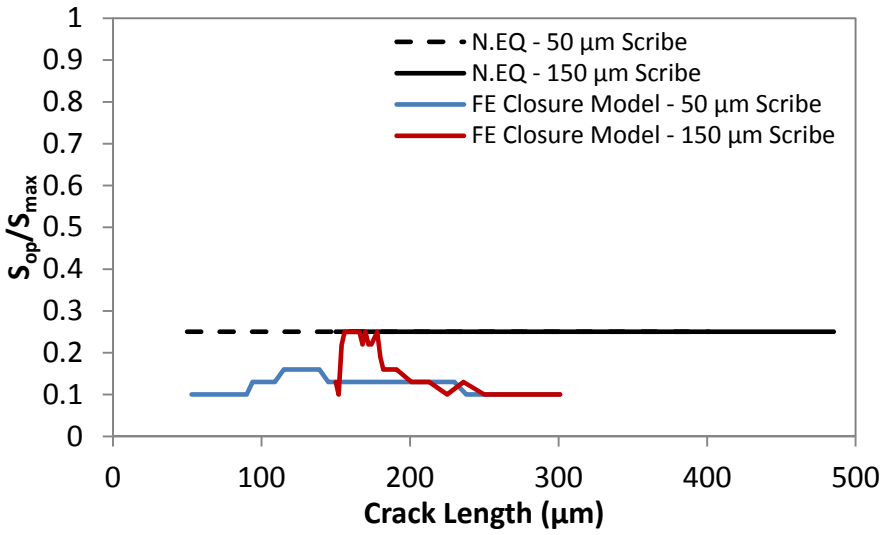

Figure 7.8: S_{op}/S_{max} predicted using the Newman equation and FE PICC analysis

The effect on opening stress of the MIC1 and MIC3 residual stress fields is considered in Figure 7.9 (A) and (B) respectively. Using the Newman equation the opening stress ratio was predicted between 0.23 and 0.35 of the maximum applied stress. In this case the opening stress ratio did change with crack length since the R ratio changed as the crack advanced through the residual stress field, as shown in Figure 7.3 (B). The opening stress ratio predicted using the FE PICC model was 0.1 of the maximum applied stress noting that the applied stress ratio R was also .1. Considering the MIC induced residual stress fields were mostly in tension this prediction is expected.

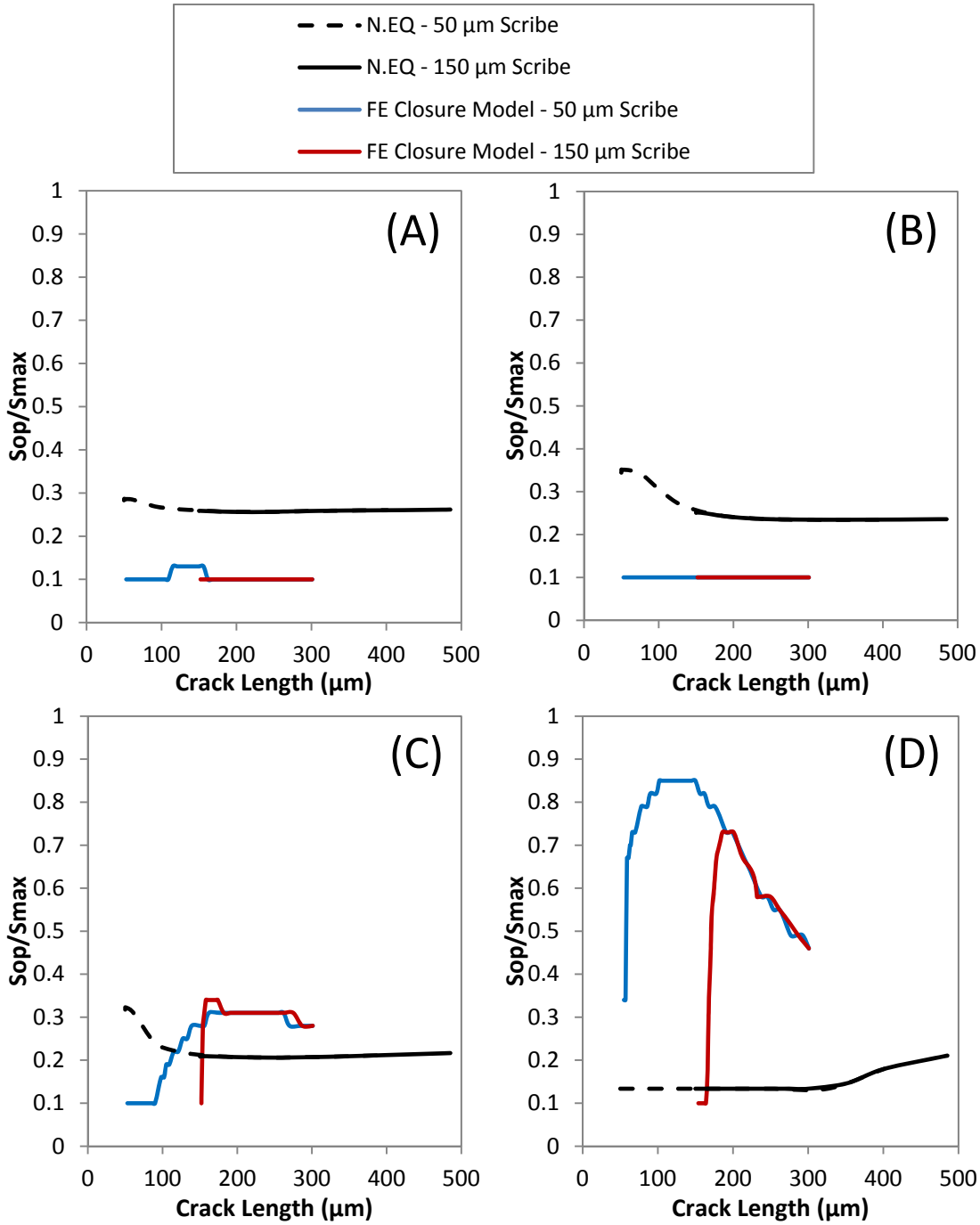

Figure 7.9: Crack tip S_{op}/S_{max} in residual stress field (A) MIC1, (B) MIC3, (C) UPM and (D) TOSH

The crack tip stress opening ratio in the UPM induced residual stress field is shown in Figure 7.9 (C). The opening ratio predicted using the Newman equation was initially 0.32 but decreased with crack advance to 0.2 and foloows the trend of R_{eff} (Figure 7.3 (B)). In contrast the opening stress ratio predicted using FE PICC was initially 0.1 and increased with crack advance to 0.31. Considering the residual stress field induced via the UPM peening was in tension near the peened surface crack closure would not be

expected in the early stages of crack growth. As the crack advanced into the compressive residual stress region the closure level would be expected to increase. The Newman equation failed to predict the expected behaviour since it is a function of stress ratio only.

The stress opening ratio in the TOSH induced residual stress field is shown in Figure 7.9 (D). The opening stress ratio predicted using the FE PICC model increased during early crack advance and peaked at 0.85 before decreasing. The trend followed that of the TOSH residual stress field. In contrast the opening stress ration predicted using the Newman equation was between 0.13 and 0.21.

To calculate fatigue lives the S_{op}/S_{max} values were related to ΔK_{eff} using equation 7.6 below.

$$\Delta K_{eff} = \left[K_{app,max} + K_{res}\right] \sigma_{op}/\sigma_{max} \quad (7.6)$$

The relationship between FCGR and ΔK_{eff} was characterised using a rearrangment Paris relationship as shown in equation 7.5. The material constants used were the same as in previous sections. The predicted fatigue lives are given in Table 7.3 below with experimental measured lives and those predicted using the Neman equation also provided for reference. Good correlation between predicted and experimental fatigue lives in the unpeened condition was obtained.

The effect of MIC peening on fatigue life was underestimated by the FE PICC model. In fact the fatigue lives predicted were less than those predicted for the unpeened condition. This reduction in predicted fatigue life is caused by the measured MIC induced residual stress field being mostly in tension. The mechanism how the MIC treatment actually resulted in increased fatigue performance of the scribed material is discussed further in the chapter 8.

The fatigue lives predicted using the FE PICC model for the UPM treatment were less than experimental lives by up to a factor of 1.5 in the case of crack growth from the 50 µm deep scribe. The fatigue lives were howveer closer to the experiemental lives than those predicted using the Newman equation.

Predicted fatigue life of a crack advanced through the TOSH residual stress was greater than the experimental lives. The FE PICC model effectively predicted a fatigue run out. As mentioned previously interrupted fatigue tests indicated that although a crack initiated at the root of the scribe it arrested due to the compressive residual stress field. In this instance the samples failed due crack initiation remote from the scribe caused by distortion induced bending loads. The FE model therefore correctly predicted the behaviour of the fatigue crack that initiated at the scribe.

Table 7.3: Predicted fatigue life using Newman equation and FE based crack closure prediction methodologies

LSP	Depth of Scribe (μm)	Fatigue Life (cycles)		
		Measured	N.EQ	FE Model
None	50	69868	70507	61560
	150	19728	17369	19579
MIC1	50	67868	61834	48512
	150	24410	16485	15009
MIC3	50	107106	56364	39428
	150	35612	19069	18525
UPM	50	220590*	93772	143842
	150	69662	42178	67177
TOSH	50	316012*	1×10^7	1×10^9
	150	297623*	5.4×10^6	3.1×10^7

* Note fracture of fatigue sample was remote from scribe

7.2 Methodology used for Residual Stress Field Sensitivity Study

A residual stress field sensitivity studied was performed to study the effect of residual stress on fatigue life. The elastic finite element model described in section 4.7 was used for this study. Stress intensity factors were calculated using VCCT and the effect of crack closure was considered using the Newman equations. Four characteristic features of the residual stress field were considered in the study. These were the compressive residual stress field depth, the maximum compressive residual stress and the position of the maximum compressive residual stress relative to the surface. These are illustrated in Figure 7.10. The final characteristic considered was the effect of the residual stress field near the surface. The methodology used to study each characteristic is described in sections 7.2.1 to 7.2.4 and the results of the study are presented in section 7.3.

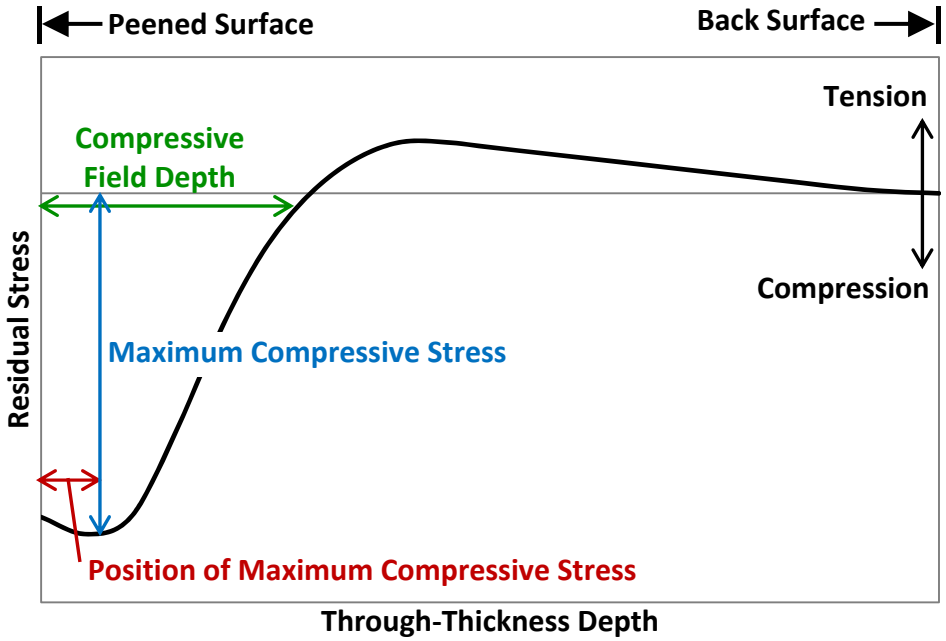

Figure 7.10: Characteristics studied in residual stress field sensitivity study

7.2.1 Depth of Compressive Residual Stress Field

The effect on fatigue life of the depth of the compressive residual stress field was studied by modelling a -100 MPa compressive stress field that extended from the peened surface through the thickness. The distance from the surface that the residual stress field extended was increased in increments and fatigue life was predicted at each increment. As an example two residual stress fields studied are illustrated in Figure 7.11 noting that outside the compressive field the residual stress was 0 MPa until 1 mm from the surface. The remaining depth (i.e. between 1-2 mm) was used for residual stress field balancing. Ten residual stress fields were analysed and are detailed in Table 7.4.

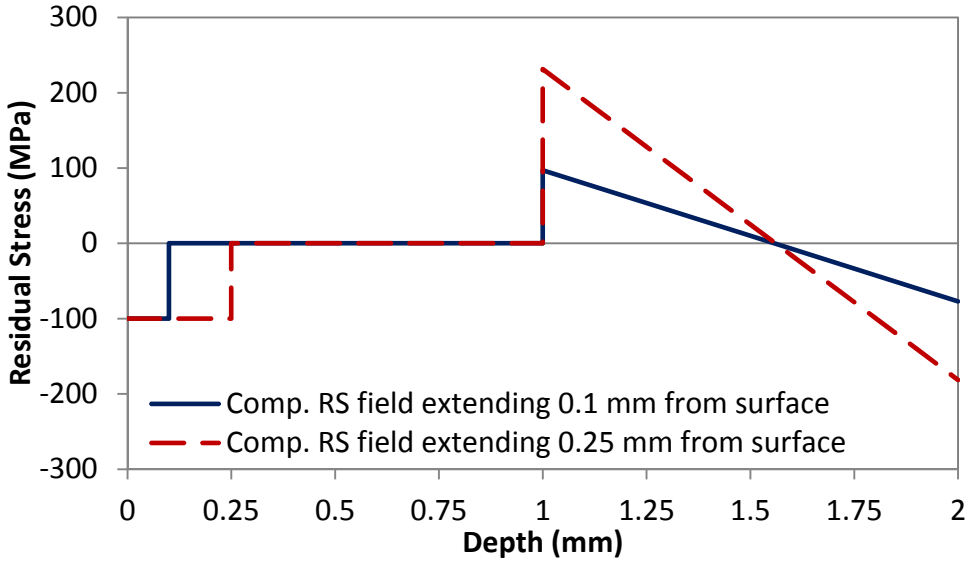

Figure 7.11: Two residual stress fields used to study effect on fatigue life of depth of compressive residual stress field

Table 7.4: Residual stress fields used to study the effect on fatigue life of compressive residual stress field depth

Analysis No.	Analysis Field Stress (MPa)	Analysis Field Depth (mm)	Max. Balancing Stress (MPa)	Min. Balancing Stress (MPa)
1	-100	0.050	49	-39
2	-100	0.100	97	-77
3	-100	0.125	120	-95
4	-100	0.150	143	-113
5	-100	0.175	166	-131
6	-100	0.200	188	-148
7	-100	0.250	231	-181
8	-100	0.500	425	-325
9	-100	0.750	581	-431
10	-100	1.000	702	-502

7.2.2 Maximum Compressive Residual Stress

The effect of the maximum compressive residual stress was studied by modelling a constant magnitude residual stress field from the peened surface until 1 mm from the surface. The magnitude of the residual stress field was decreased in increments from 100 MPa in tension until -150 MPa in compression. Fatigue life was predicted at each increment. For example two of the residual stress fields studied are presented in Figure 7.12 noting that the depth from 1 to 2 mm was used for residual stress field

balancing. Eight residual stress fields were analysed and these are detailed in Table 7.5.

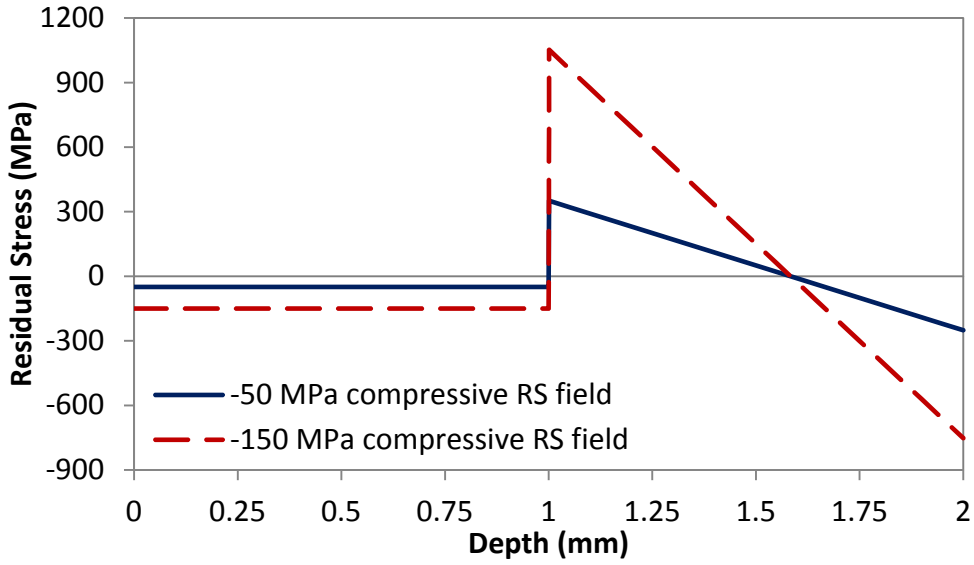

Figure 7.12: Two of the residual stress fields used to study the effect on fatigue life of the maximum compressive residual stress

Table 7.5: Residual stress fields used to study the effect on fatigue life of the maximum compressive residual stress

Analysis No.	Analysis Field Stress (MPa)	Analysis Field Depth (mm)	Max. Balancing Stress (MPa)	Min. Balancing Stress (MPa)
1	+100	1.0	-702	502
2	0	1.0	0	0
3	-50	1.0	351	-251
4	-100	1.0	702	-502
5	-110	1.0	772	-552
6	-120	1.0	842	-602
7	-140	1.0	982	-702
8	-150	1.0	1052	-752

7.2.3 Position of the Maximum Compressive Residual Stress

The effect on fatigue life of distance from the peened surface of the maximum compressive residual stress was studied by considering a compressive residual stress field of magnitude of -100 MPa and width 100 µm. The distance from the surface of the stress field was increased in increments and fatigue life was calculated at each increment. Two of the residual stress fields considered in the study are shown in

Figure 7.13. Outside the compressive stress field the residual stress was 0 MPa to a distance 1 mm from the surface. The remaining depth (1 to 2mm) was used for residual stress field balancing. Ten residual stress fields were analysed and these are detailed in Table 7.6.

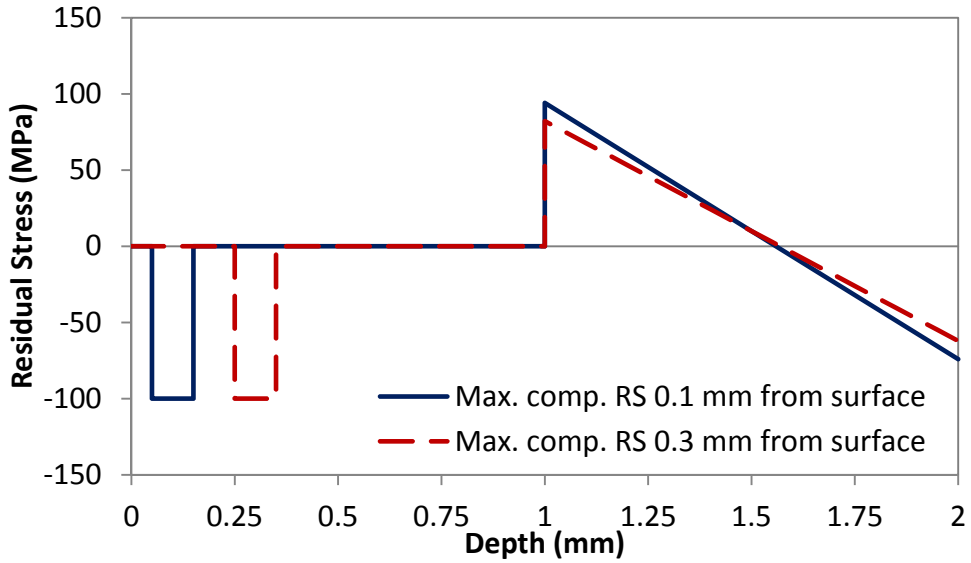

Figure 7.13: Two residual stress fields used to study the effect on fatigue life of the position of the maximum compressive residual stress

Table 7.6: Residual stress fields used to study the effect on fatigue life of the position of the maximum compressive residual stress

Analysis No.	Analysis Field Stress (MPa)	Centre of Analysis Field (mm)	Max. Balancing Stress (MPa)	Min. Balancing Stress (MPa)
1	-100	0.050	97	-77
2	-100	0.075	96	-76
3	-100	0.100	94	-74
4	-100	0.125	93	-73
5	-100	0.150	91	-71
6	-100	0.175	90	-70
7	-100	0.200	88	-68
8	-100	0.250	85	-65
9	-100	0.300	82	-62
10	-100	0.500	70	-50

7.2.4 Near Surface Residual Stress Field

The effect on fatigue life of near surface residual stress was studied by considering a compressive residual stress field of magnitude -100 MPa that extended 1 mm from the peened surface. The distance from the surface of the beginning of the compressive residual stress field was increased in increments and fatigue life was calculated at each increment. Shown in Figure 7.14 are two of the residual stress fields used in the study. The depth between 1 to 2 mm was used for residual stress field balancing. A total of twelve residual stress fields were analysed and these are detailed in Table 7.7.

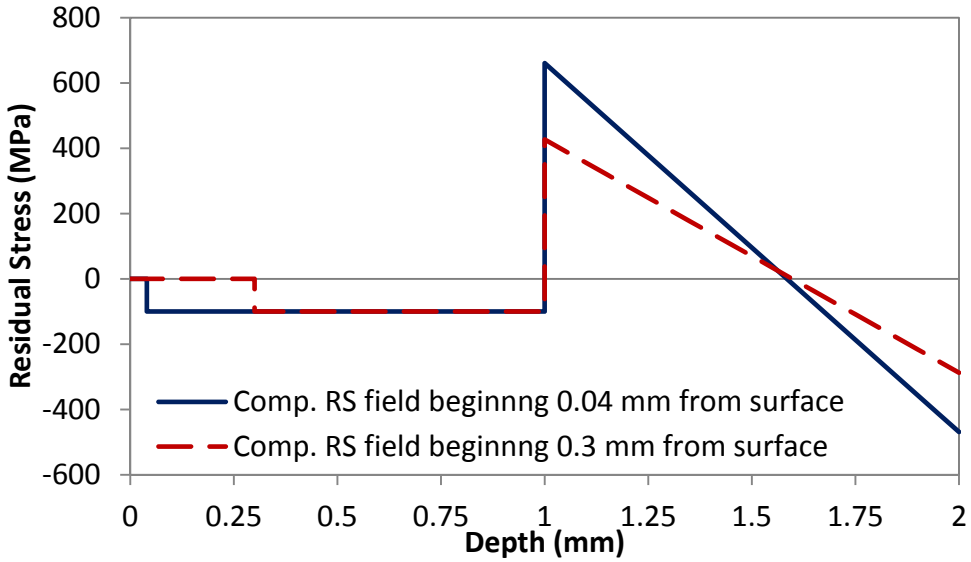

Figure 7.14: Two residual stress fields used to study the effect on fatigue life of near surface residual stress

Table 7.7: Residual stress fields used to study the effect on fatigue life of near surface residual stress

Analysis No.	Analysis Field Stress (MPa)	Beginning of Analysis Field (mm)	Max. Balancing Stress (MPa)	Min. Balancing Stress (MPa)
1	-100	0.000	702	-502
2	-100	0.005	695	-496
3	-100	0.010	690	-492
4	-100	0.015	685	-488
5	-100	0.020	680	-484
6	-100	0.040	661	-469
7	-100	0.080	622	-438
8	-100	0.130	575	-401
9	-100	0.150	557	-387
10	-100	0.170	539	-373
11	-100	0.220	495	-339
12	-100	0.300	427	-287

7.3 Sensitivity study of the effect on Fatigue Life of RS fields

The residual stress field sensitivity study considered the effect on fatigue life of four characteristics of residual stress fields. These were the compressive residual stress field depth, the maximum compressive residual stress, the position of the maximum compressive residual stress relative to the surface and near surface residual stress field. The analyses were performed using the FE modelled geometry with a scribe 150 µm deep. The results of the studies are detailed in sections 7.3.1 to 7.3.4 and the findings are summarised in section 7.3.5.

7.3.1 Depth of Compressive Stress Field

The results from the sensitivity study on the effect on fatigue life of the depth of the compressive residual stress field are presented in Figure 7.15. It was found that as the distance from the surface of the compressive residual stress field was increased that the predicted fatigue life also increased until a depth of 250 µm. Compressive residual stress further than 250 µm from the surface had little effect on the predicted fatigue life.

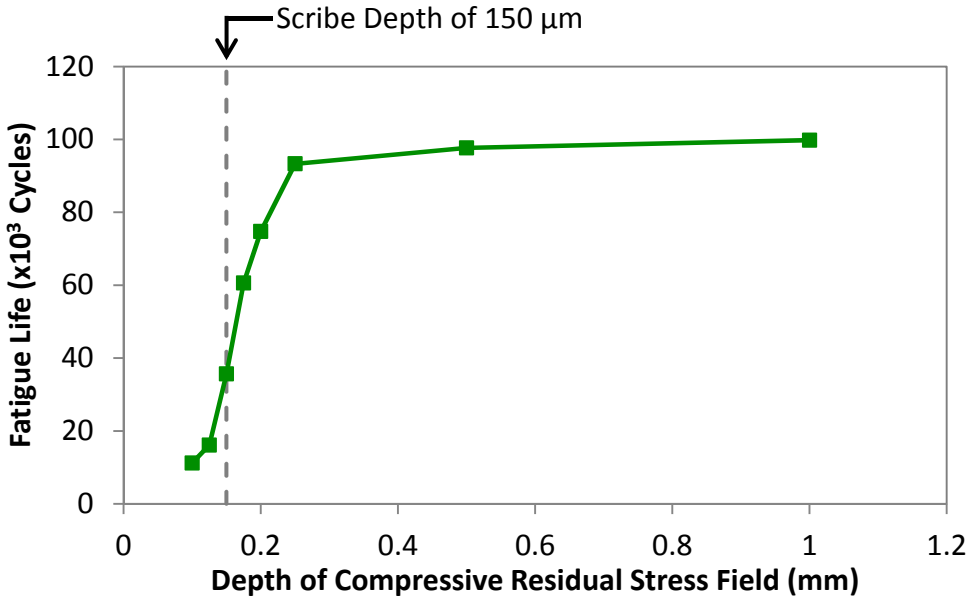

Figure 7.15: Effect on fatigue life of the depth of the compressive residual stress field

7.3.2 Maximum Compressive Residual Stress

The results of the sensitivity study on the maximum compressive residual stress are shown in Figure 7.16. Predicted fatigue life is plotted against the maximum of the compressive residual stress. It was found that compressive residual stress less than -100 MPa had little effect predicted fatigue life. The predicted fatigue life increased exponentially as the maximum compressive residual stress was increased greater than -120 MPa.

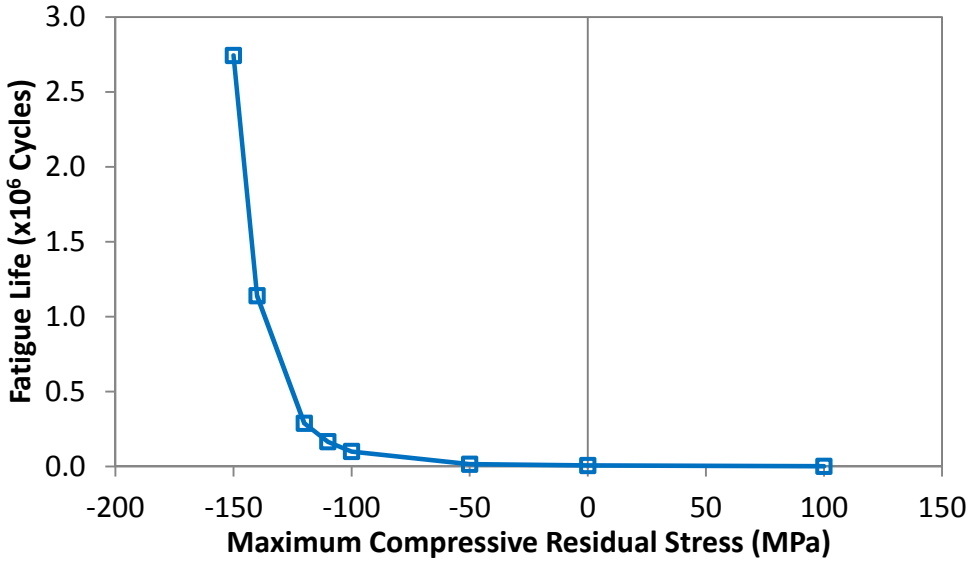

Figure 7.16: Effect on fatigue life of the maximum compressive residual stress

7.3.3 Position of Maximum Compressive Residual Stress

The results from the sensitivity study on the position of the maximum compressive residual stress are presented in Figure 7.17. Predicted fatigue life is plotted against the distance from the peened surface of the maximum compressive residual stress. The predicted fatigue life peaked when the maximum compressive residual stress was 125 µm from the peened surface. When the maximum compressive residual stress was located closer or further than 125 µm from the peened surface the predicted fatigue life decreased.

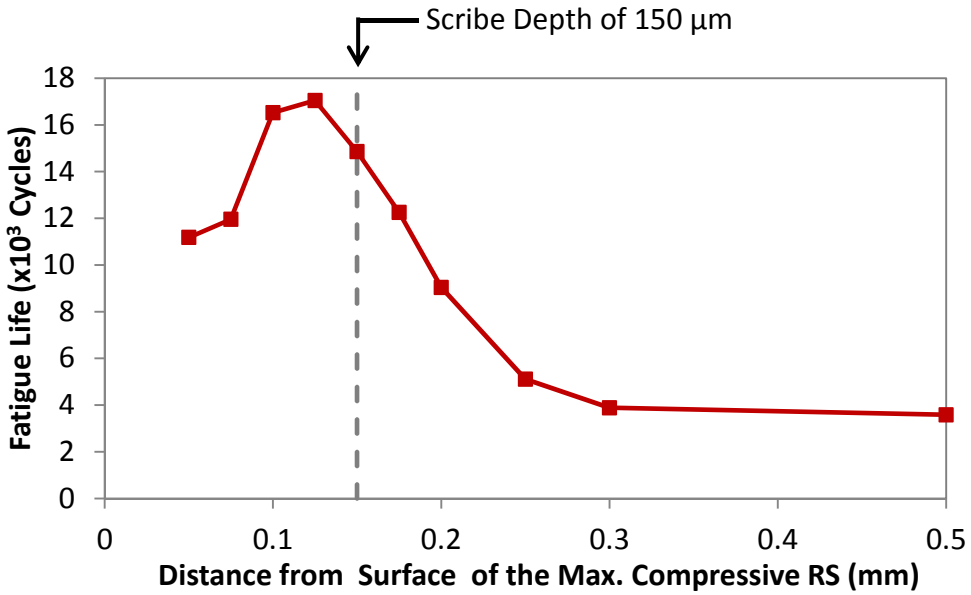

Figure 7.17: Effect on fatigue life of the distance from the peened surface of the maximum compressive residual stress

7.3.4 Near Surface Compressive Residual Stress Field

The results of the sensitivity study on the effect of the near surface compressive residual stress field are presented in Figure 7.18. The predicted fatigue lives are plotted against the distance from the surface of the beginning of the compressive residual stress field. It was found that as the distance from the surface of the start of the compressive residual stress field increased the predicted fatigue life decreased.

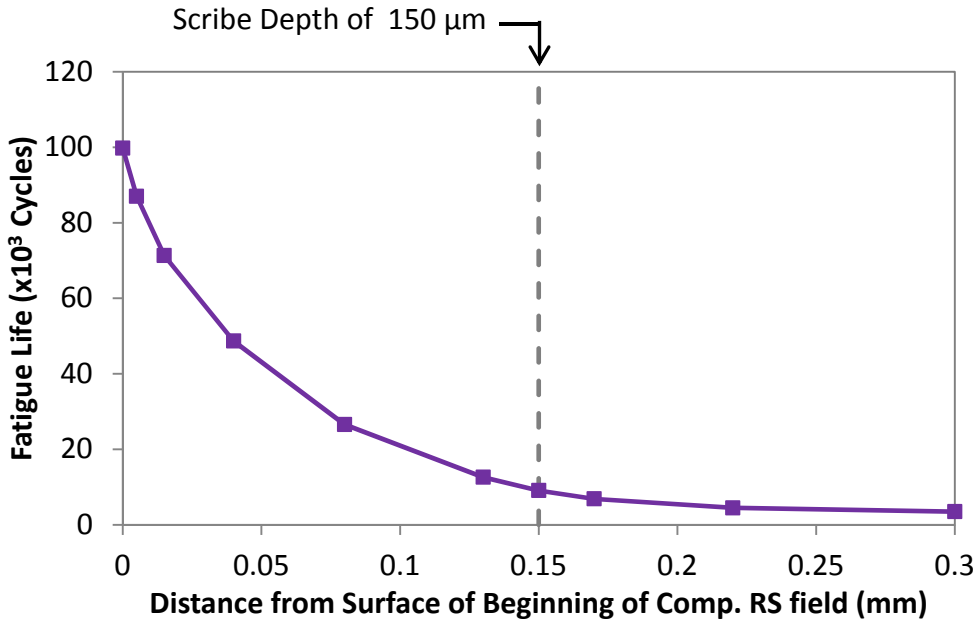

Figure 7.18: Effect on fatigue life of near surface compressive residual stress

7.3.5 Summary of Residual Stress Field Sensitivity Study

The residual stress field sensitivity study considered the effect on fatigue life of four characteristics of the residual stress field. The analyses were performed using a FE model with a scribe of depth 150 µm. The sensitivity study demonstrated that compressive residual stress greater than 250 µm from the peened surface had minimal effect on the fatigue life enhancement. The study indicated that compressive residual stress of magnitude less than 120 MPa has minimal beneficial effect on the fatigue life. The optimum position for the maximum compressive residual stress for fatigue life enhancement was 125 µm from the peened surface. Finally compressive residual stress behind the notch root / crack tip has a significant effect on fatigue life and the LSP induced residual stress field near the surface should therefore be in compression with the balancing tensile field located ahead of the crack.

The residual stress sensitivity study was performed after MIC and UPM LSP treatment of fatigue test samples. However the results of the sensitivity study were in fact during development by Toshiba of their LSP treatment.

8 Discussion

The discussion section contains five subsections. The first section discusses the assumputions used for FE modelling, the fatigue life prediction methodology as well as some other interesting topics that arose during numerical modelling. The second section discusses and compares the predicted and experimental fatigue lives. The third section discusses the optimum residual stress field predicted to restore the fatigue life of the scribe damage material to that of the baseline pristine material. The fourth section dicusses in more detail the experimental results and in the final section scribe / notch effects are reviewed.

8.1 FE Modelling and Fatigue Life Prediction Methodology

8.1.1 Modelling assumptions

The FE models are described in sections 5 through 7. The first model used elastic material properties. The mechanisms of fatigue crack growth were not simulated directly instead a crack was advanced from the root of the scribe using a node release scheme. The primary objective of the FE model was to determine at different crack lengths the residual SIF. By inputting different residual stress fields into the model the effect on the residual SIF and ultimately fatigue life could be assessed and an optimum residual stress field determined.

It was concluded by Jones and Dunn [88] that crack growth rate through residual stress fields may be predicted provided the residual stress field is accurately known. The experimental residual stress field data input to the FE models was measured on flat planar specimens that did not contain scribes. The Abaqus command ‘unbalanced stress’ was used to redistribute the residual stress field around the scribe. How the actual stress field and modelled stress field around the root of scribe compared is unknown. Differences would be a source of error in the prediction of fatigue lives. No method for measurement of residual stress around the root of the scribe was available however future advances in residual stress measurement could make this possible. Another difference between the experimental and modelled residual stress fields was that laser peening was localised to within 2.5 – 15 mm of the scribe line depending on the treatment applied. Therefore the induced compressive residual stress field would be localised to peened / scribed region only. However in the FE analysis the residual stress field extended the full length of the model. It was not envisaged that the width of the peened region would affect the residual stress field and an analysis where the length of the model was varied supported this assumption.

A separate model was developed to investigate the effect on crack closure of plasticity and initial residual stress. To model PICC accurate prediction of the reversed

plastic zone is critical since this develops the plastic wake. As the reversed plastic zone is usually around ten times smaller than the plastic zone and at least four elements are desirable within it, prediction of the reversed plastic zone requires an extremely fine mesh. When modelling crack advance is also required, not only a fine mesh at the initial crack tip is needed but also along the entire crack path. In short FE modelling of PICC is computationally demanding and there are numerous modelling options in addition to mesh refinement that need to be considered such as element type, material model, contact model, crack advance scheme, stabilisation of crack opening load and crack opening assessment criteria. An overview of the modelling options, the option chosen and the reasoning why an option was chosen was detailed in section 6.1. However there is still no general consensus in literature on best practice for modelling of crack closure. La Rue & Daniewicz [79] stated crack growth simulations utilizing plasticity-induced crack closure concepts are highly sensitive to the crack growth rate relationship $da/dN = g(\Delta Keff)$ used. As with any numerical modelling method the best option is to validate results against experimental measurements. However experimental measurement of the crack closure and FCGR was not possible in the current research due to the geometry of the test specimens.

The percentage of the applied load cycle that the crack open ($\Delta\sigma_{a,open}$) for a crack advanced from a scribe 50 µm deep under plane stress and plane strain conditions was presented in Figure 6.4. These results are compared in Figure 8.1 to numerical predictions using the Newman equations as described in section 7.1. In the Newman equations plane strain and plane stress is characterised by changing the α parameter from 1 to 3 respectively. $\Delta\sigma_{a,open}$ for plane strain was less than for plane stress using both FE analysis and the Newman equation. This was expected as it has been well established that crack closure is less in plane strain than plane stress conditions as described in depth in section 2.3.2. Firstly considering plane strain, $\Delta\sigma_{a,open}$ predicted using the Newman equation was greater than predicted using FE analysis. Using the Newman equation it was predicted that the crack remained open for 83% of the load cycle whereas using FE analysis it was predicated that the crack would remain open for 93% of the load cycle (at the peak closure level). In contrast for plane stress conditions predicted $\Delta\sigma_{a,open}$ using the two methods was similar with the crack predicted to be open for about 63% of the load cycle.

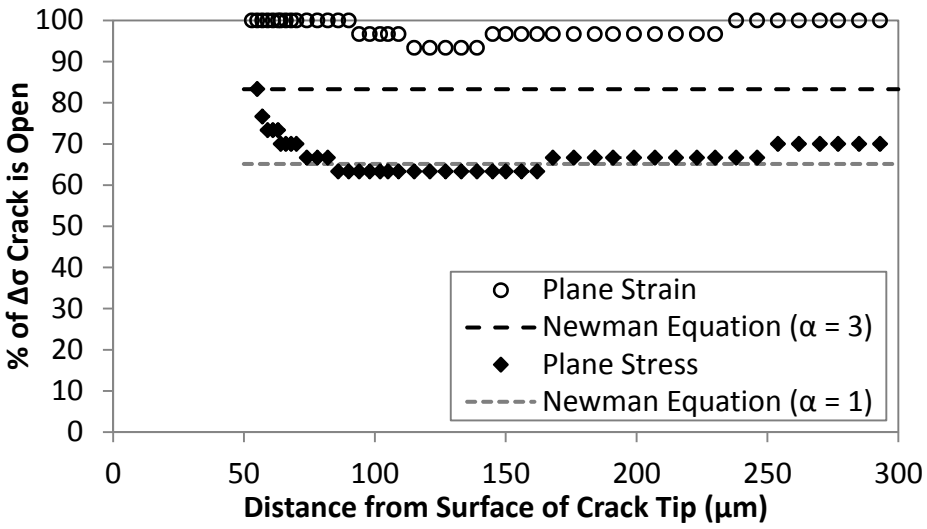

Figure 8.1: Crack closure level for plane strain and plane stress predicted using the FE method and Newman equation

The predicted plane stress crack opening values in Figure 8.1 show a similar trend to those contained in the literature review in that during early crack growth the crack closure level increased as the plastic wake built up due to cyclic plasticity. At a crack length of 86 µm the crack opening stabilized at 63% of the applied load cycle. However a notable feature of the crack opening values in the current study are that the crack opening began to increase at crack lengths greater than 156 µm (at a crack length of 250 µm the crack was open for 70% of the load cycle). This was most apparent for plane stress but was also observed for plane strain conditions where the crack opening level began to increase at crack lengths greater than 139 µm.

The reduction of crack closure at longer crack lengths may be due to limited remaining ligament length where remaining ligament length is defined as the distance from the crack tip to the back surface. Indeed decaying levels of crack opening value were reported [76] as a crack approached the other end of a specimen and the remaining ligament became small. McClung [263] also reported similar behaviour as the remaining ligament length reduced and in fact reduced to such an extent that little closure remained. The effect on plastic zone size of remaining ligament length is shown in Figure 8.2 where a 2 mm wide geometry is compared with geometry 5 mm wide. The crack tip plastic zone at the maximum applied stress for cracks of length 50, 150 and 300 µm is reported. Therefore remaining ligament length was 1.95, 1.85 and 1.7 mm for 2 mm wide geometry and 4.95, 4.85 and 4.7 mm for 5 mm wide geometry.

The plastic zone at the tip of a crack of length 50 µm was 1 µm larger for 2 mm wide geometry than 5 mm wide geometry. The effect on the crack tip plastic zone of

remaining ligament length increased at longer crack lengths. The plastic zone was 5 and 30 µm larger for 2 mm wide geometry than 5 mm at the tip of cracks of length 150 and 300 µm respectively.

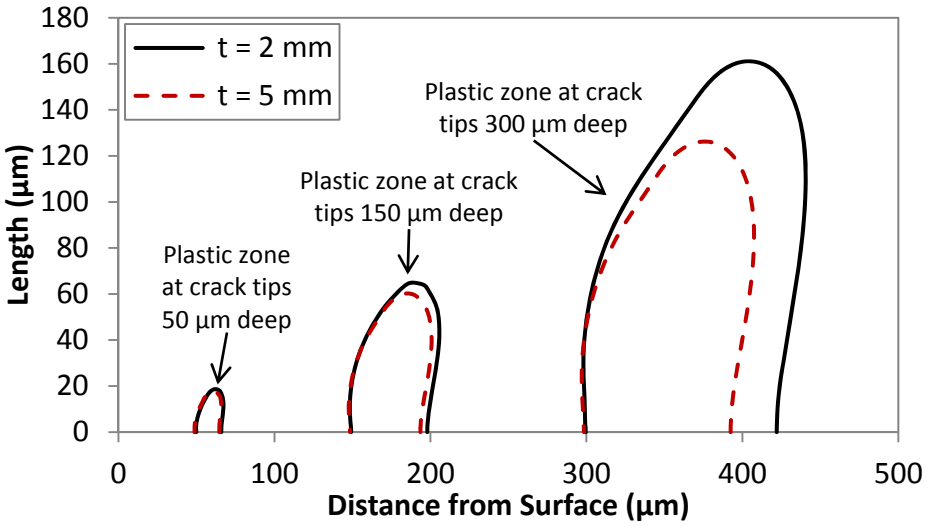

Figure 8.2: Comparison of crack tip plastic zones for 2 and 5 mm wide geometries

8.1.2 Fatigue life prediction methodology

As mentioned in section 2.1 total fatigue life can generally be subdivided into an initiation stage, a crack growth stage and final fracture. A major assumption of the life prediction methodology used was that there was no initiation stage, only crack growth and fracture. In unnotched samples or at stress amplitudes just above the endurance limit crack initiation can account for the majority of total fatigue life however at greater stress amplitudes cracks can initiate early and crack growth will be the substantial part of total fatigue life [276]. Interrupted fatigue tests, described in section 4.6, indicated that fatigue crack initiation occurred at the root of the scribe very early in the fatigue life. This short initiation period is attributed to the large K_t associated with the scribes. Therefore based on the experimental results the modelling assumption would seem valid. Another assumption was the application of long FCGR data to a short crack. This has been discussed in more detail in section 8.1.4.

The FE element model was a 2D representation of the geometry. It was evident on the fracture surface of samples that the crack growth from the root of scribes near the sample edge was influenced by edge effects and possibly a change in stress state, refer to section 4.5. However theses affected were minimised by removal of the scribe near the edges through polishing. However other 3D crack affects were observed on the fracture. The fatigue cracks initiated at multiple sites along the root of the scribe and eventually coalesced with crack growth. This was particularly

noticeable on the interrupted fatigue specimens described in section 4.6. This was not considered in the model but would certainly have had an influence on crack growth for instance semi-circular and elliptical cracks have different beta values than an edge crack. Another assumption of the prediction model was that the fatigue crack propagated with every load cycle. In situ SEM observations by Zhang *et al.* [60] found that small fatigue crack growth in a discontinuous process and that fatigue crack growth may not happen every load cycle. However the interrupted fatigue test results did not indicate discontinuous growth behaviour, this will become more evident when it the FCGR rates derived from the interrupted test measurements are compared with long crack data in section 8.1.4.

8.1.3 When fatigue cracks at the scribe root behave like surface cracks of equivalent length

In section 5.3 an analysis was performed to determine the portion of fatigue crack growth influenced by the scribe geometry. The modelling results implied that close to the root of the scribes the SIF was less than that of a crack of equivalent length advanced from the sample surface. This was due to the scribe geometry altering the surrounding stress field. It was found that when the crack was advanced approximately 7 µm from the root of a scribe 50 µm deep and 15 µm from the root of a scribe 150 µm deep the SIF was equivalent to that of a surface crack of equivalent length i.e. 57 µm and 165 µm respectively.

These lengths represent the extent of crack growth affected by the local scribe root stress field. Cracks of length greater than this will be unaffected by the scribes and will propagate at the same FCGR as a crack initiated from the surface. Indeed the crack growth rates estimated from measurement of striation spacings on the sample fracture surfaces indicated the equivalent FCGR for cracks propagating from the two scribe geometries as shown in Figure 8.3 below (noting striations were not visible in the region close to the root of the scribes).

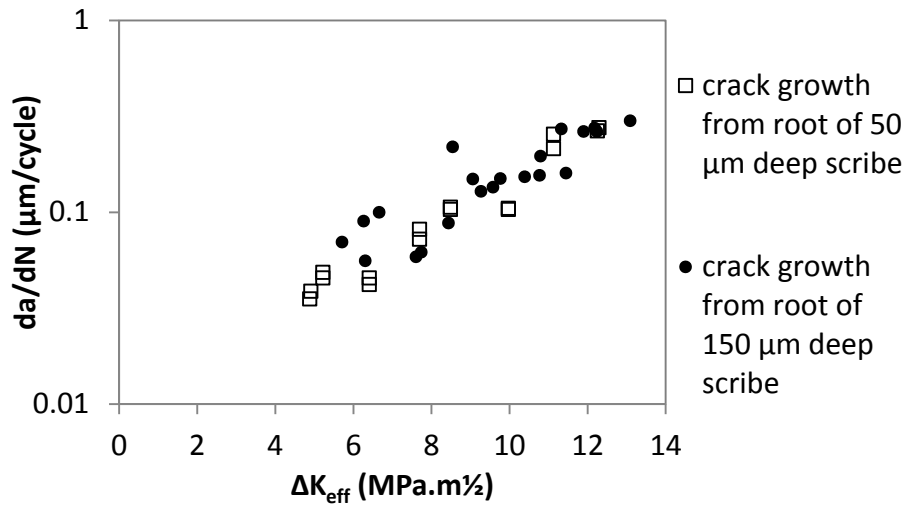

Figure 8.3: FCGR estimated from measurement of striation spacings on fracture surfaces of samples tested in tension-tension

These results are considered together with the interrupted test measurements for the 150 µm deep scribed samples in Figure 8.4 (no measurements were possible for the scribe 50 µm deep). The comparison shows that 8% of the total fatigue life was spent propagating the crack to 15 µm i.e. to the limit of notch affected zone. The first interrupted test measurement for the TOSH peened samples was made after 3.4% of the fatigue life had passed and the crack length had reached 18.7 µm. This indicated that after TOSH peening the crack spent less than 3% of the total fatigue life within the notch affected zone. However the LSP samples were distorted which caused an imbalance to the applied loading induced stress and this could have altered the size of the notch affected zone.

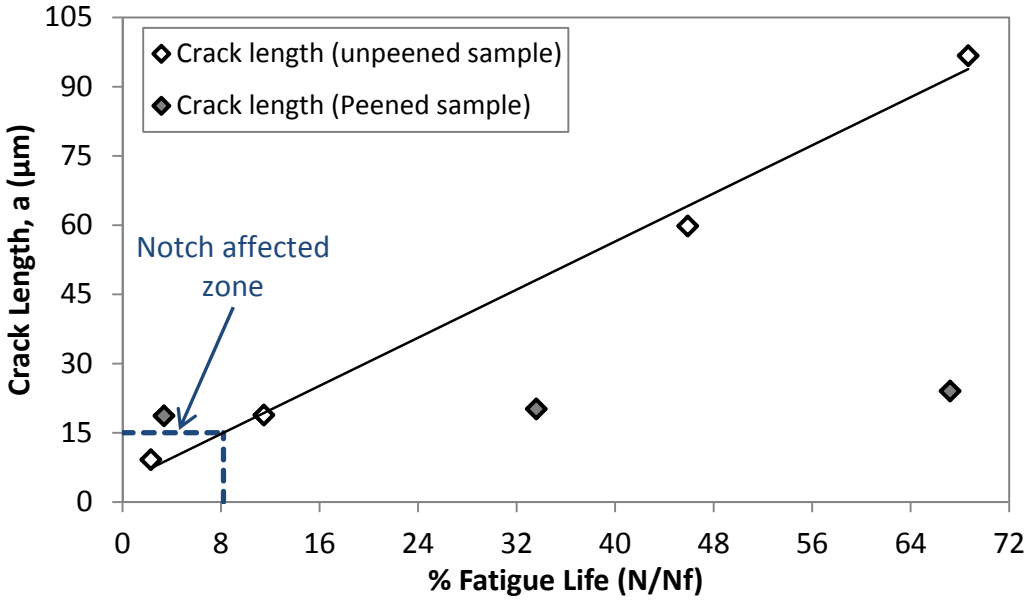

Figure 8.4: Percentage of total fatigue life that crack propagating from root of 150 µm deep scribe is within the notch affected zone

8.1.4 Applying long FCGR data to a short crack problem

The fatigue cracks that propagated from the root of the scribes were short, less than 300 µm at fracture, and propagated in the L-S orientation. Only limited fatigue crack growth rate data in this direction calculated using striation spacing measurements was available at the time of the fatigue life prediction analysis. Therefore fatigue life predictions reported section 7 used Al2024-T351 long crack from the NASMAT material database [275].

Many studies [277,278,279,280] have reported that at equivalent values of stress intensity factor range (ΔK) short fatigue cracks propagate at faster rates than long cracks. The differences are usually greatest at small ΔK values and for negative R ratios. Also short cracks often appear not to have a threshold stress intensity value (ΔK_{th}) and will grow at values below long crack threshold [279,281,282]. The absence of crack closure for short cracks is often cited as having the greatest influence on the difference with long crack behaviour. Indeed FE analysis in section 6 did not predict significant levels PICC for the cracks advanced from the root of the scribes. However some authors [283,283] have attributed the difference between long and short crack growth behaviour in the ΔK_{th} region to load-history effects from residual-plastic deformations caused by the ΔK decreasing test procedure.

FCGR data gathered in the current work is compared with with long crack data from the NASMAT material database [275] and short crack data of Halliday *et al.* [284] in Figure 8.5. The data gathered in the current work was a combination of FCGR data estimated from measurements made on fracture surfaces of striation spacings (data

points between ΔK values of 7 and 13 MPa.m^{½}) and from direct measurement of crack length using interrupted fatigue test (data points less than ΔK of 7 MPa.m^{½}). The crack growth orientation was on the L-S plane. The NASMAT [275] long crack data is for Al2024-T351 material gathered in the L-T direction at an R = 0.1. Halliday's FCGR data was for Al 2024-T351 for cracks that propagated in the L-S direction near the surface and in the L-T direction at peak depth. The samples were tested in four point bend at an R ratio between 0.025 and 0.05.

There was a clear difference between the Halliday [284] short crack threshold behaviour and the NASMAT [275] long crack threshold behaviour shown in Figure 8.5. The long crack had a ΔK_{th} of approximately 3 MPa.m^{½} whereas for the short crack the threshold was not so clearly identifiable. There was also considerable scatter in the short crack data near the threshold region. This is normally attributed to microstructural effects such as inclusions and grain orientations [279,285]. At increased crack length and ΔK short crack scatter reduced and the data merged with the long crack growth data. The short FCG data gathered using interrupted fatigue tests implied the crack was propagating at a faster rate than the short FCG data gathered by Halliday [284]. However since the R ratio used in the current work (0.1) was greater than that used by Halliday (between 0.025 and 0.05) the faster growth rate would be expected. The short crack propagated at a faster rate than the long crack for ΔK between 4.5 and 5.6 MPa.m^{½}. The short crack growth behaviour from the root of the scribes was equivalent to long crack growth data for ΔK values greater than 7.8 MPa.m^{½}. As stated short crack behaviour is most pronounced at small ΔK values so the merging of short and long crack growth at larger ΔK values here is consistent with previous work. However the change of slope of long crack data (i.e. growth rate) appears to occur at a greater ΔK (≈ 7 MPa.m^{½}) than the short crack data (≈ 6 MPa.m^{½}) although only limited data points were gathered in the transition region.

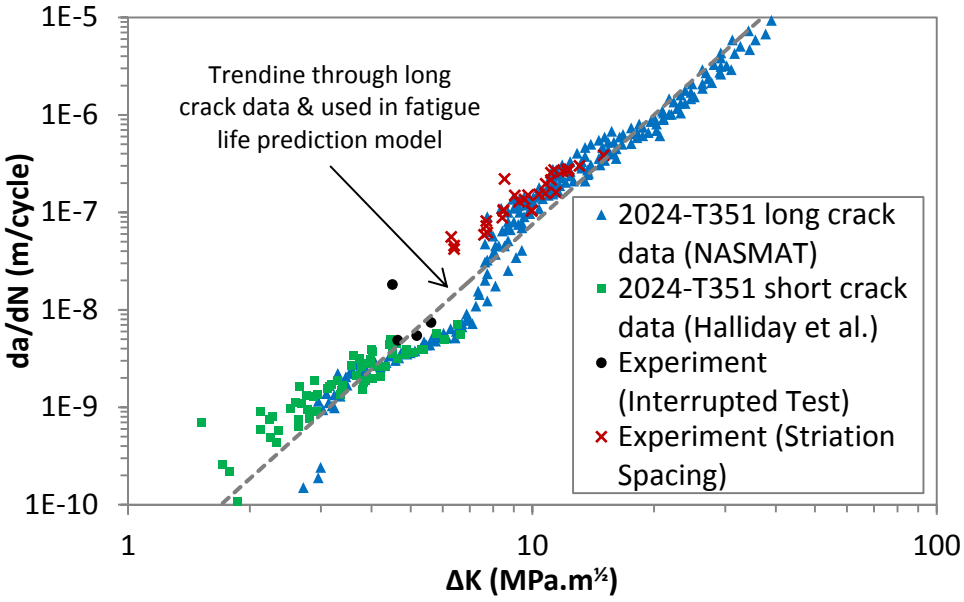

Figure 8.5: Comparison of long and short 2024-T351 FCGR data

8.1.5 The effect of plasticity and residual stress on crack closure and ΔK_{eff}

Plasticity induced crack closure is caused by a reversed plastic wake left behind a fatigue crack propagating under cyclic loading. Hill and Kim [286] noted that residual stress fields affected fatigue crack growth in two distinct ways. Firstly combined with the external applied load it alters the SIF at the crack tip and secondly it changes the crack closure behaviour. Compressive residual stress can act as an additional mechanism to that forces the crack closed. Also the initial strain field that creates the residual stress field alters the shape of the crack faces and this can affect crack closure. The effect on crack closure of residual stress is purely elastic as will be explored further later.

Compared in Figure 8.6 is the COD at the crack tip opening stress level predicted using FE analysis where (A) is the case of external applied loading only and (B) is the case of applied loading combined with the TOSH residual stress field. The external applied loading case demonstrated typical crack opening behaviour. The crack first opened at the crack mouth and as the applied load was increased the crack 'unzipped' towards the crack tip. At K_{op} the crack opened at the tip and this is the shown in Figure 8.6 (A). For a component containing a residual stress field, crack face contact is influenced by the residual strain field in the material. The residual strain field can deform the crack faces and cause the crack to open first at a location between the crack mouth and the crack tip. This behaviour has been described by Beghini & Bertini [80] whom refer to it as partial crack opening. Indeed this behaviour was predicted for a crack advanced through the TOSH residual stress field as shown in Figure 8.6 (B). In this case as the applied load was increased the crack first opened at

a point between the crack mouth and the crack tip. As the load was increased further the crack unzipped towards the crack mouth and tip and eventually it opened at the tip as shown in Figure 8.6 (B). However at this point it still had not fully opened at the mouth. As the applied load was increased even further the crack eventually fully opened.

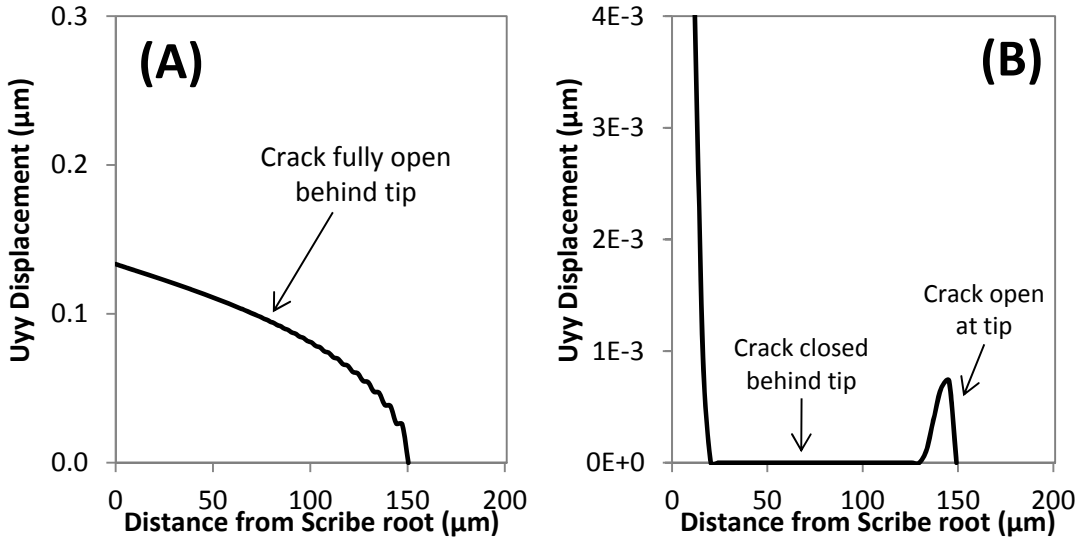

Figure 8.6: COD at K_{op} for (A) applied loading only and (B) applied loading combined with TOSH residual stress field

Jones & Dunn [88] emphasied the effect, if any, of partial crack closure must be taken into account in the FCGR prediction process. For the applied loading only case, K_{op} was simply the SIF when the crack opened at the crack tip. Therefore SIF range (ΔK) was simply K_{max} - K_{op}. For the case including a residual stress field three options are available for definition of ΔK. Considering the crack opening behaviour in TOSH residual stress field described above, K_{op} could be defined in three ways. K_{op} could be the SIF when the crack first opens, it could be defined as the SIF when the crack opens at the crack tip or it could be defined as the SIF when the crack is fully open. In the current work the second option was chosen as it was assumed that it is only the SIF range experienced at crack tip that would be the damaging part of the cycle regardless of any partial closure behind the tip.

The predicted crack opening behaviour of a crack advanced through the TOSH residual stress field is shown Figure 8.7. Compared is the crack opening level predicted using elastic material properties and elastic-plastic material properties in the FE model. The predicted opening levels are equivalent for crack lengths up to 240 µm. As noted [85] when a crack grows in a component without compressive residual stress it leaves behind a plastic wake. When compressive residual stress is present the residual stress acts as closing mechanism that forces the crack closed and therefore

reduces the amount of plastically at the crack tip. This results in an opening stress due to plasticity that is less than the original opening stress level in the absence of an initial residual stress field [85]. At crack lengths greater than 240 µm the closure level is greater for the elastic-plastic material. This is because the compressive residual stress field was lower in magnitude at this depth and therefore there was more plasticity at the crack tip. In contrast a tensile residual stress field would result in greater plastically material at the crack tip than applied loading alone however a tensile residuals field would naturally reduce the crack closure behaviour.

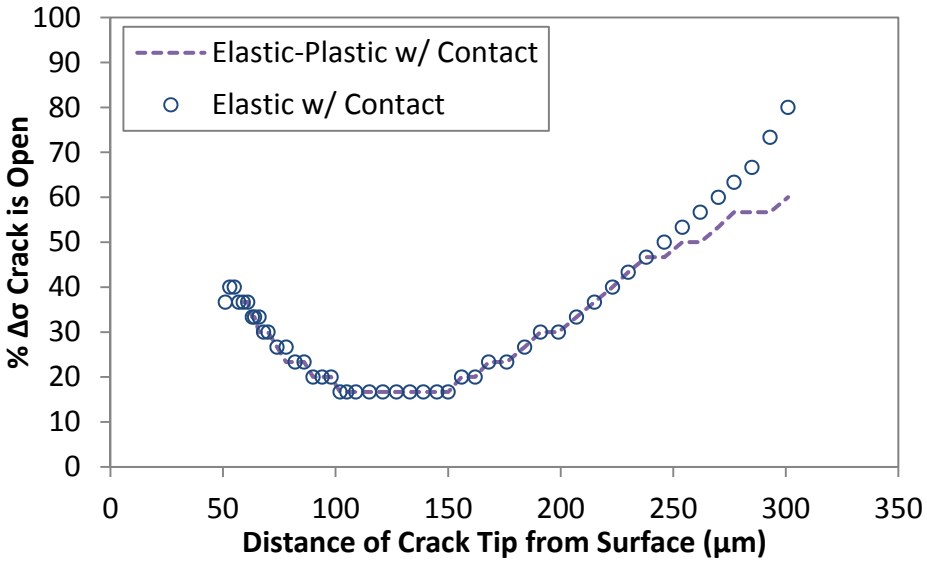

Figure 8.7: Effect on crack open level of residual stress predicted using elastic and elastic-plastic FE models.

8.2 Comparison of Measured and Predicted Fatigue Lives

Some authors have attempted to predict the effect on fatigue life of residual stress for instance Zhao *et al.* [235] simulated a residual stress field induced via LSP using FE analysis. The residual stress field along the crack path was used in a crack growth program to determine fatigue life. This method did not consider the effect of residual stress redistribution with crack advance and no comparison was made to experimental data. Liu *et al.* [287] used a cohesive zone FE model to study the effect on crack growth of residual stress induced via shot peening. Retardation of fatigue crack growth increased with greater shot peening intensity however again no comparison was made with experimental data.

Claudio *et al.* [288] developed three models to study the effect of shot peening induced residual stress on crack initiation, early crack propagation, and long crack propagation separately. The specimens contained scratches 50 or 100 µm deep with 50 µm root radius (k_t of 3.98 and 5.03 respectively). Similar to the current work they concluded that shot peening had a limited effect on crack initiation especially for

scratched geometries. This was due to cyclic relaxation of the shot peening effect at the surface and was in agreement to other author's findings [289,290]. Predicted fatigue lives were within a factor of 1.8 of experimental lives. The prediction method used was similar to the current study i.e. Paris law used based on experimental material constants and K was calculated using FEA and included crack closure effects. However their model did not consider residual stress redistribution with crack advance and this was cited as one potential source of error.

In section 6 three methodologies to determine the stress intensity factor range (ΔK) and the stress ratio (R) were defined namely the superposition method, the modified superposition method, and the Newman crack closure approach. In section 7 fatigue lives were predicted using the Walker or Paris fatigue crack growth equations based on experimental 2024-T351 aluminium FCGR curves. Also proposed in section 7 was a fatigue life prediction methodology based on elastic-plastic FE crack closure analysis. Fatigue lives were predicted for samples scribed to 50 and 150 µm depth in the unpeened condition and with MIC1, MIC3, UPM and TOSH LSP treatments.

The experimental measured fatigue lives are compared to predicted fatigue lives in Figure 8.8 based on ΔK and R calculated using (A) superposition method, (B) modified superposition method and (C) the Newman crack closure approach. In the figures a scatter factor is shown that encompasses the predicted lives (note: the TOSH lives were ignored in determining the scatter factor as sample failure occurred remote from the scribe and these experimental lives are considered run outs).

Firstly consider Figure 8.8 (A) based on the superposition method. For superposition crack face contact is not considered and ΔK is therefore unaffected by the residual stress field. The only effect on predicted fatigue life of the residual stress field is caused by changes to R (i.e. R_{eff}). The predicted fatigue lives were conservative and less than the measured fatigue lives. A scatter factor of 3 encompassed the predicted fatigue lives as shown Figure 8.8 (A).

Consider Figure 8.8 (B) based on the modified superposition method. For modified superposition both ΔK and R are affected by the residual stress field i.e. $K_{tot,min}$ less than zero is set equal to zero. In most instances the predicted fatigue lives were less than measured lives. The predicted fatigue lives were however closer to measured lives than for the superposition method. A scatter factor of 2.5 encompassed the predicted fatigue lives. Predicted fatigue lives of the TOSH residual stress field were at least 6× greater than the measured fatigue lives.

Next consider Figure 8.8 (C) based on the Newman crack closure approach. As for modified superposition in most instances the predicted fatigue lives were less than the measured fatigue lives. A scatter factor of 2 encompassed the predicted fatigue

lives. Again the fatigue lives predicted for the TOSH residual stress field were greater than measured fatigue lives.

In Figure 8.9 is a comparison of the experimental lives and predicted lives using the elastic-plastic FE analysis. The predicted fatigue lives were conservative and fit within a scatter factor of 2.5. The predicted fatigue lives for the TOSH residual stress field were far greater than those measured.

Similarily Jones & Dunn [88] considered FCGR through residual stress field. They compared experimental FCGR data to three LEFM approaches: (1) superposition method, (2) modified superposition and (3) superposition contact method using FE analysis. The superposition contact method resulted in the closest agreement with experimental to a factor of 2 to FCGR data and 1.2 to fatigue life.

In all cases the fatigue lives predicted for MIC peening were less than measured fatigue lives and in some cases the predicted fatigue lives were actually less those predicted for unpeened samples. This is unsurprising considering the comparatively little compressive residual stress induced via MIC peening (refer to Figure 4.8). However experiments showed MIC peening did in fact increase fatigue life compared to unpeened samples. The MIC peened samples were visibly more distorted than any of the other peened samples. Unfortunately these samples were tested early in the project and prior to the influence of distortion on the applied stress range being appreciated. As such the effect on the applied stress range of MIC induced distortion was not characterised. As has being mentioned sample distortion reduces the applied stress range on the peened face and so artificially increases fatigue performance. It is probable, considering the induced residual stress fields, the majority of fatigue performance improvement in the case of MIC peening was due to LSP induced sample distortion and not the induced residual stress fields. It is also worth noting from Figure 8.8 and Figure 8.9 that the outlying predicted fatigue lives increasing the scatter factors were for MIC peening. Had the effect on applied stress of the LSP distortion been characterised during the experiments a modified prediction methodology could have been adapted similar to that used to account for UPM induced distortion as described section 7.1.1. Correcting for measured applied stress range would increase predicted fatigue lives for MIC peening and hence reduce the scatter factor.

From Figure 8.8 and Figure 8.9 initially it appears the prediction methodologies overestimated the effect on fatigue performance of TOSH peening. The TOSH peened fatigue samples did not fracture at the scribes but instead due to crack initiation on the unpeened face and remote from the peened area. However a fatigue crack had initiated at the root of the scribe. Interrupted fatigue tests indicated that after an

initial period of crack growth the fatigue crack stopped propagating (or at least the FCGR reduced significantly) likely due to the compressive residual stress field induced via TOSH LSP. The behaviour of the fatigue crack at the root of the scribe was predicted by the model noting the model. The model was not created to predict crack initiation remote from the scribe.

Fatigue samples scribed to 50 µm depth and peened using UPM LSP also did not fracture at the scribe but instead due to crack initiation on the unpeened face. However predicted fatigue lives (based on crack initiation at the root of the scribe) were similar to experimental measured lives and the modelling results did not indicate the residual stress field was great enough to arrest FCG as for TOSH peening. A fatigue crack was observed using SEM to have initiated at the root the scribe. It is possible that the greater stress range on the unpeened face (due to the distortion) resulted in fracture before the crack propagating from the scribe root reached a critical length to cause fracture. This theory could be explored further through interrupted fatigue tests however no spare UPM peened samples were available for testing.

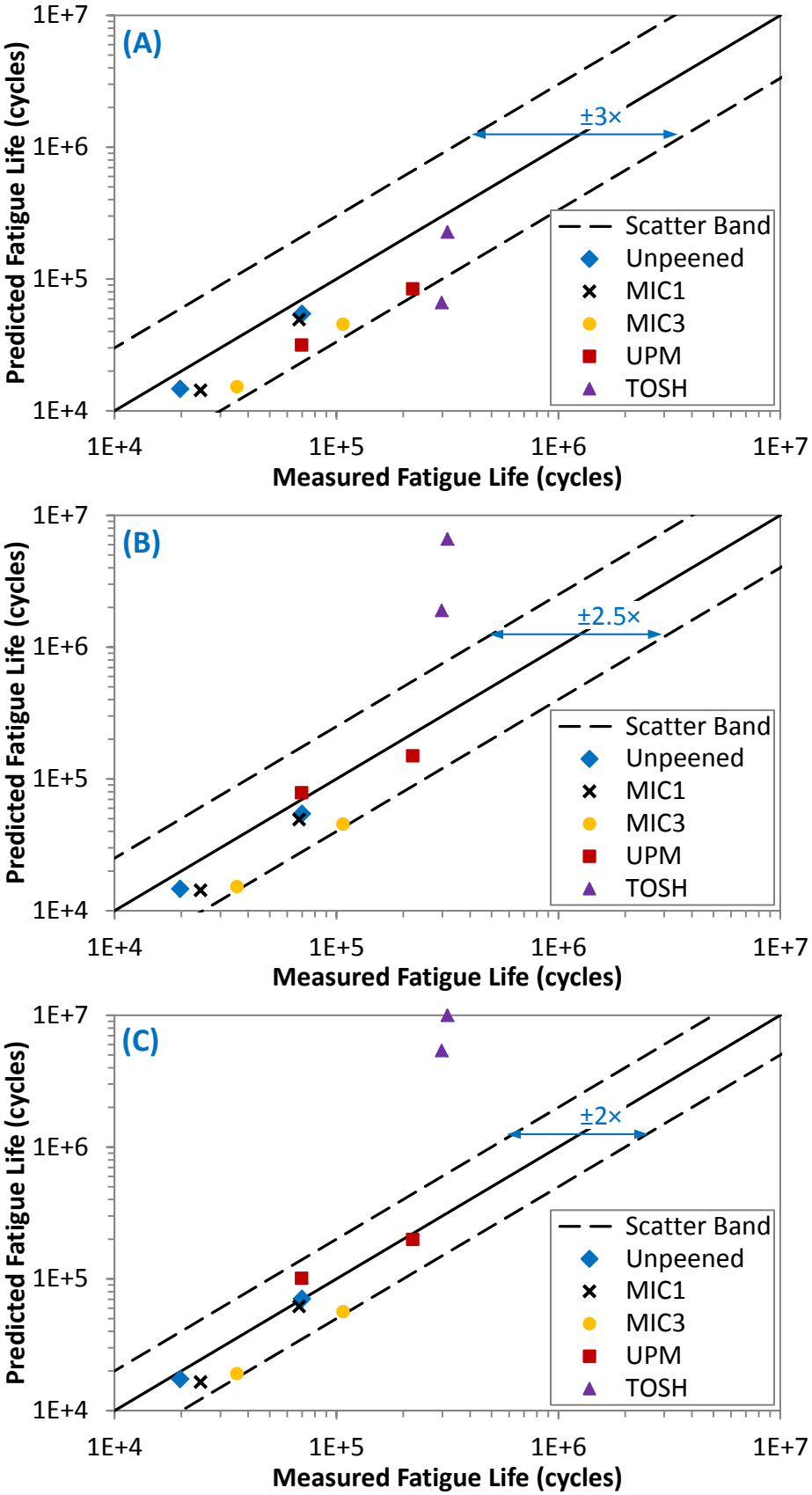

Figure 8.8: Comparison of measured fatigue life to fatigue life predicted using (A) superposition, (B) modified superposition and (C) Newman crack closure

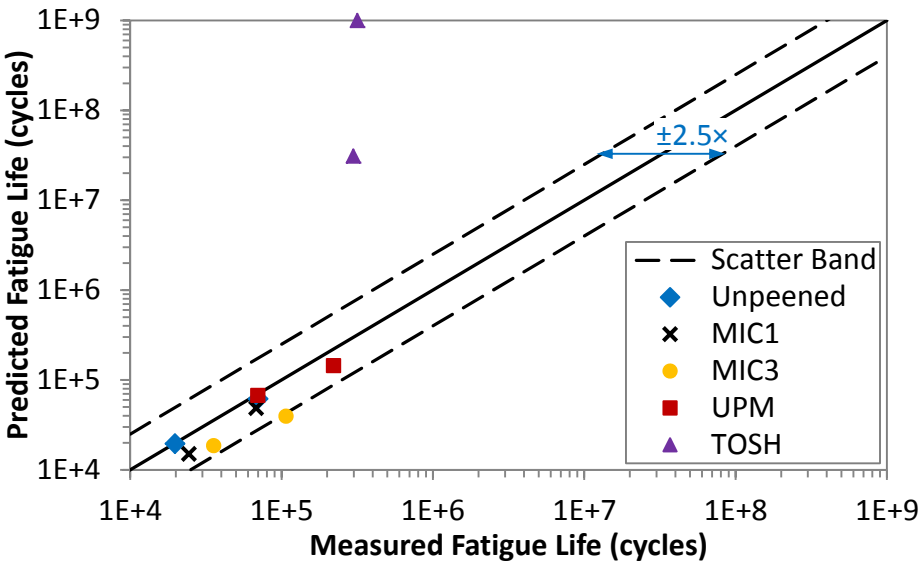

Figure 8.9: Comparison of measured fatigue life to fatigue life predicted using crack closure based elastic-plastic FE analysis

8.3 Predicted Optimum Residual Stress Field

A sensitivity study on fatigue life of residual stress was performed and detailed in section 7.2 and 7.3. The aim of the study was to determine the optimum residual stress field that restored the fatigue performance of scribed samples back to that of pristine material. The study considered four characteristics of the residual stress field namely the compressive residual stress field depth, maximum compressive residual stress, position of maximum compressive residual stress relative to peened surface and the near surface residual stress field.

The sensitivity study considered the effect of these characteristics on a crack advanced from a scribe 150 µm deep only. An assumption was made that a residual stress field that recovered the fatigue performance of material with a scribe 150 µm deep to that of pristine material would also recover the fatigue performance of material with a scribe 50 µm deep.

The results of the sensitivity study indicated that to achieve significant enhancement of fatigue performance residual stress must be greater than 120 MPa in compression. The maximum compressive residual stress induced by the MIC1, MIC3 and UPM treatments was 5, 44 and 106 MPa respectively i.e. all were less than the 120 MPa threshold as indicated in Figure 8.10. The fatigue lives of samples scribed to 150 µm depth with these treatments increased by a factor of 1.2, 1.8 and 3.4 respectively. In contrast the compressive residual stress induced by the TOSH LSP treatment was greater than 120 MPa between 30 µm and 230 µm from the peened surface and the fatigue lives of samples with this treatment increased by a factor of 15.

The results of the sensitivity study indicated that compressive residual stress was most effective within 250 µm from the peened surface; a marker line indicates this depth in Figure 8.10. This is because the SIF at the crack tip will increase rapidly as the crack propagates from the root of the scribe as shown in Figure 5.5. The aim of the compressive residual stress is to reduce the SIF at the crack tip. To do this most efficiently it is desiravle to induce a large compressive residual stress field in the area where the crack length is still short and ΔK small i.e. within 250 µm from the peened surface as indicated by the sensitivity study. For the MIC1 treatment the residual stress field is tensile at depths greater than 250 µm. The residual stress field induced by MIC3 and UPM LSP treatments are significantly in compression at depths greater than 250 µm. This compressive stress will have little effect on fatigue performance since the K_{res} induced is small and ΔK_{app} is large. The TOSH induced residual stress field is compressive until 350 µm from the peened surface however the majority of the compressive residual stress field is located closer than 250 µm to the peened surface.

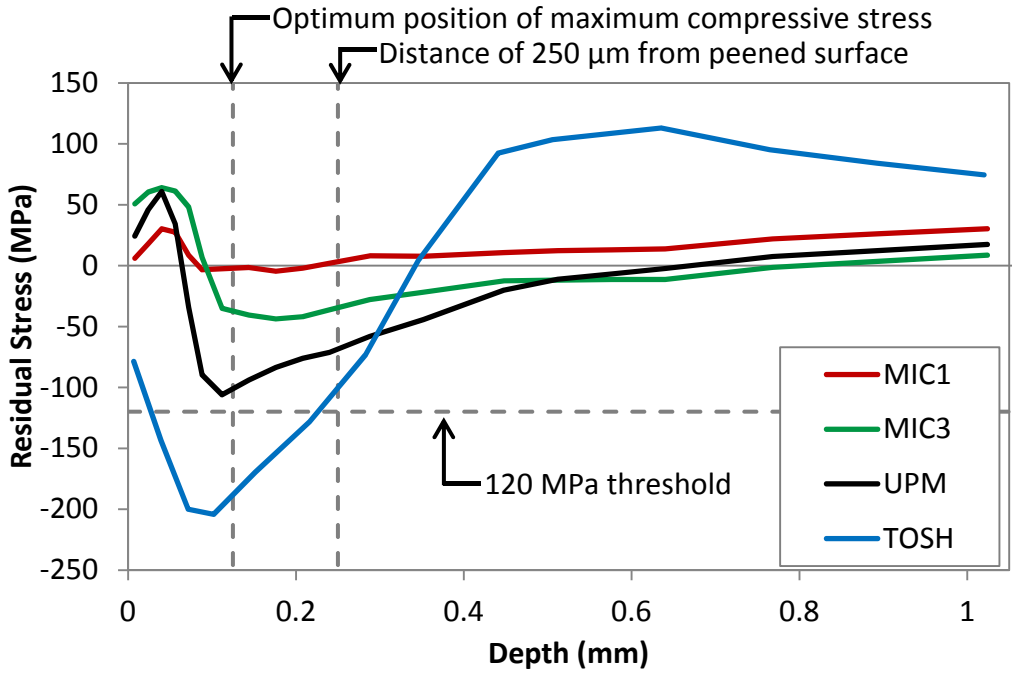

Figure 8.10: LSP induced residual stress fields used in fatigue tests as measured by Toparli [132] compared with sensitivity study requirements

The results of the sensitivity study indicated the optimum position for the peak compressive residual stress was between 100 and 125 µm from the peened surface. The peak compressive residual stress induced by the MIC1 and MIC3 peening was actually located 176 µm from the peened surface for both treatments. The peak compressive residual stress after UPM and TOSH LSP was located 112 and 100 µm from the peened surface respectively.

Finally the results of the sensitivity study indicated that residual stress behind the crack tip can affect fatigue performance. It is therefore desirable to have compressive residual stress at the surface and balancing tensile residual stress located deep in the section i.e. preferably greater than 250 from the surface. The MIC 1 row, 3 row, and UPM LSP treatments all induced tensile residual stress in the near surface region whereas the residual stress field induced by TOSH LSP was compressive from the surface.

The TOSH LSP treatment was the only treatment developed after the sensitivity study was performed and the findings of the study were actually used as targets to be met by the peening provider. It is clear that the TOSH LSP treatment fulfils all of the requirements set by the sensitivity study and indeed provided the greatest increase in fatigue life of the LSP treatments tested. Although fatigue crack initiation still occurred at the root of the scribes, interrupted fatigue tests demonstrated that the induced compressive residual stress field arrested crack propagation and the samples only failed due to crack initiation remote from the scribe caused by distortion related effects. Fatigue tests performed in four point bend avoided the distortion issues and demonstrated the fatigue performance of scribed material after TOSH LSP treatment was equivalent to that of pristine material.

8.4 Discussion of Experimental Results

The results of fatigue tests in tension-tension and four point bend are compared in Figure 8.11 where (A) are samples that contained scribes 50 µm deep and (B) are samples that contained scribes 150 µm deep. In the figure three sample conditions are compared. These are unpeened, peened using UPM LSP treatment and peened using TOSH LSP treatment.

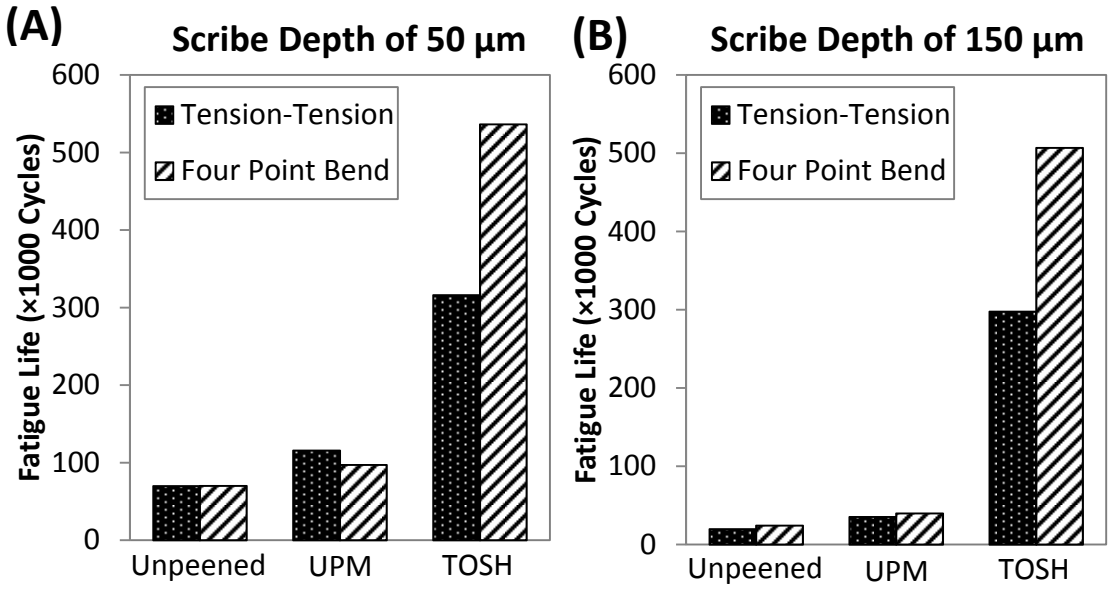

Figure 8.11: Comparison of tension-tension and four point bend fatigue lives for (A) samples scribed to 50 µm depth and (B) 150 µm depth

Firstly consider the unpeened samples. Fracture occurred at the scribe in all samples. The percentage difference between the fatigue lives of samples tested in four point bend and tension-tension was 0.2% and 18% for samples with scribes of 50 µm and 150 µm depth respectively. Measured fatigue lives were within scatter normally associated with fatigue tests. This implied that the two applied loading conditions provided comparable results.

Next consider samples with UPM LSP treatment in Figure 8.11. Firstly note that the tension-tension results are for samples that received no edge rework as this was the same condition tested in four point bend. In all tests fracture of the samples occurred at the scribe. The percentage difference between fatigue lives of samples tested in four point bend and tension-tension was 16% and 11% for samples with scribes of depth 50 µm and 150 µm respectively. Again differences between the fatigue lives measured in bending and tension-tension is within the scatter associated with fatigue tests.

Finally consider samples with TOSH LSP treatment in Figure 8.11. The samples tested in tension-tension failed due to fatigue cracks that initiated on the unpeened face. As described in section 4.5 this was attributed to the greater stress range experienced on the unpeened face due to residual stress induced distortion. However a fatigue crack was observed using an SEM to have initiated at the root of the scribes (see Figure 4.22 and Figure 4.23). The fatigue lives of samples scribed 50 and 150 µm deep tested in four point bend was 70% greater than for samples tested in tension-tension. In four point bend the unpeened surface is in compression and therefore inhibits

crack initiation on the unpeened face due to the residual stress induced distortion. The samples tested in four point bend fractured due to crack initiation caused by fretting at the position of the contact rollers. A pristine sample tested in four point bend also fractured due to crack initiation caused by fretting at the contact rollers. The fatigue life of the pristine sample was 550,114 cycles as reported in section 4.4. The average fatigue life of the four samples tested in four point bend was 521,546 cycles or 95% of the pristine life. However since fracture was due to crack initiation isolated from the scribe it can be concluded that the LSP treatment restored the fatigue life to that of pristine material.

The interrupted fatigue tests showed that the LSP induced residual stress field had no effect on fatigue crack initiation at the root of the scribes. Fatigue performance was determined through a combination of the effect on crack growth of the induced compressive residual stress field and the resultant specimen distortion. For instance the limiting factor on fatigue life of the TOSH LSP treated samples tested in tension-tension was the resultant distortion. The distortion caused an imbalance of the applied stress range on the peened and unpeened surfaces. The resultant stress range on the unpeened surface was greater than intended and therefore caused premature crack initiation and failure of the specimens. The four point bend results indicated that if the LSP induced distortion can be reduced whilst maintaining a similar residual stress profile in the region of the scribe, the fatigue life measured in tension-tension would increase as predicted by the fatigue life model. This could be achieved by reducing the width of the peening patch which would reduce sample distortion and should still maintain the same level of residual stress.

8.5 Notch Effects

In section 4.3 fatigue tests were performed at reduced maximum applied stress to study the effect on fatigue strength of 50 and 150 µm deep scribes. The results are compared with those of Nader [31] in Figure 8.12 below. Nader tested 2024-T3 aluminium samples under constant amplitude loading at R = 0.1. The specimens contained scribes of root radius of 83 µm and wall angle of 90° (note: in the current work the scribe root was 5 µm and wall angle 60°). Nader set the fatigue limit as 10^6 cycles whilst in the current work it was 10^7 cycles.

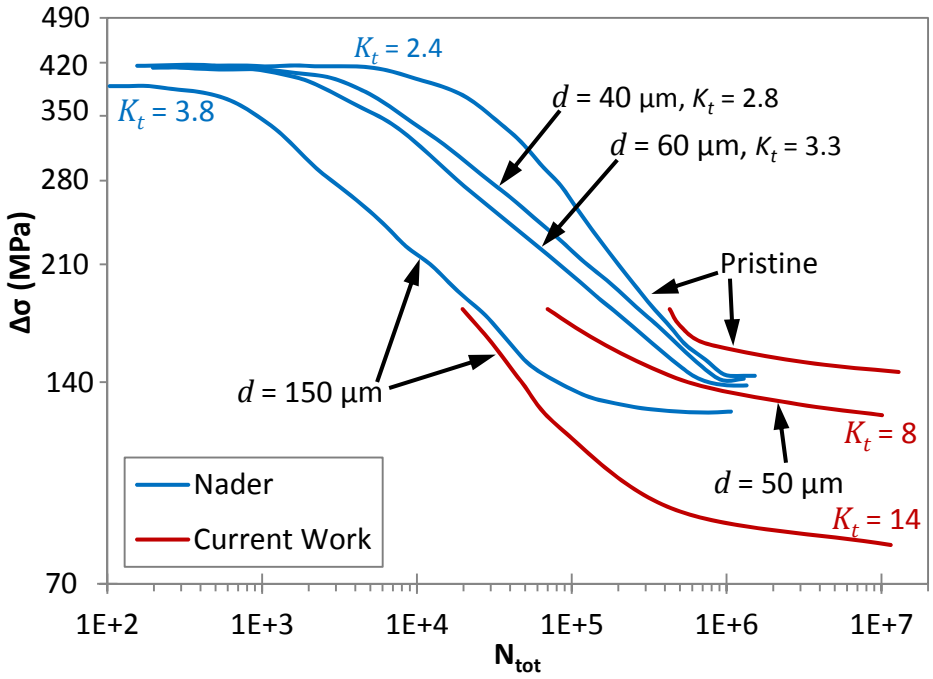

Figure 8.12: S-N curve for scribed components compared to results of Nader [31]

It is clear from Figure 8.12 that unscribed samples were more resistant to fatigue damage than scribed samples. As the depth of the scribe was increased fatigue life decreased as did fatigue strength. However there are differences between Nader's results and the current work. For instance the endurance limit of a scribe 50 µm deep (K_t = 8) was 140 MPa roughly equivalent to the endurance limit of Nader's scribe 150 µm deep (K_t = 3.8). The fatigue strength at 10^5 cycles of a scribe 50 µm deep was 170 MPa whereas for Nader's scribe 150 µm deep it was only 135 MPa despite having a smaller K_t. These results imply that fatigue strength was not solely a function of scribe depth or K_t. Nader's scribes were created using a modified milling process. It is likely that differences in the results were caused by residual stress induced during scribing.

The fatigue tests at reduced stress range allowed for calculation of the fatigue stress concentration factor (K_f) and the notch sensitivity factor (q). K_f is the ratio of the endurance limit of an unnotched specimen to the endurance limit of a notched specimen tested under the same conditions. K_f is calculated using equation 8.1 below [7]. q is a measure of agreement between K_f and K_t and is calculated using equation 8.2 below [7]. Where β is a characteristic material parameter and ρ is the radius of the notch root. If q = 0 then K_f = 1 and the material has no sensitivity to notches whereas if q = 1 then $K_f = K_t$ and the material has full notch sensitivity.

$$K_f = \frac{Endurance\ Limit\ Unnotched}{Endurance\ Limit\ Notched} \qquad (8.1)$$

$$q = \frac{1}{1 + \beta/\rho} = \frac{K_f - 1}{K_t - 1} \qquad (8.2)$$

Using the experimental data from Figure 8.12 K_f of 1.2 and 1.8 was calculated for the scribes 50 and 150 µm deep respectively. As stated previously the fatigue geometric stress concentration factor (K_t) associated with the 50 µm and 150 µm notches was calculated as 8 and 14 respectively i.e. approximately 7× greater than K_f. Hertzberg *et al.* [7] stated that K_f increases slower than K_t with decreasing notch root radii and attributed this to a lack of distinction made between fatigue crack initiation and fatigue crack propagation processes. Therefore it is unsurprising that there are large differences between K_f and K_t observed in the current work since it has been demonstrated that there was no initiation period for fatigue cracks at the root of the scribes.

From equation 8.2 a q of 0.03 and 0.06 was calculated for the 50 and 150 µm deep scribes respectively. There is a discrepancy between calculated q values for samples with 50 and 150 µm deep scribes. Determining the endurance limit of aluminium is difficult as it is not as distinct as for ferrous metals. In addition limited samples were available for the S-N tests and ideally more samples were required to determine precisely the endurance limit at 10^7 cycles. A q of 0.11 was measured [33] for 2024-T3 aluminium with scratches between 40 and 150 µm deep with a root radii of 83 µm. Therefore q measured in the current work is less even though the radius of the notch root is smaller i.e. the material is less sensitive to the sharper notch. Similar observations are well publicised [7].

The fatigue stress concentration factor can be predicted using equations 8.3 and 8.4 from Neuber [291] and Peterson [292] respectively. The notch geometry is defined by the stress concentration factor (K_t) and the root radius, ρ. The material constants, c_n and c_p were taken as c_n = 1270 µm and c_p = 635 µm for 2024-T3 aluminium [293].

$$K_f = 1 + \frac{K_t - 1}{1 + \sqrt{\frac{c_n}{\rho}}} \qquad (8.3)$$

$$K_f = 1 + \frac{K_t - 1}{1 + \frac{c_p}{\rho}} \qquad (8.4)$$

Predicted and experimental fatigue stress concentration factors using Nader's data [31] and results from the current work are compared in Table 8.1. Both predicted and experimental K_f increased with increasing notch depth and K_t. The K_f values for the samples in the current work were greater than those of Nader at the same scratch depth due the difference in scribe root radius as explained earlier in terms of q. The Neuber rule generally overestimated K_f compared to the experimental K_f from the

current and Nader's work. Predicted K_f were within -2% and +28% of experimental K_f. The Peterson rule again overestimated Nader's experimental K_f (+5% to + 15%) however were closer than those predicted using the Neuber rule. For the current work the Peterson rule underestimated K_f by up to -63%. It has been noted [294] that since both the Neuber and Peterson rules are empirical fitting equations they have limitations when the empirical constants are not directly calibrated with experiments.

Table 8.1: Comparison of K_f predicted using Neuber and Peterson rules with experimental K_f

	Scratch Geometry				Test	Neuber		Peterson	
	d [μm]	ρ [μm]	θ [deg]	K_t	K_f	K_f	e [%]	K_f	e [%]
Nader	40	83	90	2.45	1.01	1.29	22	1.17	13
	60	83	90	2.77	1.04	1.36	24	1.20	14
	100	83	90	3.29	1.08	1.47	27	1.26	15
	150	83	90	3.81	1.13	1.57	28	1.32	14
	225	83	90	4.45	1.33	1.70	22	1.40	5
Current	50	5	60	8.07	1.2	1.42	15	1.05	-14
	150	5	60	13.95	1.8	1.76	-2	1.10	-63

It is well established that residual stress fields induced by cold working such as shot and laser peening can increase the endurance limit of the material [35,140,142,156,158,160,176,203,295,296]. Some authors [297-302] have investigated the effect on the endurance limit of notched components with residual stress fields. Xu *et al.* [297,298] tested shot peened notched specimens (K_t = 2.85) and compared the results to predictions based on Neuber rule to assess local stress and strains and the Goodman criterion to account for mean stress. The predicted values of fatigue strength were within 15% of the experimental values. Benedetti *et al.* [299] considered shot peened notched 7075 aluminium (K_t = 1.53 and 2.33). They measured greater increase of notch fatigue strength due to the induced residual stress field for the more critical notches. It was beyond the scope of the current work to investigate the effect on endurance limit of notched components with residual stress due to the quantity of samples required and the expense of the peening treatment. However a recommendation has been made for future work.

9 Conclusions

The following conclusions are made based on the research presented.

1. The number of cycles to failure of dogbone shaped samples 2mm thick and scribed to a depth of 50 µm reduced 84% compared to the pristine material. For samples scribed to 150 µm depth the cycle to failure reduced by 95%. The failure of the scribed samples was caused by fatigue crack initiation the root of the scribes and propagation of the crack thought thickness until fracture.

2. The threshold fatigue limit of pristine clad 2024-T351 aluminium 2mm thick was was 145 MPa at an R of 0.1. The fatigue limit reduced by 14% to 125 MPa for samples that contained scribes 50 µm deep and by 45% to 80 MPa for samples that contained scribes 150 µm deep.

3. The effect of laser shock peening on fatigue life of scribed samples varied from a further 3% reduction on scribed fatigue life to a 74% recovery of the pristine material life. Failure for the majority of samples was caused by fatigue crack initiation at the root of the scribes. However samples that had the greatest fatigue life recovery, failure was caused by crack initiation remote from the scribes and on the unpeened face. This initiation was caused by an increased applied stress range on the unpeened face resulting from sample distortion induced during peening.

4. Fatigue tests performed in four point bend avoided distortion related issues experienced in tension-tension. In the best case the fatigue life of peened samples was equivalent to that of the base material. However in these instances the fatigue crack initiation that caused sample fracture initiated due to fretting between the sample surface and the contact rollers of the test jig.

5. Analysis of sample fracture surfaces indicated that LSP had no effect on fatigue crack initiation behaviour at the scribes but did reduce the FCGR. In fact interrupted fatigue tests indicated that for some peened samples the induced compressive residual stress field fully arrested fatigue crack propagation from the root of the scribes.

6. A finite element model was developed based on elastic material properties that used virtual crack closure technique for calculation of stress intensity factors. Crack advance was modelled through a node release scheme. It was found when a crack advances 7 µm from the root of a scribe 50 µm deep and 15 µm from the

root of a scribe 150 µm deep that the SIF is equivalent to a crack of the same length i.e. 57 µm and 165 µm respectively.

7. The superposition, modified superposition and Newman crack closure methodologies as a basis for fatigue crack growth prediction were compared. The Newman crack closure approach resulted in the closest correlation between experimental and predicted fatigue lives which were within a factor of two difference.

8. A Finite element model that used elastic-plastic material properties and contact conditions along the crack path was developed to study the effect of residual stress on crack closure. In the unpeened condition the crack was open for a minimum 93% of the applied load cycle. In comparison the crack was open for a minimum 17% of the applied load cycle in the most compressive of the residual stress fields studied. The analysis showed that the shape of the residual stress field can influence the behaviour of the crack face contact behind the crack tip.

9. A sensitivity study was performed that determined the residual stress field to restore the fatigue life of scribed material back to that of pristine unscribed material. It was found that residual compressive stress of at least 120 MPa is required, that the compressive peak stress located between 100-125 µm from the surface is most effective and that compressive stress greater than 250 µm from the surface has no effect on fatigue performance.

10 Recommendations for Future Work

In this section recommendations are proposed for future work.

1. The fatigue life of the peened samples tested in tension-tension was limited by LSP induced sample distortion and resultant increased applied stress range this caused on the unpeened face. Eliminating or reducing distortion would extend fatigue lives of the peened and scribed samples assuming the residual stress profile is maintained. This could be achieved through further refinement of the LSP processing parameters. A narrower LSP strip width would also reduce distortion however this could affect the induced residual stress field.

2. The effect on material fatigue strength of 50 µm and 150 µm deep scribes was investigated. The effect on fatigue strength of material scribed and then peened could be investigated experimentally and results compared to predictions of fatigue strength.

3. The experimental residual stress field data used in the fatigue life prediction models were measured on unscribed samples. A rebalancing operation was performed during the first step of the FE analysis to redistribute the residual stress field around the scribe. A complete residual stress field measurement including around the scribe could greatly improve prediction of fatigue lives. During the research no current method for residual stress measurement was capable of measuring the residual stress field at the scribe however future advances may make this possible with the contour method currently looking the most promising.

4. Validation of predicted crack closure levels by comparison to experimental measurements of crack closure. Remote crack tip closure in the presence of the residual stress fields could make measurement of crack closure even more difficult. No such issue would be expected for samples in the unpeened state.

5. Development of a method to determine the SIF for situations that include external applied stress and internal stress (i.e. residual stress) in FE models that use elastic-plastic material properties.

6. Other variables could be considered in the residual stress field sensitivity study. This could include variables such as the effect of residual stress on sample distortion and on crack closure level.

7. In the current work the size of the notch affected zone was investigated using FEA for notches of depth 50 µm and 150 µm with 5 µm root radius. This work could be expanded on to determine the effect on the notch affected zone for notches with the same K_t but different notch dimensions i.e. depth and root radii.

11 References

1. Transport Canada (2004) *Paint and sealant removal process*, Airworthiness Notice No. B071.
2. Federal Aviation Administration (2010) Airworthiness Directive No. FAA-2009-0913.
3. Department of Civil Aviation Malaysia (2005) *Multiple "scribe mark" scratches*, Airworthiness Notice No. 91.
4. Das, G.K., Kosai, M., Miller, M. 2007 "Development of a method for damage tolerance analysis for scribe marks adjacent to fuselage longitudinal and circumferential splices", in Lazzeri, L. and Salvetti, A., eds., *24th Symposium of the International Committee on Aeronautical Fatigue*, Naples, Italy, 16-18 May, p. 306-321.
5. Flight Global (2004) *FLS denies paint-strip damage led to Ryanair aircraft retirement* [online], available: http://www.flightglobal.com/news/articles/fls-denies-paint-strip-damage-led-to-ryanair-aircraft-177379/ [accessed 05/12/2012].
6. Anderson, T.L. (2005) *Fracture Mechanics Fundamentals and Applications*, 3rd ed., CRC Press.
7. Hertzberg, R.W., Vinci, R.P. and Hertzberg, J.L. (2012) *Deformation and Fracture Mechanics of Engineering Materials*, 5th ed., John Wiley & Sons.
8. Griffith, A.A. 1920 "The phenomena of rupture and flow in solids" *Philosophical Transactions*, Series A, vol. 221, pp. 163-198.
9. Janssen, M., Zuidema, J. and Wanhill, R. (2004) *Fracture mechanics,* 2nd ed., CRC Press.
10. Suresh, S. (1998) *Fatigue of Materials*, 2nd ed., Cambridge: Cambridge University Press.
11. Schijve, J. (2009) *Fatigue of Structure and Materials*, 2nd ed., Springer.
12. Paris, P.C. & Erdogan, F. 1960, "A critical analysis of crack propagation laws." *Journal of Basic Engineering*, vol. 85, pp. 528–534.
13. Walker, K. 1970, 'The effect of stress ratio during crack propagation and fatigue for 2024-T3 and 7075-T6 aluminum," *ASTM STP 462*.
14. Forman, R.G., Hearney, V.E., & Engle, R.M. 1967, "Numerical analysis of crack propagation in cyclic-loaded structures," *Journal of Basic Engineering*, vol. 89, pp. 459-464.
15. Klesnil, M. & Lukas, P. 1972, "Influence of strength and stress history on growth and stabilistaion of fatigue cracks" *Engineering Fracture Mechanics*, vol. 4, pp. 77-92.
16. Forman, R.G. & Mettu, S.R. 1992, "Behavior of surface and corner cracks subjected to tensile and bending loads in Ti-6A1-4V alloy," *ASTM STP 1131*.

17. Pearson, S. 1975 “Initiation of fatigue cracks in commercial aluminium alloys and the subsequent propagation of very short cracks”, *Engineering Fracture Mechanics*, vol. 7, no. 2, pp. 235-247.
18. Ritchie, R.O. & Lankford, J. 1986 “Overview of the small crack problem”, in Ritchie, R.O. & Lankford, J., eds., *Proceeding of Small Fatigue Cracks*, The Metallurgical Society, Warrendale, PA., pp. 1-5.
19. Newman, J.C. & Edwards, P.R. 1988 “Short-crack growth behaviour in various aircraft materials”, *AGARD Report*, no. 732.
20. Newman, J.C. 1983 “A nonlinear fracture mechanics approach to the growth of small cracks”, AGARD CP-328, pp.6.1-6.26.
21. Newman, J.C., Swain, M.H., Philips, E.P. 1986 “An Assessment of the small-crack effect for 2024-T3 aluminum alloy”, in Ritchie, R.O. & Lankford, J., eds., Proceeding of Small Fatigue Cracks, The Metallurgical Society, Warrendale, PA., pp. 427-452.
22. Miller, K.J. 1987, "The behaviour of short fatigue cracks and their initiation. Part II – A general summary", *Fatigue and Fracture of Engineering Materials and Structures*, vol. 10, no. 2, pp. 93-113.
23. Forsyth, P.J.E. & Ryder, D.A. 1960 “Fatigue fracture”, *Aircraft Engineering*, vol. 32, pp. 96-99.
24. Connors, W.C., 1994 “Fatigue striation spacing analysis”, *Materials Characterization*, vol. 33, pp. 245-253.
25. Khan, Z., Rauf, A. and Younas, M., 1997 “Prediction of fatigue crack propagation life in notched members under variable amplitude loading”, *Journal of Materials Engineering and Performance*, vol. 6, pp. 365-373.
26. Ordico, J. and LeGall, P., “Striation counting on fatigue fractured light alloys”, *Reviews Physics Applied*, vol. 9, pp. 673-681.
27. Poursaeidi, E., Sanaieei, M. & Bakhtyari, H. 2013, "Life estimate of a compressor blade through fractography", *International Journal of Engineering*, vol. 26, no. 4, pp. 393-400.
28. Schijve, J. 2015, "The application of small overloads for fractography of small fatigue cracks initiated under constant-amplitude loading", International Journal of Fatigue, vol. 70, pp. 63-72.
29. Totten, G. 2008, “Fatigue crack propagation”, *Advanced Materials & Processes*, vol. 166, no. 5, pp. 39-41.
30. DeVries, P.H., Ruth, K.T. & Dennies, D.P. 2010, "Counting on fatigue: Striations and their measure", *Journal of Failure Analysis and Prevention*, vol. 10, no. 2, pp. 120-137.
31. Nader, N. A. (1993) *The effect of scratches on fatigue life and fatigue crack growth of Al 2024-T3 clad*, unpublished thesis (PhD), Wichita State University.

32. Inchekel, A. & Talia, J.E. 1994, “Effect of scratches on the fatigue behaviour of an Al-Li alloy”, *Fatigue & Fracture of Engineering Materials & Structures*, vol. 17, No. 5, pp. 501-507.
33. Talia, M. & Talia, J.E. 1997, “The effects of scratches and shot peening on the high cycle fatigue crack growth of aluminium alloy 2024-T3” in *High Cycle Fatigue of Structural Materials*, Indianapolis Indiana USA, 14-18 Sept 1997, pp. 409-426.
34. Talia, M. & Talia, J.E. 1997, "Crack propagation modeling for surface generated scratches in Al 2024-T3 clad alloy", *Journal of the Mechanical Behavior of Materials*, vol. 8, no. 2, pp. 117-139.
35. Everett Jr., R.A., Newman Jr., J.C. & Phillips, E.P. 2002, "The effects of a machining-like scratch on the fatigue life of 4340 steel", *Journal of the American Helicopter Society*, vol. 47, no. 3, pp. 151-155.
36. Kyle, C. (2006) *Investigation of the transformation of defects in aircraft structures into cracks*, unpublished thesis (MSc), Cranfield University.
37. Morency, R. (2007) *Fatigue crack initiation and growth from scratches in 2024 T-351 aluminium*, unpublished thesis (MSc), Cranfield University.
38. Walmsley, S. W. (2008) *Fatigue potential of tool scratches on clad 2024-T351 aluminium alloy*, unpublished thesis (MSc), Cranfield University.
39. Jozelich, A. M. (2009) *Investigation of the transformation of defects into fatigue cracks*, unpublished thesis (MSc), Cranfield University.
40. Tizard, D. G. (2010) *The influence of plasticity and residual stress in the fatigue performance of real world scribes in fuselage materials*, unpublished thesis (MSc), Cranfield University.
41. Khan, M. K. (2009) *Scribe marks at fuselage joints - determination of residual stress and effect of fatigue loading using nanoindentation and synchrotron X-ray diffraction*, unpublished thesis (PhD), The Open University.
42. Cini, A. (2012) *Scribe marks at fuselage joints: initiation and propagation of fatigue cracks from mechanical defects in aluminium alloys*, unpublished thesis (PhD), Cranfield University.
43. McEvily, A.J. 1988, “On Crack Closure in Fatigue Crack Growth” *ASTM STP 982*.
44. Elber, W. 1970, “Fatigue crack closure under cyclic tension” *Engineering Fracture Mechanics*, vol.2, pp. 37-45.
45. McClung, R.C. & Sehitoglu, H. 1989, "On the finite element analysis of fatigue crack closure-1. Basic modeling issues", *Engineering Fracture Mechanics,* vol. 33, no. 2, pp. 237-252.
46. Elber, W. 1971, “The significance of crack closure”, *ASTM STP 486*, pp. 230-242.
47. Schijve, J. 1981, "Some formulas for the crack opening stress level", *Engineering Fracture Mechanics*, vol. 14, no. 3, pp. 461-465.
48. De Koning, A.U. 1980, “A simple crack closure model for prediction of fatigue crack growth rates under variable amplitude loading” *NLR MP 80006*.

49. Pang, C.-M. & Song, J.-H. 1994, "Crack growth and closure behavior of short fatigue cracks", *Engineering Fracture Mechanics*, vol. 47, no. 3, pp. 327-343.
50. Kujawski, D. 2003, "ΔKeff parameter under re-examination", *International Journal of Fatigue*, vol. 25, no. 9-11, pp. 793-800.
51. Kujawski, D. 2005, "On assumptions associated with Δkeff and their implications on FCG predictions", *International Journal of Fatigue*, vol. 27, no. 10-12, pp. 1267-1276.
52. Vor, K., Gardin, C., Sarrazin-Baudoux, C. & Petit, J. 2013, "Wake length and loading history effects on crack closure of through-thickness long and short cracks in 304L: Part I – Experiments", *Engineering Fracture Mechanics*, vol. 99, pp. 266-277.
53. Vor, K., Gardin, C., Sarrazin-Baudoux, C. & Petit, J. 2013, "Wake length and loading history effects on crack closure of through-thickness long and short cracks in 304L: Part II – 3D numerical simulation", *Engineering Fracture Mechanics*, vol. 99, pp. 306-323.
54. Sarzosa, D.F.B., Godefroid, L.B. & Ruggieri, C. 2013, "Fatigue crack growth assessments in welded components including crack closure effects: Experiments and 3-D numerical modeling", *International Journal of Fatigue*, vol. 47, no. 0, pp. 279-291.
55. Zhu, X.Y. & Shaw, W.J.D. 1996, "Fatigue crack closure and its effect on life prediction in compact tension specimens", *International Journal of Fatigue*, vol. 18, no. 7, pp. 499-505.
56. Antunes, F.V., Branco, R., Costa, J.D. & Rodrigues, D.M. 2010, "Plasticity induced crack closure in Middle-Crack Tension specimen: Numerical versus experimental", *Fatigue and Fracture of Engineering Materials and Structures*, vol. 33, no. 10, pp. 673-686.
57. Alizadeh, H., Simandjuntak, S., Smith, D. & Pavier, M. 2007, "Prediction of fatigue crack growth rates using crack closure finite element analysis", *International Journal of Fatigue*, vol. 29, no. 9-11, pp. 1711-1715.
58. Akiniwa, Y., Tanaka, K. & Kimura, H. 2001, "Microstructural effects on crack closure and propagation thresholds of small fatigue cracks", *Fatigue and Fracture of Engineering Materials and Structures*, vol. 24, no. 12, pp. 817-829.
59. Newman Jr., J.C. 1984, "A crack opening stress equation for fatigue crack growth", *International Journal of Fracture*, vol. 24, no. 4, pp. R131-R135.
60. Zhang, J.Z., Halliday, M.D., Poole, P. & Bowen, P. 1997, "Crack closure in small fatigue cracks - A comparison of finite element predictions with in-situ scanning electron microscope measurements", *Fatigue and Fracture of Engineering Materials and Structures*, vol. 20, no. 9, pp. 1279-1293.
61. Fleck, N.A. & Newman, J.C. 1988, “Analysis of crack closure under plane-strain conditions” *ASTM STP 982*, pp. 319–341.

62. Dougherty, J.D., Padovan, J. & Srivatsan, T.S. 1997, "Fatigue crack propagation and closure behavior of modified 1070 steel: Finite element study", *Engineering Fracture Mechanics,* vol. 56, no. 2, pp. 189-212.
63. Ewalds, H.L. & Furnee, R.T. 1978 “Crack closure measurements along the crack front in center cracked specimens” *International Journal of Fracture*, vol. 14, pp. R53-R55.
64. McClung, R.C., Thacker, B.H. & Roy, S. 1991 “Finite element visualization of fatigue crack closure in plane-stress and plane-strain” *International Journal of Fracture*, vol. 50, no. 1, pp.27–49.
65. Riemelmoser, F.O. & Pippan, R. 1998, "Mechanical reasons for plasticity-induced crack closure under plane strain conditions", *Fatigue and Fracture of Engineering Materials and Structures*, vol. 21, no. 12, pp. 1425-1433.
66. Antunes, F.V., Branco, R. & Rodrigues, D.M. 2011 “Plasticity induced crack closure under plane strain conditions” *Key Engineering Materials*, vol. 465, pp. 548-551.
67. Toribio, J. & Kharin, V. 2011, "Plasticity-induced crack closure: A contribution to the debate", *European Journal of Mechanics A/Solids*, vol. 30, no. 2, pp. 105-112.
68. Singh, K.D., Parry, M.R. & Sinclair, I. 2008, "Some issues on finite element modelling of plasticity induced crack closure due to constant amplitude loading", *International Journal of Fatigue*, vol. 30, no. 10-11, pp. 1898-1920.
69. Alizadeh, H., Hills, D.A., de Matos, P.F.P., Nowell, D., Pavier, M.J., Paynter, R.J., Smith D.J. & Simandjuntak, S. 2007 “A comparison of two and three-dimensional analyses of fatigue crack closure” *International Journal of Fatigue*, vol. 29, no. 2 pp. 222-231.
70. de Matos, P.F.P. & Nowell, D. 2008, "Numerical simulation of plasticity-induced fatigue crack closure with emphasis on the crack growth scheme: 2D and 3D analyses", *Engineering Fracture Mechanics*, vol. 75, no. 8, pp. 2087-2114.
71. de Matos, P.F.P. & Nowell, D. 2009, "Experimental and numerical investigation of thickness effects in plasticity-induced fatigue crack closure", *International Journal of Fatigue*, vol. 31, no. 11–12, pp. 1795-1804.
72. Lugo, M. & Daniewicz, S.R. 2011, "The influence of T-stress on plasticity induced crack closure under plane strain conditions", *International Journal of Fatigue*, vol. 33, no. 2, pp. 176-185.
73. Fleck, N.A. 1986, "Finite element analysis of plasticity-induced crack closure under plane strain conditions", *Engineering Fracture Mechanics*, vol. 25, no. 4, pp. 441-449.
74. Lei, Y. 2008, "Finite element crack closure analysis of a compact tension specimen", *International Journal of Fatigue*, vol. 30, no. 1, pp. 21-31.
75. Antunes, F.V., Marques, G.A.S., Chegini, A.G. & Correia, L. 2014, "Transient behaviour in the numerical analysis of plasticity induced crack closure", *Fatigue & Fracture of Engineering Materials & Structures*, vol. 37, no. 5, pp. 526-538.

76. Solanki, K., Daniewicz, S.R. & Newman Jr., J.C. 2004, "Finite element analysis of plasticity-induced fatigue crack closure: An overview", *Engineering Fracture Mechanics*, vol. 71, no. 2, pp. 149-171.
77. Wu, J. & Ellyin, F. 1996, "Study of fatigue closure by elastic-plastic finite element analysis for constant-amplitude loading", *International Journal of Fracture,* vol. 82, no. 1, pp. 43-65.
78. Lee, H.-J. & Song, J.-H. 2003, "Finite-element analysis of fatigue crack closure under plane strain conditions: stabilization behaviour and mesh size effect", *Fatigue and Fracture of Engineering Materials and Structures*, vol. 28, no. 3, pp. 333-342.
79. LaRue, J.E. & Daniewicz, S.R. 2007, "Predicting the effect of residual stress on fatigue crack growth", *International Journal of Fatigue*, vol. 29, no. 3, pp. 508-515.
80. Beghini, M. & Bertini, L. 1990, "Fatigue crack propagation through residual stress fields with closure phenomena", *Engineering Fracture Mechanics*, vol. 36, no. 3, pp. 379-387.
81. Kang, K.J., Song, J.H. & Earmme, Y.Y. 1990, "Fatigue crack growth and closure behaviour through a compressive residual stress field", *Fatigue and Fracture of Engineering Materials and Structures*, vol. 13, no. 1, pp. 1-13.
82. Choi, H.-. & Song, J.-. 1995, "Finite element analysis of closure behaviour of fatigue cracks in residual stress fields", *Fatigue and Fracture of Engineering Materials and Structures*, vol. 18, no. 1, pp. 105-117.
83. Kang, K.J., Song, J.H. & Earmme, Y.Y. 1989, "Fatigue crack growth and closure through a tensile residual stress field under compressive applied loading", *Fatigue and Fracture of Engineering Materials and Structures*, vol. 12, no. 5, pp. 363-376.
84. Schnubel, D. & Huber, N. 2012, "The influence of crack face contact on the prediction of fatigue crack propagation in residual stress fields", *Engineering Fracture Mechanics*, vol. 84, pp. 15-24.
85. Moshier, M.A. & Hillberry, B.M. 1999, "Inclusion of compressive residual stress effects in crack growth modelling", *Fatigue and Fracture of Engineering Materials and Structures*, vol. 22, no. 6, pp. 519-526.
86. Gozin, M.H. & Aghaie-Khafri, M. 2012, "2D and 3D finite element analysis of crack growth under compressive residual stress field", *International Journal of Solids and Structures*, vol. 49, no. 23-24, pp. 3316-3322.
87. Liljedahl, C.D.M., Brouard, J., Zanellato, O., Lin, J., Tan, M.L., Ganguly, S., Irving, P.E., Fitzpatrick, M.E., Zhang, X. & Edwards, L. 2009, "Weld residual stress effects on fatigue crack growth behaviour of aluminium alloy 2024-T351", *International Journal of Fatigue*, vol. 31, no. 6, pp. 1081-1088.
88. Jones, K.W. & Dunn, M.L. 2008, "Fatigue crack growth through a residual stress field introduced by plastic beam bending", *Fatigue and Fracture of Engineering Materials and Structures*, vol. 31, no. 10, pp. 863-875.

89. Wang, C.H., Barter, S.A. & Liu, Q. 2003, "A closure model to crack growth under large-scale yielding and through residual stress fields", *Journal of Engineering Materials and Technology*, Transactions of the ASME, vol. 125, no. 2, pp. 183-190.
90. Ma, Y.E., Staron, P., Fischer, T. & Irving, P.E. 2011, "Size effects on residual stress and fatigue crack growth in friction stir welded 2195-T8 aluminium - Part II: Modelling", *International Journal of Fatigue*, vol. 33, no. 11, pp. 1426-1434.
91. Zhu, X.Y. & Shaw, W.J.D. 1995, "Correlation of fatigue crack growth behaviour with crack closure in peened specimens", *Fatigue and Fracture of Engineering Materials and Structures*, vol. 18, no. 7-8, pp. 811-820.
92. Ruschau, J.J., John, R., Thompson, S.R. & Nicholas, T. 1999, "Fatigue crack growth rate characteristics of laser shock peened Ti-6Al-4V", *Journal of Engineering Materials and Technology*, vol. 121, no. 3, pp. 321-329.
93. Ruschau, J.J., John, R., Thompson, S.R. & Nicholas, T. 1999, "Fatigue crack nucleation and growth rate behavior of laser shock peened titanium", *International Journal of Fatigue*, vol. 21, no. Suppl. 1, pp. S199-S209.
94. Hill, M.R. & Kim, J. 2012, "Fatigue crack closure in residual stress bearing materials", *Journal of ASTM International*, vol. 9, no. 1, pp. 1-16.
95. De Matos, P.F.P. & Nowell, D. 2008, "Analytical and numerical modelling of plasticity-induced crack closure in cold-expanded holes", *Fatigue and Fracture of Engineering Materials and Structures*, vol. 31, no. 6, pp. 488-503.
96. Cary, P.E. 1982, "History of shot peening", *Shot Peener*, pp. 23-28.
97. Soady, K.A. 2013, "Life assessment methodologies incoroporating shot peening process effects: Mechanistic consideration of residual stresses and strain hardening: Part 1 - Effect of shot peening on fatigue resistance", *Materials Science and Technology*, vol. 29, no. 6, pp. 637-651.
98. Metal Improvement Company (2012) "Shot Peening" [online], available: http://www.metalimprovement.com/shot_peening.php [accessed 16 February 2012].
99. Prater, T. 2014, "Friction stir welding of metal matrix composites for use in aerospace structures", *Acta Astronautica*, vol. 93, pp. 366-373.
100. Imuta, M. & Kamimuki, K. 2005, "Development and application of friction stir welding for aerospace industry", *Welding Research Abroad*, vol. 51, no. 1, pp. 35-41.
101. Freeman, R. 2008, "Welding and joining developments in the aerospace industry", *Welding and Cutting*, vol. 7, no. 5, pp. 274-275.
102. White, R.M. 1963, "Elastic wave generation by electron bombardment or electromagnetic wave absorption", *Journal of Applied Physics*, vol. 34, no. 7, pp. 2123-2124.
103. Mallozi, P.J. & Fairand, B.P., Industrial Materials Limited (1974) Altering material properties, U.S. Pat. 3,850,698.

104. Mannava, S., McDaniel, A.E., Cowie, W.D., Halila, H., Rhoda, J.E., Gutknecht, J.E., General Electric Company, (1997) Laser shock peened gas turbine engine fan blade edges, U.S. Pat. 5,591,009.
105. Shidid, D.P., Gollo, M.H., Brandt, M. & Mahdavian, M. 2013, "Study of effect of process parameters on titanium sheet metal bending using Nd: YAG laser", *Optics and Laser Technology*, vol. 47, pp. 242-247.
106. Hu, Y., Xu, X., Yao, Z. & Hu, J. 2010, "Laser peen forming induced two way bending of thin sheet metals and its mechanisms", *Journal of Applied Physics*, vol. 108, no. 7.
107. Ganesh, P., Sundar, R., Kumar, H., Kaul, R., Ranganathan, K., Hedaoo, P., Tiwari, P., Kukreja, L.M., Oak, S.M., Dasari, S. & Raghavendra, G. 2012, "Studies on laser peening of spring steel for automotive applications", *Optics and Lasers in Engineering*, vol. 50, no. 5, pp. 678-686.
108. Zhu, J., Jiao, X., Zhou, C. & Gao, H. 2012, "Applications of Underwater Laser Peening in Nuclear Power Plant Maintenance", *Energy Procedia*, vol. 16, pp. 153-158.
109. Hu, Y. & Yao, Z. 2008, "Overlapping rate effect on laser shock processing of 1045 steel by small spots with Nd:YAG pulsed laser", *Surface and Coatings Technology*, vol. 202, no. 8, pp. 1517-1525.
110. Kalainathan, S., Sathyajith, S. & Swaroop, S. 2012, "Effect of laser shot peening without coating on the surface properties and corrosion behavior of 316L steel", *Optics and Lasers in Engineering*, vol. 50, pp. 1740-1745.
111. Ling, X., Peng, W. & Ma, G. 2008, "Influence of laser peening parameters on residual stress field of 304 stainless steel", *Journal of Pressure Vessel Technology*, Transactions of the ASME, vol. 130, no. 2, pp. 0212011-0212018.
112. Fang, Y.W., Li, Y.H., He, W.F. & Li, P.Y. 2013, "Effects of laser shock processing with different parameters and ways on residual stresses fields of a TC4 alloy blade", *Materials Science and Engineering A*, vol. 559, pp. 683-692.
113. Smith, P.R., Shepard, M.J., Prevéy III, P.S. & Clauer, A.H. 2000, "Effect of power density and pulse repetition on laser shock peening of Ti-6Al-4V", *Journal of Materials Engineering and Performance*, vol. 9, no. 1, pp. 33-37.
114. Cao, Y., Shin, Y.C. & Wu, B. 2010, "Parametric study on single shot and overlapping laser shock peening on various metals via modeling and experiments", *Journal of Manufacturing Science and Engineering*, Transactions of the ASME, vol. 132, no. 6, pp. 0610101-06101010.
115. Gomez-Rosas, G., Rubio-Gonzalez, C., Ocaña, J.L., Molpeceres, C., Porro, J.A., Morales, M. & Casillas, F.J. 2010, "Laser Shock Processing of 6061-T6 Al alloy with 1064 nm and 532 nm wavelengths", *Applied Surface Science*, vol. 256, no. 20, pp. 5828-5831.

116. Sathyajith, S., Kalainathan, S. & Swaroop, S. 2013, "Laser peening without coating on aluminum alloy Al-6061-T6 using low energy Nd:YAG laser", *Optics & Laser Technology*, vol. 45, no. 0, pp. 389-394.
117. Rankin, J.E., Hill, M.R. & Hackel, L.A. 2003, "The effects of process variations on residual stress in laser peened 7049 T73 aluminum alloy", *Materials Science and Engineering A*, vol. 349, no. 1-2, pp. 279-291.
118. Ocaña, J.L., Morales, M., Molpeceres, C., Torres, J., Porro, J.A., Gómez, G. & Rubio, C. 2004, "Predictive assessment and experimental characterization of the influence of irradiation parameters on surface deformation and residual stresses in laser shock processed metallic alloys", in Phipps, C.R., eds., *High-Power Laser Ablarion V: Proceedings of SPIE*, 20 Sep, Taos, New Mexico, vol. 5448, pp. 642-653.
119. Yilbas, B.S. & Arif, A.F.M. 2007, "Laser shock processing of aluminium: Model and experimental study", *Journal of Physics D: Applied Physics*, vol. 40, no. 21, pp. 6740-6747.
120. Hu, Y.X., Yao, Z.Q. & Hu, J. 2009, "An Analytical Model to Predict Residual Stress Field Induced by Laser Shock Peening", *Journal of Manufacturing Science and Engineering-Transactions of the Asme*, vol. 131, no. 3, pp. 0310171-0310177.
121. Brockman, R.A., Braisted, W.R., Olson, S.E., Tenaglia, R.D., Clauer, A.H., Langer, K. & Shepard, M.J. 2012, "Prediction and characterization of residual stresses from laser shock peening", *International Journal of Fatigue*, vol. 36, no. 1, pp. 96-108.
122. Montross, C.S., Florea, V. & Swain, M.V. 2001, "The influence of coatings on subsurface mechanical properties of laser peened 2011-T3 aluminum", *Journal of Materials Science*, vol. 36, no. 7, pp. 1801-1807.
123. Peyre, P. & Fabbro, R. 1995, "Laser shock processing: a review of the physics and applications", *Optical and Quantum Electronics*, vol. 27, no. 12, pp. 1213-1229.
124. Clauer, A.H. & Lahrman, D.F. 2001, "Laser shock processing as a surface enhancement process", *Key Engineering Materials*, vol. 197, pp. 121-142.
125. Fabbro, R., Fournier, J., Ballard, P., Devaux, D. & Virmont, J. 1990, "Physical study of laser-produced plasma in confined geometry", *Journal of Applied Physics,* vol. 68, no. 2, pp. 775-784.
126. Heckenberger, U.C., Hombergsmeier, E., Holzinger, V. & Von Bestenbostel, W. 2011, "Laser shock peening to improve the fatigue resistance of AA7050 components", *International Journal of Structural Integrity*, vol. 2, no. 1, pp. 22-33.
127. Masse, J.-E. & Barreau, G. 1995, "Surface modification by laser induced shock waves", *Surface Engineering*, vol. 11, no. 2, pp. 131-132.
128. Hatamleh, O. 2008, "The effects of laser peening and shot peening on mechanical properties in friction stir welded 7075-T7351 aluminum", *Journal of Materials Engineering and Performance*, vol. 17, no. 5, pp. 688-694.

129. Montross, C.S., Wei, T., Ye, L., Clark, G. & Mai, Y.,-W. 2002, "Laser shock processing and its effects on microstructure and properties of metal alloys: A review", *International Journal of Fatigue*, vol. 24, no. 10, pp. 1021-1036.
130. Peyre, P., Berthe, L., Fabbro, R., Scherpereel, X. & Bartnicki, E. 1997, "Laser shock processing of materials: Characterisation and application of the process", in Beckmann, L.H.J.F., ed., *Lasers in Materials Processing: Proceedings of SPIE*, 16-20 June, Munich, Germany, vol. 3097, pp. 558-569.
131. Rossini, N.S., Dassisti, M., Benyounis, K.Y. & Olabi, A.G. 2012, "Methods of measuring residual stresses in components", *Materials and Design*, vol. 35, pp. 572-588.
132. Toparli, M.B. 2012, Analysis of residual stress fields in aerospace materials after laser peening, unpublished thesis (PhD), The Open University.
133. ASTM Standard (2013) E837-13a, *Standard test method for determining residual stresses by the hole-drilling strain-gage method*, West Conshohocken, PA:ASTM international.
134. Grant, P.V., Lord, J.D. & Whitehead, P.S. (2006) "The Measurement of Residual Stresses by the Incremental Hole Drilling Technique" *National Physics Laboratory Measurement Good Practice Guide*, no. 53.
135. Beghini, M., Bertini, L. & Vitale, E. 1994, "Fatigue crack growth in residual stress fields: experimental results and modelling", *Fatigue & Fracture of Engineering Materials & Structures*, vol. 17, no. 12, pp. 1433-1444.
136. Bussu, G. & Irving, P.E. 2003, "The role of residual stress and heat affected zone properties on fatigue crack propagation in friction stir welded 2024-T351 aluminium joints" *International Journal of Fatigue*, vol. 25 no. 1 pp. 77-88.
137. Liljedahl, C.D.M., Tan, M.L., Zanellato, O., Ganguly, S., Fitzpatrick, M.E. & Edwards, L. 2008, "Evolution of residual stresses with fatigue loading and subsequent crack growth in a welded aluminium alloy middle tension specimen", *Engineering Fracture Mechanics*, vol. 75, no. 13, pp. 3881-3894.
138. Reed, E.C. & Viens, J.A. 1960, "The Influence of Surface Residual Stress on Fatigue Limit of Titanium," *Journal of Engineering for Industry*, Vol. 82, pp. 76-78.
139. Mutoh, Y., Fair, G.H., Noble, B. & Waterhouse, R.B. 1987, "The effect of residual stresses induced by shot-peening on fatigue crack propagation in two high strength aluminium alloys", *Fatigue and Fracture of Engineering Materials and Structures*, vol. 10, no. 4, pp. 261-272.
140. Hammond, D.W. & Meguid, S.A. 1990, "Crack propagation in the presence of shot-peening residual stresses", *Engineering Fracture Mechanics*, vol. 37, no. 2, pp. 373-387.
141. Sridhar, B.R., Ramachandra, K. & Padmanabhan, K.A. 1996, "Effect of Shot Peening on the Fatigue and Fracture Behaviour of Two Titanium Alloys," *Journal of Materials Science*, vol. 31, pp. 5953-5960.

142. Misumi, M. & Ohkubo, M. 1987, "Deceleration of small crack growth by shot-peening ", *International Journal of Materials and Product Technology*, vol. 2, no. 1, pp. 36-47.
143. De Los Rios, E.R., Mercier, P. & El-Sehily, B.M. 1996, "Short crack growth behaviour under variable amplitude loading of shot peened surfaces", *Fatigue and Fracture of Engineering Materials and Structures*, vol. 19, no. 2, pp. 175-184.
144. Natkaniec-Kocanda, D., Kocanda, S. & Miller, K.J. 1996, "Influence of shot-peening on short crack behaviour in a medium carbon steel", *Fatigue and Fracture of Engineering Materials and Structures*, vol. 19, no. 7, pp. 911-917.
145. Černý, I. 2011, "Growth and retardation of physically short fatigue cracks in an aircraft Al-alloy after shot peening", *Procedia Engineering*, vol. 10, pp. 3411-3416.
146. Černý, I., Sís, J. & Mikulová, D. 2012, "Short fatigue crack growth in an aircraft Al-alloy of a 7075 type after shot peening", Surface and Coatings Technology, vol. 243, pp.20-27.
147. Everett Jr., R.A., Matthews, W.T., Prabhakaran, R., Newman Jr., J.C. & Dubberly, M.J. 2001, "The effects of shot and laser peening on crack growth and fatigue life in 2024 aluminum alloy and 4340 steel", NASA Technical Memorandum, no. 210843, pp. 1-18.
148. Cláudio, R.A., Burgess, A., Branco, C.M. & Byrne, J. 2009, "Failure analysis of scratch damaged shot peened simulated components at high temperature", *Engineering Failure Analysis*, vol. 16, no. 4, pp. 1208-1220.
149. Clauer, A.H. & Fairand, B.P. 1979, "Interaction of laser-induced stress waves with metals", *proceedings of Applications of Laser in Material Processing*, 18-20 April, Washington, D.C., pp. 291-315.
150. Liao, Y., Suslov, S., Ye, C. & Cheng, G.J. 2012, "The mechanisms of thermal engineered laser shock peening for enhanced fatigue performance", *Acta Materialia*, vol. 60, no. 13-14, pp. 4997-5009.
151. Peyre, P., Merrien, P., Lieurade, H.P., Fabbro, R. & Bignonnet, A. 1993, "Optimization of the residual stresses induced by laser shock treatment and fatigue life improvement of 2 cast aluminium alloys" accepted for *The fifth international conference on shot peening*, Oxford, UK.
152. Ochi, Y., Masaki, K., Matsumura, T., Sano, Y., Akita, K. & Kajiwara, K. 2007, “Effects of laser peening on fatigue crack behaviors in pre-cracked cast aluminum alloy” vol. 345-346, pp. 255-258.
153. Ochi, Y., Matsumura, T., Ikarashi, T., Masaki, K., Kakiuchi, T., Sano, Y. & Adachi, T. 2010, "Effects of laser peening treatment without protective coating on axial fatigue property of aluminum alloy", *Procedia Engineering*, vol. 2, no. 1, pp. 491-498.
154. Ochi, Y., Masaki, K., Matsumura, T., Ikarashi, T. & Sano, Y. 2009, “Effects of laser peening treatment on high cycle fatigue and crack propagation behaviors in

austenitic stainless steel" *proceedings of 17th International Conference on Nuclear Engineering*, 12-16 July, Brussels, Belgium, vol. 1, pp. 707-707.

155. Zhang, Y.K., Lu, J.Z., Ren, X.D., Yao, H.B. & Yao, H.X. 2009, "Effect of laser shock processing on the mechanical properties and fatigue lives of the turbojet engine blades manufactured by LY2 aluminum alloy", *Materials and Design*, vol. 30, no. 5, pp. 1697-1703.
156. Masaki, K., Ochi, Y., Matsumura, T. & Sano, Y. 2007, "Effects of laser peening treatment on high cycle fatigue properties of degassing-processed cast aluminum alloy", *Materials Science and Engineering A*, vol. 468-470, pp. 171-175.
157. Ganesh, P., Sundar, R., Kumar, H., Kaul, R., Ranganathan, K., Hedaoo, P., Raghavendra, G., Anand Kumar, S., Tiwari, P., Nagpure, D.C., Bindra, K.S., Kukreja, L.M. & Oak, S.M. 2014, "Studies on fatigue life enhancement of pre-fatigued spring steel specimens using laser shock peening", *Materials and Design*, vol. 54, pp. 734-741.
158. Zhang, X.C., Zhang, Y.K., Lu, J.Z., Xuan, F.Z., Wang, Z.D. & Tu, S.T. 2010, "Improvement of fatigue life of Ti-6Al-4V alloy by laser shock peening", *Materials Science and Engineering A*, vol. 527, no. 15, pp. 3411-3415.
159. Hill, M.R., Pistochini, T.E. & DeWald, A. 2005, "Optimization of residual stress and fatigue life in laser peened components" accepted for *The ninth international conference of shot peening*, Marne la Vallee, France.
160. Hill, M.R., Pistochini, T.E. & Dewald, A.T. 2005, "Fatigue performance of laser peened materials ", *proceedings of Pressure Vessels and Piping Conference*, 17-21 July, Denver, Ohio, vol. 7, pp. 203-207.
161. Langer, K., Vanhoogen, S. & Hoover, J. 2008, "Fatigue response of aluminum aircraft structure under engineered residual stress processing", *Journal of ASTM International*, vol. 5, no. 7.
162. Hu, J., Lou, J., Sheng, H., Wu, S., Chen, G., Huang, K., Ye, L., Liu, Z., Shi, Y. & Yin, S. 2012, "The effects of laser shock peening on microstructure and properties of metals and alloys: A review" *Advanced Material Research*, Vol. 347-353, pp.1596-1604.
163. Luong, H. & Hill, M.R. 2008, "The effects of laser peening on high-cycle fatigue in 7085-T7651 aluminum alloy", *Materials Science and Engineering A*, vol. 477, no. 1-2, pp. 208-216.
164. Hatamleh, O. 2009, "A comprehensive investigation on the effects of laser and shot peening on fatigue crack growth in friction stir welded AA 2195 joints", *International Journal of Fatigue*, vol. 31, no. 5, pp. 974-988.
165. Hatamleh, O., Lyons, J. & Forman, R. 2007, "Laser and shot peening effects on fatigue crack growth in friction stir welded 7075-T7351 aluminum alloy joints", *International Journal of Fatigue*, vol. 29, no. 3, pp. 421-434.

166. Hatamleh, O., Lyons, J. & Forman, R. 2007, "Laser peening and shot peening effects on fatigue life and surface roughness of friction stir welded 7075-T7351 aluminum", *Fatigue and Fracture of Engineering Materials and Structures*, vol. 30, no. 2, pp. 115-130.
167. Hatamleh, O., Forth, S. & Reynolds, A.P. 2010, "Fatigue crack growth of peened friction stir-welded 7075 aluminum alloy under different load ratios", *Journal of Materials Engineering and Performance*, vol. 19, no. 1, pp. 99-106.
168. Pistochini, T.E. & Hill, M.R. 2011, "Effect of laser peening on fatigue performance in 300M steel", *Fatigue and Fracture of Engineering Materials and Structures*, vol. 34, no. 7, pp. 521-533.
169. Wagner, L., Mhaede, M., Wollmann, M., Altenberger, I. & Sano, Y. 2011, "Surface layer properties and fatigue behavior in Al 7075-T73 and Ti-6Al-4V Comparing results after laser peening; Shot peening and ball-burnishing", *International Journal of Structural Integrity*, vol. 2, no. 2, pp. 185-199.
170. Peyre, P., Fabbro, R., Merrien, P. & Lieurade, H.P. 1996, "Laser shock processing of aluminium alloys. Application to high cycle fatigue behaviour", *Materials Science and Engineering A*, vol. 210, no. 1-2, pp. 102-113.
171. Hammersley, G., Hackel, L.A. & Harris, F. 2000, "Surface prestressing to improve fatigue strength of components by laser shot peening", *Optics and Lasers in Engineering*, vol. 34, no. 4-6, pp. 327-337.
172. Gao, Y.K. 2011, "Improvement of fatigue property in 7050-T7451 aluminum alloy by laser peening and shot peening", *Materials Science and Engineering A*, vol. 528, no. 10-11, pp. 3823-3828.
173. Vázquez, J., Navarro, C. & Domínguez, J. 2012, "Experimental results in fretting fatigue with shot and laser peened Al 7075-T651 specimens", *International Journal of Fatigue*, vol. 40, pp. 143-153.
174. Rodopoulos, C.A., Romero, J.S., Curtis, S.A., De los Rios, E.R. & Peyre, P. 2003, "Effect of controlled shot peening and laser shock peening on the fatigue performance of 2024-T351 aluminum alloy", *Journal of Materials Engineering and Performance*, vol. 12, no. 4, pp. 414-419.
175. Rodopoulos, C.A., Kermanidis, A.T., Statnikov, E., Vityazev, V. & Korolkov, O. 2007, "The effect of surface engineering treatments on the fatigue behavior of 2024-T351 aluminum alloy", *Journal of Materials Engineering and Performance*, vol. 16, no. 1, pp. 30-34.
176. Luong, H. & Hill, M.R. 2010, "The effects of laser peening and shot peening on high cycle fatigue in 7050-T7451 aluminum alloy", *Materials Science and Engineering A*, vol. 527, no. 3, pp. 699-707.
177. Ren, X.D., Zhang, Y.K., Yongzhuo, H.F., Ruan, L., Jiang, D.W., Zhang, T. & Chen, K.M. 2011, "Effect of laser shock processing on the fatigue crack initiation and

propagation of 7050-T7451 aluminum alloy", *Materials Science and Engineering A*, vol. 528, no. 6, pp. 2899-2903.

178. Ren, X.D., Zhan, Q.B., Yang, H.M., Dai, F.Z., Cui, C.Y., Sun, G.F. & Ruan, L. 2013, "The effects of residual stress on fatigue behavior and crack propagation from laser shock processing-worked hole", *Materials and Design*, vol. 44, pp. 149-154.
179. Spanrad, S. & Tong, J. 2011, "Characterisation of foreign object damage (FOD) and early fatigue crack growth in laser shock peened Ti-6Al-4V aerofoil specimens", *Materials Science and Engineering A*, vol. 528, no. 4-5, pp. 2128-2136.
180. Sakino, Y., Sano, Y., Sumiya, R. & Kim, Y.-. 2012, "Major factor causing improvement in fatigue strength of butt welded steel joints after laser peening without coating", *Science and Technology of Welding and Joining*, vol. 17, no. 5, pp. 402-407.
181. Adekola, T.R., Diep, H.T., Ramulu, M. & Kobayashi, A.S. 2007, "Effects of peening on fatigue crack propagation" SEM Annual Conference and Exposition on Experimental and Applied Mechanics, Springfield, MA, 3-6 June, *Proceedings of the SEM Annual Conference and Exposition on Experimental and Applied Mechanics 2007*, vol. 3, pp. 1391-1399.
182. Wang, C.D., Zhou, J.Z., Huang, S., Yang, X.D., Xu, Z.C. & Ruan, H.Y. 2011, “Study on the improvement of fatigue crack growth performance of 6061-T6 aluminum alloy subject to laser shot peening” *Key Engineering Materials*, vol. 464, pp.391-394.
183. Tsay, L.W., Young, M.C. & Chen, C. 2003, “Fatigue crack growth behavior of laser-processed 304 stainless steel in air and gaseous hydrogen”, *Corrosion Science*, vol. 45, no. 9, pp. 1985-1997.
184. Ren, X.D., Zhang, T., Zhang, Y.K., Jiang, D.W. & Chen, K.M. 2010, “Analysis of 7050 aluminum alloy crack growth by laser shock processing” *Advanced Materials Research*, vol.97-101, pp.3852-3856.
185. Hill, M.R. & Vandalen, J.E. 2008, "Evaluation of residual stress corrections to fracture toughness values", *Journal of ASTM International*, vol. 5, no. 8.
186. Wong, W. & Hill, M.R. 2013, "Superposition and Destructive Residual Stress Measurements", *Experimental Mechanics*, vol. 53, no. 3, pp. 339-344.
187. Huang, S., Zhou, J.Z., Sheng, J., Lu, J.Z., Sun, G.F., Meng, X.K., Zuo, L.D., Ruan, H.Y. & Chen, H.S. 2013, "Effects of laser energy on fatigue crack growth properties of 6061-T6 aluminum alloy subjected to multiple laser peening", *Engineering Fracture Mechanics*, vol. 99, pp. 87-100.
188. Huang, S., Zhou, J.Z., Sheng, J., Luo, K.Y., Lu, J.Z., Xu, Z.C., Meng, X.K., Dai, L., Zuo, L.D., Ruan, H.Y. & Chen, H.S. 2013, "Effects of laser peening with different coverage areas on fatigue crack growth properties of 6061-T6 aluminum alloy", *International Journal of Fatigue*, vol. 47, pp. 292-299.

189. Rubio-Gonzalez, C., Felix-Martinez, C., Gomez-Rosas, G., Ocaña, J.L., Morales, M. & Porro, J.A. 2011, "Effect of laser shock processing on fatigue crack growth of duplex stainless steel", *Materials Science and Engineering A*, vol. 528, no. 3, pp. 914-919.

190. Rubio-Gonzalez, C., Gomez-Rosas, G., Molpeceres, C., Paredes, M., Banderas, A., Porro, J. & Morales, M. 2004, "Effect of laser shock processing on fatigue crack growth and fracture toughness of 6061-T6 aluminum alloy", *Materials Science and Engineering A*, vol. 386, no. 1-2, pp. 291-295.

191. Nikitin, I. & Altenberger, I. 2007, "Comparison of the fatigue behavior and residual stress stability of laser-shock peened and deep rolled austenitic stainless steel AISI 304 in the temperature range 25-600 °C", *Materials Science and Engineering A*, vol. 465, no. 1-2, pp. 176-182.

192. Nalla, R.K., Altenberger, I., Noster, U., Liu, G.Y., Scholtes, B. & Ritchie, R.O. 2003, "On the influence of mechanical surface treatments-deep rolling and laser shock peening-on the fatigue behavior of Ti-6Al-4V at ambient and elevated temperatures", *Materials Science and Engineering A*, vol. 355, no. 1-2, pp. 216-230.

193. Altenberger, I., Nalla, R.K., Sano, Y., Wagner, L. & Ritchie, R.O. 2012, "On the effect of deep-rolling and laser-peening on the stress-controlled low- and high-cycle fatigue behavior of Ti–6Al–4V at elevated temperatures up to 550 °C", *International Journal of Fatigue*, vol. 44, pp. 292-302.

194. King, A., Steuwer, A., Woodward, C. & Withers, P.J. 2006, "Effects of fatigue and fretting on residual stresses introduced by laser shock peening", *Materials Science and Engineering A*, vol. 435-436, pp. 12-18.

195. Liu, K.K. & Hill, M.R. 2009, "The effects of laser peening and shot peening on fretting fatigue in Ti-6Al-4V coupons", *Tribology International*, vol. 42, no. 9, pp. 1250-1262.

196. Srinivasan, S., Garcia, D.B., Gean, M.C., Murthy, H. & Farris, T.N. 2009, "Fretting fatigue of laser shock peened Ti-6Al-4V", *Tribology International*, vol. 42, no. 9, pp. 1324-1329.

197. Zhang, H., Zhang, Y.-. & Yu, C.-. 1999, "Surface treatment of aluminum alloy by laser shock processing", *Surface Engineering*, vol. 15, no. 6, pp. 454-456.

198. Clauer, A.H., Walters, C.T. & Ford, S.C. 1983, "The Effects of Laser Shock Processing on the Fatigue Properties of 2024-T3 Aluminum" Metzbower, E.A., ed., *proceedings of Lasers in Materials Processing*, 21-26 Jan, Los Angeles, California, American Society for Metals, Mars, Pennsyvania, pp. 7-22.

199. Achintha, M., Nowell, D., Fufari, D., Sackett, E.E. & Bache, M.R. 2013, "Fatigue behaviour of geometric features subjected to laser shock peening: Experiments and modelling", *International Journal of Fatigue*, vol. 62, pp. 171-179.

200. Zhang, L., Lu, J.Z., Zhang, Y.K., Luo, K.Y., Zhong, J.W., Cui, C.Y., Kong, D.J., Guan, H.B. & Qian, X.M. 2011, "Effects of different shocked paths on fatigue property of 7050-T7451 aluminum alloy during two-sided laser shock processing", *Materials and Design*, vol. 32, no. 2, pp. 480-486.
201. Cuellar, S.D., Hill, M.R., DeWald, A.T. & Rankin, J.E. 2012, "Residual stress and fatigue life in laser shock peened open hole samples", *International Journal of Fatigue*, vol. 44, pp. 8-13.
202. Lu, J.Z., Luo, K.Y., Yang, D.K., Cheng, X.N., Hu, J.L., Dai, F.Z., Qi, H., Zhang, L., Zhong, J.S., Wang, Q.W. & Zhang, Y.K. 2012, "Effects of laser peening on stress corrosion cracking (SCC) of ANSI 304 austenitic stainless steel", *Corrosion Science*, vol. 60, pp. 145-152.
203. Sano, Y., Obata, M., Kubo, T., Mukai, N., Yoda, M., Masaki, K. & Ochi, Y. 2006, "Retardation of crack initiation and growth in austenitic stainless steels by laser peening without protective coating", *Materials Science and Engineering A*, vol. 417, no. 1-2, pp. 334-340.
204. Obata, M., Sano, Y., Mukai, N., Yoda, M., Shima, S. & Kanno, M. 1999, "Effects of laser peening on residual stress and stress corrosion cracking for type 304 stainless steel" accepted for *The seventh international conference on shot peening*, Warsaw, Poland.
205. Liu, Q., Yang, C.H., Ding, K., Barter, S.A. & Ye, L. 2007, "The effect of laser power density on the fatigue life of laser-shock-peened 7050 aluminium alloy", *Fatigue and Fracture of Engineering Materials and Structures*, vol. 30, no. 11, pp. 1110-1124.
206. Maawad, E., Sano, Y., Wagner, L., Brokmeier, H.-. & Genzel, C. 2012, "Investigation of laser shock peening effects on residual stress state and fatigue performance of titanium alloys", *Materials Science and Engineering A*, vol. 536, pp. 82-91.
207. Chahardehi, A., Brennan, F.P. & Steuwer, A. 2010, "The effect of residual stresses arising from laser shock peening on fatigue crack growth", *Engineering Fracture Mechanics*, vol. 77, no. 11, pp. 2033-2039.
208. Ivetic, G., Meneghin, I., Troiani, E., Molinari, G., Ocaña, J.L., Morales, M., Porro, J., Lanciotti, A., Ristori, V., Polese, C., Plaisier, J. & Lausi, A. 2012, "Fatigue in laser shock peened open-hole thin aluminium specimens", *Materials Science and Engineering A*, vol. 534, pp. 573-579.
209. Tan, Y., Wu, G., Yang, J.-. & Pan, T. 2004, "Laser shock peening on fatigue crack growth behaviour of aluminium alloy", *Fatigue and Fracture of Engineering Materials and Structures*, vol. 27, no. 8, pp. 649-656.
210. Yang, J.-., Her, Y.C., Han, N. & Clauer, A.H. 2001, "Laser shock peening on fatigue behavior of 2024-T3 Al alloy with fastener holes and stopholes", *Materials Science and Engineering A*, vol. 298, no. 1-2, pp. 296-299.

211. Tang, Y., Zhang, Y., Zhang, H. & Yu, C. 2000, "Effect of laser shock processing (LSP) on the fatigue resistance of an aluminum alloy", *Journal of Engineering Materials and Technology*, Transactions of the ASME, vol. 122, no. 1, pp. 104-107.
212. Zhou, J.Z., Huang, S., Sheng, J., Lu, J.Z., Wang, C.D., Chen, K.M., Ruan, H.Y. & Chen, H.S. 2012, "Effect of repeated impacts on mechanical properties and fatigue fracture morphologies of 6061-T6 aluminum subject to laser peening", *Materials Science and Engineering A*, vol. 539, pp. 360-368.
213. Sano, Y., Masaki, K., Gushi, T. & Sano, T. 2012, "Improvement in fatigue performance of friction stir welded A6061-T6 aluminum alloy by laser peening without coating", *Materials and Design*, vol. 36, pp. 809-814.
214. Toparli, M.B. & Fitzpatrick, M.E. 2011, "Residual stresses induced by laser peening of thin aluminium plates" in Scardi, P. and Azanza Ricardo, C.L., eds., *8th European Conference on Residual Stresses*, Trento, Italy, 26-28 June 2010, Materials Science Forum, vol. 681, pp. 504-509.
215. Bhamare, S., Ramakrishnan, G., Mannava, S.R., Langer, K., Vasudevan, V.K. & Qian, D. 2013, "Simulation-based optimization of laser shock peening process for improved bending fatigue life of Ti-6Al-2Sn-4Zr-2Mo alloy", *Surface and Coatings Technology*, vol. 232, pp. 464-474.
216. Grevey, D., Maiffredy, L. & Vannes, A.B. 1992, "Laser shock on a TRIP alloy: mechanical and metallurgical consequences", *Journal of Materials Science*, vol. 27, no. 8, pp. 2110-2116.
217. Chu, J.P., Rigsbee, J.M., Banaś, G. & Elsayed-Ali, H.E. 1999, "Laser-shock processing effects on surface microstructure and mechanical properties of low carbon steel", *Materials Science and Engineering A*, vol. 260, no. 1-2, pp. 260-268.
218. Yilbas, B.S., Arif, A.F.M., Shuja, S.Z., Gondal, M.A. & Shirokof, J. 2004, "Investigation Into Laser Shock Processing", *Journal of Materials Engineering and Performance*, vol. 13, no. 1, pp. 47-54.
219. Yilbas, B.S., Gondal, M.A., Arif, A.M.F. & Shuja, S.Z. 2004, "Laser shock processing of Ti-6Al-4V alloy", *Proceedings of the Institution of Mechanical Engineers, Part B: Journal of Engineering Manufacture*, vol. 218, no. 5, pp. 473-482.
220. Ivetic, G. 2011, "Three-dimensional FEM analysis of laser shock peening of aluminium alloy 2024-T351 thin sheets", *Surface Engineering*, vol. 27, no. 6, pp. 445-453.
221. Ding, K., Ye, L., 2006, *Laser Shock Peening: Performance And Process Simulation*, Woodhead, Cambridge.
222. Jiang, Y.F., Fang, L., Li, Z. & Tang, Z. 2011, "Effects of sheet thickness on residual stress distribution by laser shock processing of 7050-T7451 aluminum alloy", *Advanced Materials Research*, vol. 189-193, pp. 3778-3781.

223. Zhang, Y.K., Zhang, X.R., Wang, X.D., Zhang, S.Y., Gao, C.Y., Zhou, J.Z., Yang, J.C. & Cai, L. 2001, "Elastic properties modification in aluminum alloy induced by laser-shock processing", *Materials Science and Engineering A*, vol. 297, no. 1-2, pp. 138-143.

224. Lu, J.Z., Luo, K.Y., Zhang, Y.K., Sun, G.F., Gu, Y.Y., Zhou, J.Z., Ren, X.D., Zhang, X.C., Zhang, L.F., Chen, K.M., Cui, C.Y., Jiang, Y.F., Feng, A.X. & Zhang, L. 2010, "Grain refinement mechanism of multiple laser shock processing impacts on ANSI 304 stainless steel", *Acta Materialia*, vol. 58, no. 16, pp. 5354-5362.

225. Lu, J.Z., Luo, K.Y., Zhang, Y.K., Cui, C.Y., Sun, G.F., Zhou, J.Z., Zhang, L., You, J., Chen, K.M. & Zhong, J.W. 2010, "Grain refinement of LY2 aluminum alloy induced by ultra-high plastic strain during multiple laser shock processing impacts", *Acta Materialia*, vol. 58, no. 11, pp. 3984-3994.

226. Luo, K.-., Lu, J.-., Zhang, L.-., Zhong, J.-., Guan, H.-. & Qian, X.-. 2010, "The microstructural mechanism for mechanical property of LY2 aluminum alloy after laser shock processing", *Materials and Design*, vol. 31, no. 5, pp. 2599-2603.

227. Dorman, M., Toparli, M.B., Smyth, N., Cini, A., Fitzpatrick, M.E. & Irving, P.E. 2012 "Effect of laser shock peening on residual stress and fatigue life of clad 2024 aluminium sheet containing scribe defects", *Materials Science and Engineering: A*, vol. 548, pp.142-151.

228. Bao, R., Zhang, X. & Yahaya, N.A. 2010, "Evaluating stress intensity factors due to weld residual stresses by the weight function and finite element methods", *Engineering Fracture Mechanics*, vol. 77, no. 13, pp. 2550-2566.

229. Underwood, J.H., Pook, L.P. & Sharples, J.K. 1977, “Fatigue-crack propagation through a measured residual stress field in alloy steel” *ASTM STP 631*, pp. 402–215.

230. Kapadia, B.M. 1978, “Influence of residual stresses on fatigue crack propagation in electroslag welds” *ASTM STP 648*, pp. 244–260.

231. Lam, Y.C. and Lian, K.S. 1989, “The effect of residual stress and its redistribution on fatigue crack growth” Theoretical and Applied Fracture Mechanics, vol. 12, no. 1, pp. 59–66.

232. Todoroki A. & Kobayashi, H. 1991, “Prediction of fatigue crack growth rate in residual stress fields”, *Key Engineering Materials*, vol. 51–52, pp. 367-372.

233. Parker, A.P. 1982, “Stress intensity factors, crack profiles, and fatigue crack growth rates in residual stress fields” *ASTM STP 776*, pp. 13–31.

234. Servetti, G. 2011, *Modelling and predicting fatigue crack growth behaviour in weld induced residual stress fields* (PhD), Cranfield University.

235. Zhao, J., Zhou, J., Huang, S., Jiang, S. & Fan, Y. 2009, "Numerical simulation on fatigue crack growth of metal sheet induced by laser shot peening", *International Journal of Modern Physics B*, vol. 23, no. 6-7, pp. 1646-1651.

236. Im, J. & Grandhi, R.V. 2010, "Residual stress intensity factor based fatigue crack growth life prediction for laser peened structures", 51st AIAA/ASME/ASCE/AHS/ASC Structures, Structural Dynamics, and Materials Conference, 12-15 April, Orlando, Florida.
237. Lei, Y. 2005, "J-integral evaluation for cases involving non-proportional stressing", *Engineering Fracture Mechanics*, vol. 72, no. 4, pp. 577-596.
238. Lei, Y., O'Dowd, N.P. & Webster, G.A. 2000, "Fracture mechanics analysis of a crack in a residual stress field", *International Journal of Fracture*, vol. 106, no. 3, pp. 195-216.
239. Sherry, A.H., Da Fonseca, J.Q., Goldthorpe, M.R. & Taylor, K. 2007, "Measurement and modelling of residual stress effects on cracks", *Fatigue and Fracture of Engineering Materials and Structures*, vol. 30, no. 3, pp. 243-257.
240. SPD-10-036: Alloy 2024 sheet and plate (2001) United States: Alcoa Mill Products.
241. E8/E8M-09: Standard test methods for tension testing of metallic materials (2010) United States: ASTM International.
242. Furfari, D. (2007) *Scribe Marks – A300 – IMA Desdaen Tests*, Internal Airbus Technical Report, unpublished.
243. Abaqus version 6.11 Analysis User Manua, Dasssult Systemes.
244. Timoshenko S.P. and Goodier J.N. (1970) *Theory of elasticity*, 3rd ed. Singapore: McGraw-Hill.
245. Krueger, R. 2004, "The virtual crack closure technique: history, approach, and applications", *Applied Mechanics Reviews*, vol. 57, no. 1-6, pp. 109-143.
246. Ogura, K. & Ohji, K. 1977 “FEM analysis of crack closure and delay effect in fatigue crack growth under variable amplitude loading”. Engineering Fracture Mechanics, vol.9 pp. 471–480.
247. Ohji, K., Ogura, K. & Ohkubo, Y. 1975 “Cyclic analyses of propagating crack and its correlation with fatigue crack growth” Engineering Fracture Mechanics, vol. 7 pp.457–464.
248. Ohji, K., Ogura, K., & Ohkubo, Y. 1974 “On the closure of fatigue cracks under cyclic tensile loading” *International Journal of Fracture*, vol. 10, pp. 123-124.
249. Socie, D.F. 1977 “Prediction of fatigue crack growth in notched members under variable amplitude loading histories” *Engineering Fracture Mechanics*, vol. 9, pp. 849-865.
250. Newman, J.C. 1976 “A Finite-Element Analysis of Fatigue Crack Closure” ASTM STP 590, pp.281-301.
251. Zapatero, J., Moreno, B. & González-Herrera, A. 2008, "Fatigue crack closure determination by means of finite element analysis", *Engineering Fracture Mechanics,* vol. 75, no. 1, pp. 41-57.

252. González-Herrera, A. & Zapatero, J. 2009, "Numerical study of the effect of plastic wake on plasticity-induced fatigue crack closure", *Fatigue and Fracture of Engineering Materials and Structures,* vol. 32, no. 3, pp. 249-260.
253. Pommier, S. 2001 “Plane strain crack closure and cyclic hardening” Engineering Fracture Mechanics, vol. 69, no. 1, pp. 25-44.
254. Antunes, F.V., Borrego, L.F.P., Costa J.D. & Ferreira, J.M. 2004 “A numerical study of fatigue crack closure induced by plasticity”, *Fatigue and Fracture of Engineering Materials & Structures*, vol. 27, pp. 825-835.
255. Park, S.-., Earmme, Y.-. & Song, J.-. 1997, "Determination of the most appropriate mesh size for a 2-D finite element analysis of fatigue crack closure behaviour", *Fatigue and Fracture of Engineering Materials and Structures,* vol. 20, no. 4, pp. 533-545.
256. Wang, C.H., Rose, L.R.F. & Newman, J.C. 2002 “Closure of plane-strain cracks under large-scale yielding conditions” Fatigue and Fracture of Engineering Materials and Structures, vol. 25, pp.127-139.
257. Nagtegaal, J.C., Parks, D.M. & Rice, J.R. 1974 “On numerically accurate finite element solutions in the fully plastic range” *Computer Methods in Applied Mechanics and Engineering*, vol. 4, no. 2, pp. 153-177.
258. González-Herrera, A. & Zapatero, J. 2005, "Influence of minimum element size to determine crack closure stress by the finite element method", *Engineering Fracture Mechanics,* vol. 72, no. 3, pp. 337-355.
259. Singh, K.D., Parry, M.R. & Sinclair, I. 2011, "A short summary on finite element modelling of fatigue crack closure", *Journal of Mechanical Science and Technology,* vol. 25, no. 12, pp. 3015-3024.
260. Rodrigues, D.M. & Antunes, F.V. 2009, "Finite element simulation of plasticity induced crack closure with different material constitutive models", *Engineering Fracture Mechanics,* vol. 76, no. 9, pp. 1215-1230.
261. Kamp, N., Parry, M.R., Singh, K.D. & Sinclair, I. 2004 “Finite element and analytical modelling of roughness induced fatigue crack closure” *Acta Materialia*, vol. 52, no. 2, pp. 343-353.
262. McClung, R.C. & Sehitoglu, H. 1989, "On the finite element analysis of fatigue crack closure-2. Numerical results", *Engineering Fracture Mechanics,* vol. 33, no. 2, pp. 253-272.
263. McClung, R.C. 1991, "The influence of applied stress, crack length, and stress intensity factor on crack closure", *Metallurgical Transactions A*, vol. 22, no. 7, pp. 1559-1571.
264. Solanki, K., Daniewicz, S.R. & Newman Jr., J.C. 2004, "A new methodology for computing crack opening values from finite element analyses", *Engineering Fracture Mechanics,* vol. 71, no. 7-8, pp. 1185-1195.

265. Solanki, K., Daniewicz, S.R. & Newman Jr., J.C. 2003, "Finite element modeling of plasticity-induced crack closure with emphasis on geometry and mesh refinement effects", *Engineering Fracture Mechanics,* vol. 70, no. 12, pp. 1475-1489.
266. Blom, A.F. & Holm, D.K. 1985, "An experimental and numerical study of crack closure", *Engineering Fracture Mechanics*, vol. 22, no. 6, pp. 997-1011.
267. Palazotto, A. & Bendnarz, E. 1989 “A finite element investigation of viscoplastic-induced closure of short cracks at high temperatures” *ASTM STP 1020*, pp. 530–547.
268. Nakagaki, M. & Atluri, S.N. 1979 “Fatigue crack closure and delay effects under mode I spectrum loading: an efficient elastic–plastic analysis procedure”. *Fatigue and Fracture of Engineering Materials and Structures*, vol. 1, no. 4, pp.412–429.
269. Ashbaugh, N.E., Dattaguru, B., Khobaib, M., Nicholas, T., Prakash, R.V., Ramamurthy, T.S., Seshadri, B.R. & Sunder, R. 1997, "Experimental and analytical estimates of fatigue crack closure in an aluminium-copper alloy part II: A finite element analysis", *Fatigue and Fracture of Engineering Materials and Structures,* vol. 20, no. 7, pp. 963-974.
270. Roychowdhury, S. & Dodds, R.H. 2003 “Three-dimensional effects on fatigue crack closure in the small scale-yielding regime – a finite element study”. *Fatigue and Fracture of Engineering Materials and Structures,* vol. 26, no. 8, pp. 663-673.
271. McClung, R.C. 1991, "Crack closure and plastic zone sizes in fatigue", *Fatigue and Fracture of Engineering Materials and Structures*, vol. 14, no. 4, pp. 455-468.
272. Antunes, F.V. & Rodrigues, D.M. 2008, "Numerical simulation of plasticity induced crack closure: Identification and discussion of parameters", *Engineering Fracture Mechanics,* vol. 75, no. 10, pp. 3101-3120.
273. de Matos, P.F.P. & Nowell, D. 2007, "On the accurate assessment of crack opening and closing stresses in plasticity-induced fatigue crack closure problems", *Engineering Fracture Mechanics,* vol. 74, no. 10, pp. 1579-1601.
274. Lugo, M., Daniewicz, S.R. & Newman Jr., J.C. 2011, "A mechanics based study of crack closure measurement techniques under constant amplitude loading", *International Journal of Fatigue,* vol. 33, no. 2, pp. 186-193.
275. NASGRO Fracture Mechanics and Fatigue Crack Growth Analysis Software, Version 4.02, NASA-JSC and SwRI, September 2002.
276. Beden, S.M., Abdullah, S. & Ariffin, A.K. 2009, "Review of fatigue crack propagation models for metallic components", *European Journal of Scientific Research*, vol. 28, no. 3, pp. 364-397.
277. Hudak, S.J. 1981 “Small crack behaviour and the prediction of fatigue life”, *Journal of Engineering Materials and Technology*, vol. 103, pp.26-35.

278. El Haddad, M.H., Dowling, N.E., Topper, T.H. & Smith, K.N. 1980 “J-Integral application for short fatigue cracks at notches”, *International Journal of Fracture*, vol. 16, no. 1, pp.15-30.
279. Kaynak, C., Ankara, A. & Baker, T.J. 1996, "A comparison of short and long fatigue crack growth in steel", *International Journal of Fatigue*, vol. 18, no. 1, pp. 17-23.
280. Schijve, J. 2014 “The significance of fatigue crack initiation for predictions of the fatigue limit of specimens and structures”, *International Journal of Fatigue*, vol. 61, pp. 39-45.
281. Edwards, P.R. & Newman, J.C. 1990 *Short-crack growth behaviour in various aircraft material*, AGARD Repor No. 767.
282. ESDU (1993) *Fatigue propagation behaviour of short cracks in aluminium alloys*, 92030.
283. Newman, J.C. & Yamada, Y. 2010 “Compression precracking methods to generate near-threshold fatigue-crack-growth-rate data” *International Journal of Fatigue*, vol. 32, pp. 879-885.
284. Halliday, M.D., Cooper, C., Poole, P. & Bowen, P. 2003, "On predicting small fatigue crack growth and fatigue life from long crack data in 2024 aluminium alloy", *International Journal of Fatigue*, vol. 25, no. 8, pp. 709-718.
285. Kucharczyk, P., Sharaf, M. & Münstermann, S. 2012, "On the influence of steel microstructure on short crack growth under cyclic loading", *International Journal of Fatigue*, vol. 41, pp. 83-89.
286. Hill, M.R. & Kim, J. 2012, "Fatigue crack closure in residual stress bearing materials", ASTM STP 1586, pp. 65-86.
287. Liu, J., Yuan, H. & Liao, R. 2010, "Prediction of fatigue crack growth and residual stress relaxations in shot-peened material", *Materials Science and Engineering* A, vol. 527, no. 21-22, pp. 5962-5968.
288. Cláudio, R.A., Silva, J.M. & Byrne, J. 2012, "Fatigue life prediction of scratch damaged shot peened components", *International Journal of Structural Integrity*, vol. 3, no. 4, pp. 396-408.
289. Song, P.S. & Wen, C.C. 1999, "Crack closure and crack growth behaviour in shot peened fatigued specimen", *Engineering Fracture Mechanics*, vol. 63, no. 3, pp. 295-304.
290. Guagliano, M. & Vergani, L. 2004, "An approach for prediction of fatigue strength of shot peened components", *Engineering Fracture Mechanics*, vol. 71, no. 4-6, pp. 501-512.
291. Neuber, H. Theory of notch stresses: principle for exact stress calculation ed. Ann Arbor, MI: Edwards, 1946.
292. Peterson, R.E. Notch sensitivity. In: Metal fatigue, edited by Sines, G. and Waisman J. L. New York: MacGraw-Hill, 1959, pp. 293-306.

293. Peterson, R.E. 1959, “Analystical approach to stress concentration in aircraft materials” *WADC TR5959-507*.
294. Ciavarella, M., Meneghetti, G. 2004, “On fatigue limit in the presence of notches: Classical vs. recent unified formulations”, *International Journal of Fatigue*, vol. 26, no. 3, pp. 298-298.
295. Nishida, S.-., Zhou, C., Hattori, N. & Wang, S. 2007, "Fatigue strength improvement of notched structural steels with work hardening", *Materials Science and Engineering A*, vol. 468-470, no. SPEC. ISS., pp. 176-183.
296. Sadeler, R., Ozel, A., Kaymaz, I. & Totik, Y. 2005, "The effect of residual stresses induced by restraining on fatigue life of notched specimens", *Journal of Materials Engineering and Performance*, vol. 14, no. 3, pp. 351-355.
297. Xu, K., Hu, N. & Zhou, H. 1996, "Prediction of notch fatigue limits in a compressive residual stress field", *Engineering Fracture Mechanics*, vol. 54, no. 2, pp. 171-176.
298. Xu, K., He, J. & Zhou, H. 1994, "Effect of residual stress on fatigue behaviour of notches", *International Journal of Fatigue*, vol. 16, no. 5, pp. 337-343.
299. Benedetti, M., Fontanari, V., Santus, C. & Bandini, M. "Notch fatigue behaviour of shot peened high-strength aluminium alloys: Experiments and predictions using a critical distance method", *International Journal of Fatigue*, vol. 32, no. 10, pp. 1600-1611.
300. Zhang, P., Lindemann, J. & Leyens, C. 2010, "Influence of shot peening on notched fatigue strength of the high-strength wrought magnesium alloy AZ80", *Journal of Alloys and Compounds*, vol. 497, no. 1-2, pp. 380-385.
301. Bagherifard, S., Colombo, C. & Guagliano, M. 2013, "Application of different fatigue strength criteria to shot peened notched components. Part 1: Fracture Mechanics based approaches", *Applied Surface Science*, vol. 289, pp. 180-187.
302. Bagherifard, S. & Guagliano, M. 2013, "Application of different fatigue strength criteria on shot peened notched parts. Part 2: nominal and local stress approaches", *Applied Surface Science*, vol. 289, pp. 173-179.

A. Residual Stress Fields induced by Laser Shock Peening

The residual stress fields induced by laser shock peening were measured using the incremental hole drilling method by Toparli [132]. The incremental hole drilling technique provides residual stress in increments through the depth and in two perpendicular directions depending on the alignment of the strain gauge. The alignment of the strain gauges by Toparli [132] provided measurement of stress parallel and perpendicular to the scribe as illustrated in Figure 4.7. Throughout the current work the direction parallel to the scribe line is termed S1 and perpendicular to the scribe line (i.e. the applied loading direction) is termed S2. Details of the LSP treatments are found in section 3.5.

The residual stress field induced by the MIC1 LSP treatment is shown in Figure A.1. The induced stress field was not equibiaxial. The residual stress in the S1 direction was approximately 22× greater in magnitude in compression than the stress in the S2 direction. The residual stress in the S2 direction was in tension through most of the depth measured. There was a tensile peak of 30 MPa 40 µm from the peened surface. The residual stress field was in compression between 0.1 and 0.2 mm from the peened surface and peaked at -4.5 MPa. At depth greater than 0.2 mm from the peened surface the stress field was in tension.

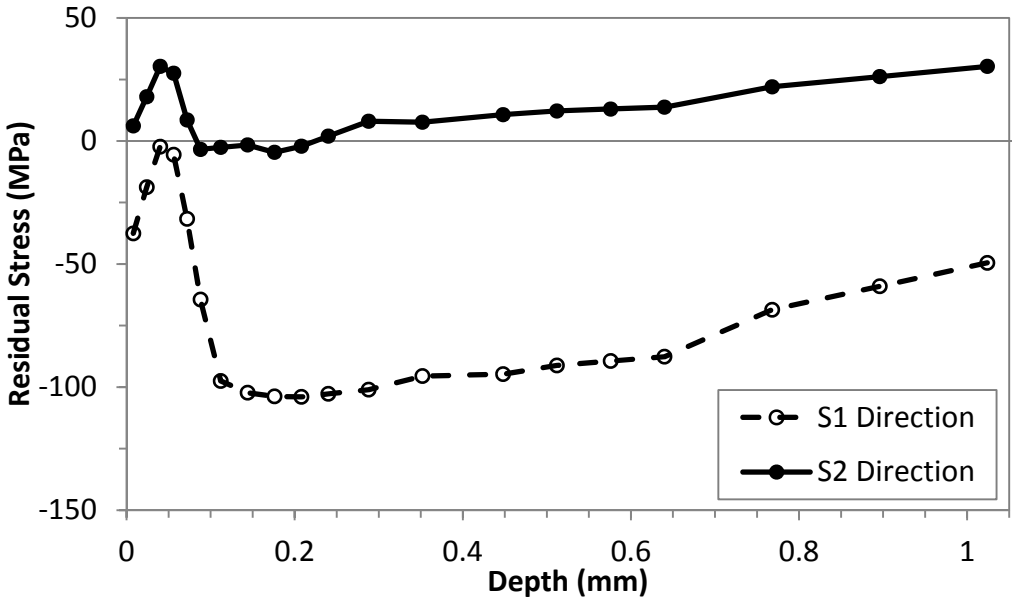

Figure A.1: Residual stress field induced by MIC1 LSP treatment and measured using incremental hole drilling technique by Toplarli [132]

The residual stress field induced by the MIC3 LSP treatment is presented in Figure A.2. Again the residual stress field was not equibiaxial. The compressive residual stress measured in the S1 direction was approximately 2× magnitude greater than the stress in the S2 direction. The residual stress in the S2 direction was in tension near

the peened surface. The tensile stress peaked at 64 MPa 40 µm from the surface. The residual stress field was in compression between 0.09 mm and 0.8 from the surface. The peak compressive stress was 44 MPa 0.21 mm from the surface.

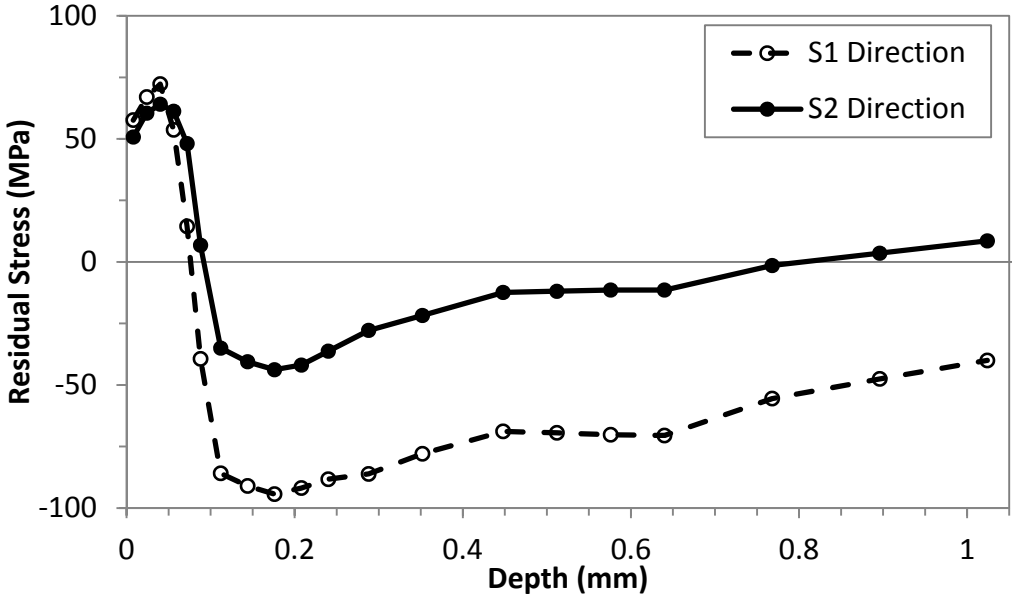

Figure A.2: Residual stress field induced by MIC3 LSP treatment and measured using incremental hole drilling technique by Toplarli [132]

The residual stress field induced by the UPM LSP treatment is shown in Figure A.3. Similar to the MIC induced residual stress fields the UPM stress field was not equibiaxial. The compressive stress measured in the S1 direction was approximately 3× greater in magnitude than the stress measured in the S2 direction. The residual stress in the S2 direction peaked in compression -106 MPa 0.11 mm from the peened surface. The compressive stress gradually reduced with increased depth and became tensile at a depth of approximately 0.7 mm. The residual stress field was in tension at the peened surface until a depth of 0.06 mm. It peaked at 61 MPa 0.04 mm from the surface.

In contrast to the previous three LSP induced residual stress fields the TOSH 0.4Ø-18 LSP treatment induced a residual stress field that was approximately equibiaxial as shown in Figure A.4. The maximum compressive stress was 223 MPa and 204 MPa in the S1 and S2 directions respectively and was 0.1 mm from the peened surface. Both compressive stress fields decreased with increased depth and transitioned to tension approximately 0.42 and 0.35 mm from the surface in the S1 and S2 directions respectively.

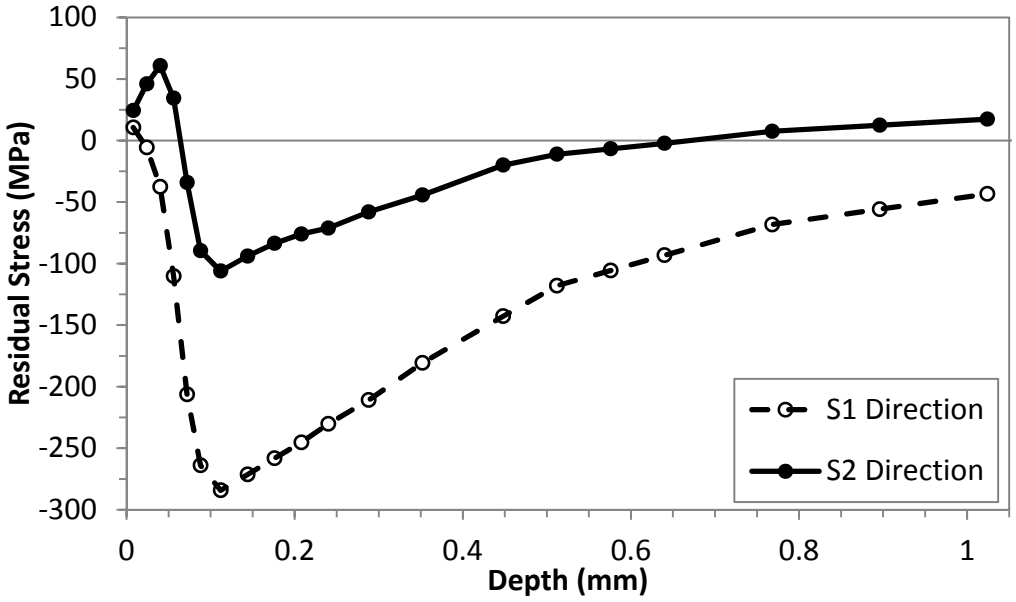

Figure A.3 Residual stress field induced by UPM LSP treatment and measured using incremental hole drilling technique by Toplarli [132]

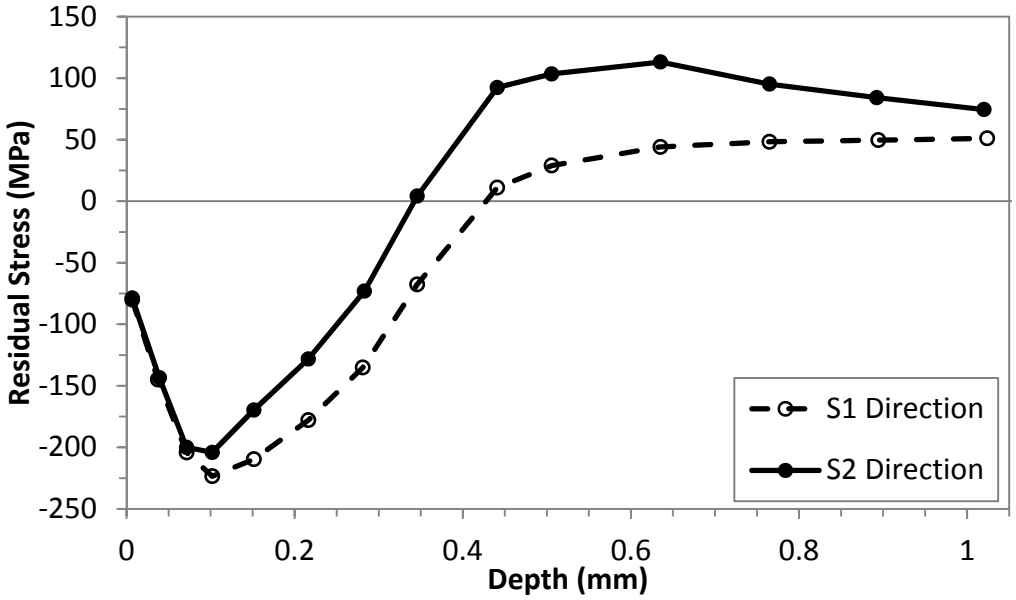

Figure A.4: Residual stress field induced by Toshiba 20-0.4Ø-18/mm^2 LSP treatment and measured using incremental hole drilling technique by Toplarli [132]

Similarly the TOSH 0.4Ø-54 treatment induced an approximately equibiaxial residual stress field that was in compression at the peened as shown in Figure A.5. The maximum compressive residual stress was -268 MPa 0.11 mm from the peened surface in the S1 direction and -299 MPa 0.08 mm from the peened surface in S2 direction. The stress fields became tensile at 0.55 mm and 0.42 mm depth in the S1 and S2 directions.

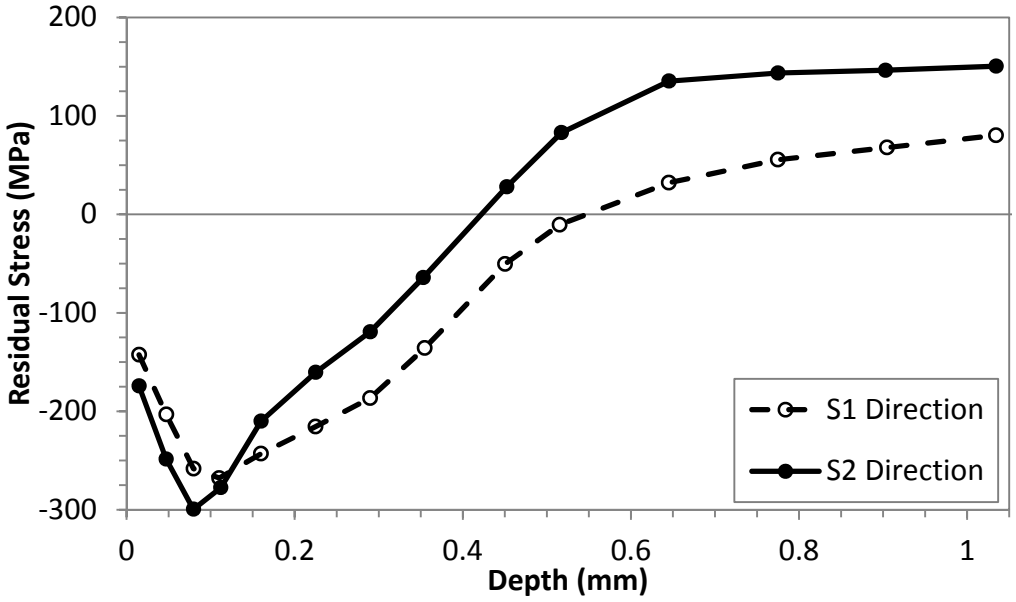

Figure A.5: Residual stress fields induced by Toshiba 20-0.4Ø-54/mm^2 LSP treatment and measured using incremental hole drilling technique by Toplarli [132]